Instituto de Microelectrónica de Madrid
Centro Nacional de Microelectrónica
Consejo Superior de Investigaciones Científicas

INSTITUTO DE MICROELECTRÓNICA DE MADRID
(CENTRO NACIONAL DE MICROELECTRÓNICA)

UNIVERSIDAD DE GRANADA
Facultad de Ciencias
Departamento de Física Aplicada

CdTe-based compounds growth by Vapor Phase Techniques

Memoria de tesis para optar al grado de doctor por la Universidad de Granada presentada por:

Marián Abellán Rubio

Director:

Prof. Dr. Fernando González-Caballero

Granada, Marzo 2011

Editor: Editorial de la Universidad de Granada
Autor: Marián Abellán Rubio
D.L.: GR 2417-2011
ISBN: 978-84-694-2911-2

Fernando González-Caballero, Catedrático de la Universidad de Granada en Granada, AUTORIZA la presentación a trámite de la Tesis Doctoral de Marián Abellán Rubio, titulada "CdTe- based compounds growth by Vapor Phase Techniques".

Granada, 10 de Enero de 2011

Fdo.: Fernando González-Caballero

Fdo. Marián Abellán Rubio

"Caminante, son tus huellas
el camino y nada más;
caminante, no hay camino,
se hace camino al andar
…"
Antonio Machado

"No hay que temer a nada en la vida, sólo tratar de comprender."

Maria Sklodowska-Curie

CSIC
Consejo Superior de Investigaciones Científicas
IMM nano
Instituto de Microelectrónica de Madrid
(Centro Nacional de Microelectrónica)

La presente Tesis Doctoral ha sido realizada en:
Instituto de Microelectrónica de Madrid
(IMM-CNM-CSIC)
C/ Isaac Newton 8, PTM
28760 Tres Cantos (Madrid)

To my father

AGRADECIMIENTOS

A estas alturas no creo que haga falta decir que esta tesis ha sido posible gracias al trabajo de muchas personas, por lo que en estas líneas me gustaría no solo reconocer sino también agradecer su contribución tanto científica como personal. La lista es extensa, pero me gustaría expresar un agradecimiento especial a las siguientes personas.

En primer lugar creo que es justo comenzar por el Dr. Nikolai Sochinskii, que me dio la oportunidad y la independencia con que pude realizar mi trabajo que se resume en esta tesis. A mi actual director el Prof. Fernando González-Caballero por ayudarme a la finalización de esta tesis.

Al Prof. Fernando Briones por mis comienzos en este mundo, del que he aprendido tanto y siempre me ha brindado su apoyo.

Por su influencia científica y personal, con un cariño especial, a "mi maestro" el Dr Pepe Anguita, por su dedicación e infinita paciencia al enseñarme a moverme en sala blanca, por sus consejos a la hora de enfrentarme a un problema de fabricación y sobre todo a disfrutar de ello. Gracias por hacérmelo todo tan fácil.

A la Dra Raquel Gonzalez no solo por las medidas RBS sino también por la corrección de este manuscrito. Gracias por ayudarme a ordenar mi caos, por transmitirme tu positivismo y entusiasmo. Y sobre todo por ayudarme, apoyarme y estar conmigo en los momentos más difíciles.

Continuando con el IMM, muchas gracias a todos!!, por vuestro apoyo y ayuda sobre todo al final de la tesis. En especial quiero agradecer a aquellos con los que he tenido la suerte de trabajar y dicho trabajo se ve reflejado en esta tesis: a los Drs, Juan Pedro Silveira, Marisol Martin y, David Fuster.

Al grupo del MBE por dejarme usar sus equipos PL y AFM.

A mis compañeros de sala blanca, Alija, Iván, Josito, Javier Martínez, Antonio Rivera y a Merce. Pero muy especialmente a Rasito, por ser el mejor compi IMMero que se puede tener.

No quisiera olvidarme de Liber del ICMAB y ahora IMB con la que compartí muchas horas de E-beam y, RIBE. Gracias por esas meriendas y esas risas.

Al Dr Edgardo Saucedo del laboratorio de crecimiento de cristales de la Universidad Autónoma de Madrid, por la colaboración en el crecimiento Bridgman, en las medidas de PL, fotoconductividad, Raman, SPS y todo lo que surgiera, tanto en la UAM como durante mi estancia en el Institute of Research and Development of Photovoltaic Energy (IRDEP-EDF-CNRS) de Paris. Sin él este trabajo tampoco habría salido a la luz.

A la mini familia del grupo de caracterización del IRDEP, dirigido por la Dra Verónica Bermúdez por permitirme la familiarización con la caracterización eléctrica y por mi agradable estancia allí. También me gustaría agradecer a la Dra Carmen Ruiz con la que compartí laboratorio, compañía y ayuda. Y al futuro o ya Dr Victor Izquierdo, compañero de estancia, por descubrirme ese apasionante mundo de la espectroscopía Raman.

A la Dra Gema Martínez-Criado por mis estancias en el ESRF, por las medidas XRD, XRF, por estar siempre dispuesta a ayudarme. A Alejandro, Jose Angel y a Julio Cesar Rimada por esos buenos momentos tanto dentro como fuera del ESRF.

Al Dr Pedro Hidalgo del departamento de física de materiales de la UCM por la ayuda en las medidas de CL.

Al Prof. Javier Marti del Centro de Nanofotónica de Valencia NTC, por la colaboración en la caracterización de las guías de onda basadas en CdTe. A Javi Blasco, Ico y Jose Ayucar.

A mis amigos del IMM, Elena, Dani, Jony, Juanito, Ram, Merce, Nuria, ZP, Javi, Raquel, Patricia, Antonio, Raquel …por el desestres que conlleva esas comidas no tan científicas y esos viernes de patinaje.

A la extensión de compañeros de administración y, mantenimiento, en especial a Margarita por ser tan buena persona.

Por último me gustaría agradecer todo el apoyo y fuerza que me transmite mi familia, la mejor que se puede tener. Gracias por enseñarme a querer y a luchar ante las adversidades sin tirar la toalla, gracias por enseñarme que juntos y con una sonrisa todo es mucho más fácil de llevar. Y el más sincero y fuerte abrazo a mis padres, gracias a ellos soy todo lo que soy.

INDEX

Chapter 1

Motivation and objectives

Chapter 1

MOTIVATION AND OBJECTIVES

The last decades have experimented remarkable developments and technological advances based on new materials and processing techniques. These advances have revolutionized the knowledge of materials science, leading to novel forms of matter with unprecedented mechanical, chemical, magnetic, optical and electrical properties. In fact, material physics is a scientific field of huge interest not only from the fundamental point of view but also from the industrial one. Industries have interest in new and more advanced materials. In this way, it is obvious that at every "moment" a new knowledge is being produced all around the world.

In this sense, probably the semiconductors have been the most studied materials in research and increasingly used on industrial scale in the last years. Clearly this fact is due to the wide range of applications from small home- equipment/ devices to even the most specialized and complex supercomputers. In the last decade, this success has starred by Silicon, Si, as semiconductor for any device.

However in recent years due to advances in new technologies, other semiconductors materials have emerged in direct competition with Si. Current technology requires the applied science to its advance, but also requires basic science which will be the basis of tomorrow's technology.

This is the case of Cadmium Telluride, CdTe and CdTe- compounds. Although these materials have been studied since the sixties, their development is significantly lower than for other semiconductors such as Si, Ge, GaAs or InP. The intrinsic characteristics of CdTe, its high atomic number, high density and relatively high value of energy gap, makes it an ideal component for many applications, such as solar cells, X- and γ- radiation detectors, dosimeters, detectors substrate for the infrared range (IR), optical waveguides and so one [1-3].

For these applications other semiconductors have been used, such as Si, and, Ge, and there is no doubt that the main reason is the vast knowledge in the preparation of these materials. Indeed, for these semiconductors, the industrial production is enormous and there are no problems for the preparation of any type of Si and Ge material, geometry, characteristics,

properties, etc, defendants in the market. However, this does not apply to CdTe- based materials, where the first barrier in their preparation is not already solved: currently, ingots of 2 inch diameter at industrial scale with acceptable quality are obtained. However, the problem is that they contain numerous grains, so only around 15% of the ingot has the quality required for subsequent applications.

In addition to the requirements of the crystal quality for CdTe material, as uniformity in composition, low density of dislocations, etc, common to any application. We have to add other specific properties depending on the final application. For example when the application is focused on radiation detectors, it is essential that the material has high resistivity, in the order of $10^9\ \Omega \cdot cm$ or higher [4,5]. Currently, obtaining material of high resistivity CdTe is still a matter of discussion at the scientific level and only very specific companies (e.g. in France Acroread) produce these materials with a specific dopant. Therefore, the research area described is unresolved issue which requires basic research, but eventually it will lead to benefits to the society in general.

The aim of this thesis is a better understanding of the properties of polycristalline CdTe to further implement its industrial applications.

Among other possibilities, CdTe- based thin films growth by Vapor Phase Epitaxy, technique, VPE, has been consider the most suitable in the manufacture of thin layer for applications, which requires the development of a simple and efficient industrial-like growth method. The VPE is a growth technique that is being used extensively in the study of II-VI semiconductor materials, and allows fast growth of $Cd_{1-x}Zn_xTe$ large area layers with an uniform composition and low manufacturing cost. While these expectations have been satisfied in many cases, other difficulties have arisen mainly due to the defects appeared during growth and the difficulty of doping because of the selfcompensating phenomena.

In the report presented here, we summarized the principal results obtained during our studies. Within this context, this dissertation is focused on trying to solve and understand fundamental aspects related to CdTe that are still unexplored. In particular to obtain high quality crystals free of Te precipitates mean a quantum leap in its development. Thus that the **organization of the thesis** is as follows:

In Chapter 2, some basic properties of CdTe material necessaries are described.

Chapter 3 is focused on the characterization techniques used to deeper understand of both CdTe- based sources and thin films growth.

Chapter 4 and 5 are focused on the optimization of both growth methods for CdTe- based compound sources and thin films, respectively. Also the role of some dopants such as: Ge, Bi, Yb and Zn in the improvement of material properties were studied.

Another fundamental aspect studied in this work is to obtain semi-insulating crystals with optimal transport charge properties. The control of the resistivity of CdTe is an exceedingly difficult task, and depends on donor dopant selection to compensate exactly the acceptor impurities and defects present in the material. The most interesting contribution studied in this field is the use of **Bi** as dopant for semi-insulating CdTe, which has very high photosensitivity and excellent properties of charge transport.

Chapter 6 is dedicated to the remarkable improvement in the quality of CdTe films after post growth thermal annealing. We will show that heating the samples, notably improves both its crystalline quality and its surface morphology. These facts that allows significantly reducing the typical concentration of native and foreign defects.

Also in chapter 7, special attention is paid to the technological process to achieve the optimal dry etching conditions suitable for CdTe- based waveguides, as well as, to the growth of CdZnTe films into nanoporous alumina. The formation of Cd(Zn)Te crystalline columnar nanostructures may be very attractive for the fabrication of micropixels suitable for further development of X-and γ-ray high resolution imaging devices.

In chapter 8, we report on theoretical and experimental results on the use of CdTe and Cd(Zn)Te as core materials for the development of all- optical photonic devices.

This idea of using (CdTe compounds) Cd(Zn)Te as optical material for implementation of highly dense all- optical photonic integrated circuits is intended to overcome the limitations in terms of nonlinear interaction that occurs in Si (mainly, the high values of two-photon absorption (TPA) and the induced free-carried absorption) whilst preserving the main advantages of the Silicon-on-insulator, SOI- based photonic technology: high index contrast (small size of the photonic components) and manufacturability with CMOS tools and process (which ensures large scale fabrication and low cost of manufacturing).

Finally, some conclusions about the work carried out are presented in chapter 9.

References

[1] D. De Nobel, F. A. Kröger, US Patent No. 3033, (1962), 791.

[2] M. Bruder, H. Figgemeier, R. Schimtt, H. Maiter. Materials Science and Engineering, **B16**, (1993), 40-43.

[3] Y. Eisen, A. Shor, C. Gilah, M. Tsabarim, P. Chouraqui, C.Hellman, E.Lubin. Nuclear Instruments and Methods in Physics Research **A 380**, (1996), 474- 478.

[4] M. Fiederle, C. Eiche, M. Salk, R. Schwarz, K.W. Benz W. Stadler, D.M. Hofmann, B.K. Meyer. J. Appl. Phys. **84** ,(1998), 6689-6692.

[5] M. Fiederle, A. Fauler, J. Konrath, V. Babentsov, J, Franc, R.B. James, IEEE. Trans Nucl. Sci. **51**, (2004), 1864-1868.

Chapter 2

General properties of CdTe

Chapter 2

GENERAL PROPERTIES OF CdTe

In this chapter we are going to review the most important physical and chemical properties of CdTe, as its crystalline structure, phase diagram, electronic properties, etc, which will be necessary to take into account for the understanding of the next chapters.

2.1 General aspects of CdTe

CdTe is an IIB-VIA semiconductor that arises from the chemical interaction between the (2+) valence states of Cadmium, **Cd**, with the (2-) valence state of Tellurium, **Te**, to form CdTe. This simple material, with a direct band gap of 1.47 eV, has many unique properties that make it appropriate for device applications. Compared to most common semiconductors CdTe has a high atomic number (Z_{Cd} = 48, Z_{Te} = 52) and, a density of 5.86 g/cm^3 which is approximately 2.5 times denser than Si (Z_{Si} = 14). As result, it strongly interacts with both X- and γ- ray radiation. Optically, it is a strong absorber in both the near-infrared (NIR) and visible regions of the electromagnetic spectrum and exhibits unusually high nonlinear optical coefficients. Like most semiconductors, CdTe's properties can be widely varied through doping. Since there are extensive researches on this topic only a few important examples will be given here. Doping CdTe with group IV elements, such Germanium, **Ge,** or Tin, **Sn**, results in the formation of deep donor levels [1]. These levels increase the resistivity of the material which is important for limiting the leakage current in detector applications. Doping with Vanadium, **V**, is considered important to the formation of the deep levels traps needed in photorefractive applications [2]. More recently, it has been discovery that Bismuth, **Bi-** doping can result in an increased photoconductivity, a finding that could be important for solar cell applications [3].

Alloying CdTe with other elements further expands its remarkable properties. Replacing some **Cd** by mercury, **Hg** atoms, to form $\mathbf{Hg_{1-x}Cd_xTe}$, allows the band gap to continuously vary from 0 to 1.47 eV [4]. This property is used to create a good detector material for both the mid- and far- infrared regions of the spectrum. Replacing **Cd** by Zinc, **Zn** atoms, to form $\mathbf{Cd_{1-x}Zn_xTe}$, results in the formation of a material with a consistently high and reproducible resistivity. Beside it has the advantage of removing parasitic **Te** precipitates that often are formed in the pure material [5]. This is important for device applications involving the detection of X- and γ-

ray radiation. Replacing some **Cd** with Manganese, **Mn** atoms, to form $\mathbf{Cd_{1-x}Mn_xTe}$, results in the formation of a diluted magnetic semiconductor (DMS) [6]. Such materials are of considerable interest as they have applications in the emerging field of spintronics, where quantum spin states are used as the medium for mass storage devices.

2.2 Crystalline structure

The dependence of the ionic character on the bond of the II-VI semiconductors compounds can present different stables lattice structures at room temperature being the **zinc blende** and **hexagonal** the most usually.

Under normal pressure and temperature conditions, CdTe presents zinc blende structure (space group F43m) which consist in two interpenetrating face centred cubic (fcc) crystals displaced one quarter of the way along the cube's body diagonal. One of the fcc is formed by Cd atoms while the second is made up of Te atoms [7]. This structure, which is identical to that of diamond, but with two types of atoms instead of one, is schematically shown in figure 2.1.

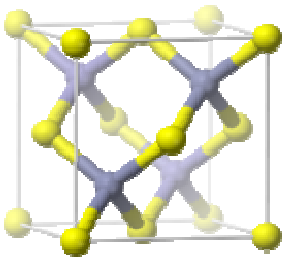

Figure 2.1. Schema of the CdTe zinc blende unit cell. (Cd atoms (gray) and Te atoms (yellow)).

While this description is adequate, a more intuitive understanding of the structure is obtained by looking normal to its (111) axis. Along this direction the structure consists of alternating layers of Cd and Te atoms. Every layer in the structure, regardless of whether it is made up of Cd or Te, takes on the form shown schematically in figure 2.2 [8].

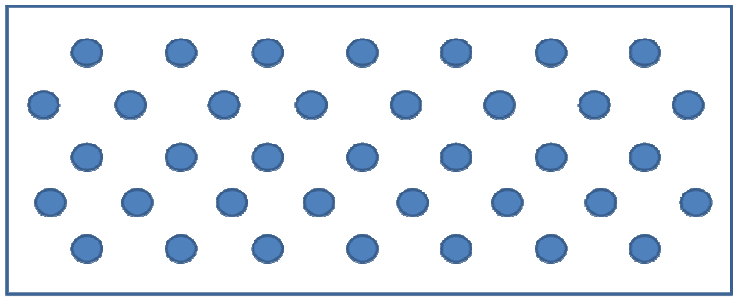

Figure 2.2. Schema of the atoms arrangement for any layer along the (111) direction. Note the six- fold symmetry.

It is important to remark that this two dimensional layer presents a six- fold symmetry. However, this is the unique stacking sequence of these layers that gives rise to the zinc blende structure. It is common to describe the stacking order for this structure as ABCABC…, meaning that the two dimensional Cd layers are laterally offset relative to each other in three unique positions (see figure 2.3).

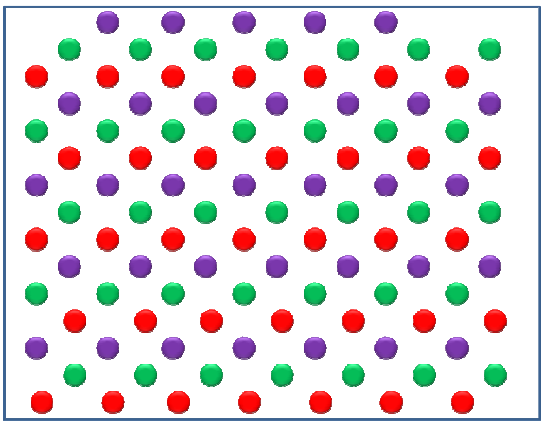

Figure 2.3. Schematic illustrating the stacking order of Cd layers (or alternatively Te) for planes along the (111) direction. Each layer (colored red, green and purple) has the same arrangement as shown in figure 2.2. The Cd layers form a stacking order along the (111) direction with a red, green, purple sequence repeated over and over.

With this being true for both the Cd and Te layers, it takes a total of six layers before the sequence is repeated. Along this stacking sequence each Cd atom tetrahedrally bonds to four Te atoms and vice versa. One of the bonds will be normal to the Cd layers while the other three laterally extend in the opposite direction at an angle of 19.47º. The in- plane rotation of these three bonds sets the stacking sequence.

At room temperature the lattice parameter reported in the literature is 6.481Å [9]. Although this value can be modify by changing the compound stochiometry.

Other II-VI semiconductors, such as CdS and CdSe, can exist in both the zinc blende and wurtzite crystal structures with the structure acquired depending upon the growth conditions [7,10]. CdTe has under rare circumstances shown this ability, but to much less of an extent [11,12]. For instance, under high pressure conditions this structure develops to ClNa structure. This hexagonal structure is given rise when a micrometric or minor crystal can be obtained. The wurtzite crystal structure of CdTe is shown schematically in figure 2.4.

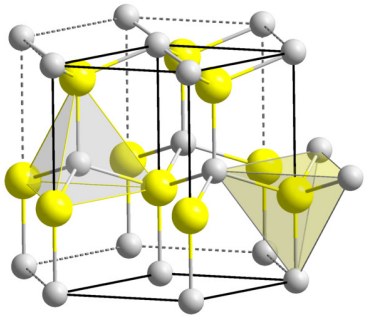

Figure 2.4. Schematic of the wurtzite unit cell of CdTe.

It exhibits a hexagonal symmetry with lattice parameter equal to a=4.58 Å and interplanar distance c=7.50 Å. While this crystal structure appears to be quite different from the zinc blende structure it is remarkably similar. Along its c- axis the wurtzite structure consists of alternating layers of Cd and Te atoms identical to that shown in figure 2.2. In fact, the only difference between the two structures is their stacking sequence. For the wurtzite structure the Cd layers are laterally offset relative to each other in one of only two unique positions, instead of the three. With the Te layers also having only two unique positions, the stacking order becomes ABAB..., for a total of four layers before the sequence is repeated. As it was the case for the zinc blende structure, each Cd atom is tetrahedrally bonded to four Te atoms and vice versa, with interatomic spacing that are virtually identical. While the wurtzite crystal structure has been studied to some extent, many of its other properties remain unknown due to limited availability and questionable quality of the material formed.

Owing to the growth condition carried out in the experiments, only the zinc blende structure is presented in this thesis.

2.3 Defects and crystalline quality

The problems present in CdTe due to its melting properties and growth conditions can limit the quality of the material. These handicaps falls into two categories: contributions of bulk volume and, surface contributions.

2.3.1 Defects of CdTe

2.3.1.1 Punctual defects

Inside of a crystal lattice, there are a number of defects linked to the atoms position. These types of defects are called punctual defects and, can be divided into **intrinsic,** which are characteristic of the material, and **extrinsic**, caused by the presence of elements not belonging to the material.

The punctual defects can be caused by a missing of one atom corresponding to its lattice position. In this case are called **vacancies**. Or an atom is placed in an interstitial position in the lattice. Therefore, these are called **interstitials**. And finally, there are **substitutional** or **antisities** defects where an atom occupies a position in the crystal lattice that does not belong them (see figure 2.5).

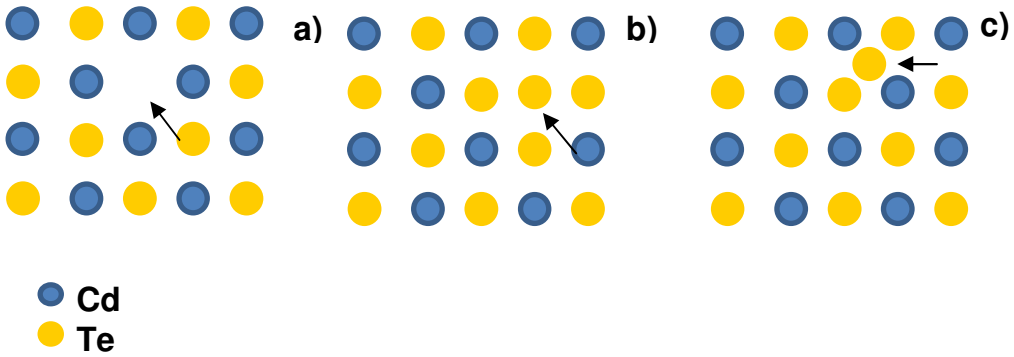

Figure 2.5. Punctual intrinsic defects in CdTe: a) vacancy, $\mathbf{V_{Cd}}$, b) antisite, $\mathbf{Cd_{Te}}$, and c) interstitial, $\mathbf{Cd_i}$.

These defects are largely responsible for the electrical behaviour of the material, and can be intentionally introduced by doping or due to native impurities incorporated into the starting material.

2.3.1.2 Lineal defects

The stress generated by thermal differences is a very common problem in crystals growth and the **dislocations** can be formed as a result of them. A dislocation is a crystallographic defect or irregularity, within a crystal structure. In fact, the ideal growth, free of all stress is impossible to achieve because of the growth processes typically occur under a temperature gradient. So this type of defect is always present in materials prepared by melting. Therefore, they can be

considerered as lineal imperfection in the crystalline lattice in which a part of the lattice crystal moves along a plane. In the particular case of CdTe materials, the dislocations give rise for the contraction of the crystal during the cooling processes. Typically, the dislocations are revealed after a chemical process (see figure 2.6).

2.3.1.3 Volumetric defects

Grain boundaries or **interfaces**, both are very common in polycrystalline CdTe bulk and thin films. In general these zones have high chemical reactivity and can be classified in coherent and incoherent.

The incoherent boundaries called **grain boundaries,** separate the crystal zones with different crystallines orientations (**grains**), while the coherent boundaries separate zones with the same crystalline specie (**twins**) grouped so that two crystallographic directions are common in both crystals (see figure 2.6). Twinning is very common in CdTe.

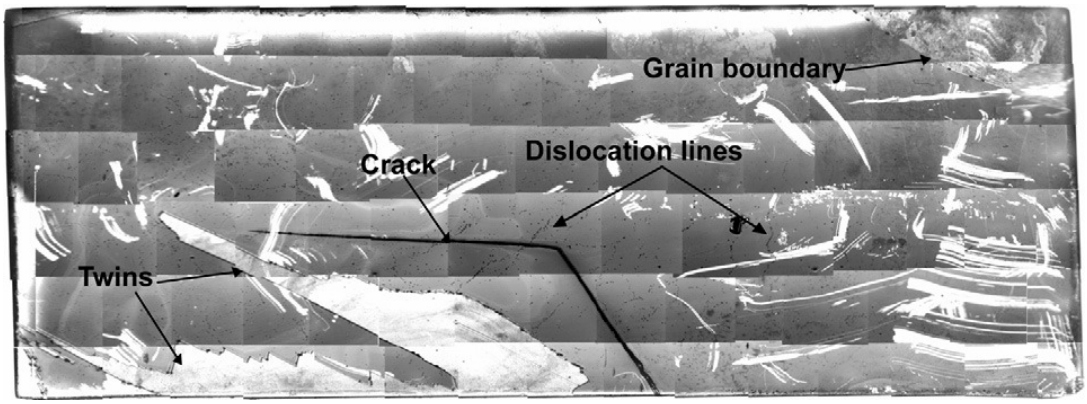

Figure 2.6. Image of the etched surface for one representative sample [13].

Other (bidimensional) volumetric defect frequently present in CdTe materials are the **cracks** originated by high thermal stress, from the heat up and cooling down processes (see figure 2.6). They can arise in the boundaries of the crystals and, can propagate along grains and twins. The problematic of the cracks is that they present a majority of impurity concentration, which significantly deteriorate the quality of the material.

On the other hand, special interest has CdTe tridimensional defects such as the **precipitates** and **inclusions**, which are the most common in semiconductors. In general, these defects appear by accumulation of the constituents of the crystals, i.e. a new phase of the

material in solid form and with different composition. The fundamental differences between these two types of defects arise because of their origin and size.

In the case of polycrystalline films the value of resistivity is affected essentially by point defects and grain boundaries, which can act as recombination centres.

The **inclusions** arise as a result of a morphological instability in the growth interface. The **Te**- rich melt is captured from the diffusion layer and accumulate at the interface. Typically, has a diameter between 1-2 μm, and can reach 30 μm. Some Te inclusions [13] are shown in following figure 2.7.

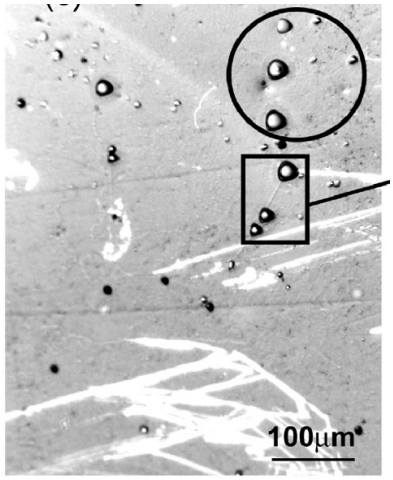

Figure 2.7. Image of a typical surface of CdZnTe: the Te inclusions lying on or near the surface [13].

The **precipitates** grow in the solid due to the retrograde character of the Te in terms of its solubility in front of the Cd and, they are formed during the cooling process. Their size is normally is not greater than 10-30 nm.

There is evidence that both inclusion and precipitates are associated with stress. Where the critical stress for dislocation nucleation is exceed, dislocation form and are associated with the inclusion or precipitates. Therefore, the distinction between the two concepts is very difficult and usually the authors tend to unify them. However, both the size and distribution of these defects are known as important parameters that greatly modify the properties of the crystal under study.

2.4 Phase diagram of CdTe

The knowledge of the phase diagram of the material is absolutely necessary to understand the results of CdTe grown by vapor phase method. In this sense, both Bridgman and Vapor Phase Epitaxy (VPE) techniques used in this thesis, require an accurate knowledge of the melt vapor transition temperature, composition and pressure of the system.

The melting points for Cd and Te are 327 ºC and 450 ºC, respectively. And the temperature at which both element react to form CdTe is approximately 650 ºC, giving rise to an exothermic reaction [14].

CdTe temperature-composition, T-X, phase diagram is depicted in figure 2.8, where the melting point maximum at 1092 ± 1 ºC for a 50% Te solid composition is shown.

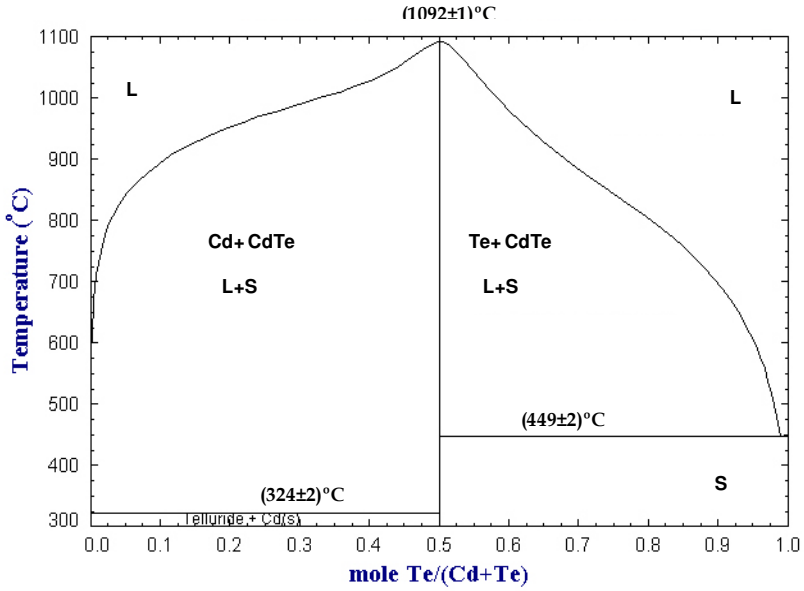

Figure 2.8. Temperature as a function of Te atomic fraction phase diagram [15].

A notably asymmetry in the region of the stoichiometric composition (Te, Cd= 50%) can be observed. This sharp zone indicates a strong interaction between the components and, it is consequence of the predominant ionic character of the Cd-Te bond. To observe this zone with more detail, in figure 2.9 we notice the influence of small variations in the Te composition on material (i.e. [16-20]).

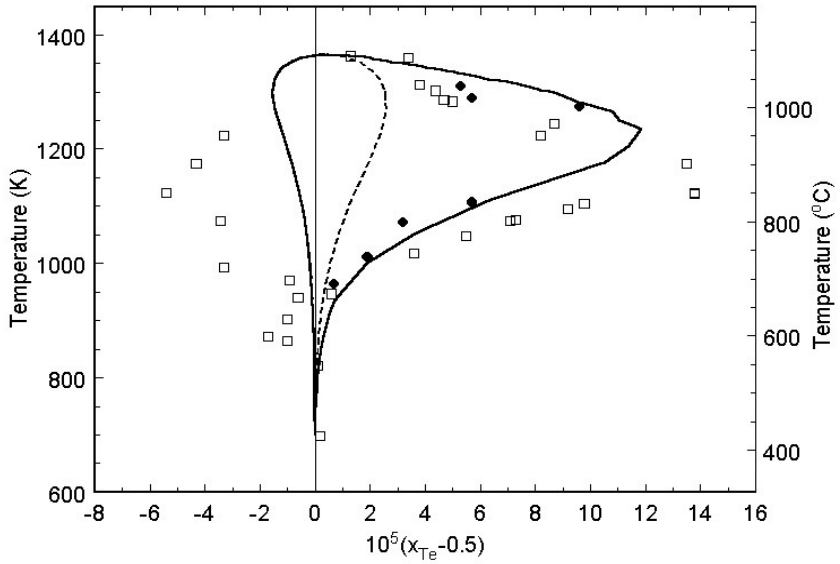

Figure 2.9. Detail of the congruent region in the T-X diagram [17]. (The best fit of the Te atom fraction in CdTe along the three phase curve (solid line) together with relevant experiments [18] (full circle), [19] (open square). The result with excluded CdTe is plotted by dash line).

As shown in figure 2.9 the maximum melting point for CdTe happens at 1092 ± 1ºC which corresponds with a slightly excess of Te. At higher temperatures the compositional homogeneity region is wider in the area that has a slight excess of Te. Therefore, the CdTe crystals growth from stoichiometric melting would have necessary a Te excess. This deviation from stoichiometric gives rise to the presence of Cd vancancies, ($\mathbf{V_{Cd}}$), and Te- antisites, ($\mathbf{Te_{Cd}}$), which results in a crystal with p- type conductivity. Under growth conditions with excess of Cd, the Cd interstitials, ($\mathbf{Cd_i}$), are the majority defects thus the n- type conductivity can be obtained [16].

It is worthwhile to mention that at lower temperatures, the deviation from stoichiometric is less significant than at higher temperatures. This is a factor to be taken into account in the cases where we prepare thin films at low temperatures or single crystals growth from the vapor phase.

Due to the general conditions of vapour phase growth, we can consider that the process occurs at approximately **constant pressure**, so both (P-T) and (P-X) projections do not provide meaningful information in these cases.

However, in general for semiconductors and especially for CdTe case, deviations in the stoichiometry during crystal growth processes have an enormous influence on optical and electrical properties of the material. Namely, non stoichiometric growth conditions cause the

condensation of point defects during the cooling process (vacancies, interstitial antisites) due to decreased retrograde of the solid-liquid line (see figure 2.7).

2.5 Band structure of CdTe

In a periodic lattice, (considered under a simple approach) it can be assumed that the atoms are joined by springs, so they can oscillate about its equilibrium position with a frequency of vibration, **ω**.

A phonon is a quantum of energy associated with lattice vibration, which is transmitted along the crystal in both longitudinal and transverse modes at different speeds. For longitudinal vibrations, the atoms move in the same direction while for transversal vibrations the atoms move perpendicular to the direction of the vibrating wave. Although the presence of phonons affects the occupation of energy level and charge transport through the crystal, it does not introduce new levels in the band gap.

If we represent the variation of the vibration frequencies along a direction in the reciprocal space $\vec{k}$(dispersion curve), we obtain two branches, called acoustical and optical. In general the acoustical branch presents the lower vibration frequencies and for small values of *k* it is observe a lineal relation. The main difference between the two branches is due to the fact that while the acoustic branch is associated with the movement of all atoms which compound the lattice, (which moves in phase as if they were a unit), the optical branch is characterized by un-phased movement of the atoms [21]. Therefore, the phonons can be classified as: (i) longitudinal optical (LO) and transversal optical (TO) and, (ii) longitudinal acoustical (LA) and transversal acoustical (TA).

The dispersion curves belonging to CdTe are presented in figure 2.10 and they have been experimental calculated by means of neutron dispersion measurements [22]. As we can observe the direction of the propagation appears with a maximum symmetry for instance in the (100), (111) and (110) directions.

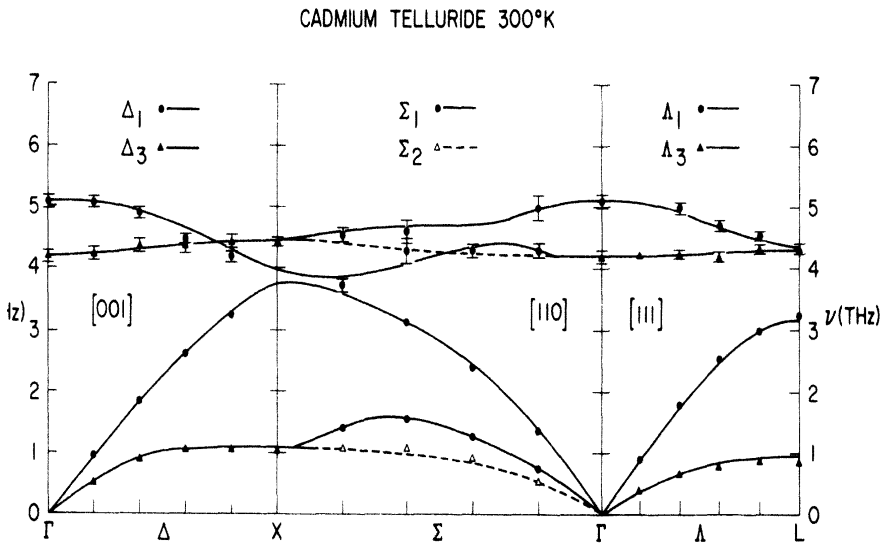

Figure 2.10. Dispersion relation curve for CdTe at 300 K [22]. Symbols represent neutron dispersion measurement; solid lines represent shell model calculation described in [22].

Like the compounds which have zinc blende structure, CdTe has three acoustic vibrational modes and, three optical modes (two transversal and one longitudinal in each case). The transversal modes present degeneration at high symmetry directions [23]. Indeed, the transversal and longitudinal optical modes in the centre of Brillouin zone of the direction Γ ($\vec{k}$=0) present values of 141 cm^{-1} (17.8 meV) and 168 cm^{-1} (21.3 meV) respectively.

The band structure associated to CdTe is calculated by means of complex calculations using pseudopotentials based on accuracy of current density functional theory (DFT) and, the local density approximation (LDA). All calculations are performed using the Spanish Initiative for Electronic Simulations with Thousand of Atoms (SIESTA) code [24], as it is shown in figure 2.11.

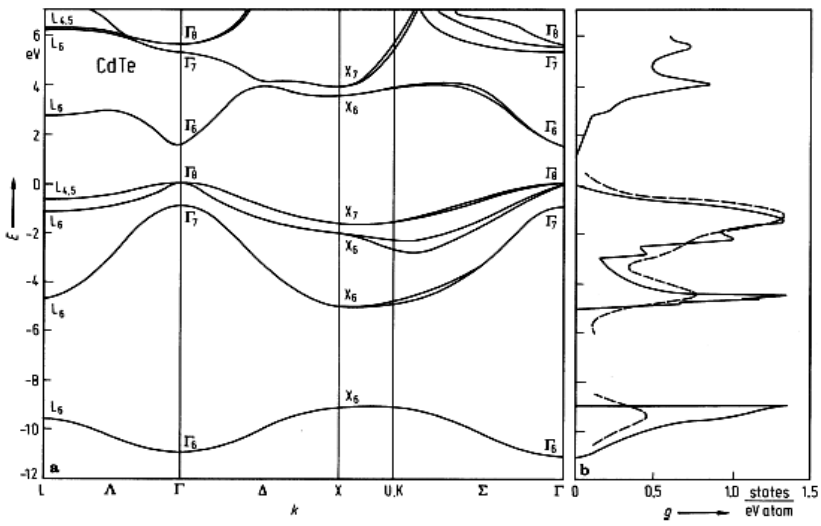

Figure 2.11. Calculated band structure for CdTe [24].

The minimum of the conduction band is at the same level of the maximum of the valence band in the **Γ** point, it shows therefore a direct transition, with a value of the band gap of 1.47 eV at room temperature.

Having this in mind, in chapters 4-7 the results of photoluminescence experiments at different temperatures (up to 4 K) are going to be presented. Founthal et al. [14] from adjust of the experimental data demonstrate that, the effect on the PL peak position due to the material quality and conductivity could be used to explain the different band gap values at room temperature. The obtained values are quite near to the variation of CdTe band gap energy with temperature follows the **Manoogian – Wooley** expression [25]:

$$E_g(T) = E_g(0) + U \cdot T^x + V \cdot \Theta\left[\coth\left(\frac{\Theta}{2T}\right) - 1\right] \qquad (2.1)$$

where $E_g(0)$ is the band gap at T = 0 K, the second term represent effect of thermal expansion of the lattice and the third tem is related to electron-phonon interactions. From this equation, the band gap energy was obtained from the value of the exciton energy measured experimentally, which corresponds to the exciton binding energy.

2.6 Transport charge properties and compensation model

The transport charge properties are determined by the carrier's properties as for instance its effective mass. For CdTe, the effective mass of electrons is relatively low (0.11 m_0) what means good transport properties. The generally accepted effective mass for holes is $0.4m_0$ [15], (being $m_0 = 9.11 \cdot 10^{-28}$ g).

2.6.1 Modified compensation model for CdTe

Generally, CdTe prepared by melting presents Cd- vacancies ($\mathbf{V_{Cd}}$) (intrinsic acceptors defects), and normally as majority impurities Na, K, Cu, etc. This gives rise to p-type conductivity. This excess of charge acceptor defects, dramatically decreases the resistivity of the material to values typically between 10^3-10^6 Ω·cm.

On one hand, the impurities introduce additional electrons on the Conduction Band, CB, and additional holes on the Valence Band, VB. Their presence breaks the periodicity of the lattice locally disturbing the band structure and, therefore appears a discrete energy level located inside of the band gap. This energy level can be situated near to the CB or VB. However, it has been shown that the compensation between shallow levels is not sufficient to explain the high resistivity of the material.

On the other hand, there is the possibility to obtain semi-insulating CdTe by three different ways: un- doped, doped with shallow or with deep donor [26-30]. The electrical properties in all these cases can be theoretically described by using a model developed in the first instance for GaAs even when for CdTe. Nevertheless, the compensation mechanism is still an open question in the literature [31,32]. Fiederle et al. [33] have presented a compensation model following the existing model for GaAs (mentioned above), which explains the high resistivity in the entire ingot by means of the **compensation with a deep donor**. The control of the concentration of this deep donor is not so sensitive to changes in composition as in the case of the shallow donors, because the resistivity is a function of surface concentration of acceptors, shallow donor and deep donor. This leds to the development of crystals with nearly constant resistivity throughout the material.

This theoretical fundament of the CdTe electrical compensation model by means of the incorporation of a deep donor in the band- gap, will be applied in Chapter 4 to explain the electrical properties of CdTe doped crystal. However this theory can be easily extended to other cases, for instance to deep acceptor level or several levels in the band gap.

In spite of that there is still disagreement about which intrinsic defects are responsible for the compensation mechanism. It is generally accepted that Te- antisite, ($\mathbf{Te}_{Cd}$), is the deep donor which explains the high resistivity. However, further investigations are needed to confirm or nominate new defects and to understand and therefore, to control the seminsulating state in CdTe.

A simplified schematic diagram of energy levels for the two cases of interest, i.e. the donor doped CdTe with deep and shallow donor [34] is shown in figure 2.12.

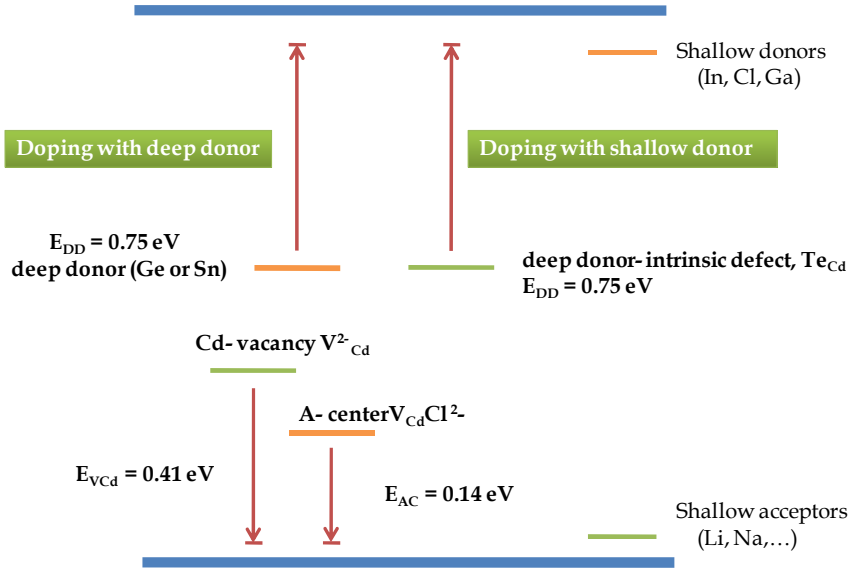

Figure 2.12. Energy levels in the band gap for the doping case with a deep donor (Ge, Sn) or, with shallow donors (In, Cl, Ga) [34].

Then, considering the doped case with a **deep donor impurity**, the free carrier densities of electrons (**n**) and of holes (**p**) in a semiconductor are defined by a nonlinear set of equations. N_{DP}^{+} is the deep donor concentration. The carrier densities and the concentrations of ionized donors N_{D}^{+} and acceptors N_{A}^{-} are coupled by the charge neutrality equation (which can be refereed to figure 2.13) [1,31]:

$$p + N_{D}^{+} + N_{DP}^{+} = n + N_{A}^{-} \qquad (2.2)$$

From the carrier density (both for n and p case) give by the Fermi- Dirac statistic we have:

$$n \cong N_{C} e^{-(E_{C}-E_{F})/kT} \qquad (2.3)$$

$$p \cong N_{V} e^{-(E_{F}-E_{V})/kT} \qquad (2.4)$$

where, $\mathbf{N_C}$ and $\mathbf{N_V}$ are the effective densities of states in the CB and the VB, respectively. $\mathbf{E_C}$ and $\mathbf{E_V}$ are the energy values of the CB and VB and, the band gap, $E_g = E_C - E_V$, **k** the Boltzmann constant and **T** is the temperature. The effective densities of states are given by:

$$N_{C} = 2\left(\frac{m_{C}^{*} kT}{2\pi\hbar^{2}}\right)^{3/2} \qquad (2.5)$$

$$N_{V} = 2\left(\frac{m_{V}^{*} kT}{2\pi\hbar^{2}}\right)^{3/2} \qquad (2.6)$$

Considering that the electron (hole) effective mass as $\mathbf{m^*_C}$ = 0.096 and $\mathbf{m^*_V}$ = 0.84, we can determine the values of $\mathbf{N_C}$ and $\mathbf{N_V}$ at a temperature of 300 K to be 7.4×10^{17} cm^{-3} and 1.9×10^{19} cm^{-3}, respectively.

Also the number of carriers in the VB must be similar than that in the CB and they are related with the intrinsic carrier number, ($\mathbf{n_i}$):

$$n_i^2 = np \cong N_C N_V e^{-E_g / kT} \qquad (2.7)$$

Once established the relationship between free carriers, we must evaluate each term of equation 2.2. Where, we have to distinguish between two types of impurities, which introduce shallow levels and the deep levels. In both cases the contribution to the density of free carriers is given by the degree of dissociation of the impurity, i.e. the density of ionized impurities that actively contribute to the net charge. This quantity is related to the total concentration of impurities according to Fermi-Dirac statistics, and then one can assert that:

$$N_A^- = \frac{N_A}{1 + e^{(E_A - E_F)/kT}} \cong N_A \qquad (2.8)$$

$$N_D^+ = \frac{N_D}{1 + e^{(E_F - E_D)/kT}} \cong N_D \qquad (2.9)$$

For acceptor (equation 2.8) and donor (equation 2.9) impurities cases that introduce shallow levels at room temperature. We can consider as optimum approximation that the concentration of ionized impurities is practically equal to the total concentration of impurities. However, this approach is not valid in that case in which an impurity incorporates a deep level, where we have:

$$N_{DP}^+ = \frac{N_{DP}}{1 + e^{(E_{DP} - E_F)/kT}} \qquad (2.10)$$

Replacing the equations from 2.8 to 2.10 in equation 2.2 so that we eliminated p, we can obtain the cubic equation for the density of electrons (**n**):

$$\frac{n^2 + n(N_A - N_D) - n_i^2}{n^2 + n(N_A - N_D - N_{DP}) - n_i^2} = -\frac{N_C}{n} e^{(E_{DP} - E_C)/kT} \qquad (2.11)$$

And therefore using for instance the equation 2.9 we can obtain de holes density, **p**. Having these two parameters the electric resistivity of the material, **ρ**, can be calculated as follows:

$$\rho = \frac{1}{q(\mu_n n + \mu_p p)} \qquad (2.12)$$

being **q** the electron charge, μ_n the mobility of electron (1000 $cm^2/V \cdot s$) and, μ_p the mobility of holes (80 $cm^2/V \cdot s$).

From these data one can concluded that high resistivity is only achieved when a deep level at 0.75 eV is assumed. This level corresponds to the middle of the band gap.

For the compensation case without a deep donor, high resistivity is only achieved at the compensation point with $N_D=N_A$. Within current technological possibilities, it is not possible to obtain high resistivity as a reproducible way. This would require that the concentrations of impurities and intrinsic defects must be controlled within 10^8 cm^{-3}.

Thus that the position of the Fermi level can be modified inside of the band gap, being a function of the temperature and, the carrier density which are a function of the impurities present in the material.

2.7 Applications of CdTe

Extensive researches have been devoted to this material, focusing in different applications. Among them the most important are as X- and γ- detectors, substrate material for MCT infrared detectors, nonlineal photonic material, solar cells, photorefractive material, etc.

2.7.1 CdTe as X- and γ- ray detectors

One of the most important CdTe device applications is as X- and γ-ray detectors. These detectors operate on the principle of photoelectric absorption where electron hole pairs are generated by the absorption of an X- or γ- ray photon [35]. CdTe is in many ways an ideal

material for the fabrication of such detectors. Compared to other semiconductors it contains high atomic number elements which are able to increase the photoelectric absorption cross-section. This effect is further enhanced by its relatively high density. With a large band gap and a low intrinsic carrier concentration it has a high enough resistivity (>10^9 Ω·cm) to maintain a low detector leakage current, critical for low noise operation. It is also high enough to limit thermally generated currents that would otherwise reduce energy resolution due to noise. At the same time, the band gap is low enough to ensure small electron-hole ionization energy. Efficient detector operation also relies on the charge carriers' ability to reach the contacts. CdTe is able to achieve this criterion as it has a high $\mu\tau$ product where μ is the carrier mobility and τ is the carrier lifetime [36].

The main advantage of these CdTe based detectors is that they can operate at room temperature while most competing technologies operate at cryogenic temperature. Removing the cryogenic cooling results in a cost reduction, lower power consumption, simplifies its operation and allows for the device to operate unattended for long periods of time. These detectors have a wide range of applications in the areas of medical imaging, industrial process monitoring, environmental safety and basic science. Most of the commercially available detectors use high quality single crystals of CdTe as the detector material. Recently, there has been a great interest in fabricating large area arrays of these detectors for imaging purposes. The most important application for such arrays is for medical X- ray imaging [37]. The substitution of analogical photographic images with a revolutionary digital technology allows for a superior image quality, faster capture readout - display process, and a computer storage capability. While the idea of large area detector arrays is very attractive, there widespread adoption has been frustrated by materials related issues. Most of the commercially available X- and γ- ray detectors use CdTe in the single crystal form as it offers high purity, homogeneous, defect free material. To obtain large area arrays, however, it is necessary for the present technologies to move away from using single crystal material and towards thick film technologies on commercially viable substrates.

The quality of existing films is far from adequate as the grain boundaries compromise the charge transport properties due to the low mobility and charge trapping. The fabrication of single domain films would obviously overcome this difficulty. Many companies use these large area detector technologies in pursuit of the very lucrative radiology market. Presently, the frontrunners are using either CdTe or amorphous selenium (α-Se) based detectors. Both of these materials have advantages and disadvantages, but by simply comparing the intrinsic properties of these two materials CdTe is the obvious choice [38]. Achieving this potential will entirely

depend upon the resolution of the material related issues associated with thick film technologies.

2.7.2 CdTe as substrate material for $Hg_{1-x}Cd_xTe$ infrared detectors

Mercury Cadmium Telluride (MCT) has become one of the most important detector materials for infrared detection. Detector arrays of this material, commonly referred to as focal plane arrays (FPAs), are used in the most sophisticated night vision equipment available [39]. It offers a high infrared absorption coefficient, high electronic mobility, a small thermal carrier generation rate and an adjustable band gap. While it offers many advantages it is a difficult material to fabricate in past because of the high vapor pressure of mercury, Hg. Initially, detectors were fabricated from bulk single crystals, but the need for large areas has driven most infrared detector applications towards thin film technologies.

The growth of high quality $Hg_{1-x}Cd_xTe$ on Si substrates would provide the best case scenario for FPAs as it would allow for the integration with Si- based readout electronics (ROIC). Its deposition on this substrate, however, has been proved to be difficult. Significant improvements have been made by introducing intermediate layers that have an improved epitaxial relationship with silicon while at the same time provide an improved template for MCT deposition [40]. CdTe has been demonstrated to be an excellent choice for this purpose. Being transparent out to 30 μm allows for the desirable backside illumination through both it and the silicon substrate. Other materials are potential sources of contamination that could result in unwanted dopants in MCT, but this is obviously not an issue for CdTe. Its use as an intermediate layer has allowed for high quality MCT to be deposited on (211) Si using molecular beam epitaxy (MBE) [41] and on (111) Si using liquid phase epitaxy (LPE) [42].

While CdTe has dramatically improved MCT detector performance, detector sensitivity is still limited by the CdTe layer. Presently, state of the art films have defect densities in the range of 10^6- 10^7 cm^{-2} [43]. This is of great concern since defects in the CdTe layer tend to introduce defects in the MCT film. Thus, any reduction in CdTe defect densities will be of immediate benefit to detector performance. It is also highly desirable for the MCT detector to be deposited on a (100) Si substrate as it is the most technologically relevant substrate. While desirable, CdTe's large lattice mismatch, significant thermal expansion coefficient mismatch, valence mismatch and a multidomain/multi-polarity growth mode, makes this a particularly challenging problem [44]. These complications lead to films with high dislocation densities, numerous stacking defects and compromised surface morphologies. As a result, many

approaches have been tried to improve the quality of the CdTe including the deposition on miscut substrates, [45] the passivation of the Si surface with As [46], the introduction of a ZnTe layer between the Si and CdTe [47], and an interrupted multi-layer anneal cycle [48]. The technological demands put on the CdTe intermediate layer will undoubtedly necessitate further novel approaches to film fabrication.

2.7.3 CdTe as novel nonlinear photonic material

More recently, there is considerable interest in using CdTe in the fabrication of non-linear optical devices. Its suitability for such devices is based on its high Kerr coefficient [49]. This coefficient ***K*** refers to a material ability to change its index of refraction in response to an electric field where the induced change is proportional to the square of the applied field:

$$\Delta n = \lambda K E^2 \qquad (2.13)$$

where **Δn** is the difference in index of refraction, **λ** is the wavelength of the light, ***K*** is the Kerr constant, and ***E*** is the amplitude of the electric field.

In addition to the high Kerr coefficient, CdTe also possesses some complimentary properties that make it a promising material for photonic applications. It has low absorption losses and a high refractive index at the telecom wavelength of 1550 nm [50]. Also, the partial substitution of Zn for Cd, to form $Cd_{1-x}Zn_xTe$, results in a drastic increase in the transmittance at 1550 nm [51]. Nonlinear photonic materials play a key role in the telecom industry. One of the most attractive applications for exploiting CdTe's nonlinear properties is in the fabrication of all optical logic gates. In fact, an international consortium has been setup to investigate the viability of such devices. The objective to PHOLOGIC (PHOtonic crystal LOGIC gates) project is to design devices based on CdTe's nonlinear effects that, if successfully implemented, could prove attractive to the telecom industry.

While the proposed devices appear very promising, significant hurdles must still be overcome. IMM, as a PHOLOGIC partner, was involved in trying to solve some of the material related issues associated with the fabrication of the proposed devices. The main challenge is to create a two-layer structure on a Si substrate, with the first layer being a ~ 4 μm thick SiO_x layer and the second layer being between (300-500) nm CdTe thin films.

This combination was chosen to obtain a high contrast in the refraction indices between the two layers. This is necessary to obtain a waveguide with a high confinement of the propagating wave. While SiO_x is an excellent choice based on its optical properties and its compatibility with Si semiconductor processing, it is a poor choice based on its suitability for CdTe film growth. SiO_x has an amorphous crystal structure and this rule out any possibility of an epitaxial relationship between it and the overlying CdTe film. Films deposited without this relationship will show a granular structure that gives rise to degradation in the optical properties. Furthermore, many of the proposed structures are photonic crystal waveguides, based on periodic arrays of pillars or cavities, with submicron feature sizes [52]. The granular nature of the films makes it difficult to pattern such small feature sizes in a predictable manner. Finding solutions to these problems may decide the success or failure of this project.

2.7.4 CdTe- based solar cell

Recently, there has been renewed interest in solar cell materials as they represent a zero carbon emission source of renewable energy. They also have many niche applications, ranging from parking meters to satellite power systems, where alternate sources of power are not readily available. With such a wide range of applications it is not surprising that the demands on the solar cells also vary widely. For example, satellite applications demand light weight, high efficiency photovoltaics where cost is of secondary importance. Large scale power systems, on the other hand, must look at the tradeoffs between cost and efficiency. Within this mixture of applications and potential applications CdTe may play an important role.

Si wafer based solar cells are, by far, the most dominant photovoltaic technology. With a market share in excess of 85%, they offer adequate efficiencies at reasonable prices. GaAs based cells are used for applications requiring the highest power output per unit area, but at a considerable cost. At the opposite extreme are solar cell materials offering the lowest manufacturing cost per unit of output power. It is here where thin film technologies can provide a real cost advantage as a relatively small amount of active material can be deposited on an inexpensive substrate. Utilizing this advantage, CdTe solar cells have become a serious challenger to other competing technologies.

CdTe is an obvious candidate for photovoltaic applications as its band gap of 1.5 eV matches well to the solar spectrum (see figure 2.13). Its absorption coefficient is very high for frequencies in the visible part of the electromagnetic spectrum.

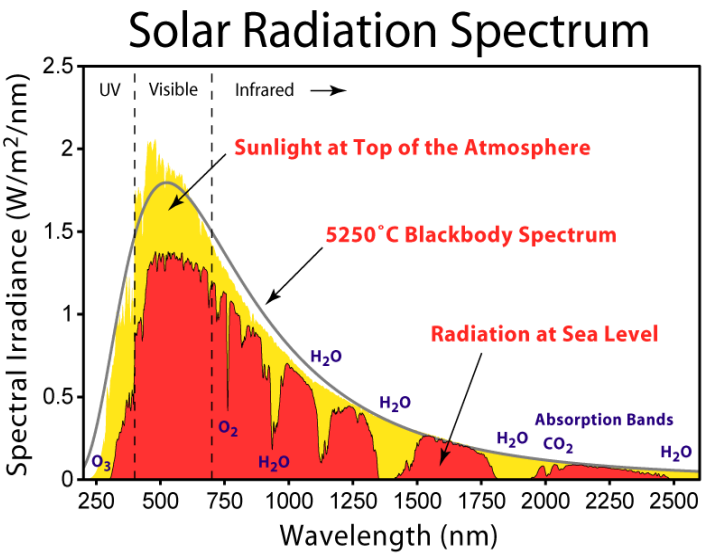

Figure 2.13. Diagram of solar radiation spectrum.

Thus, it only takes a few micrometers of material to absorb 90% of the incident light [53]. It is also easily doped as V_{Cd} readily form at the high temperatures used in the film deposition process [54]. These vacancies give rise to the p- type carriers that are needed to form a heterojunction with the n- type carriers found in CdS. Once formed, the cell is very durable as it has a high level of chemical and thermal stability.

As a result of these properties CdTe- based solar cells have received significant attention and are considered a viable alternative to Si- based technologies. In fact, CdTe solar cells yield higher wattage per square foot, at a lower price per watt of capacity. Several large scale power generation facilities have been put into operation to test the commercial viability of these solar cells in a mass production setting. There currently exists a CdTe- based solar power plant in Ohio operating at 40 MW. A second 10 MW plant is located in Germany and it will be scaled up to 100 MW in the near future.

While great strides have been made there still exist many issues that are limiting the potential of this technology. Initially, there was rapid progress in the development of these solar cells, but their maximum efficiency has been stalled at 16.5% for over ten years. With a theoretical efficiency of 29% there is still much room for improvement. In following figure 2.14 it is shown the evolution of CdTe- based solar cells and in comparison with other semiconductor technologies.

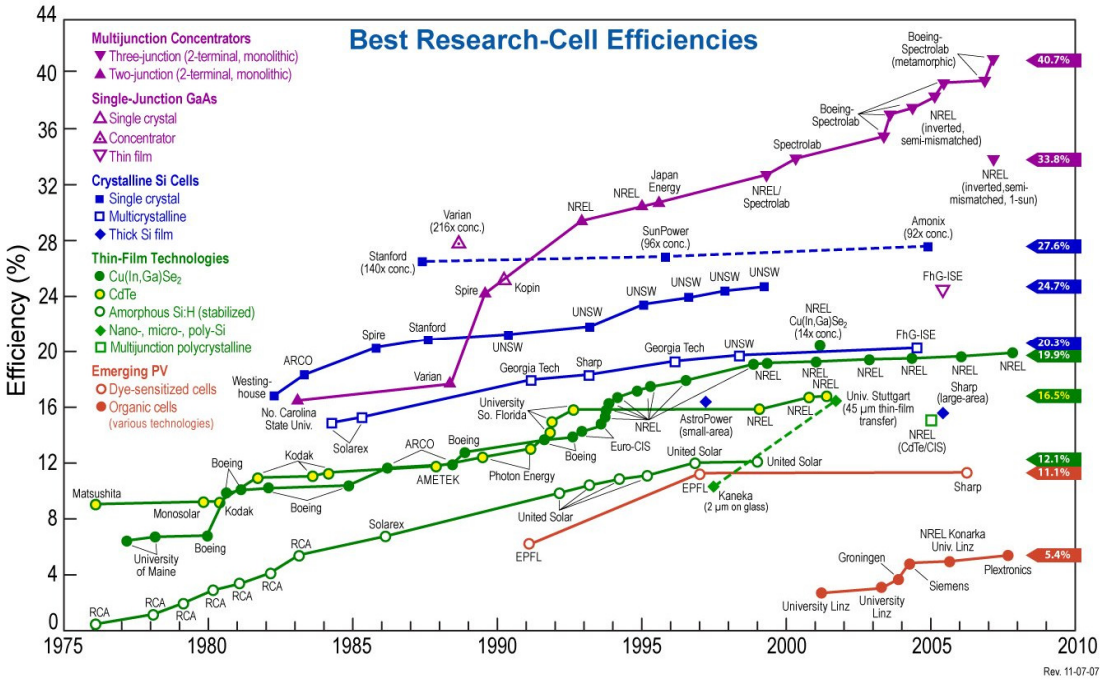

Figure 2.14. Evolution of the performance of different solar cells.

One of the main problems is that when CdTe films are deposited on inexpensive substrates such as glass the material is either polycrystalline or textured in nature. The grain boundaries associated with such morphology give rise to trapping centres that result in carrier recombination, diminishing the charge transport in the cell. Also other significant issues involve the fabrication of reliable ohmic contacts to the CdTe film and ridding the films of pinholes [55].

With the emergence of nanotechnology have come several new concepts in solar cell design that provide photovoltaic power without relying on the traditional p-n junction to separate the charge carriers. For some time there has been considerable interest in polymer based solar cells. The expectation is that they would operate at much lower efficiencies than traditional technologies, but the low fabrication costs would more than offset this limitation. If it successfully implemented such cells would provide mechanical flexibility and disposability that would be unparalleled by other solar cell technologies. Progress, however, was slow with solar cell efficiencies below 2%. It was then discovered that dramatic improvements could be made to the efficiencies by simply incorporating nanocrystals into the active area of the solar cell. The doubling of efficiencies that resulted was considered a major step forward [56]. This discovery was quickly followed by the realization that embedded nanowires provided an advantage over nanocrystals in that they provided directional charge transport that could partially offset the poor charge transport of the polymer [57]. A more recent discovery by a research group in Los Alamos has attracted considerable attention. They showed that PbSe nanoparticles exhibited quantum efficiencies substantially higher than its bulk counterpart [58].

This ability was attributed to single photons generating multiple electronic excitations and was immediately recognized for its potential in the development of high efficiency photovoltaic solar cells. With theoretical solar conversion efficiencies in excess of 40%, this discovery has become a primary driver for solar cell research. The major obstacle in obtaining such efficiencies is the harvesting of the electronic excitations from the nanoparticles to obtain charge transport. Initial attempts relied on nanoparticles imbedded in photosensitive polymers. While this approach is still being vigorously pursued, an alternative approach that utilizes nanowire technologies is gaining much attention. Here, the nanoparticles are replaced by a dense, highly crystalline nanowire array [59]. Once again, nanowires are used instead of nanoparticles to provide a directional electronic pathway able to facilitate the rapid collection of charge carriers.

While these new discoveries are very promising they are still in their beginning. Considerable effort is needed to find the most appropriate nanowire material for polymer based cells. Also, the PbSe quantum efficiencies, while impressive, may lack commercial viability as lead based products are generally avoided in commercial applications due to toxicity issues. It is still unclear whether CdTe will be the material of choice for any of these applications, but many of the properties that made it so useful to traditional solar cell technologies make it an excellent candidate for these new nanotechnologies. Much effort has gone into the fabrication of CdTe nanoparticles and nanowires using low cost, low temperature solution based routes. These materials are now being vigorously tested to determine their suitability for a variety of applications including solar cell technologies.

2.7.5 CdTe as a photorefractive material

Photorefractive materials are a class of materials that have generated much interest as they have the ability to alter their index of refraction in response to incident light. When spatially non uniform light is directed onto such a material it produces mobile charge carriers by photoionization of impurities. These charge carriers drift and diffuse in response to this non uniformity creating a local electric field variation within the material, with the resulting electric field modulation giving rise to a spatially nonuniform refractive index through the electro-optic effect. Once the illumination is removed these carriers become trapped and immobile leaving the material optically altered. This holographic memory is obviously an attractive property as it allows for the optical storage of information. With the ability to superimpose many holograms on the same volume, through variations in the angle of incidence as well as the wavelength of the incident light, it is possible to dramatically increase the optical storage density [60].

Photorefractive materials can be divided into three subgroups. The first group, which includes such prominent electro-optic materials as and lithium niobate, $LiNO_3$, and barium titanate, $BaTiO_3$, have the largest electro-optic coefficients, leading to large nonlinear effects. While these materials are excellent for long duration data storage applications, their small charge carrier mobilities lead to a relatively slow response and poor sensitivity. The second group, comprised of a group of materials referred to as the sillenites, show smaller nonlinear effects, but with a faster response. The third group, made up of compound semiconductors such as CdTe, GaP, and InP, are the fast photorefractive materials with sensitivities near the theoretical limit due to their large mobilities. While this group is impractical for long term optical storage applications their fast response times make them excellent candidates for real time holography [61].

CdTe is a promising photorefractive material for device applications. When considering such materials, a figure of merit equal to $\frac{n^3 r}{\varepsilon_r}$ is used to evaluate the nonlinear response, where **n** is the refractive index, **r** the electro-optic coefficient and $\boldsymbol{\varepsilon_r}$ is the dielectric constant. It is a measure of the index of refraction, variation induced per unit charge displaced. CdTe has the highest figure of merit with a value 1.2 times higher than for $LiNO_3$. Unlike ferroelectrics which are photosensitive at visible wavelengths, CdTe exhibits nonlinear effects in the near- infrared, a property that makes it attractive for telecom applications. With a high mobility and high recombination time it is a prime candidate for fast response applications [62].

Photorefractive applications are particularly demanding on the material properties. In fact, these limitations are the main barrier to enhance device performance. When evaluating a material its figure of merit determines the potential of material. In practice, however, the response is critically dependent on the defect structure of the material. This structure is highly sensitive to the growth conditions and to the incorporated dopants. The best photorefractive material is not the purest epitaxial film, but instead is the one where deep level defects have been controlled and optimized. CdTe, like all photorefractive semiconductors, suffers from a lack of these deep level traps. Efforts continue in this regard with the best response, thus far, being obtained for CdTe doped with V or Ti [63]. These results, however, have been obtained for bulk single crystals. Like so many other CdTe applications it will be necessary to obtain high quality films, but with the added complexity of controlling these defect traps to obtain the optimum photorefractive properties.

References

[1] M. Fiederle, A. Fauler, J. Konrath, V. Babentsov, J. Franc, and R. James, IEEE Trans. Nucl. Sci. **51**, (2004), 1864.

[2] G. Bremond, A. Zerrai, G. Marrakchi, A. Aoudia, Y. Marfaing, R. Triboulet, M.C. Busch, J.M.Koebbel, M. Hage-Ali, P. Siffert, and J.Y. Moisan, Optical Materials, **4**, (1995), 246.

[3] C.M. Ruiz, O. Vigil, E. Saucedo, G. Contreras-Puente, and V. Bermúdez, J. Phys.: Condens. Matter **18**, (2006), 7163.

[4] O.K. Wu, R.D. Rajavel, and J.E. Jensen, Materials Chemistry and Physics **4**3, (1996), 103.

[5] M. Chu, S. Terterian, and D. Ting, IEEE Trans. Nucl. Sci. **51**, (2004), 2405.

[6] A.E. Merad, M.B. Kanoun, and S. Goumri-Said, J. Magn. Magn. Mater. **302**, (2006), 536.

[7] "*Semiconductors: Data Handbook*", Otfried Madelung, Springer Ed., 3rd Edition, Berlin 2004, Secc. 2.39, 232.

[8] "*The Deposition of CdTe using exotic growth pathways*". Svetlana Neretina, PhD Thesis, Mc Master University (2007).

[9] R. Xu, Y. Wang, G. Jiac, W. Xu, S. Liang, D. Yin, J. Cryst. Growth **299**, (2007), 28-32.

[10] E. Deligoz, K. Colakoglu, and Y. Ciftci, Physica B **373**, (2006), 124.

[11] K.V. Shalimova, O.S. Bulatov, E.N. Voronkov, and V.A. Dmitriev, Soviet Physics-Crystallography **11**, (1966), 431-433.

[12] S. Neretina, R.A. Hughes, N. Braidy, W.H. Gong, J.F. Britten, N.V. Sochinskii, P. Dippo, J.S. Preston, and P. Mascher, Appl. Phys. Lett. **89**, (2006), 133101.

[13] A.Hossain, A.E.Bolotnikov, G.S.Camarda, Y.Cui, G.Yang, R.B.James, Journal of Crystal Growth **310,** (2008), 4493–4498.

[14] G. Fonthal, L. Tirado-Mejía, J.I. Marín-Hurtado, H. Ariza-Calderón, J.G. Mendoza-Alvarez, J. Phys. Chem. Solids **61** ,(2000), 579-583.

[15] "*Materials Preparation in Semiconductors and Semimetals: Cadmium Telluride*". K.Zanio, Ed. Academic Press, London (1978).

[16] M.A. Berding, Appl. Phys. Lett, **74**, (1999), 552-554.

[17] R. Grill, J. Franc, P. Höschl, I. Turkevych, E. Belas, P. Moravec, M. Fiederle and K. W. Benz. Nuclear Science Symposium Conference Record, 2001 IEEE, (2002), 2348-2352.

[18] R. Fang and R.F Brebrick, J. Phys. Chem. Solids **57**, (1996), 443-450.

[19] J. H. Greenberg, V. N. Guskov, V. B. Lazarev, and O. V. Shebershneva, "Vapor-Pressure Scanning of Nonstoichiometry in Cadmium Telluride" Mater. Res. Bull. **27**, (1992), 847-854.

[20] D. de Nobel, Philips Res. Reports **14** ,(1959), 361.

[21] "*Classical theory of the harmonic crystal" en Solid State Physics*", N.W. Ashcroft y N.D. Mermin Ed. Saunders college Publishing, New York (1976).

[22] J. M. Rowe, R. M. Nicklow, D. L. Price and K.Zanio, Phys. Rev. **B 10**, (1974), 671-675.

[23] P. Yu and M. Cardona, "*Fundamentals of Semiconductors: Physical and materials Properties, Section 2: Electronic Band Structures*". Four Edition, Springer, Berlin, (1996), 17-94.

[24] D. J. Chadi, J.P. Walter, M.L. Cohen, Y. Petroff, Phys. Rev. **B 5**, (1972), 3058-3064.

[25] A. Manoogian, J.C. Wooley, Can. J. Phys. **C 62** ,(1984), 285.

[26] A. Zappettini, T. Görog M. Zha, L. Zanotti, G. Zuccalli, C. Paorici. Journal of Crystal Growth **214/215**, (2000), 14-18.

[27] M. Fiederle, V. Babensov, J. Franc, A. Fauler, J.P Kourath, Cryst. Res. Technol, **38**, No. 7-8, (2003), 588-597.

[28] O. Panchuk, A. Savitskiy, P. Fochuk, Ye. Nykonyuk, O. Parfenyuk, L. Shcherbak, M. Ilashchuk, L. Yatsunyk and P. Feychuk. J. Crystal Growth **197**, (1999), 607-611.

[29] M. Fiederle, D. Ebling, C. Eiche, P.Hug, W. Jerger, M. Laasch, R. Schwarz, M. Salk, L. W. Benz, J. Crystal Growth **146**, (1995), 142-147.

[30]. Schwarz, W. Joerger, C. Eichie, M. Fiederle, L.W. Benz, J. Crystal Growth **146**, (1995), 92-97.

[31] E.J.Johnson, J.A. Kafalas, and R.W.Davies, J.Appl.Phys. **54** (1), (1983), 204-207.

[32] G.M. Martin, J.P. Farges, G. Jacob, J.P.Hallais and G. Poiblaud, , J.Appl.Phys. **51** (5), (1980), 2640-2852.

[33] M.Fiederle, C. Eiche, M. Salk, R. Schwarx, K. W. Benz, W. Stadler, D.M. Hofman, and B.K. Meyer, J. Appl. Phys, **84**, (1998), 6689.

[34] M. Fiederle, A. Fauler, J.P Kourath, V. Babensov,J. Franc,R.B.James , Trans. Nucl. Sci, **51**, (2004), 1864.

[35] Y. Eisen, A. Shor, and I. Mardor, IEEE Trans. Nucl. Sci. **51**, (2004), 1191.

[36] C. Szeles, Phys. Stat. Sol. (b) **241**, (2004) 783.

[37] "*Si, CdTe and CdZnTe radiation detectors for imaging applications*," T. Schulman, Ph.D. Thesis, University of Helsinki (2006).

[38] M.J. Yaffe and J.A. Rowlands, Phys. Med. Biol. **42**, (1997), 1.

[39] P. Norton, Opto-Electronics Review, **14**, (2006), 1.

[40] J.M. Peterson, J.A. Franklin, M. Reddy, S.M. Johnson, E. Smith, W.A. Radford, and I. Kasai, J.Electron. Mater. **35**, (2006), 1283.

[41] T.J. de Lyon, D. Rajavel, S.M. Johnson, and C.A. Cockrum, Appl. Phys. Lett. **66**, (1995), 2119.

[42] S.M. Johnson, J.A. Vigil, J. B. James, C.A. Cocrum, W.H. Konkel, M.H. Kalisher, R.F. Risser,T. Tung, W.J. Hamilton, W.L. Ahlgren, J.M. Myrosznyk, J. Electron. Mater. **22**, (1993), 835.

[43] L. He, L. Chen, Y. Wu, X.L. Fu, Y.Z. Wang, J.Wu, M.F. Yu, J.R. Yang, R.J. Ding, X.N. Hu,Y.J. Li, Q.Y. Zhang, J. Cryst. Growth **301–302**, (2007), 268.

[44] "*Molecular Beam Epitaxial Growth of High-Quality Cadmium Telluride on Silicon*", Y. Chen, Ph.D. Thesis, University of Illinois at Chicago (1995).

[45] Y. Xin, N.D. Browning, S. Rujirawat, S. Sivananthan, Y.P. Chen, P.D. Nellist, and S.J.Pennycook, J. Appl. Phys. **84**, (1998), 4292.

[46] M. Jaime-Vasquez, M. Martinka, R.N. Jacobs, and M. Groenert, J. Electron. Mater. **35**, (2006), 1455.

[47] G. Brill, Y. Chen, N.K. Dhar, and R. Singh, J. Electron. Mater. **32**, (2003), 717.

[48] Z. Guoming, G. Guiochon, A. Million, N.K. Dhar, and J.H. Dinan, J. Cryst. Growth **159**, (1996), 76.

[49] S. Tatsuura, T. Matsubara, H. Mitsu, Y. Sato, I. Iwasa, M. Tian, and M. Furuki, Appl. Phys.Lett. **87**, (2005), 251110.

[50] J. Rams, N.V. Sochinskii, V. Muñoz, J.M. Cabrera, Appl. Phys. A **71**, (2000), 277.

[51] J. Franc, P. Hlıdek, P. Moravec, E. Belas, P. Hoschl, L. Turjanska, and R. Varghova, Semicond.Sci. Technol. **15**, (2000), 561.

[52] M. Soljacic, S.G. Johnson, S. Fan, M. Ibanescu, E. Ippen, and J.D. Joannopoulos, J. Opt. Soc.Am. B **19**, (2002), 2052.

[53] A. Morles-Acevedo, Solar Energy **80**, (2005), 675.

[54] J. Li, Y.F. Zheng, J.B. Xu, and K Dai, Semicond. Sci. Technol. **18**, (2003), 611.

[55] M. Burgelman, J. Verschraegen, S. Degrave, P. Nollet, Thin Solid Films **480-481**, (2005), 392.

[56] I. Gur, N.A. Fromer, M.L. Geier, and A.P. Alivisatos, Science **310**, (2005), 462.

[57] B.A. Gregg and M.C. Hanna, J. Appl. Phys. **93**, (2002), 3605.

[58] R.D. Schaller, M.A. Petruska, and Victor I. Klimov, Appl. Phys. Lett. **87**, (2005), 253102.

[59] J.B. Baxter, A.M. Walker, K. van Ommering, and E.S. Aydi, Nanotechnology **17**, (2006), S304.

[60] G.C. Valley, M.B. Klein, R.A. Mullen, D. Rytz, and B. Wechsler, Ann. Rev. Mater. Sci. **18**, (1998), 165.

[61] A. Borshch, M.S. Brodin, V.I. Volkov, and V.I. Rudenko, Quantum Electron **28,** (1998), 66.

[62] H.J. von Bardeleben, J.C. Launay, and V. Mazoyer, Appl. Phys. Lett. **6**3, (1993), 1140.

[63] I. Sugiyama and Y. Nishijima, Appl. Phys. Lett. **66**, (1995), 2798.

Chapter 3

Experimental techniques

Chapter 3

EXPERIMENTAL TECHNIQUES

In this thesis, we have studied both bulk and thin films based on CdTe and CdTe-compounds obtained by Bridgman and Vapor Phase Epitaxy (VPE), respectively. For that purpose, we have employed a number of characterization techniques.

CdTe un- doped, doped with Bi and Ge, co- doped with Bi:Yb and Ge:Yb, and Cd(Zn)Te were fabricated and analyzed morphological, structural, compositional, optical and electrically, with the objective of understanding and controlling the growth process and the composition required for their different applications. The identification and removal of impurities in and from the component elements was an essential requirement.

3.1 Growth techniques for CdTe

The established methods of melt growth and vapor growth are rigorously reviewed in the literature. These and some other related studies by other authors on the preparation of doped materials and their potential relationship to structural complexes, have led to remarkable progress.

A distinctive feature of CdTe and related materials, in contrasts to materials of groups IVs and III- Vs, is the omnipresence of grain boundaries. This, together with the easy formation of dislocations, precipitates and inclusions, creates formidable challenges for material scientists.

We have just mentioned that the Bridgman technique was employed to grow bulk CdTe sources. These polycrystals were subsequently used to grow thin films by VPE.

3.1.1 Bulk crystal growth by Bridgman method

Several methods for growth of CdTe bulk crystals are now under study and development at research level. Among them, we can mention:

- The vertical Bridgman method which is usually used on an industrial scale although it is technologically complex.
- The VGF (Vertical Gradient Freeze) method [1].
- The THM (Travelling Heater Method) method [2,3].
- And other more complex from vapor phase, as Markov technique [4,5].

The vertical Bridgman method provides bulk crystal with higher quality [6-8] and bigger size than other techniques. However, its major drawback derives from the contact between the wall of the quartz and the crystal.

3.1.1.1 The Bridgman technique

This method is used to obtain crystalline materials where the starting material is contained in a growth ampoule. The ampoule is moved at a controlled rate in a furnace that has the adequate temperature gradient. When the molten material is moved vertically along the temperature gradient produces a controlled solidification along the ampoule resulting in an ingot of material required.

In this method the materials can be added separately. However, due to their different melting points, and to the exothermic chemical reaction between Cd and Te at high temperature, this method is relatively complex.

The whole growth process consists on three phases:

1) **Fusion or synthesis-reaction:** The furnace achieves a temperature above the CdTe melting point. During this process the elements inside the ampoule are melted and thus, start the chemical reaction that will lead to the semiconductor formation.

2) **Homogenization:** To avoid the segregation of the metals inside the ampoule, the furnace is oscillated by a transverse axis. The movement allows that the molten is mixed and therefore the densest element can move to the bottom of the ampoule. At the same time, the dopant segregation effect is minimized.

3) **Growth or cooling process:** Once the process of homogenization is finished, it gives way to the material solidification. For that, the ampoule will move inside the furnace thermal profile at low speed. In this way, all the material in liquid state is passed

through an area where the temperature requires it to solidify, but at such rate that the process to be carried out does not cause major tensions within the semiconductor.

Once the material is solidified, it continues to cool down slowly to room temperature. The obtained ingot is formed by a large CdTe polycrystal.

The Bridgman equipment used for the preparation of CdTe bulk crystals is shown in figure 3.1a and belongs to Crystal Growth Laboratories of the Universidad Autónoma de Madrid (LCC-UAM). A schematic view of the setup is depicted in figure 3.1b where different components of the equipment are detailed.

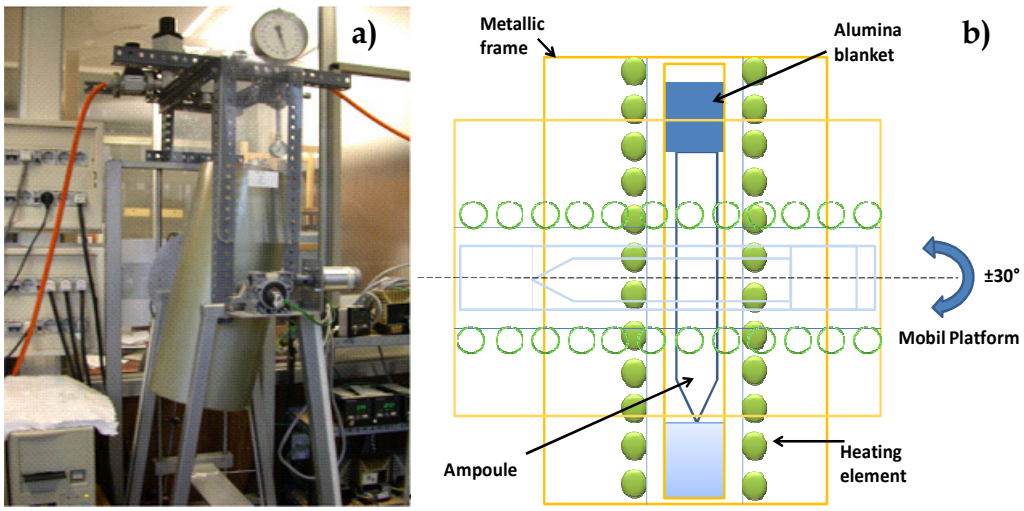

Figure 3.1. Photograph and schema of Bridgman system used for CdTe crystals growth.

It consists on a furnace with a super-Kanthal heating element that can work at temperatures up to 1300 ºC, with the possibility to oscillate down to 360 ºC at rates between 1–360 º/h. Indeed, it has a mobile platform where the displacement rate is adjustable from 0.2-100 mm/h. The system is fully automated by means of programs for temperature, ampoule movement and oscillation of the furnace.

To obtain a CdTe ingot, the semiconductor elements were introduced into a quartz ampoule sealed under vacuum. In our case, Cd, Te and the specific dopants required for each particular experiment (i.e, Ge, Bi or Yb), were the elements used. Note that, a graphite layer has been previously deposited in the ampoule to prevent the contact between the melted CdTe and the quartz [6,8].

Once loaded the ampoule, it is coupled to a turbo molecular pump, where vacuum is made for 8 hours to achieve a system pressure of $1x10^{-6}$ mbar. Afterwards, the system is sealed using the flame of a mixture of propane and oxygen.

Once the ampoule is sealed, it is mounted in a temperature-resistant ceramic platform and placed in the furnace so that the centre of the CdTe charge coincides with the furnace center. Finally, bearing in mind that the furnace has a parabolic temperature profile, with the temperature maximum at the center, it is programmed for the synthesis [7].

In the following tables 3.I, 3.II and 3.III the parameters used in the synthesis, homogenization and cooling steps, are shown.

Step	$T_{initial}$ (°C)	Ramp (°C/h)	T_{final} (°C)	t at T_{final} (h)
1	RT	50	500	12
2	500	50	900	12
3	900	50	1110	48

Table 3.I. Parameters for the reaction process between Cd and Te [7].

Note that, the process of reaction between Cd and Te is made by means of a soft ramp at low temperatures. The first step is a reaction at 500 °C, temperature slightly above the Te melting point (T_F = 450 °C). Since the reaction between Cd and Te to form CdTe is highly exothermic, it causes local temperature enhancement and might provoke damage in the growth ampoule, or even rupture.

Step	T(°C)	$Angle_{initial}$ (°)	$Angle_{final}$ (°)	Oscilating rate (°/h)	$t_{oscilation}$ (h)
1	1100	30	-30	12	24

Table 3.II. Parameters for the homogenization process of CdTe synthesized and melted [7].

Step	$T_{initial}$(°C)	Ramp (°C/h)	T_{final} (°C)	t at T_{final} (h)
1	1100	50	RT	x

Table 3.III. Parameters for the cooling process of CdTe once synthesized and homogenized [7].

As we can see in figure 3.2, the obtained ingot is formed by a large CdTe polycrystal.

Figure 3.2. CdTe polycrystal ingot growth by Bridgman technique**.**

However, the dopant segregation is largely inevitable, so prior to the use of the source material to grow thin films, it is necessary to perform a preliminary analysis of the concentration of the elements and dopants in different parts of the ingot [7-10].

3.1.1.2 CdTe growth by Bridgman method with overheating

After the synthesized process, the synthesized CdTe is introduced in other ampoule to obtain the final crystal. This new ampoule has an area to place the CdTe polycristal source and, other specific zone to place the CdTe- seed (previously prepared by Bridgman method and it is formed by two or three grains with an acceptable quality) and the seed support, as it is shown in figure 3.3.

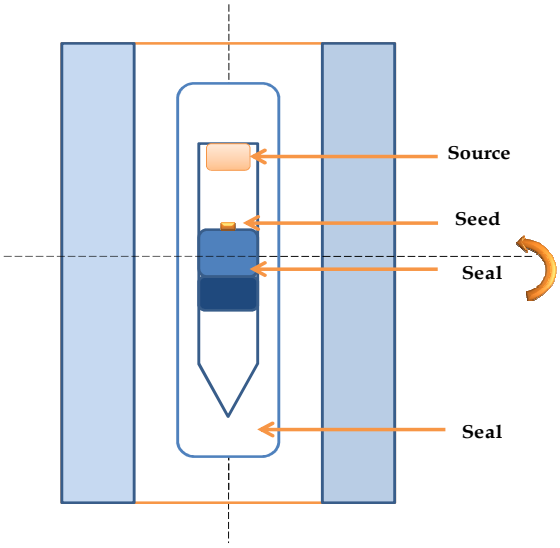

Figure 3.3. Schematic of a Bridgman furnace with overheating. The furnace can be rotated up to 130º [7].

In the same way than for synthesized process, the ampoule was placed in the furnace and it is rotated at 130º to the vertical growth axis. This is the starting position in which the CdTe crystal and seed do not make contact. With this geometry, although the source is overheated,

the temperature of the seed does not exceed the melting point, namely less than 1092 ºC (usually is between 1060-1070 ºC for different experiments tested). So, to reach the overheating condition, the temperature of the system goes from RT to ~1070 ºC at overheating rates of ~50 ºC/h. After that, the system temperature is maintained for 24 hours. Under these conditions with the furnace at 130 ºC, the melting is not in contact with the seed. When this treatment is finished, the temperature used for the growth (1110 ºC) rapidly decreases, and the furnace is then rotated 130º at a rate of about 360º/h, being therefore the source and the seed in contact. Once the vertical position is reached, with the melt at 1100 °C, we maintain these conditions during 2 hours to allow the equilibrium state to be reached. Thus, it can start the movement of the ampoule to solidify the material and obtain the final CdTe crystal. In all cases, the displacement rate of the ampoule is 0.4 mm/h. Once the melt is crystallized, the growth is stopped and the cooling process, which can elapse for 10 to 15 days, starts. The steps to follow during the cooling process are shown in table 3.IV.

Step	$T_{initial}$ (ºC)	Ramp (ºC/h)	T_{final} (ºC)	t at T_{final} (h)
1	1110	2	1050	0
2	1050	5	900	0
3	900	15	RT	X

Table 3.IV. Parameters used in the Bridgman technique with overheating.

Finally, when the system reaches room temperature the crystal obtained is extracted from the ampoule and thus, the material is prepared to be used as source for thin film growth and to be characterized.

3.1.2 Thin films growth from vapor phase

The evaporation term is often used in a generic sense to refer to different deposition processes, such as sputtering,VPE, Close Space Sublimation (CSS), Chemical Bath Deposition (CBD), Molecular Beam Epitaxial (MBE), Metalorganic vapor phase epitaxy (MOVPE), Pulse Laser Deposition (PLD), etc. In all these methods the deposited material comes from the vapor phase by means some of physical method.

VPE growth technology, is mainly applied in the semiconductor industry, and has its origin about 40 years ago [11], when evaporation surpasses sputtering as the preferred film deposition. The advantage of this technique is related to its flexibility, the control of the process

parameters, as well as its adaptability to industrial processes. This may be regarded as a peculiarity of this deposition technique.

This technology has matured relatively quickly. Therefore, taking into account that the degree of maturity of any epitaxial system seems to be inversely proportional to the physical and chemical complexity of the system, the degree of interest also influences the progress of any technology. Besides of the particular problems which take place during the process, it has other problems common to other growth techniques such as the orientation of the substrate, doping, autodoping, the system design, etc. In conclusion, some improvement is still needed in different areas.

3.1.2.1 Vapor Phase Epitaxy (VPE)

The thermal evaporation technique consists in heating until evaporation of the material to be deposited, in our case CdTe. The material vapor finally condenses in form of thin film on both cold and heated substrates surface as Si, SiO_x, sapphire, etc. Usually low pressures are used, about 10^{-6} or 10^{-5} mbar, to avoid reaction between the vapor and atmosphere. At these low pressures, the mean free path (MFP) of vapor atoms is of the same order than the vacuum chamber dimensions (~50 cm), so these particles travel in straight lines from the evaporation source towards the substrate. This originates 'shadowing' phenomena with 3D objects, especially in those regions that are not directly accessible from the evaporation source (crucible). Besides, the average energy of vapor which reach the substrate surface is generally low (about kT, i.e. tenths of eV). This fact seriously affects the morphology of the films, often resulting in little adherent material [12-14].

The **equipment** available at the IMM laboratory, a Pfeiffer Classic 500 coating system with modified growth chamber and setup geometry, is shown in figure 3.4.

The metal used as heating resistance was Molybdenum (Mo) which has a vapor pressure practically zero at the evaporation temperature (T_{evap} = 1000-2000 °C). The substrate holder has a rotated system to obtain high homogeneity in the wafers.

For our experiments, CdTe and CdTe- compounds were heated until fusion by means of an electrical current passing through the heating resistance (Joule effect). The thin films deposited were generated by the vapor flux of the material to be condensed over the substrate. The substrates were heated at temperatures between 600-850 ^{o}C, and the substrate holder was

rotated to obtain homogeneity all over the surface. Under these conditions, the deposition rate was between 1–10 nm/s.

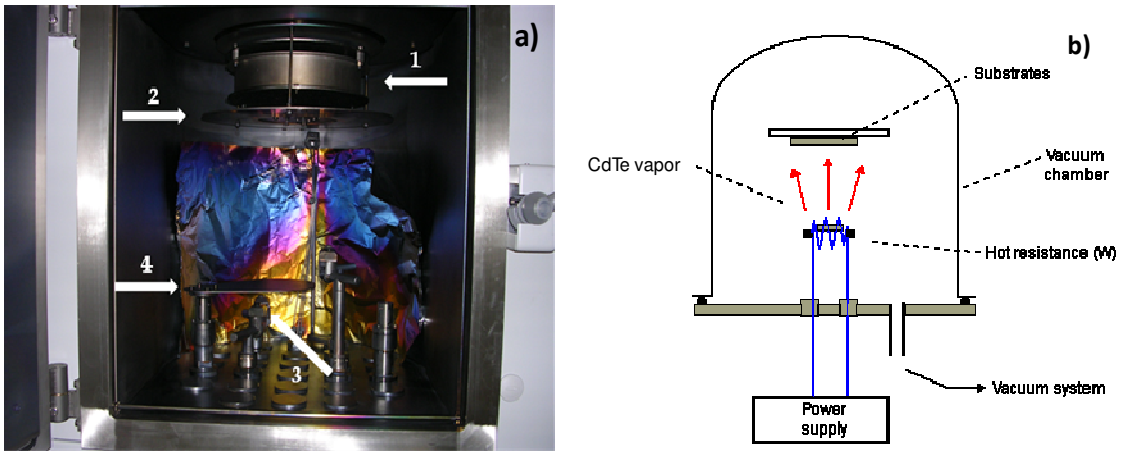

Figure 3.4. (a) Growth chamber of the VPE equipment (Pfeiffer Classic 500 system): (1) substrate heater, (2) substrate holder (3) the heated tungsten crucible with CdTe source and, (4) the shutter. (b) Schema of the growth process.

From a practical point of view, various important aspects related to the evaporation process must be considered:

a) The **Latent heat:** the heat necessary to rise the temperature (energy) of the material so that the phase change can occur.

b) The **evaporation rate of the material:** when a liquid is in equilibrium with its vapor (in a thermodynamically isolated system), the number of molecules of the gas phase, $\mathbf{N_{evap}}$, that reach the surface per unit area, **A**, and time, **t**, is equal to those that leave the liquid, and its value $\mathbf{dN_{evap}/Adt}$ is related to the liquid vapor pressure, **p***, by means the following equation:

$$\frac{dN_{evap}}{Adt} = \frac{p^*}{\sqrt{2\pi mkT}} \qquad (3.1)$$

where **m** is the mass of the molecule, **k** is the Boltzmann constant and, **T** the absolute temperature of the system.

From equation 3.1, we can show that, under optimal vacuum evaporation conditions (i.e, 10^{-6} mbar), the **time needed to form a monolayer** of residual gas on any surface inside the camera is of ≈ 1 s (assuming that all the residual gas molecules are absorbed).

c) The **transport of the material from the evaporation sources to the substrate:** the thermal evaporation is usually done with a residual pressure in the chamber, < 10^{-4} mbar.

$$MFP(cm) = \frac{5}{P(mtorr)} \qquad (3.2)$$

Under these conditions, and in contrast to other methods, thermal evaporation is a **directional process**, and only the surface of the substrate surface which is visible from the evaporation source is covered. This fact has important implications related to the thickness uniformity, overall when we want to grow thin films over large areas.

Then, three effects are combined to determine the film thickness over a substrate; the source to substrate distance, the solid angle and the angle of incidence on the substrate. So, we can make an estimate of the film thickness considering the case of a punctual source (i.e. a small area compared with the dimensions of the substrate). In this case, the number of evaporated particles (in a time **dt**), dN_{evap} from A_{evap} surface (punctual) within a solid angle **dω** in the direction **φ** with respect to the normal is so-called "law of cosine "by the geometry: $\cos\theta/r^2$ (see figure 3.5):

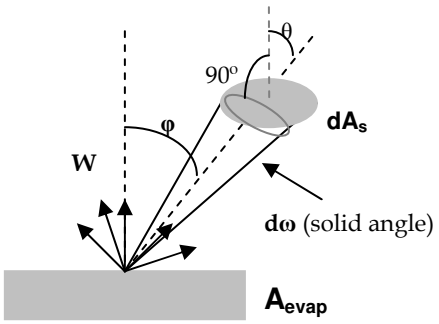

Figure 3.5. Schematic of the evaporation process from the source assuming that it behaves as a punctual surface.

$$dN_{evap}(\varphi) = V_{evap} A_{evap} dt \cdot \cos\varphi \cdot \frac{d\omega}{\pi} \qquad (3.3)$$

d) Another fact to be considered is the **average of kinetic energy** for evaporated atoms, $\mathbf{E}_c$. This is the energy imparted to the vapor in excess of the minimum necessary for phase change. According to the kinetic theory of the gases, this energy is given by:

$$E_c = \frac{3}{2} kT_{evap} \qquad (3.4)$$

Considering the typical temperatures for thermal evaporation, this energy is usually very low, about E_c = 0.2 eV, and therefore much less than the binding energy of atoms to the material.

This implies that the atoms reach the substrate surface with little energy, and thus the distance in the surface diffusion process to reach the equilibrium positions is small. This fact makes the deposited layers not very dense, and even with poor adherence to substrate [14].

In table 3.V some data collected during the last 30 years is shown as reference [15].

Name	Melting Point (°C)	Bulk Density (g/cm³)	Acustic Impedance Ratio, Z	Index of refraction @ microns	Temperature (°C) vapor pressure		Evaporation Techniques		
					10^{-8}	10^{-4}	Electron Beam	Resistance	
								Source	Material
Bi	271	9.80	0.81	.82 @ .35 4.5 @ 1.0	330	520	Xlnt.	Boat	Mo
Bi_2Te_3	585	6.82				≈600		Boat	Mo
Cd	321	8.65	0.6	1.13 @ .6	64	180	Fair	Boat	Mo
CdTe	1041	6.20	0.98	2.68 @ 4.0 2.51 @ 32		450		Box Boat	Mo Mo
Ge	937	5.32	0.51	4.20@ 2.1 4.00 @ 20	812	1167	Xlnt.	Boat Crucible	.02-.04 w
Pd	1552	12.02	0.38	1.5 @ .30 2.3 @ .54	8.42	1192	Xlnt.	Boat	.02 w
Te	452	6.25	.53	4.9 @ 6.0	157	277	Poor	Boat	Mo
Zn	419	7.14	.50	2.62 @ .69	127	250	Xlnt.	Boat Coil	Mo W
ZnTe	1240	6.34		3.56 @ .59 2.80 @ 8.0	≈600			Boat	Mo

Inficon Z- Ratio = acoustic impedance ratio, Z.
Z- Ratio Leybold Inficon.
Maxtec Inc. Acoustic Impedance (A.I.) = 8.83/ Z.
(*) Temperature at which the vapor pressure is, $p^* = 10^{-2}$ Torr.

Table 3.V. Some parameters used during this thesis.

Source- Substrate geometry

In all systems with rotated substrate holders and having the source centered under the axis of rotation, the film is thickest in the centre of the holder. This is because sources radiate in a beam subtending a narrow angle. Some studies demonstrate that the uniformity can be improved by moving the source from beneath the axis of rotation out toward the edge of the holder [16].

3.2 Rapid Thermal Annealing (RTA)

Rapid Thermal Annealing is a process used in semiconductor manufacturing that consists of heating a wafer to modify its structural properties. Thermal treatments can activate dopants, relax internal stress, diffuse materials to the interface, crystallize an amorphous layer, etc, [17-19].

The thermal treatments were carried out using a RTP-600S Rapid Thermal Processing System. Tungsten halogen lamps and cold heating chamber walls allow fast wafer heating and cooling rates. The RTA, **setup** located at CAI at the UCM is shown if figure 3.6.

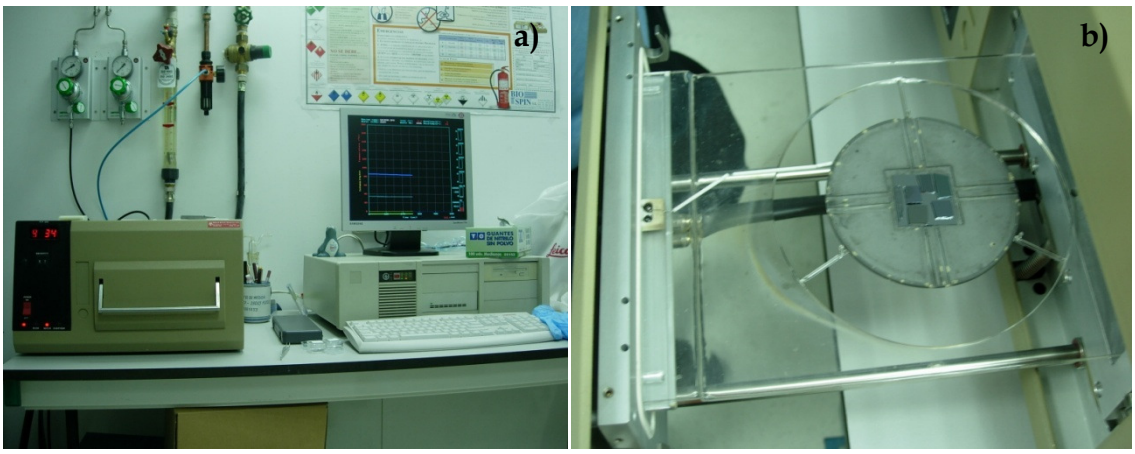

Figure 3.6. (a) RTA equipment and (b) substrate holder located at CAI (UCM).

The thermal annealing was carried out in different atmospheres such as O_2, Ar, and H_2. The temperature was selected to vary in the range between 450-1050 °C and the treatment elapsed between 10-20 s. During cooling, however, sample temperatures must be brought down slowly so the samples do not break due to thermal shock.

To protect CdTe:PdI/Si samples from impurities, they were enclosed in a graphite boat.

3.3 Characterization techniques

In this thesis, a large number of techniques are combined to obtain an optimal characterization. We have studied the results of the growth processes by both Bridgman and VPE techniques, putting effort on improving the material properties mainly regarding their crystalline quality.

Samples were morphological, structural, compositional, optical and electrically analyzed, with the objective of understanding and controlling the growth process required for different applications.

In the following table 3.VI we **summarize the characterization techniques** with their principal features used during our work.

	Technique	Requeriments	Objetives
Morphological characterization	**SEM**	Metallization	Morphological surface and, cross-section
	AFM		Morphological surface
Compositional characterization	**ICP-MS**	Aqua regia digestion	Impurities concentration, dopants, stoichiometry, minority components
	EDX	Polished surface for sources samples. Metallization	Surface composition, Precipitates (second phases)
	RBS		Elemental composition (bulk)
Estructural and Optical characterization	**XRD**		Crystalline structure, crystalline quality, lattice parameter, interplanar distance
	HS-XRD		Crystalline quality, Interplanar distance
	Raman		Lattice order degree, crystal lattice
	FTIR	Polished surface for sources samples	Crystalline quality, Te precipitates, holes concentration
	Photoluminescence	Polished surface for sources samples	Crystalline quality, impurities and compensation studies
	Cathodoluminescence	Polished surface for sources samples	Crystalline quality, impurities and compensation studies
Electrical characterization	**I-V**	Polished surface for sources samples, Metallic contacts	Impurity and compensation studies
	SPS		E_g studies and conductivity

Table 3.VI. Overview of characterization techniques with their most important features and the objectives of their applications.

3.3.1 Morphological techniques

The morphology of the samples was studied by means of Scanning Electron Microscopy (SEM) and Atomic Force Microscopy (AFM).

3.3.1.1Electronic Microscopy

The electronic microscopy is a technique used for both surface and cross-section local characterization. In our case, it was essential to understand the CdTe morphology. For thin films both its interface and cross-section with the substrate and, quantify the porosity of the material, namely a complete microscopical analysis of the samples were studied.

The scanning electron microscope (SEM) is an instrument that uses an accelerate electron beam with energies ranging from 2 KeV to 40 KeV that, by means a series of lenses, (electrical and magnetic fields applied to the beam), this is directed to the sample surface. Then, the focused beam interacts with the sample generating secondary electrons, which are detected and analyzed producing signals that contain information about the sample's surface topography.

The samples must be electrically conductive, at least on the surface. So, CdTe samples usually are coated with Au ultrathin layer of Au for SEM inspection. Coating prevents the accumulation of static electric charge on the sample during electron irradiation. The best resolution arises because backscattering and secondary electron emission near the surface are enhanced and thus an image of the surface can formed.

The **SEM Hitachi S-800 equipment** used in this thesis is located at IMM laboratories and has a field emission gun (FEG) (see figure 3.7). A FEG produce an electron beam that is smaller in diameter, more coherent and, with up to three orders of magnitude greater current density or brightness than can be achieved with conventional thermionic emitters such as tungsten or lanthanum hexaboride (LaB_6)-tipped filaments. The principal advantage in the result is a significantly improved signal-to-noise ratio and spatial resolution. This substantially improves emitter´s life and reliability compared with thermionic devices. Thus, SEM´s with FEG can reach a resolution of 20Å versus the 50 and 20Å obtained in SEM with other type of filaments [20,21].

Figure 3.7. SEM Hitachi S-800 located at IMM laboratories.

3.3.1.2 Atomic Force Microscopy, AFM

Atomic force microscopy is a powerful tool allowing a variety of surfaces to be characterized and modified at the atomic level. This technique belongs to Scanning probe microscopes (SPM) group instruments used to image and measure properties of material, chemical, and biological surfaces. The two primary forms of SPM are scanning tunneling microscopy (STM) and atomic force microscopy (AFM). In all these techniques a sharp tip is rastering across the sample and interacts with it. Then, some characteristic parameters of the interaction depends of tip- sample distance.

In the AFM case, the deflection of a very sensitive cantilever gives us information the tip-sample interaction. The cantilever is ending in an extremely sharp pyramidal tip which has a typical curvature radius of about 10 nm and is manufactured in Si and Si_xN_{1-x}.

The operation scheme of a typical AFM is shown in figure 3.8a. A laser beam is sent to the back of the cantilever, whose reflection is collected on a photodiode segmented into four sections. In order to operate and be able to get a surface image, the interaction force between the atoms of the tip located at the end of the cantilever and those of the sample surface must be kept constant. This is achieved by maintaining constant cantilever properties as its deflection, amplitude or frequency of oscillation. Depending on the function of the property to control, the AFM can operate in different modes, such as contact mode, the modulation in amplitude or frequency [22,23].

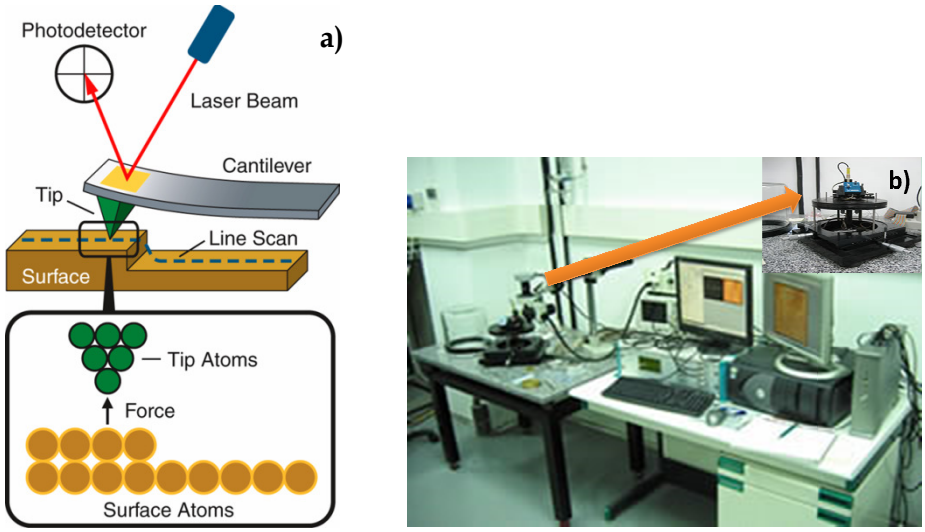

Figure 3.8. (a) Schematic of the operation of a typical AFM. (b) Nanotec AFM system, which can work in contact, and tapping mode.

Initially, we choose a value related to the property that we keep constant (deflection, amplitude or frequency of oscillation). This value corresponds to a certain intensity of light reached by the photodiode, when the tip starts moving on the surface. Topography changes can cause changes in the interaction forces in the atoms between the tip and the sample. So the property which we desire to maintain constant can change (the tip is deflected up or down, or it its oscillation amplitude can be cushioned, or the oscillation frequency can move to larger or smaller values). The feedback of the device can detect these changes in the intensity of light captured by the photodiode and send a signal to the piezoelectric. The piezoelectric can also contract or expand to recover the initial value of the property. The voltages applied to the piezoelectric are collected on a computer that transforms them into displacements from the sensitivity of the piezoelectric. In this way, it is possible make a local topographic map of the sample in the three spatial directions.

As function of the work mode of the piezoelectric (the sample movement respect the tip), the AFM can work in different regimes, as is depicted in figure 3.9.

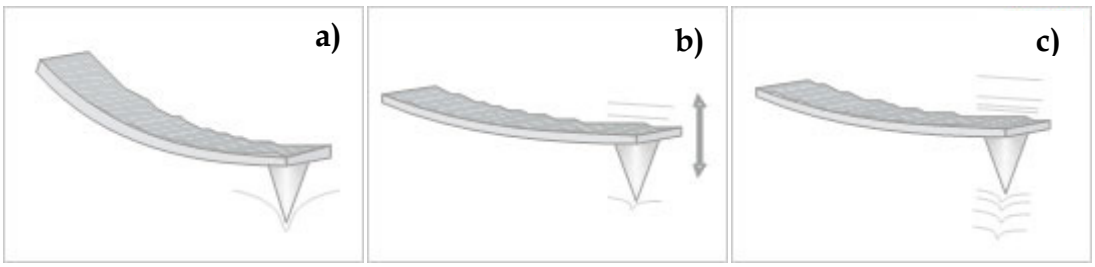

Figure 3.9. The different work modes of an AFM: (a) contact (b) non-contact and, (c) tapping mode.

Contact mode: In this mode, the deflection or repulsion between the cantilever and the sample is kept constant. The intensity of the feedback is extracted from the topographic height. Due to the fact that the topographic measurements are made with the tip perpetually in contact with the sample (see figure 3.9a), it is necessary to work with soft tips in order to avoid scratching the surface. The changes undergone by the cantilever due to repulsive forces are compensated by the displacement of piezoelectric. The basic requirement to make AFM images in contact mode is that the force of the microcantilever exerted on the sample is less than the bonding force between atoms in the tip and the sample [24].

Non-contact mode: In this mode, the tip is located about 50-150Å from the sample surface and, therefore, the Van der Waals forces acting between the tip and cantilever. For this case changes in amplitude, phase or oscillation frequency of the tip in relation with the morphology of the sample are measured, creating the image of the surface topography. This scanning provided by the feedback, and the attraction between the sample and the cantilever (which vibrates near the resonance point) remains constant (see figure 3.9b). The height is measured from the feedback intensity. The resolution in this mode is a bit lower than in contact mode due to the distance between the cantilever and sample, but the sample cannot be damaged.

Tapping mode: This mode is used to study samples when the contact mode is problematic. In this mode, Si tips sharper than conventional Si_xN_{1-x} tips can produce images of higher resolution. Besides, due to the fact that the tip is not in continuous contact with the sample surface but it is in intermittent or discrete contact, the interaction between the tip and the sample is reduced (see figure 3.9c). Indeed the friction between the sample and the tip is smaller and, it is possible to obtain atomic resolution.

By this technique the surface roughness of the samples can be calculated being usually characterized by two parameters:

- The **average roughness** that can be calculated by:

$$RMS = \sqrt{\frac{1}{N}\sum_{i=1}^{N}(z_i - Z)^2} \qquad (3.5)$$

where, $\mathbf{z_i}$ is height of a point (x,y), **N** the number of all points used in the measurement and, **Z** is defined by:

$$Z = \frac{1}{N}\sum_{i=1}^{N}(z_i - Z) \qquad (3.6)$$

- The **Hills-valleys distance**, provides information on the difference in height between the highest and lowest points on the surface [22].

Both the acquisition and the qualitative analysis from the images obtained were carried out by means the software WsxM [25].

AFM measurements were performed at IMM laboratories with **Nanotec equipment**, as is shown in figure 3.8b. It is operate in contact mode and intermittent contact (tapping). It is fitted with an optical microscope to visualize the tip-sample set so the tip can be placed on a particular area of the sample.

3.3.2 Compositional techniques

The compositional properties of the samples have been investigated by Inductively Coupled Plasma-Mass Spectroscopy (ICP-MS), Energy Dispersive X-Ray Analysis (EDX), X-ray Fluorescence, (XRF) and, Rutherford Backscattering Spectroscopy (RBS).

3.3.2.1 Inductively Coupled Plasma-Mass Spectrometry, ICP-MS

ICP-MS is used to determine the stoichiometry of the material, the dopants and different impurities concentrations, which notably influence both the optical and electrical properties of the material.

ICP technology was built upon the same principles used in atomic emission spectrometry. Samples are decomposed to neutral elements in an high temperature argon plasma and analyzed based on their mass to charge ratios. An ICP-MS can be thought of as four main processes, including sample introduction and aerosol generation, ionization by an argon plasma source, mass discrimination, and the detection system. The schematic in figure 3.10 illustrates the processes sequence.

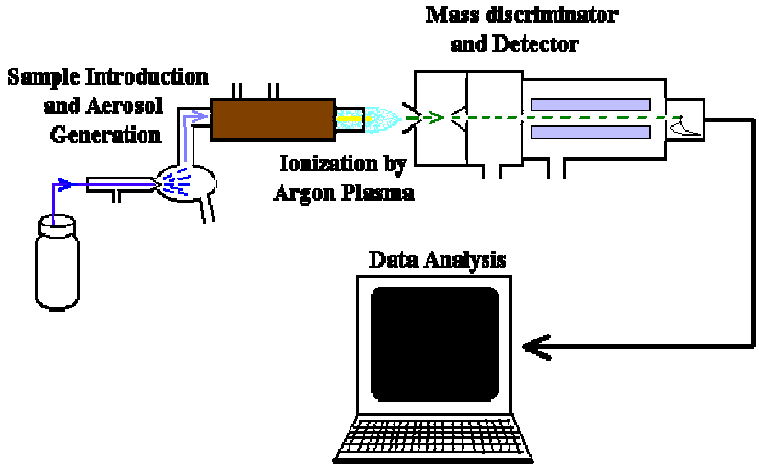

Figure 3.10. Schema of the sequence of process of a ICP-MS.

These measurements were carried out at the Interdepartmental Research Service (SIDI) of Universidad Autónoma de Madrid (UAM) by mean an **ELAN-6000 Perkin-Elmer Sciex equipment** which, consist basically of two parts: an atomizer of the sample and a mass spectrometer. To analyze the CdTe:Ge:Yb source samples, the first requirement is that it must be in aqueous solution. Due to the fact that these sources are solid, the first step is to dissolve them.

Since CdTe is an insoluble material in any medium, it requires a process of digestion to carry the sample at solution. This is done by treating the sample in hot aqua regia (~ 100 ^{o}C). Once the sample is digested in aqua regia, Cd and Te are formed, and thus they can be easily dissolved in water. Usually 2 μm of CdTe, 1 mL of aqua regia for digestion and, 2 mL of water to the solution, are used.

The sample is then injected into the atomizer forming an aerosol in the presence of an Ar flow. This aerosol is transformed at high plasma temperature due to the presence of an oscillating magnetic field, ionizing the atoms. Once the sample is atomized and ionized, the plasma enters in the mass spectrometer where a quadrupole filter separates the components according to their charge/mass ratio, to quantify its composition. The equipment used is only capable of analyzing positive ions, therefore elements such as C, N, O and the halogens cannot be quantified. The sensitivity of the equipment for most of the elements that can be quantified is in the order of parts per billion (ppb) [26].

In our particular case, this technique allows us to determine the Cd/Te ratio, (it is an approximation of the stoichiometry of the materials), to analyze the dopants concentration (for

instance to see their distribution along the ingot), and to analyze almost all impurities present in the sample.

3.3.2.2 Energy dispersive X- ray spectroscopy, EDX

EDX or EDS is a chemical microanalysis technique used in conjunction with scanning electron microscopy (SEM). This technique is capable of providing elemental imaging of the main phases as well as of the trace elements at a submicrometer scale.

The operating principle of the EDX analyzer is related to the characteristic X- rays emitted from the sample surface, when it is excited by the electrons that impact on it from the electron beam microscope. Namely, the electrons from the electron microscope are accelerated with a voltage of ~20 kV and they impact on the surface of the sample, exciting the elements present which are de-excited emitting their characteristic X- rays. The study of the emission spectrum allows us to identify the elements present in the samples [27,28].

The sensitivity of the technique is poor, usually 1% by mass and it is only useful to identify and quantify seconds phases, precipitates, etc., i.e., the kind of defects with high concentration of its components. In some cases it is capable of quantifying impurities in low concentrations. The areas to be examined are from hundreds of nanometers to several millimeters. Figure 3.11 shows a typical EDX spectrum obtained from a CdTe sample nominally pure.

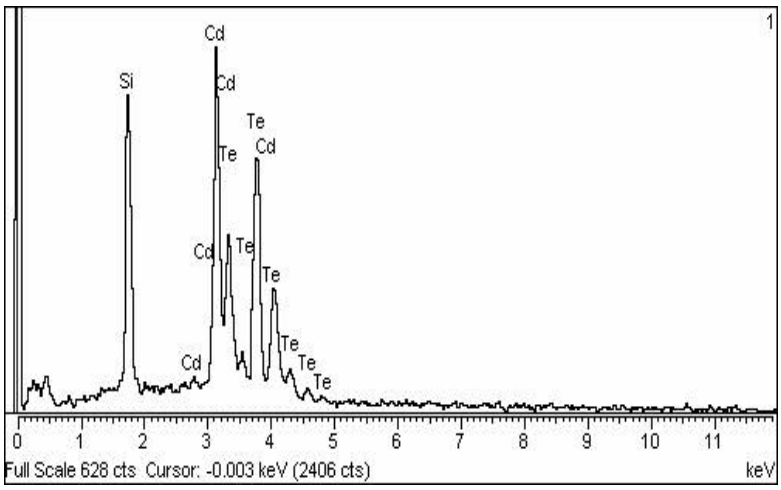

Figure 3.11. Typical EDX spectra of a CdTe/Si thin film growth by VPE.

This technique is available at the Interdepartmental Research Service (SIDI) of Universidad Autónoma de Madrid (UAM) and, in the material department of the Universidad Complutense de Madrid (UCM). SIDI equipment consists on a DX4i EDAX analyzer coupled to a Philips XL30 SEM.

3.3.2.3 X- ray Fluorescence, XRF

X- ray fluorescence is another technique used to obtain elemental and chemical imaging of the main phases and the trace elements at submicrometer scale.

This technique is powerful to carry out quantitative elemental analysis in semiconductors [29,30]. Using exciting radiation that it is produced at a synchrotron radiation (SR) source, we have the advantage of providing an extremely high number of photons from a small source, which can be subsequently focused in order to carry out measurements with spot sizes within the range of microns. Moreover, while the source itself provides continuous radiation over a wide energy range, it is possible to optimize the recording conditions by selecting the excitation energy with a monochromator.

The measurements were performed at the **ID18F beamline at the European Radiation Facility (ESRF)** in Grenoble France. The setup is shown in figure 3.12.

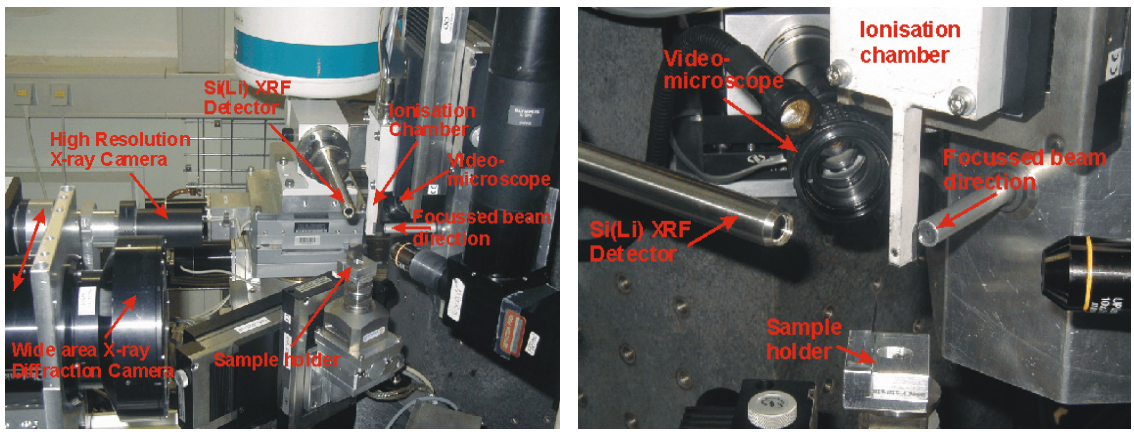

Figure 3.12. XRF setup located at ESRF installations.

The beamline is equipped with three undulated sources and a fixed-exit double Si (111) crystal monochromator with an energy resolution of $\Delta E/E \sim 10^{-4}$. The monochromatic beam is focused on the sample surface by means of an Al compound refractive lenses, which yields ~10^9 photons/sat 28 keV as excitation energy [31]. The optical stack uses 112 lenses with a parabolic

profile and a radius of curvature of 196 μm [32]. The intensity of the incident X- ray beam is monitored with a mini-ionization chamber [33]. A single-element solid state Si(Li) detector (150 eV/energy resolution at Mn-Kα edge, 4 ms shaping time; 30 mm^2 active area; 4 mm active thickness) collects the characteristic XRF lines. By creating a secondary source using the beamline slits (0.1×0.1 mm), the beam dimensions estimated by the Au knife-edge scan method [34] were 1.5×5.1 μm^2 (V×H) at 28 keV.

Data were analyzed with PyMCA code. X- ray imaging implements a Levenberg–Marquardt algorithm to fit the spectra with constraints on the fitting parameters (detector characteristics, detection geometry, matrix composition, excitation energy, etc). The complete emission line series was fitted using theoretical intensity ratios and line emission energies. A more detailed description of this code was given by Solé, V.A et al. [35]. The obtained fitting configuration was applied to each pixel of the 2D maps to calculate the different elemental maps through a batch treatment.

3.3.2.4 Rutherford Back Scattering, RBS

RBS is an ion scattering technique that is used for elemental compositional analysis. RBS allows quantification without the use of reference standards. During RBS measurements, ions of high energy (MeV) are directed onto a sample and the energy distribution and yield of the backscattered ions at a given angle are recorded [36-37].

The experimental **equipment** located at the Centro de Microanálisis de materiales (CMAM/UAM) consists of the accelerator, its beam lines, dedicated to various application areas and several ancillary equipments (micro-analytical techniques, sample preparation) (see figure 3.13). The accelerator, built by HVEE, is of the tandem type and reaches a maximum voltage of 5 MV at the terminal. The acceleration system is of the Cockroft-Walton type. It is provided with two sources: a plasma source for gaseous substances and a sputtering source for obtaining practically any element of the periodic table from a solid target.

This type of accelerator is the best suited for Ion Beam Analysis, (IBA), techniques applied to Materials Science, Archaeometry, Environmental Science, etc.

The Standard Beamline at CMAM is a multipurpose line, mainly used for "classical" IBA techniques over small areas.

It has an experimental chamber equipped with a 4 axis goniometer, a HPGe detector for gamma rays and two implanted silicon detectors (one fixed and one movable) for charged particles detection. For the movable detector it is possible to define different solid angles and to put absorbent foils at its entrance.

All this equipment, together with a continuously under-development set of acquisition and control programs allow us to make both Rutherford Backscattering (RBS) as other IBA techniques. The beamline can be used for irradiating samples with a large variety of ions, from H to Au, being possible to cover areas up to 8x8 mm^2. And a high sensitivity optical camera and a special viewport for far-infrared (thermal) camera, complete the offer of available instrumentation of the beamline.

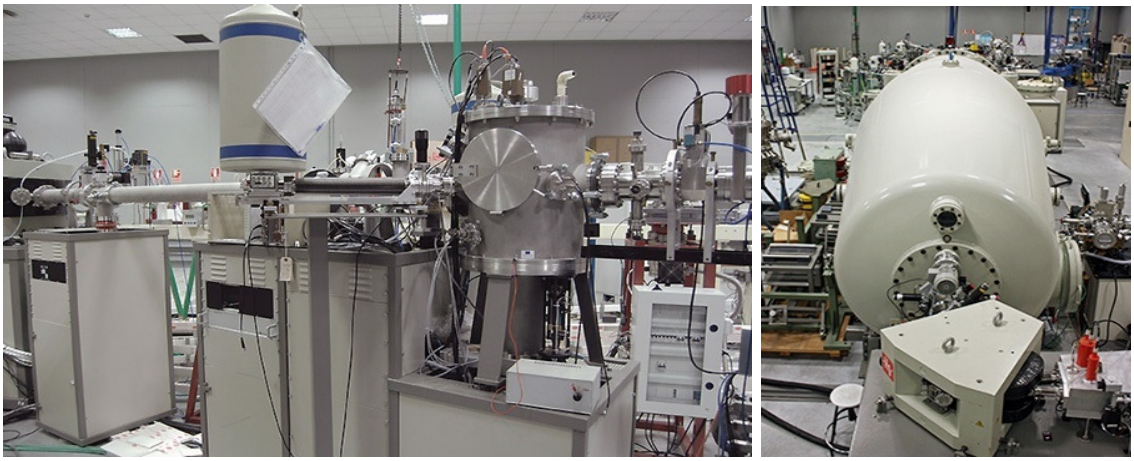

Figure 3.13. Full view of the standard beammline located at CMAM.

- **IBA Techniques**

The IBA techniques are analytical techniques which use as a probe an ion to analyze the composition (at different levels: elemental, molecular, spatial, depth…) of a sample through atomic or nuclear reactions.

When a material is bombarded with an ion beam, it can produce a large variety of reactions from which information is obtained, among other possible things, the elemental chemical composition of the sample answered in depth, see figure 3.14.

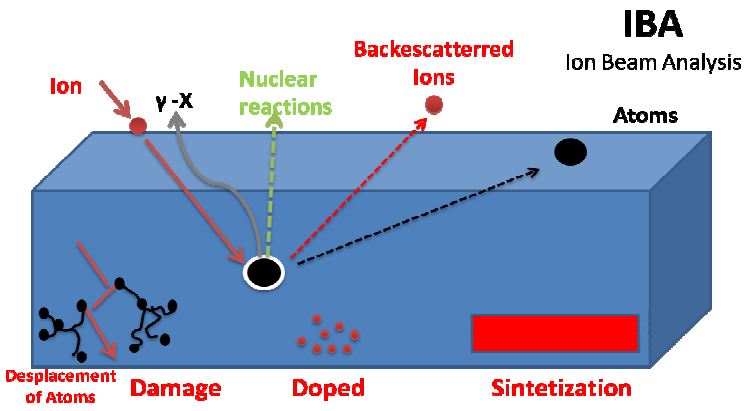

Figure 3.14. Some interaction which occur when an ion beam impact on a material.

Depending on the incident beam energy and ion-matter interaction, (see table 3.VII) IBA techniques [38] can be classified as:

Energy	Typical ion	Method of study [i]
1-10 KeV	O^+, Ar^+, He^+	SIMS, LEIS
10-100 KeV	He^+, p^+	MEIS
A few MeV	$He2^+$, p	PIXE, PIGE, RBS, Channeling, ERDA
10-100 MeV	Ag, Cu^{10+}	ERDA
1-10 MeV	He^+, D^+, p^+	NRA

[i] SIMS: Secondary Ion Mass Spectroscopy. LEIS: Low Energy Ion Scattering. MEIS: Medium Energy Ion Scattering. PIXE: Particle Induced X-ray Emission. PIGE: Particle Induced γ-ray Emission. RBS: Rutherford Backscattering Spectroscopy. ERDA: Elastic Recoil Detection Analysis. NRA: Nuclear Reaction Analysis.

Table 3.VII. Techniques for characterization of materials according to the incident beam energy together with the species most used in ion analysis.

Rutherford backscattering spectrometry (RBS) is a powerful analytical technique used in materials science for the determination of the composition. It is based on the measure of a backscattered beam of high energy ions impinging on a sample.

RBS is one of the best-established IBA techniques in thin film characterization, in which a high energy (1-10 MeV) beam (He or H) is directed to a sample. The ions that are elastically scattered by nuclei into the sample are detected: the higher the mass of an atom that is hit by an ion beam, the higher the energy of the ion will be after backscattering. This results in mass discrimination and, by counting the scattered ions as a function of energy, the number of atoms of each element present can be determined.

Apart from mass information, the main strength of RBS is the depth resolution (in the nm scale). During the flight path through the sample, the ions lose energy, and this energy loss per unit distance is known for every material, allowing the conversion of the RBS spectrum into a depth profile. For example, an ion scattered at a certain depth will lose more energy (on the way in and out of the target) than an ion scattered by the same atom but at the sample surface.

In the analysis of materials using the RBS technique usually uses a beam of ^4He ions with energy between 1 and 2 MeV. The main reasons for this are easy to get a beam of this type, its stopping power is well known in almost all elements, the energy resolution of silicon detectors is between 11 to 15 keV and the most important its cross section in this energy range, for elements heavier than Be is close to that of Rutherford.

Figure 3.15a shows the geometry of a typical measurement with a RBS spectrum which represents the number of backscattered ions (counts) versus its energy (channel number).

If the test sample is thick enough, the spectrum will typically show a flat region in the peaks corresponding to each element whose thickness is related to the thickness of the film, see the example in figure 3.15b.

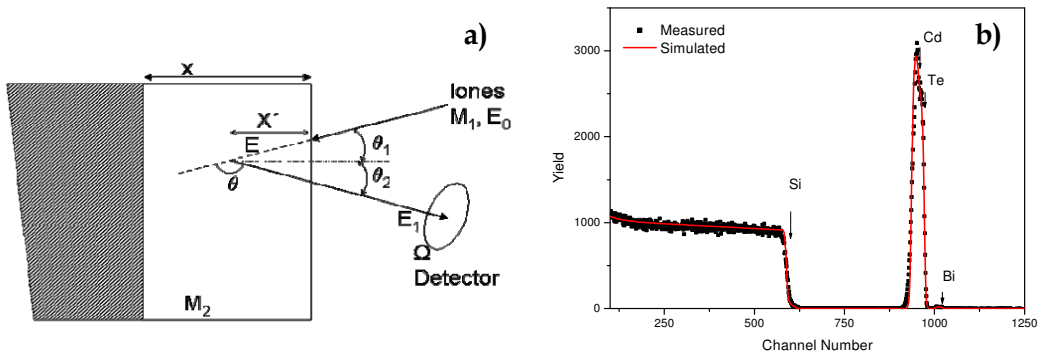

Figure 3.15. (a) Geometry typical experimental backscattering spectroscopy. (b) Backscattering spectrum of Cu foil deposited on a Si substrate.

The depth resolution is determined by the energy resolution of the detector and the random deviations of the beam energy, which is called energy straggling, since not all the ions lose energy in the same way.

To transform the energy level on a scale in depth is necessary to perform a calibration. The calibration is necessary to establish the relationship between the channel number in which the peak appears on the surface of at least two elements of different mass number and energy of backscattered particles after hitting the surface with atoms of the material used for calibration, whose density should be well known [39].

In our case, RBS measurements were performed using a He^+ ion beam at energy of 3 MeV; and the measurements of the samples were carried out by comparing the experimental measurements and simulations with commercial software SIMNRA [40].

3.3.3 Structural Techniques

The structural properties of the samples were studied by means X- ray Diffraction (XRD) and, by Raman Spectroscopy techniques.

3.3.3.1 X- ray Diffraction, XRD

XRD is a powerful nondestructive technique for characterizing crystalline and, polycrystalline materials. It provides information about structures, phases, preferred crystal orientations (texture), and other structural parameters, such as average grain size, crystallinity, strain, etc [41-42].

XRD is a physical phenomenon that occurs when a X- ray beam of a particular wavelength interacts with the atomic distribution of a material. Due to the fact that the characteristic wavelength of the X- rays (0.5-2.5 Å) is of the same order of magnitude than the typical distance between the atoms in solids, this technique very sensitive at the atomic scale, therefore, provides great information on the crystal structure of the material studied [43].

The technique is based on observing the scattered intensity of an X- ray beam that hits a sample as a function of incident and scattered angle, polarization, and wavelength or energy, respectively.

The X- rays are generated by a X- ray source, filtered to produce monochromatic radiation, collimated to concentrate, and directed towards the sample. The interaction of the incident rays with the sample produces constructive interference (and a diffracted ray) when conditions satisfy Bragg's Law **($n\lambda=2d\sin\theta$)**. This law relates the wavelength of electromagnetic radiation to the diffraction angle and the lattice spacing in a crystalline sample. The diffracted X- rays are then detected, processed and counted. By scanning the sample through a range of 2θ angles, all possible diffraction directions of the lattice should be attained due to the random orientation of the grains of the material. Conversion of the diffraction peaks to d-spacings

allows identification of the material because each material has a set of unique d-spacings. Typically, this is achieved by comparison of d-spacings with standard reference patterns.

X- rays are produced generally by either X- ray tubes or synchrotron radiation. In our particular case, we use the **Philips MRD X-ray diffractometer** with θ-2θ (Bragg-Bretano) configuration located at IMM laboratory. It has a Cu target (CuKα_1) which emit 8 KeV with a corresponding wavelength of 1.54 Å (see figure 3.16).

The schematic of the rotation curves at 2θ, where the Bragg condition is satisfied and the θ angle which shows posterior change at the exit of the sample is also depicted in figure 3.16b.

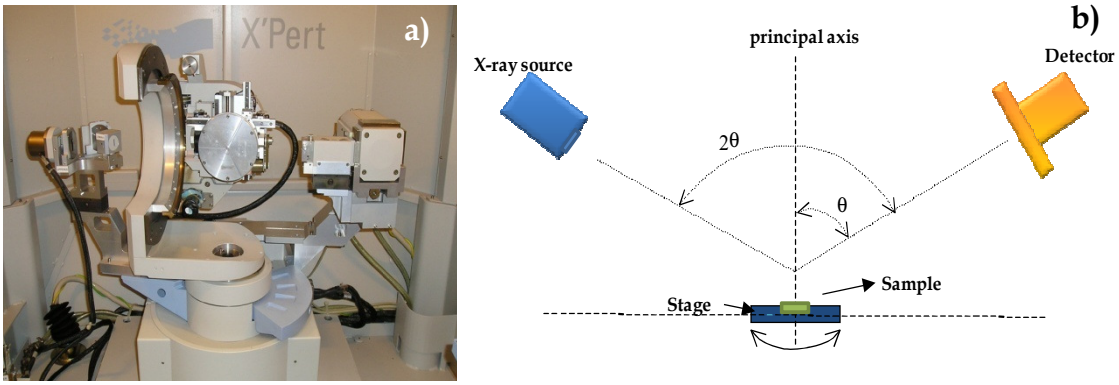

Figure 3.16. (a) Philips MRD X- ray diffractometer. And (b) schematic of the rotation curves. It is shown the 2θ where the Bragg condition are satisfied and, the θ angle which posterior change at the exit of the sample.

This technique was mainly used to characterize thin films grown on substrates, where a high quality is critical. Therefore, this method is used as an important step in the process development and control tool, as long as X- rays can penetrate through the epitaxial layers and measure the properties of both the film and the substrate.

From the peaks appearing in the XRD spectra, we can obtain information about the crystallinity and the interplanar distance by means of the width a half peak height ("Full width at half maximum" FWHM) and Bragg's formula, respectively [44].

In addition, some synchrotron radiation measurements were carried out, due to the fact that in recent years synchrotron facilities have become widely used as preferred sources for XRD measurements. Synchrotron radiation is emitted by electrons or positrons travelling at near light speed in a circular storage ring. These powerful sources, which are thousands to millions of times more intense than laboratory X-ray tubes, have become indispensable tools for a wide range of structural investigations and brought advances in numerous fields of science and technology. The **setup** used has the same configuration than that observed in figure 3.12.

3.3.3.2 Raman Spectroscopy

Raman Spectroscopy enables to determine the chemical structure of a sample and identify its compounds by means of molecular vibrations, similar to Fourier Transform Infrared Spectroscopy (FTIR). However, Raman yields better spatial resolution and enables the analysis of smaller samples. This is a good technique for the qualitative analysis of organic and/or inorganic mixed materials and can also be employed for semi-quantitative and quantitative analysis.

Raman spectroscopy is a nondestructive analysis technique based on study inelastic scattering of the light when it interacts with the matter.

Commonly, a laser is used as a powerful monochromatic light. So, most of the incident light after the impact with the material under study, is scattered at the same frequency. The majority of the photons that interact with the molecules are scattered elastically. This is called Rayleigh scattering. Rayleigh scattered photons have the same wavelength than the incident light; therefore they do not provide any information about the sample under analysis. However, approximately 1 out of a million photons are inelastically scattered. An effect first described by Sir Chandrasekhara Raman in 1922 [45]. This small portion of light experiment slight changes in frequency (or inelastic scattering Raman Effect) due to interaction with the vibrations of the molecules of the material. The detected frequency changes are characteristic of the material analyzed, and frequency independent of the incident light. A more detailed description of Raman spectroscopy technique can found in reference [46].

Figure 3.17 presents a schematic drawing of the Raman effect (a) and a typical experimental **setup** (b).

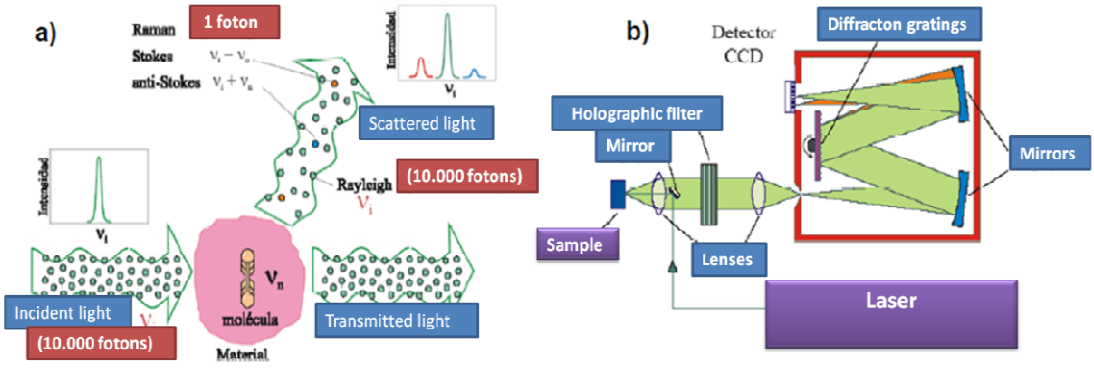

Figure 3.17. (a)Schematic representation of the Raman Effect. (b)Raman spectrometer with a single network diffraction and holographic filter to block the elastically scattered light.

These measurements were realized in Universidad de Barcelona (UB) in collaboration with Victor Izquierdo- Roca. And the samples were measured using two excitation frequencies, 514.5 nm (laser green) and 632.28 nm (red laser). Different holographic filters are also used providing access to the acoustic phonons, in the case of the green laser, to obtain complete information of the spectrum.

3.3.4 Optical Techniques

The optical characterization was carried out by photoluminescence, PL and cathodoluminescence CL studies, respectively.

3.3.4.1 Photoluminescence, PL

PL is a non destructive technique which allows evaluating the structural quality and purity of the samples. At the same time it provides us a lot of information about the different impurities and structural defects present in the material.

PL is the spontaneous emission of light from a material under optical excitation. When light with sufficient energy is incident on material, photons are absorbed and electronic excitations are created. Eventually, these excitations relax and the electrons return to the ground state. If radiative relaxation occurs, the emitted light is called PL. This light can be collected and analyzed to yield a wealth of information about the photoexcited material. The PL spectrum provides the transition energies, which can be used to determine electronic energy levels. The PL intensity gives a measure of the relative rates of radiative and nonradiative recombination. Variation of the PL intensity with external parameter like temperature and applied voltage can be used to characterize the underlying electronic states and band [47].

When the photons inside in the material surface, they have an energy, **E** which is minor or higher that its band gap energy ($\mathbf{E_g}$). Then if $E > E_g$, the material absorbs the photons. Indeed, this energy is enough to excite the carriers since the VB to CB generating electron-hole pairs. In the case that $E < E_g$ the photons transmission trough the material occurs without absorption. Other physical processes important in PL are the recombination process, namely the interaction between electron and holes of the material with radiative emission to back to initial state. The most important transitions that can be found in a PL spectrum are the following:

- **Band to band transitions:** are direct recombinations between electrons of the CB and holes of the VB. The photon energy involved is the same that the E_g.

- **Band- defect level transition:** these transitions takes place between a band and an impurity level. The emitted photons have an energy equal to the distance between the level and the band which it is recombined.

- **Transitions between defects levels:** in this case, the recombination occurs between the different defects levels, as an acceptor and a donor.

There are also excitonics transitions. These transitions correspond to electron–hole pairs recombinations.

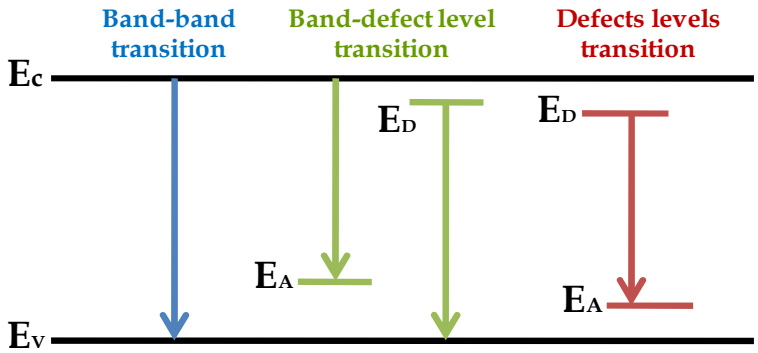

Figure 3.18. Schematic of the different transitions observed in a PL spectrum.

In semiconductors, since the interactions between excitons and the crystal are weak, they can be significantly affected by both impurities and defects. Indeed, it is observed that the luminescence of bounds between excitons and impurities or defects as well as the recombination between donor-acceptor impurity bounds yield valuable information about the energy levels structure within the bandgap.

The **setup** and schematic used during the thesis (both at IMM) are shown in figure 3.19.

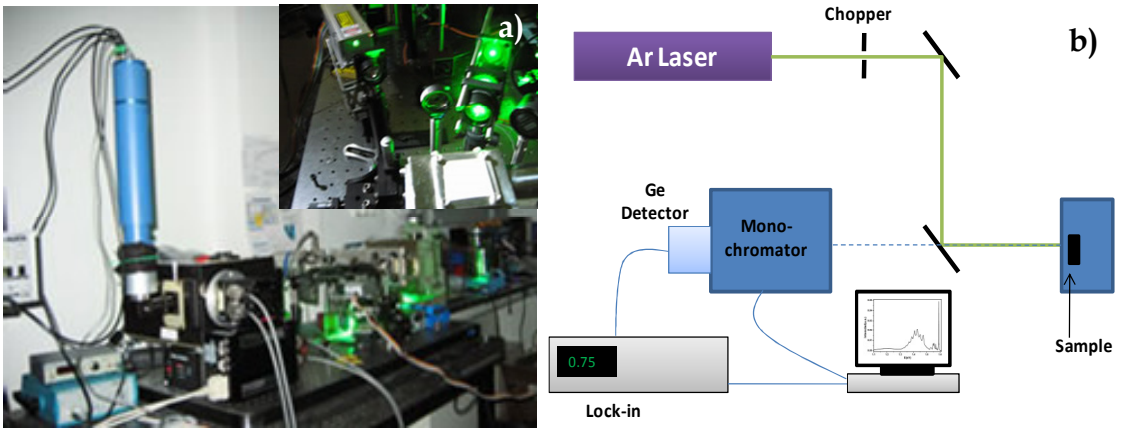

Figure 3.19. PL (a) setup and (b) schematic located at IMM laboratories.

It consists of a light source as laser excitation, a radiation detector and a monochromator. Besides, it is necessary a cryostat if the measurements are carried out at low temperatures.

As excitation source a Spectra Physic Ar laser 2020-05 with a wavelength of 5145 Å and, a power from 1-20 10^{-4} W/cm^2 is used. The light emitted by a laser goes through a filter that absorbs the infrared component and it is directed onto the sample under study by means of a series mirrors and lenses. Then, the light is focused into the sample in a holder that is inserted in a He cryostat with closed circuit. The temperature is adjusted by a controller SI 9650 which allows working in a temperature range around 20-80 K. The radiation emitted by the sample is focused on the entrance grating of the monochromator Spex 1681 0.22m. At the entrance it is placed an absorption filter to eliminate any scattered light that might exist. Thus, the light emitted goes to the monochromator coupled to a Ge detector North Coast EO-817L Scientific Corporation, at which is applied a voltage of 250 V and is cooled with N_2 (l) to reduce the dark current of the detector. Finally, the signal is treated by a Lock-in Amplifier EG & G 5207 and collected in a PC to obtain the PL spectra of the samples.

At the entrance and exit of the monochromator there are slits whose opening can be varied to control the amount of light reaching to detector, and also to determine the resolution, 32 Å/mm. The aperture used for the experiments was 50 µm.

On the other hand, to avoid that the incident light can be scattered by irregularities and increase the emission efficiency, the sample must have specular surface, with a smooth polish finished. Taking into account that at low temperatures, higher resolutions of the peaks of photoluminescence are obtained, some high resolution studies at lower temperature were made in the Mathematic and Physic Institute of Charles University in Prague. The setup belonging to the group of Prof. J. Franc uses a Fourier transform infrared spectrometer Bruker IFS 66/S and

flow helium cryostat Leybold Hereaus VSK 4-300. Under these conditions the PL excitation of CdTe films was carried out by Ti sapphire laser with excitation power 0.3-0.5 W or He-Ne laser (λ= 0.6328 mm) with the 10 mW output excitation. This radiation allows studying the recombination levels in the bandgap of the CdTe layers with the thicknesses less than 0.1 mm. Thus, the luminescence and transmittance spectra were recorded by Si or Ge detectors sensitive in the 700-2500 nm spectral range.

For our CdTe samples, PL spectra are studied taking into account four basic regions as shown in figure 3.20. It is observed that at high energies, close to the band gap, an excitonic region is formed with very intense peaks. At lower energies, between 0.4-1.3 eV, some peaks related to defect levels appear. More information about the analysis is given in the Appendix B; where the most important emission in PL spectra of CdTe and their possible assignations are summarized.

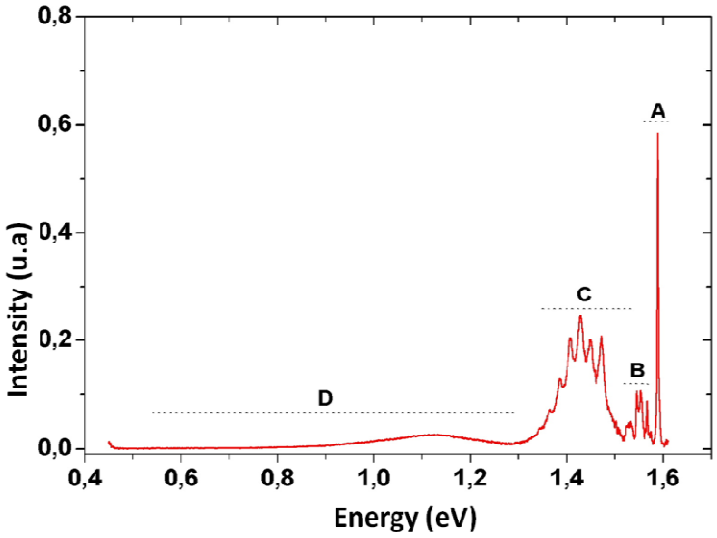

Figure 3.20. Typical PL spectrum for a CdTe sample, where the four regions studied are detailed.

Zone A. This zone, close to the edge of the band gap, is formed by the excitonic emissions due to both free (X) and bound excitons, (either donor or acceptor superficial impurities (D-X, A-X) respectively). From this zone on, one can extract important information about the crystalline quality of the sample, given by the presence of the peak corresponding to free exciton and determining the width at half height.

Zone B. This region is mainly dominated by the transition between donor and acceptor states (DAP), as well as phonon replicas of the exciton lines, usually corresponding to the line of acceptors (A-X). It also gives us critical information about the presence of different impurities, as could be seen in Appendix B.

Zone C. The 1.4 eV band is related to structural defects, dislocations, grain boundaries, stress, or Donor-Aceptor pair transition correlated with the structure (V_{Cd}-D_{Te}), i.e a complex formed by a Cd-vacancies, $\mathbf{V_{Cd}}$ and a donor in the position of Te, also called A-centre. In any case, structural defects are a characteristic photoluminescence band of each of them, so they are easily identifiable. Usually, it has a typical form by a main line (called zero-phonon replica, ZPL) and a series of phononic replicas, which can be modeled by the equation of Huang-Rhys and linked with the type of impurity that is originates [48], by:

$$I_n = I_{n-1} \sum_n \left(e^{-S} \frac{S^n}{n!} \right) \qquad (3.7)$$

Where, $\mathbf{I_n}$ is the maximum intensity of the replica **n**, $\mathbf{I_{n-1}}$, the intensity of the previous reply and **S** is the Huang-Rhys parameter is specific to each donor center.

The value of the intensity of each peak can be approximated by a Gaussian and it can be written as follows:

$$I_{n-1} = \frac{A}{(4(E - E_{Z0} + ndE)^2 + E_D^2)} \qquad (3.8)$$

In this equation, **A** is the area of the peak with energy **E**, $\mathbf{E_{Z0}}$ the energy position of the zero phonon replicas, **dE** is the phonon energy and $\mathbf{E_D}$ is a factor related to the binding energy of the exciton, in the defect part with acceptor character. Furthermore, depending on the chemical species involved in the transition, we have a different number of Huang-Rhys and this parameter can be used to identify different impurities.

For our thin films fabricated from polycrystalline material, the exciton region shows low intensity, while the regions of the defects, particularly structural defects, are the most important in the spectra.

The band originated by structural defects is centered at 1.47 eV and is called Y- band. It can be related to recombination of dislocations and grain boundaries [49]. This band can also be adjusted using the equation of Huang-Rhys, usually presenting a low of **S** because it is originated by defects that have low coupling with the lattice.

Zone D. This zone is represented by emissions from recombinations at deeper levels. The 1.1 eV band has a complex structure and at is related to Te-vacancies, $\mathbf{V_{Te}}$ [50]. Also in this

region, for the cases in which the dopant may be introduced to a deeper level, the emission can be due to these levels.

3.3.4.2 Cathodoluminescence, CL

CL technique is based on the interaction of electrons with matter. When an electron beam penetrates into a solid target, electrons can interact elastically or inelastically with it. The CL is a technique that activates the photon emission using as excitation mechanism the SEM electron beam. This electron bombardment of the materials results in a characteristic emission of light in UV, visible, or infrared parts of the spectrum. The analysis by means CL allows us to obtain information from the material according to the depth varying the beam energy. When a high energy electron coming from a SEM interacts with a semiconductor, it creates a very large number of electron-hole pairs, some of which through radiative mechanisms can recombine between them. In our case, the potential accelerations vary between 1-30 KV.

The CL signal has its origin near the surface where the electron beam is able to activate the radiative mechanisms. The volume that generates the CL signal depends on the spatial region within the material where the electron beam dissipates its energy. The volume at which these collisions occur is approximately spheric, although there is a loss in the sphericity as increasing the atomic number of the material. It is called Gruen range, the vertical dimension of this volume of energy losses. A simple expression to determine this range, in which electrons lose their energy, is that given by Kanaya and Okayama [51]:

$$R_e = \left(0.0276 \cdot \frac{A}{\rho \cdot Z^{0.889}} \right) \cdot E_h^{5/3} \qquad (3.9)$$

where, **A** is the atomic weight in g/mol, **ρ** is the density in (g/cm^3) and E_h is the energy of the electron beam in keV.

Besides, we have to take into account effects as the diffusion length of the minority carrier and the diameter of the incident electron beam over the sample to obtain an approximate value for Gruen range.

The analysis by means CL technique allows the determination of several properties of the material with a spatial resolution of less than 1 μm as a function of the beam diameter. For

example, the CL spectroscopy can be used to obtain monochromatic imaging for both identification and distribution of luminescence centres. But, in principle, a direct measurement of the absolute concentration of the luminescence centres, is not possible to realize, because the CL contrast is proportional to the ratio between the probabilities of the radiative recombination and the total recombination (including the radiative and nonradiative contribution, i.e, the CL contrast). It is determined by the local variation in the concentration of radiative recombination centers.

From spectral analyses of the emission, the identification of luminescence centres and, studies of their behavior changing the observation conditions (as temperature, excitation conditions, etc) can be performed. An excellent monograph on the CL technique is that of Yacobi and Holt [52]. There are also review articles, which makes a more thorough review of the theory, as the work of Davison [53] and Petrov [54] and more recently the thesis realized by Dr. P. Hidalgo [55].

When the electron beam is focused over a sample, a series of signals, X- rays, primary and secondary, luminescence, etc, are generated. Thus, the luminescence signal CL images can be obtained.

The signal is collected by a suitable detector and converted into electrical signal that, appropriately treated and synchronized with the SEM scanning system, allows us to obtain images of the spatial distribution of the radiative recombination centers. The schematic of the experimental **setup** is outlined in figure 3.21.

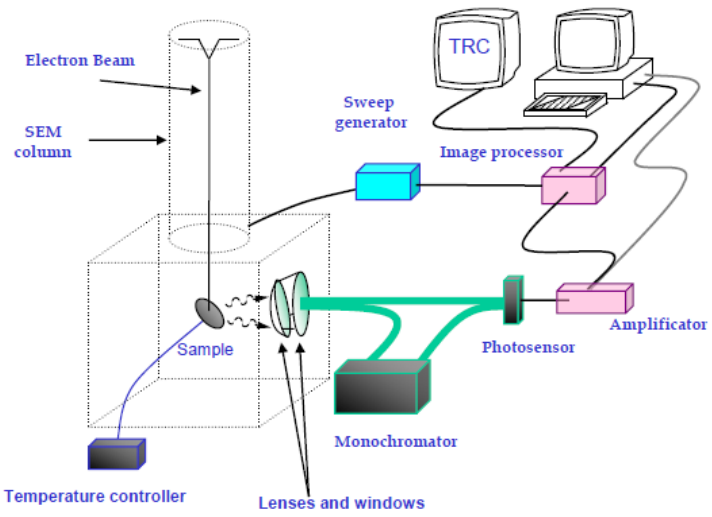

Figure 3.21. Schematic of CL setup of the micro- and nano- characterization of electronic materials group located at UCM.

The two SEM: a Hitachi S-2500 and a Leica Stereoscan 440 have been adapted to implement CL technique and are located at Universidad Complutense de Madrid (UCM). By means a lens and a windows (both of CaF), the photons generated in the material are collected. For this, the optical lens focuses the light onto the windows, to minimize the possible absorption in the infrarred. The microscope Hitachi S-2500 has a temperature control system based in a combination of N_2 liquid, N_2 gas and a thermal resistance which allows us to work in temperatures ranging between 80 K and 512 K.

Using this technique we can obtain panchromatic images, monochrome images and spectra. For panchromatic imaging the detector is adapted directly to the window of the CaF microscope by a light guide, which includes transmittance range from 300 nm to 2200 nm. Currently there are no detectors that cover a very wide detection range, so different detectors are often used. The detector used consists of a PiN diode of Ge, of ADC, cooled by N_2 liquid for operate. Its spectral detection range goes from 850 nm to 1900 nm (1.46 - 0.65 eV). The radiation reached by the detector is converted into an electrical signal that is driven to a differential amplifier video AM502 Tektronik. Subsequently, the amplified signal and noise filtering is carried to an image scanner where it is synchronized with the scanning microscope system thus obtaining the CL image. The imaging system (PIXIE-8) store the information obtained to a digital file, so after that can be analyzed on any computer.

The obtained monochromatic imaging helps us to identify luminescent centres with spatial resolution. Selecting the appropriate wavelength in the monochromator, only the radiation with the selected wavelength reaches the detector. Thus the images formed consist only of one type of radiation, and it allows analyzing the spatial distribution of radiative centers that cause this emission.

CL spectra allow the identification of different radiative processes in the sample. Further analysis of the spectra allows us to determine the wavelengths of the emission bands. The acquisition of CL spectra is done following the schema showed above in figure 3.21. The monochromator is introduced between the window and the detector. In our case, an Oriel 78 215 model is used, where the values of the wavelength can be controlled by computer via an RS232 connection. The monochromator is equipped with a diffraction grating interchangeable depending on the spectral range analyzed. For our experiments, we use a 300 lines/mm diffraction grating covering a spectral range from 1000-4000 nm. The computer controls the rotation of the lattice and at the same time, for a given wavelength, acquired through a data acquisition card, the value of the signal that contains the detector is coupled to the output of the monochromator. Thus we get a CL spectrum of the signal collected by the detector as a function of wavelength. The control program improves the ratio signal to noise averaging up to 1000

times the measure for each of the wavelengths. The spectral response of the system has been calibrated by analyzing the transmittance functions of each of the elements used, light guides, monochromator and detector.

3.3.5 Electrical techniques

Finally, for the electrical characterization, studies of I-V characteristic and surface Voltage Spectroscopy, SPS were carried out.

3.3.5.1 I-V Characteristic

The fundamental characterization of a photovoltaic cell is the measure of the current-voltage I-V characteristic. These measurements at both dark and illumination conditions are essential to describe the device [56-59]. However, in this thesis only the I-V characteristic in dark conditions is presented.

In a p-n junction the relationship between current and voltage is given by the following equation:

$$J = J_{Osc}\left(e^{\frac{qV}{nkT}} - 1 \right) \qquad (3.10)$$

where **q** is the electron charge, **k** is the Boltzmann constant and, **T** is the temperature at which it is being measured. The current density, **J,** is expressed in A/cm^2. $\mathbf{J_{Osc}}$ is the dark current and **n** is the ideality factor of the diode. For heterojuntions n has values usually between 1 and 3. When the value of n is close to 1, the transport mechanism of the charges in the cell is by diffusion. Homojunctions normally have a factor close to 1, and for epitaxial heterojunctions is around 2. In the case of CdTe- based cells, the values of this factor can widely vary. The dark current is the saturation value of current in the diode reverse configuration.

For CdS/CdTe heterojuntions the most relevant well-known charge transport mechanisms are:

- **Diffusion model**: In this model, two semiconductors with different values of band gap, dielectric constants, work functions and electron affinities are considered. The interface states in the mechanisms of transport of charge carriers are neglected.

- **Emission model:** This model combines the classical theory of the thermionic emission and diffusion model.

- **Emission-recombination model**: This model is based on the assumption that there is a thin layer at the interface of semiconductors, which has a strong influence on the rate of charge carriers recombination. The charge carriers reach the interface states by the thermal emission, exceeding their respective barriers, recombining in the states of the interface.

- **Tunnel effect model**: This model assumes that the charge carriers go through the potential barrier by a tunneling mechanism. It is assumed that tunneling through the barrier exceeds greatly the thermionic emission process.

Both the diffusion and emission model predicts the dependences of the current on the voltage, which does not fit exactly to those obtained experimentally. In the real heterojunctions the transport mechanisms are generally a combination of recombination, tunneling and thermionic emission model. The supremacy of one mechanism over the other depends on the voltage applied to the device and the particular way in which it was manufactured. In the manufacture of each heterojunction it is necessary to a proposed energy band model based on experimental results. The front contacts were taken on the TCO (Transparent Conducting Oxide) deposited on the glass.

Another interesting feature when considering this type of device is the **open circuit voltage (V_{oc})**: it is the maximum voltage that appears across the terminals of the solar cell when the current is zero in the device. The open circuit voltage is due to the direct polarization of the p-n junction when the light strikes the cell. It is expressed by:

$$V_{oc} = \frac{nkT}{q} \ln\left(\frac{J_L}{J_{0sc}} + 1\right) \qquad (3.11)$$

In this equation, $\mathbf{J_L}$ is the current density generated by light. $\mathbf{V_{oc}}$ depends logarithmically of the current generated by the reverse light and the dark current. However, while $\mathbf{J_L}$ values vary

little, $\mathbf{J_{Osc}}$ values can take several orders of magnitude of difference, so that the value of $\mathbf{V_{oc}}$ is strongly conditioned by the values of $\mathbf{J_{Osc}}$.

The dark current strongly depends on recombinant mechanisms. As fewer carriers are recombinated, lower reverse saturation current and higher values for the V_{oc} are obtained. The dark current also depends on the temperature when it increases the value of V_{oc} increases and J_{Osc} decreases. The V_{oc} value also depends on the value E_g. At higher values of E_g, greater value of V_{oc} is obtained.

The **setup** used in this thesis is located at Institut de Recherche et Développement sur l'Énergie Photovoltaïque (IRDEP (CNRS-EDF-ENSCP)) and basically consist in a Keythkey electrometer 6514 with a source of high voltage ET NHQ 105L DC in the configuration shown in figure 3.22 [60].

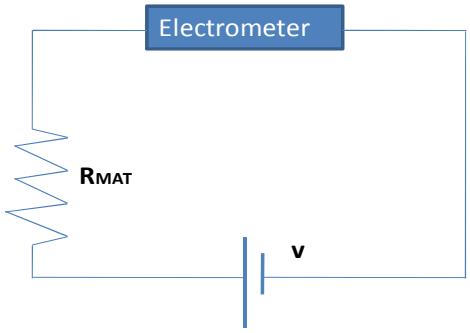

Figure 3.22. Basic configuration used for I-V characteristic measurements.

Applying to the samples a variable voltage, the current between the contacts were measured. From the representation of I versus V, parameters characteristics of solar cells as $\mathbf{J_{Osc}}$ and $\mathbf{V_{OC}}$ can be calculated.

3.3.5.2 Surface Voltage Spectroscopy, SPS

SPS provides information on the surface electronic structure. The transitions between electronic states can be sampled through photon injection. In the presence of an internal electric field, e.g., a space-charge region, the excited carriers are swept away and separated giving rise to surface charging, known as the photovoltaic effect. SPS, based on the photovoltaic effect, is a valuable method for the investigation of several semiconductor properties [61] amongst them the E_g which is defined by the threshold in the optical absorption spectra.

While other spectroscopical methods based on photoemission, e.g., X- ray photoelectron spectroscopy, require ultrahigh vacuum conditions and large scale facilities, SPS measurements can be carried out in air. Moreover, this method does not require any complicated surface preparation, thinning contact preparation, or costly apparatus.

For our experimental **setup** (Kelvin probe configuration), we assume that any change in the surface potential, causes a changes of equal magnitude in the surface work function, **W**. In absence of photochemical activity, the change in surface work function is equivalent to the Surface Photovoltage (SPV) measurement (in absolute value terms). Therefore, we can consider that the potential energy drop is equal to the difference in the work functions between CdTe:Bi/CdS/ITO film and a vibrating Au reference probe. It is, indeed, usually known as the contact potential difference, CPD [62,63].

Taking this into account, the SPV is the difference between the CPD values in dark and under illumination [64]. The dark CPD is the difference between the work function of the semiconductor (W_s) and the Kelvin Probe metal electrode (W_M).

$$W_s = \zeta - eVs + \chi - \Delta\varphi_s \qquad (3.12)$$

where ζ is the difference between the conduction band edge $\mathbf{E_C}$ and the Fermi level, $\mathbf{E_F}$ in the semiconductor bulk, **e** is the electron charge, **Vs** is the surface potential, χ is the electron affinity, and $\mathbf{\Delta\varphi_s}$ is the surface dipole energy [65].

A typical SPV spectrum of CdTe- based films as function of the wavelength of the incident photons shows that the light induced surface charging is caused by the surface photovoltage due to the generation of electron hole pairs and to the charge separation in the CdTe film. Indeed, at photon energies below the band gap film, the CPD is constant. This constant level corresponds to the **W**, at the given experimental conditions (atmospheric air).

The schematic configuration diagram of the SPV measurements is shown in figure 3.23.

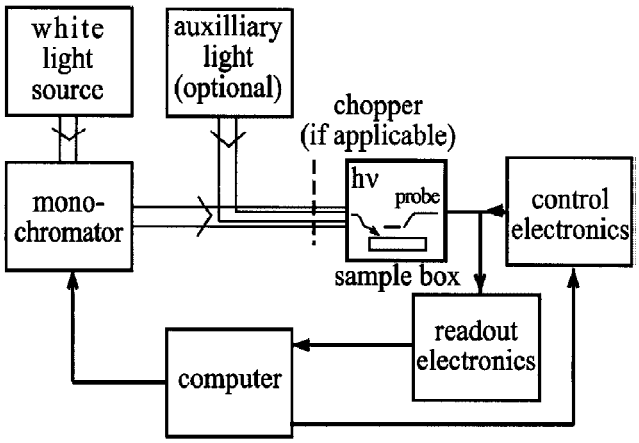

Figure 3.23. Schematic block diagram of a generic SPS setup.

The sample under study is typically placed inside a metallic box, which serves as both a dark box and a Faraday cage. This box must be such that it effectively includes the probe, be it a vibrating metal plate (i.e. a Kelvin probe). Clearly, for spectroscopic purposes one needs to generate the SPV signal using a broadly tunable light source. The default choice therefore would be the use of a 'white light' source in conjunction with a monochromator. Because the typical super-bandgap absorption coefficient is typically orders of magnitude larger than the sub-badgap coefficient, SPS is vulnerable to the spurious contribution of high-order diffraction peaks and stray light. Use of a monochromator where these effects are as small as possible is therefore highly recommended. Using a Kelvin probe, lock-in detections are made by vibration of the probe itself. The actual recording of an SPV spectrum is coordinated by a real time computer program. This program controls the monochromator motor and thus wavelength changes, operates the control electronics of the probe, reads the measurement results by interfacing with the probe readout electronics via an analogue to digital converter and finally stores the obtained spectrum for subsequent display and analysis.

The first elementary application of SPS that we discuss is the approximate determination of the E_g. This determination is based on the large increase in absorption coefficient near the band gap energy. This increase brings about a significant change of the SPV signal, which is easily identified as a sharp change in the slope of the SPV curve.

By extrapolating of $(SPV)^2$ or $(SPV)^{1/2}$ as function of the energy (hν) of the incident photons was therefore used to obtain highly accurate values of the E_g in semiconductors. The energy position is usually found by the intersection of the $(SPV)^2$ with the photon energy axis (a) [66].

Although in many cases the type of semiconductor is known a priori, in other cases SPS is used for fast and non-destructive verification of the semiconductor type in CdTe films. This is very important because the doping of CdTe is known to be non-trivial and mainly subject to compensation. This may be achieved with the help of the sign of the knee associated with the SPV curve. The SPS signal is bent upward towards the surface represents a p-type behavior. Being this fact characteristic of transitions from E_v maximum to unoccupied donor surface states in the E_g.

Therefore, the advantage of this technique comes from the fact that absorption spectra are emulated via voltage spectra; while reflection and transmission are inherently ignored (they may reduce the sensitivity of the measurement but will not interfere to any major effect with the spectra shape of the sample). A unique characteristic of SPS, however, is that it provides significant hints to determine the dominating transport mechanism. In particular, the photovoltage signal indicates the effective conductivity type of the layer.

References

[1] Y. Eisen, A. Shor, J. Crystal Growth **184/185**, (1998), 1302

[2] R. Schoenholz, R. Dian, R. Nitsche, J. Crystal Growth **72**, (1985), 72.

[3] R. Triboulet, Y. Marfaing, J. Crystal Growth **51**, (1981), 89.

[4] Z. Golacki, M. Górska, J. Makowski, A. Szczerbakow, J. Crystal Growth **56**, (1982), 213.

[5] M. Laasch, T. Kunz, C. Eiche, M. Fiederle, W. Joerger, G. Kloess, K. W. Benz, J. Crystal Growth **174,** (1997), 696.

[6] P. Rudolph, Prog. Cryst. Growth and Charact. **29,** (1994), 275.

[7] "*Crecimiento y caracterización de monocristales en volumen de CdTe dopados con Bi*", Edgardo Saucedo Silva. Tesis doctoral presentada en 2007 en la Universidad Autónoma de Madrid./PhD Thesis, Unversidad Autónoma de Madrid (2007).

[8] "*Cristalización de materiales de CdTe de alta resistividad, por métodos de vapor, fundido y en condiciones de microgravedad*", Victoria Corregidor Verdasco. Tesis doctoral presentada en 2003 en la Universidad Autónoma de Madrid. /PhD Thesis, Unversidad Autónoma de Madrid (2003).

[9] E. Saucedo, O. Martinez, O. Vigil-Galan, I. Benito, C.M. Ruiz, L. Fornaro, N.V. Sochinskii, E. Dieguez, J. Crystal Growth, **291**, (2006), 416.

[10] E. Saucedo, A. Zappettini, E. Gombia, A. Baraldi, C.M. Ruiz, V. Bermúdez, N.V. Sochinskii, E. Diéguez, J. of Appl. Phys., **100**, (2006), 104901.

[11] "*Narrow gap cadmium-based compounds*", P. Capper, Emis datareviews series nº 10, Inspec Pub., 1st Ed., England, 1994, Chapter B1, Secc.B1.3. 386-390.

[12] "*Handbook* of *sputter depositon technology; Princeples, Technology and Applications*". Kiyotana Wasa, Shigeru Hayakama. Noyes Publications (1992). Secc.2. 17-66.

[13] "*Materials Science of Thin Films: Deposition & Structure*". Edited by Milton Ohring. Elsevier (1991) Chapter 3,6 and 7.

[14] " *Láminas Delgadas y recubrimientos: preparación, propiedades y aplicaciones* " Jose Maria Albella. Colección Biblioteca de Ciencias. Editorial CSIC (2003).

[15] "Handbook of Thin Films Technology", Secc. A.1.0.8, E.B. Graper.

[16] R. Gunawan, M.Y.L. Jung, E.G. Seebauer, R.D. Braatz. Journal of Process Control **14,** (2004), 423–430.

[17] M.J. Hart and A. G.R Evans .Semicond. Sci. Technol. **3** (1988) 421-436.

[18] A.T. Fiory. Method in Rapid Thermal Annealing.

[19] A.J. Chapman, D.W. Lane, K.D. Rogers, M.E. Özsan. Thin Solid Films **403 –404,** (2002), 522–525.

[20] E. Rouska, Bioscience Reports, Vol. **7**, No. 8, (1987), 607-629.

[21] Hitachi S800 field emission gun (FEG) SEM Manual.

[22] URL:http://www.afmuniversity.org/chapter3_3.html

[23] G. Binning, H. Rohrer. Helv. Phys. Acta **55**, (1982), 726.

[24] R. García, R. Pérez. Surf. Sci, Rep. **47** (2002), 197.

[25] I. Horcas, R. Fernández, J. M. Rodríguez, J. Colchero, J. Gómez-Herrero, and M. Baro, Rev. Sci. Instrum., Vol. **78**, (2007), 013705.

[26] URL:Web de ICP-MS de Ramón Fernández Ruiz.

[27] J.Goldstein, D. Newbury, David Joy, Charles Lyman, Patrick Echlin, Eric Lifshin, Linda Sawyer, and Joseph Michael,. "Scanning Electron Microscopy and X-Ray Microanalysis". Third Edition, Springer, (2003).

[28] C.R. Brundle, C.A. Evans Jr and S. Wilson, "Encyclopedia of Materials Characterization", Butterworth-Heinemann, Boston (1992).

[29] Guerra MF. X-Ray Spectrometry **37**, (2008), 317–327.

[30] Gianoncelli A, Kourousias G. Appl Phys A **89**, (2007), 857–863.

[31] Somogyi A, Drakopoulos M, Vincze L, Vekemans B, Camerani C, Janssens K, Snigirev A, Adams F . ID18F: *"A new micro- X-ray fluorescence end-station at the European Synchrotron Radiation Facility (ESRF): preliminary results"*. X-Ray Spectrom **30,** (2001), 242–252.

[32] Lengeler B, Schroer CG, Richwin M, Tümmler J, Drakopoulos M, Snigirev A, Snigireva I. Appl Phys Lett **74**, (1999), 3924–3926.

[33] Kocsis M, Somogyi A. J Synchrotron Rad **10**, (2003), 187–190.

[34] Martínez-Criado G, Somogyi A, Ramos S, Campo J, Tucoulou R, Salome M, Susini J, Hermann M, Eickhoff M, Stutzmann. Appl Phys Lett **86**(13192), (2005), 1–3.

[35] Solé VA, Papillon E, Cotte M, Walter Ph, Susini J. Spectrochimica Acta Part B 62, (2007), 63–68.

[36] "RBS Theory Tutorial". Evans Analytical Group: Training. http://www.eaglabs.com/training/tutorials/rbs_theory_tutorial. Retrieved 2007-10-10.

[37] Hobbs, C.P.; McMillan, J.W.; Palmer, D.W. Nucl. Inst. and Meth. B **30**, (1988), 342–348

[38] URL: http://www.cmam.uam.es/

[39] "*Crecimiento, caracterización y modificación de nitruros de cobre*", Nuria Gordillo García. Tesis doctoral presentada en 2009 en la Universidad Autónoma de Madrid. /PhD Thesis, Unversidad Autónoma de Madrid (2009).

[40] M. Mayer, SIMNRA, Version 5.02, Max Plank Institut für Plasmaphysik.

[41] H. Kuzmany,"*Solid- State Spectroscopy*". (1998). Springer.

[42] K. Lenkeit, "*Superlattices and Microstructures*," Vol. 9, No. 2, (1991) 203-210.

[43] C. Kittel, *Introduction to Solid State Physics*, Ed. John Wiley and Sons. (New York, 1966).

[44] M. Cardona, with contributions by M.H. Brodsky ... [et al.], *Light scattering in solids*, Ed. Berlin ; NewYork : Springer-Verlag, 1975-©2000.

[45] "*The Raman Effect: A Unified Treatment of the Theory of Raman Scattering by Molecules*". Derek A. Long (2002) Ed. John Wiley & Sons.

[46] "*Modern Raman Sectroscopy: A Practical Approach*". Ewen Smith and Geoffrey Dent (2005) Ed. John Wiley & Sons.

[47] G.D. Gilliland, Material Science and Engineering, R**18,** (1997), 99-400.

[48] W.Stadler, D.M.Hofmann, H.C.Alt, T.Muschik, B.K.Meyer, E.Weigel, G.Müller-Vogt, M.Salk, E.Rupp, K.W.Benz, Phys. Rev.B **51**, (1995), 10619-10630.

[49].D.P. Halliday, M.D.G. Potter, J.T. Mullins, A.W. Brinkman, J. Crystal Growth **220**, (2000), 30.

[50] J. Krustok, V. Valdna, K. Hjelt, H. Collan, J. Appl. Phys. **80,** (1996), 1757.

[51] K. Kanaya, S. Okayama, J. Phys. D: Appl. Phys. **5**, (1972), 1727.

[52] B.G. Yacobi, D.B. Holt, Cathodoluminescence Microscopy of Inorganic Solid, Plenum Press, New York, (1990).

[53] S.M. Davidson, Journal of Microscopy, Vol **110**, 3, (1977), 177-204.

[54] V.I. Petrov, Phys. Stat. Sol. (a) **133**, (1992), 189-230.

[55] "*Estudio Correlativo de propiedades electrónicas locales de GaSb mediante microscopias electrónica y túnel de Barrido*". Pedro Hidalgo Alcalde. Tesis doctoral presentada en 2005 en la Universidad Complutense de Madrid. /PhD Thesis, Unversidad complutense de Madrid (2005).

[56] "Semiconductor Devices: Physics and Technology", S. M. Sze, John Wiley and Sons, 2. Ed. USA (2001).

[57] Martin A. Green, solar Cells.

[58] "Heterojunctions and Metal-Semiconductor Junctions" A.G. Milnes and D.L.Feucht, Academic Press, USA (1972).

[59] T.I. Chu, S.S. Chu and C. G. Ferekides, J. Cryst. Growth **117**, (1992), 1073.

[60] "*Modificacion de las propiedades optoelectrónicas por medio del dopado con Bi en células fotovoltaicas basadas en CdTe*". Carmen Maria Ruiz Herrero. Tesis doctoral presentada en 2007 en la Universidad Autónoma de Madrid./ PhD Thesis, Unversidad Autónoma de Madrid (2007).

[61] Leeor Kronik, Yoram Shapira. Surface Science Reports **37**, (1999), 1-206.

[62] L. Kronik, L. Burstein, and Yoram Shapira, M. Oron.Appl. Phys. Lett., Vol. **63**, No. 1, (1993), 5.

[63] Leeor Kronik and Yoram Shapira.Surf. Interface Anal. **31,** (2001), 954–965.

[64] Julius M. Mwabora , K. Ellmer, A. Belaidi, J. Rappich, W. Bohne, J. Röhrich, Th. Dittrich.Thin Solid Films **516**, (2008), 3841–3846.

[65] D. Gal, Y. Mastai, and G. Hodes, L. Kronik.Journal of Applied Physics. **86**, No10, (1999), 5573-5577.

[66] "*Properties of Narrow Gap Cadmium- based compound*". Edited by Peter Capper Inspec publication (1994).

Chapter 4

Physical properties of CdTe- based sources

Chapter 4

PHYSICAL PROPERTIES OF CdTe– BASED SOURCES

This chapter is devoted to the optimization of the growth method of CdTe and CdZnTe sources. The role of some dopants such as: Ge, Bi, Yb and Zn in the improvement of material properties is studied.

4. 1 Introduction

CdTe presents unique properties that make it appropriate for device applications. Compared to most common semiconductors its components have high atomic numbers (Z_{Cd} = 48, Z_{Te} = 52), and its density is 5.86 g/cm^3 (approximately 2.5 times denser than Si). As a result, this material strongly interacts with both X- and γ- radiation [1,2]. Optically, it is a strong absorber in both the near-infrared (NIR) and visible regions of the electromagnetic spectrum and exhibits unusually high nonlinear optical coefficients. Like most semiconductors, CdTe's properties can be widely varied by doping [3,4]. Extensive research has been devoted to this topic. However, a detailed description of all possible modifications is out of the scope of this work. Therefore, only the most relevant examples will be presented here.

The electrical conductivity of pure **(un- doped) CdTe** is mainly governed by residual impurities [5-7]. Due to the difficulty of manufacturing pure samples (since any exposition to the atmosphere results in an unacceptable contamination), impurities are commonly present.

Un- doped CdTe is much less sensitive for radiation detection than doped CdTe, especially when using Ge and Sn as dopants. However, "pure" (un- doped) CdTe samples with high resistivity are interesting as substrates for the growth of high quality epitaxial HgCdTe [8].

The majority of the impurities known in CdTe belong to the IIIA (Al, Ga and In) and VIIA (Cl, Br and I) groups and behave as **shallow donors.** On the other hand, the elements of IA (Li, Na and K) and IB (Cu, Ag and Au) groups behave as **shallow acceptors**. The elements of the group VA (N, P and As) can act so much like acceptors or shallow donors depending on the lattice position in which they are located.

To reach the semi-insulating state the density of shallow acceptors and donors has to be exactly compensated [3]. The presence of a deep level that stabilizes the Fermi level near the

centre of the band gap [3]. Several native defects have been postulated as possible deep levels (Te-antisite, $\mathbf{Te_{Cd}}$; Cd-vacancy, $\mathbf{V_{Cd}}$) to be responsible for the high resistivity of CdTe doped with shallow donor. Nevertheless this topic is still a matter of controversy.

The possibility to obtain CdTe samples of high resistivity doping with **deep donors** has been widely studied [9-14]. The most commonly dopants used for this purpose are **Ge** and **Sn** with levels: $Ge^{+2/+3}$ to ionization energy associated at these deep donors, E_C-0.95 eV (where E_c is the energy value of the Conduction Band, CB), which is far from CB, and $Sn^{+2/+3}$ to E_C-0.85 eV [14]. However, doping CdTe with Ge and Sn has some disadvantages since these dopants introduce fast recombination centres (the so-called S-centres), deteriorating its transport charge properties [13,14]. Nowadays, this is one of the major constraints for further development of CdTe-based X- and γ- ray detectors.

Recently, **Bi** has been proposed as an useful dopant which leads to an increase in photoconductivity [15,16]. This finding could be important for solar cell applications [17]. Previous studies show that photoconductivity improves with increasing Bi concentration up to a certain limit [17]. Moreover, changes in the electrical resistivity up to 5 orders of magnitude have been observed when increasing the Bi concentration from 10^{17} to 10^{19} at/cm^3. The reason for such changes is explained by taking into account the modifications that it induces in the defect level structure. It is known that for low Bi concentration ($1x10^{17}$ at./cm^3), Bi atoms occupy the $V_{Cd,}$ thus, decreasing the effective density of acceptors and therefore, increasing the resistivity [18] leading to a semi-insulating state. For a Bi concentration in the range of $1x10^{18}$ - $8x10^{18}$ at./cm^3 , Bi replaces Te from its CdTe lattice position, increasing the effective density of acceptors in comparison to the un- doped samples, (BiTe is an acceptor defect). Under these doping conditions (Bi concentration of $1x10^{17}$ at./cm^3), an increase in conductivity has been observed due to its acceptor behavior. However, since the variation in conductivity is not proportional to the variation in the holes density, the mechanism is not fully understand. Only few works in literature are devoted to the study of Bi- doped despite of its influence in the optoelectronics properties of CdTe- based solar cells and for X- ray detection applications. We have contributed to this research by showing that Bi is a suitable doping to obtain semi-insulating CdTe with high photosensitivity and excellent transport charge properties [19]. In this chapter, the energetic location of the Bi-related defects and their interaction with other structural defects will be analyzed as a essential step for further development of CdTe:Bi- based devices [20].

According to literature, substantial efforts have being made to improve the physical properties of a number of different materials by doping them with rare earth elements, in particular the influence of Ytterbium (**Yb**) doping on the physical properties of soft glass fibers

[21], ceramics [22], nonorganic compound nanocrystals [23], garnet crystals [24], phosphors [25], proton conductors [26], etc, have been carried out. It has been shown that doping III-V semiconductors (for example, GaAs), with Yb and Er, significantly increases their photoluminescence efficiency and carrier lifetime [27]. The consequences of rare earth doping are twofold: (i) formation of new defects level and (ii) ability of rare earth elements to react with residual impurities in semiconductor lattice (the so-called "cleaning" process).

Conversely, the effects of rare earth doping on magnetic and optical properties of II-VI semiconductors have been also extensively investigated (see for example Refs. 28–31). Nevertheless, much less information is found in literature related to the electrical and transport charge properties of these materials, when comparing them with the well studied III-V semiconductors.

In this chapter, it will be shown that by combining Ge and rare earth doping, we have been able to overcome the previously mentioned difficulties advising for electrical compensation theory and, to notably improve the transport charge properties of this kind of materials (up to a factor of 3 in the resistivity).

Special attention has been paid to Cd(Zn)Te bulk because of its potential use for X- and γ-ray radiation detectors operating at room temperature (see [32] and [33,34], respectively).

4.2 Growth of CdTe- based sources

Analyzing the state of the art of sources' growth, it can be seen that in the last years there has been considerable progress in the growth and characterization of doped CdTe bulk sources by different techniques. However, their commercial use is still limited by numerous technological problems, such as homogeneity in large areas, and high cost ([16,33-36]).

4.2.1 Growth and characterization of CdTe:Ge:Yb co- doped sources

As previously mentioned, the co- doping of CdTe with deep donors and rare earth element could be a promising way to overcome the difficulty of low resistivity inherent to the un-doped CdTe and to obtain semi-insulating CdTe sources with good transport charge properties [37]. Consequently, the purpose of the present study is to investigate the effect of Yb and Ge doping on the electrical resistivity of CdTe.

4.2.1.1 Growth procedure

CdTe crystals co- doped with Ge and Yb (CdTe:Ge:Yb) were grown by the vertical Bridgman method in sealed high-purity quartz ampoules using electronic-grade raw materials [18,38]. Prior to the growth process, the CdTe:Ge:Yb mixture was synthesized and homogenized at 1200 ^{o}C in an oscillating furnace for 20 hours. During the Bridgman growth, the CdTe:Ge:Yb crystals were pulled down at the rate of 0.5–2 mm/h under a thermal gradient of 5–7 ^{o}C/cm. Based on the results of previous studies on the growth and properties of doped CdTe [9], the nominal **Ge** concentration was kept constant at **5x10^{17} at./cm^{3}** and the **Yb** concentration was varied in the range of **10^{17}-10^{19} at./cm^{3}**.

In order to obtain samples suitable for characterization, after the growth procedure, the crystals were sliced perpendicularly to the growth direction to obtain 10x10 mm^{2} area and 1mm thick samples. Afterward, the sources were chemically polished in a 5% bromine–methanol solution and rinsed to remove the surface damage.

4.2.1.2 Physical properties

The physical properties were investigated by combining different (morphological, structural, electrical and optical) characterization techniques. These techniques help us to properly understand the CdTe electrical behaviour.

4.2.1.2.1 Morphological and chemical characterization

Scanning electron microscopy **(SEM)** was used for morphological characterisation of CdTe:Ge:Yb sources. Observing all sources, it was found that for CdTe:Ge:Yb (Ge - 5x10^{17} at./cm^{3}: Yb - 1x10^{19} at./cm^{3}) samples, some small dots appeared, as illustrates in figure 4.1. The size of these dots is around dozen of nm.

To elucidate the chemical origin of these small dots, energy dispersive X- ray (EDAX) analysis was carried out. In addition, inductively coupled plasma mass spectroscopy (ICP–MS) was used to determine the dopants and residual impurity concentrations. All the obtained results evidence that, as expected, these dots are Yb precipitates.

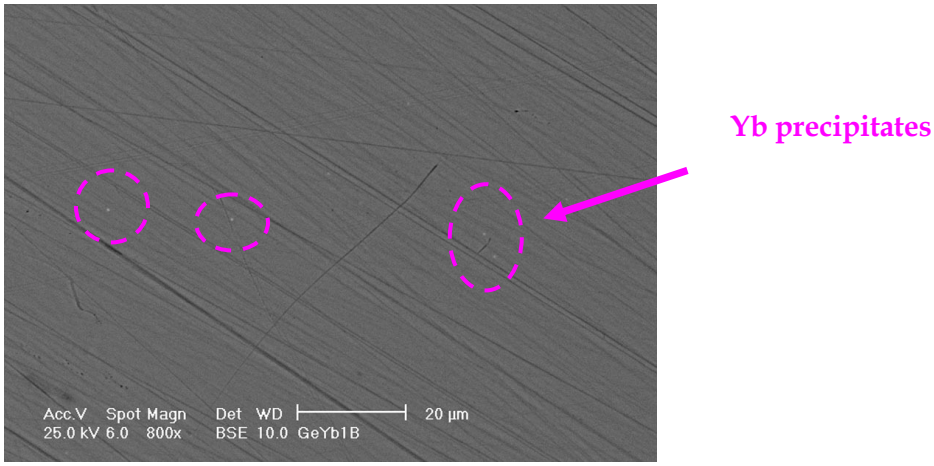

Figure 4.1. a) SEM image of a CdTe:Ge:Yb (Ge- $5x10^{18}$ at./cm^3: Yb- $1x10^{19}$ at./cm^3) sample grown by vertical Bridgman method, at 1200 ^oC in an oscillating furnace for 20 hours.

Studying the Yb solubility limit, more information about homogeneity and quality of the sources can be obtained. Note that SEM data, is an indirect way to study the solubility limit. In this sense, no evidence of Yb precipitation has been observed for a Yb doping level below **$5x10^{18}$ at./cm^3**. This result agrees quite well with EDAX data (shown later in this section) which indicate that **the solubility limit is close to ~ $5x10^{18}$ at./cm^3**.

All these data demonstrate that homogeneous CdTe:Ge:Yb crystals with Yb concentration below ~ $5x10^{18}$ at./cm^3 can be grown with a reasonably good morphological quality by tuning the growth process parameters [37]. A thorough investigation is required in this direction but we considered that was out of the scope of this thesis.

4.2.1.2.2 Electrical characterization: Effect of Yb concentration on the resistivity and lifetime of CdTe:Ge:Yb co-doped sources

The characterization of the electrical properties of the material is a key point for further development of devices, since such devices require crystals with high electrical resistivity.

For electrical characterization gold contacts were deposited by electrochemistry on samples. Afterward, I-V characteristic curves were measured. Photoconductivity lifetimes were determined as a function of light intensity by means of quadrature frequency resolved photoconductivity measurements (QFRP) carried out at room temperature [38,39].

Firstly, the dependence of electrical conductivity on Yb concentration is studied. Based on previous results on the growth properties of CdTe:Ge and considering the theoretical

simulation results reported below, the nominal Ge concentration was kept constant at $5x10^{17}$ at./cm^3 in all CdTe:Ge:Yb crystals whereas the Yb concentration was varied in the range of 10^{17} to 10^{19} at./cm^3 [40].

In order to look for the optimal doping condition, the electrical resistivity of CdTe:Ge:Yb crystals was simulated using the compensation model developed for GaAs [41-42] and adopted for CdTe. This model is based on the compensation of the shallow acceptors by a deep donor in the middle of the band gap. More details about the model can be found in the works realized by M. Fiederle et al. [43] and in section 2.6.1.

The resistivity behaviour was examined as a function of the concentrations of both dopants, assuming the presence of two deep donor levels corresponding to $Ge^{+2/+3}$ at $E_C-0.95$ eV (Ref. 14) and $Yb^{+2/+3}$ at $E_C-1.2$ eV [37].

A first set of simulations was done fixing the Yb concentration at three different values ($1x10^{17}$, $1x10^{18}$, and $1x10^{19}$ at./cm^3) and varying the Ge concentration in the range of $1x10^{16}$ - $1x10^{18}$ at./cm^3 with the aim of studying the role of Ge for a precise electrical compensation [40]. The results are shown in figure 4.2.

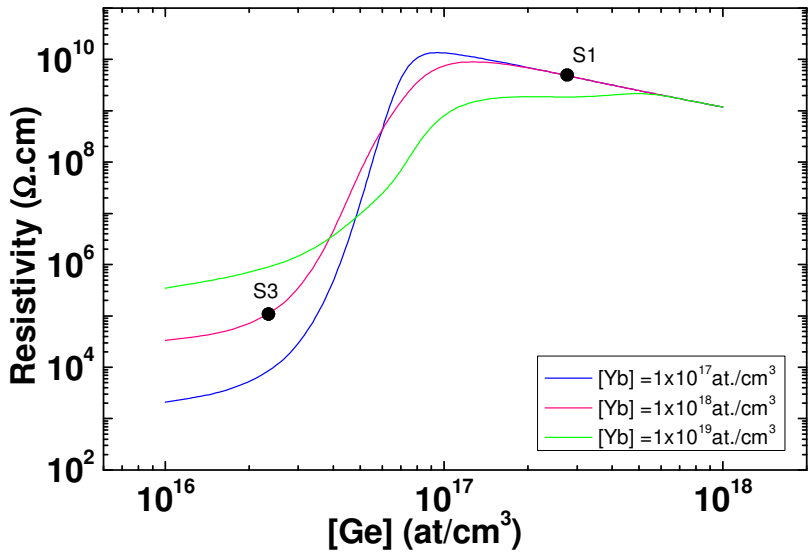

Figure 4.2. Simulated electrical resistivity values for CdTe:Ge:Yb sources as a function of Ge concentration for three different Yb concentrations (Yb 17—1 x10^{17} at./cm^3 (blue line), Yb 18—1x10^{18} at./cm^3 (red line), and Yb 19—1x10^{19} at./cm^3 (green line)). The points marked as S1 and S3 corresponds to the samples in Table I.

These results proof that the resistivity of CdTe:Ge:Yb sources strongly depends on Ge concentration. A drastic resistivity enhancement is observed for [Ge] in the range of $5x10^{16}$–10^{17} at./cm^3 and it slowly decreases for Ge concentrations higher than ~ 10^{17} at./cm^3. According to

simulations, the maximum resistivity is obtained at the lowest Yb concentration. In addition, the simulations point out that resistivity has a lower dependence on Ge concentration at larger Yb concentrations. In general, resistivity has a weak dependence on Yb concentration at Ge concentrations around ~ $5x10^{17}$ at./cm^3, varying less than half an order of magnitude in all the studied range. This is an expected result since Yb introduces a very deep donor level that is barely ionized at room temperature and, consequently, it does not affect the CdTe:Ge:Yb resistivity [44]. It is noteworthy to mention that these simulations are in agreement with later experimental data on CdTe:Ge:Yb crystals. This fact supports the idea of adopting the electrical compensation theory developed for III-VI semiconductors.

The nominal (i.e., intentionally introduced during growth) and measured concentrations of Ge and Yb dopants as well as, the concentrations of acceptors and donors in CdTe:Ge:Yb crystals are listed in table 4.I. It can be observed, that Yb doping affects the solubility of Ge co-dopants, the concentrations of electrically active residual impurities and native defects. In particular, when the Yb concentration increases, both the Ge concentration and the total acceptor and donor concentrations decrease. The latter effect can be explained by the high reactivity of Yb dopants that act as a cleaning agent, reacting with residual impurities of the group I and segregating them to the top of the CdTe:Ge:Yb crystal ingot; in a similar way as it was reported for III-V semiconductors [45]. The observed decrease in the Ge concentration with rising Yb concentration might be due either to the reaction between both co- dopants or to the fact that Ge, and Yb competes for replace Cd position in CdTe lattice, but Yb atoms might preferentially occupy this position since Yb is chemically more similar to Cd than Ge.

Sample Code	**Nominal Ge conc.(at./cm^3)**	**Nominal Yb conc.(at./cm^3)**	**Measured Ge conc.(at./cm^3)**	**Measured Yb conc.(at./cm^3)**	**N_A (at./cm^3)**	**N_D (at./cm^3)**
S1	$5x10^{17}$	$1x10^{17}$	$4x10^{17}$	$1.2x10^{17}$	$3.3x10^{16}$	$1x10^{16}$
S2	$5x10^{17}$	$1x10^{18}$	$7x10^{16}$	$8.8x10^{17}$	$2.5x10^{16}$	$1.6x10^{16}$
S3	$5x10^{17}$	$1x10^{19}$	$2.3x10^{16}$	$6x10^{18}$	$2.1x10^{16}$	$9.7x10^{15}$
S4	$5x10^{17}$	0	$3.7x10^{17}$	N.D.	$6x10^{16}$	$2.2x10^{16}$

Table 4.I Overview of nominal (i.e., intentionally introduced during the growth) and measured Ge and Yb concentration dopants, together with density of acceptors (N_A) and donors (N_D) for CdTe:Ge:Yb samples.

A second set of simulations was carried out by fixing the Ge concentration at $5x10^{17}$ at./cm^3 (which according to literature is the typical value to obtain the native acceptor compensation in Ge-doped CdTe crystals [14]) and varying the Yb concentration in the range of $1x10^{17}$-$1x10^{19}$ at./cm^3. The aim of these simulations is to demonstrate that the concentration of Yb is a key point for a precise electrical compensation.

Experimentally, the resistivity of CdTe:Ge:Yb crystals with a nominal Ge concentration of $5x10^{17}$ at./cm^3 as a function of Yb concentration is depicted in figure 4.3.

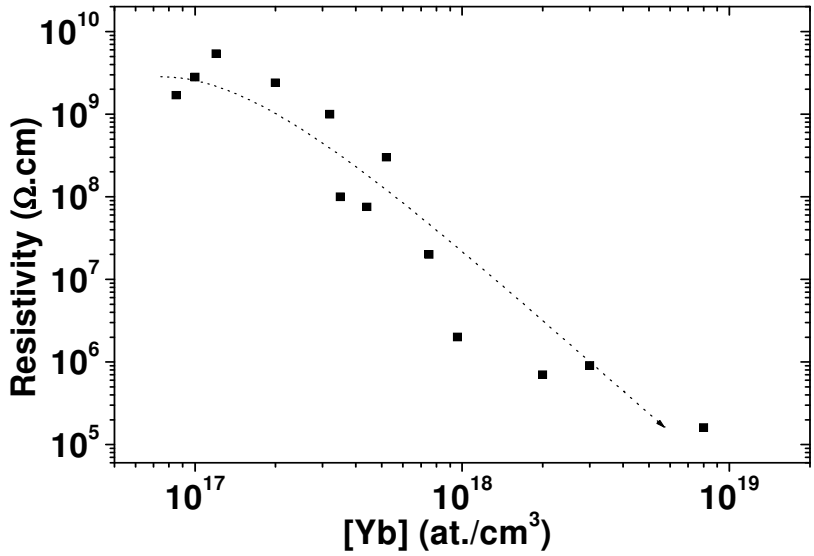

Figure 4.3. Experimental resistivity of CdTe:Ge:Yb crystals grown with a fix nominal Ge concentration of $5x10^{17}$ at./cm^3 as a function of Yb concentration. (Dotted line is only a visual guide).

Experimental data reveal a drastic reduction in resistivity of up to 10^6 Ω·cm with increasing Yb concentration from ~ $9.4x10^{17}$ to $7.9x10^{18}$ at./cm^3. Moreover, it is observed that CdTe:Yb sources keep a semi-insulating behaviour similar to that of CdTe:Ge only in a narrow $1x10^{17}$- $3x10^{17}$ at./cm^3 Yb concentration range. The resistivity in this range is larger than 10^9 Ω·cm which could be understood by taking into account the data of Table 4.I. Note that sample S1 (the one with the lowest Yb concentration in Table 4.I) has an experimental resistivity of $5.5x10^9$ Ω·cm, which is in agreement with the corresponding simulated value in figure 4.2 ($4x10^9$ Ω·cm). In this case, CdTe:Ge:Yb is very similar to CdTe:Ge because the Yb concentration is low and its influence is almost negligible. When the Yb concentration increases, the resistivity falls with the decrease of actual Ge concentration due to the substitution of Ge atoms by Yb in the Cd sublattice. Thus, we can state that the resistivity reduction is linked to a lower Ge concentration. (This fact is in agreement with the results shown in table 4.I) [46].

The effect of Yb doping on the electron lifetime was studied as a function of Yb concentration by QRFP measurements. The photoconductive response of CdTe:Ge:Yb sample as a function of the excitation light frequency [39] was obtained. The results are shown in figure 4.4.

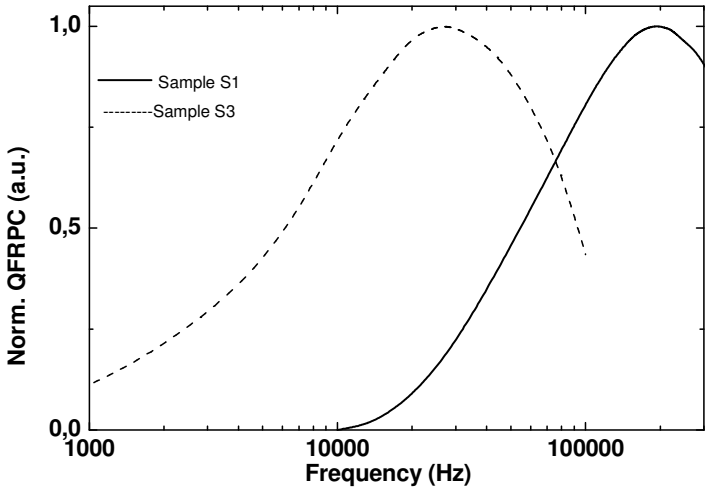

Figure 4.4. QRFP spectra for S1 (the one with the lowest Yb concentration) and S3 samples (the one with the highest Yb concentration) in table 4.I at room temperature.

In agreement with simulated data the photoconductivity increases at low frequencies up to a certain maximum ($\mathbf{f_{max}}$) and then decreases in the high frequency region [47,48]. The carrier lifetime ($\boldsymbol{\tau}$) is calculated as a function of f_{max} as follows:

$$\tau = \frac{1}{2\pi \cdot f_{\max}} \qquad (4.1)$$

The evolution of electron lifetime as a function of Yb concentration for CdTe:Ge:Yb crystals is depicted in figure 4.5. Results for un- doped and CdTe:Ge crystals are also added for sake of completeness.

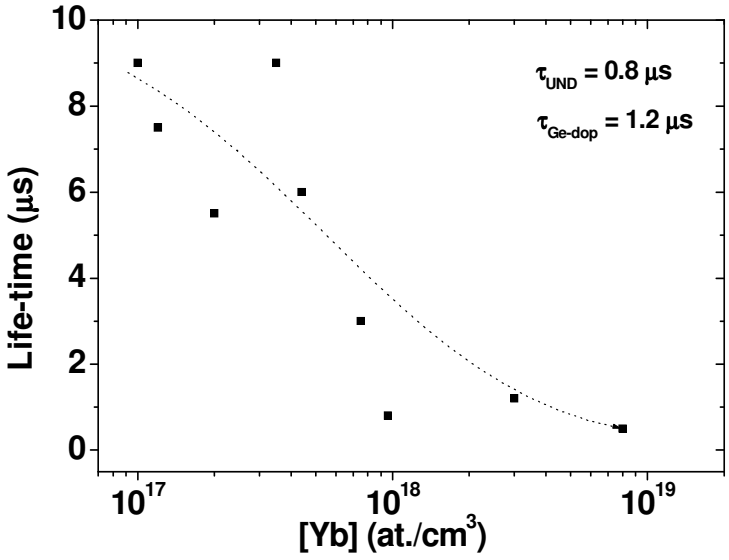

Figure 4.5. Evolution of electron lifetime as a function of Yb concentration for CdTe:Ge:Yb crystals. $\boldsymbol{\tau_{und}}$ is the electron lifetime for a typical un- doped CdTe crystal (dotted line is a visual guide). $\boldsymbol{\tau_{Ge\text{-}dop}}$ is the electron lifetime for a typical Ge-doped CdTe crystal (S4 in Table 4.I).

The most remarkable feature in this graph is that the CdTe:Ge:Yb lifetime increases from 5.5 to 9 μs with decreasing Yb concentration from $2x10^{17}$ to $1x10^{17}$ at./cm^3, where the sources are semi-insulating. Namely, a further enhancement in Yb concentration leads to a decrease of lifetime. Such behaviour could be explained by two possible mechanisms which coexist and act in different ways. The first one, and presumably the most important, is the cleaning process due to the interaction of Yb dopants with residual impurities (e.g., see Ref. 45). Note in Table 4.I that the major reduction in impurities concentration is detected for low Yb concentration. The second possible mechanism is related to the doping- induced changes in the defect level structure for CdTe:Ge:Yb sources in comparison to that of the un- doped and Ge-doped CdTe ones. Indeed, the later mechanism has been considered as a possible explanation for the observed improvement in the transport charge properties of CdTe sources doped with deep donors [49].

4.2.1.2.3 Optical characterization: PL and CL studies

Photoluminescence PL characterization of the samples was performed at 10 K. The spectra for three different CdTe samples doped with Ge ($5x10^{17}$ at./cm^3), Yb ($1x10^{18}$ at./cm^3) and co- doped with Ge:Yb ($1x10^{17}$:$1x10^{18}$ at./cm^3) are presented in figure 4.6. In general, all spectra exhibit a strong emission of neutral donor-bound excitons (D^0X) in the band-edge region, in which the PL intensity increases with rising Yb concentration. This may imply that the Yb dopant produces a shift of the Fermi level towards the conduction band, thus explaining the observed high resistivity for CdTe:Ge:Yb.

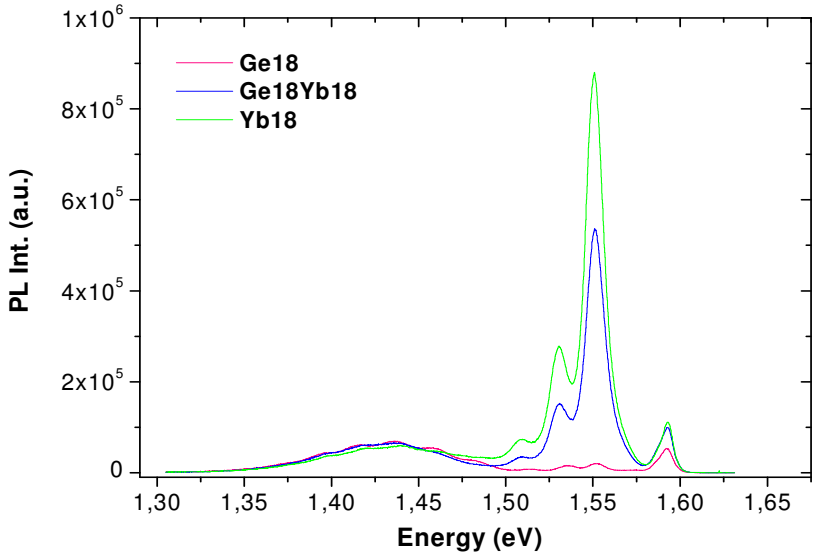

Figure 4.6. Photoluminescence spectra measured at T=10 K for samples doped with Ge (red line), Yb (green line) and co-doped with Ge:Yb (blue line).

The other important feature of PL spectra is the strong increase in the PL band centred at 1.55 eV for Yb- doped sources. The high intensity of the 1.55 eV band measured for CdTe:Ge:Yb and CdTe:Yb sources may be associated to an increase of donor defects that form complexes with V_{Cd}. This reveals that the Yb incorporation introduces donor levels in CdTe. This band for the Yb doped sources does not seem to shift in energy when changing the Yb concentration; since this emission is related with a donor–acceptor pair (DAP) transitions between hydrogen-like donor levels and acceptor levels connected to defect complex with the structure (V_{Cd}–D_{Cd}) or (V_{Cd}–$2D_{Cd}$) (a considerable part of the V_{Cd} are stabilized with donors on Cd sites, due to the formation of these complexes structure) [50-52].

A typical **Cathodoluminescence, CL** image of the surface for a CdTe:Ge:Yb ($1x10^{17}$:$1x10^{18}$ at/cm^3) source is presented in figure 4.7. It exhibits a granular crystal structure in which the grain boundaries appear as bright lines. Such a color contrast has been previously reported for similar CdTe:Ge films as well as, for other semiconductors and insulator materials [11,53]. It has been found to be due to the decoration of boundaries by impurities and/or point defects.

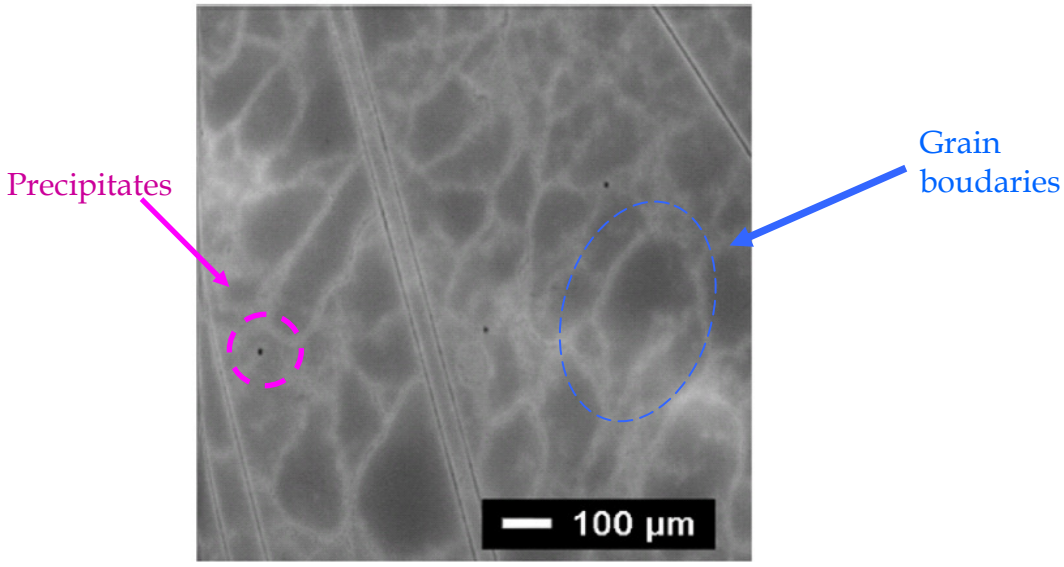

Figure 4.7. CL image of a high-resistivity CdTe:Ge:Yb source.

The area within the grains is very homogeneous without any microscale structural defects like voids, precipitates, impurity clusters, etc. Nevertheless, some of these defects are observed as non-radiative dark spots within the grain boundaries, proving their role as defect segregation centres (in figure 4.7 it is shown some precipitates). This segregation seems to be also related with the purification effect caused by the interaction of Yb dopant with the group I residual impurities.

Increasing the Yb concentration at values larger than ~ $5x10^{18}$ at./cm^3 results in a loss of homogeneity for CdTe:Ge:Yb source. High Yb doping level induces the formation of a higher number of grains in which the bright bands become for tens of microns broader.

The CL spectrum for a CdTe:Ge:Yb source ($1x10^{17}$:$1x10^{18}$ at./cm^3) is depicted in figure 4.8. In this figure two deep level bands centred at 1.10 eV and ~ 1.40 eV can be observed. Gaussian deconvolution of the most intense band (1.10 eV) shows that it has three different components centred at 0.99 eV, 1.09 eV and 1.39 eV respectively [46].

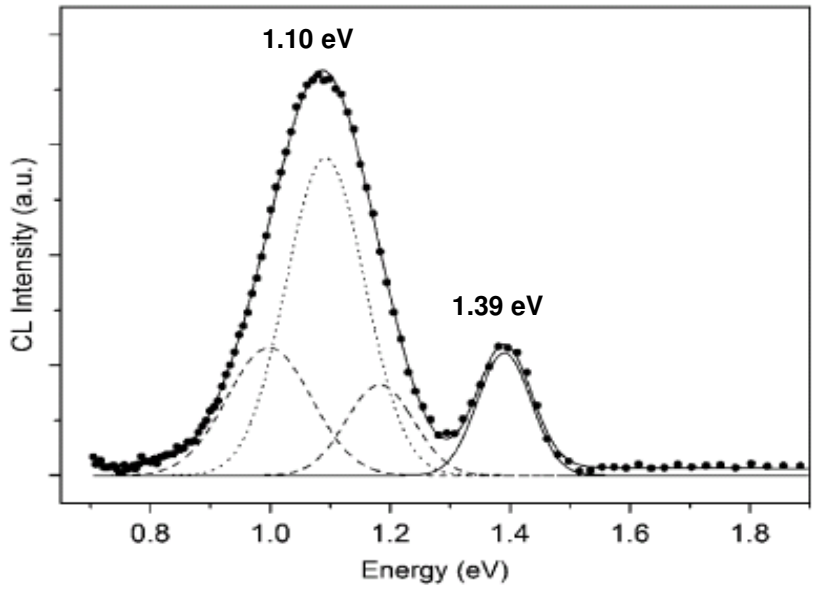

Figure 4.8. Measured (black dots) and simulated (black line) CL spectrum for a CdTe:Ge:Yb ($1x10^{17}$:$1x10^{18}$ at/cm^3) source, with a Gaussian deconvolution (dashed lines) of the band centred at 1.10 eV.

The three components can be associated to levels at about 1.10 eV below the conduction band for CdTe, which have been suggested to be related to different states of Te-vacancies, $\mathbf{V_{Te}}$ [54,55]. The high energy band at 1.39 eV might be due to the presence of radioactive recombination centres [44].

4.2.2 Growth and characterization of CdTe:Bi doped sources and CdTe:Bi:Yb co- doped sources

Bi- doping aims to achieve CdTe semi-insulating semiconductors with high photosensivity and excellent transport charge properties. The growth of CdTe:Bi is a relatively new topic. Therefore, a detailed characterization of this material is carried out, focussing on the study of its potential capabilities.

4.2.2.1 Growth procedure

CdTe:Bi and CdTe:Bi:Yb crystals were grown by the Vertical Bridgman Method in a quartz ampoule with a pyrolytic graphite coating. The growth rate was 0.4 mm/h. A temperature gradient in the solidification zone of 5 ^{o}C/cm was measured during growth.

The CdTe:Bi crystals were doped during growth with two Bi concentrations of $1x10^{17}$ at./cm^3 (sample 1) and $7x10^{17}$ at./cm^3 (sample 2). The dopant concentrations in CdTe:Bi:Yb crystals (sample 3) were $1x10^{17}$ at./cm^3 for Bi and $1x10^{18}$ at./cm^3 for Yb. More details on the growth procedure setup can be found elsewhere [16].

4.2.2.2 Physical properties

The morphological and optical properties of the samples have been characterized by means of SEM and CL, respectively.

4.2.2.2.1 Morphological characterization

The morphological characterisation of CdTe:Bi and CdTe:Bi:Yb sources has been performed by using SEM. Figure 4.9b, shows a typical SEM image for a CdTe:Bi surface.

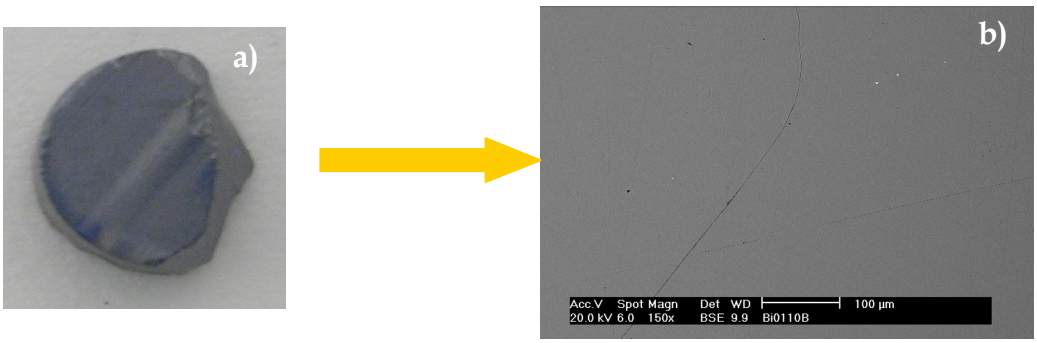

Figure 4.9. (a) Photograph and (b) SEM image of a CdTe:Bi source grown by vertical Bridgman method at 1200 ^{o}C. The growth rate was 0.4 mm/h.

The surface shows high homogeneity, without nothing significant to mention. Indeed, no significant differences between the surface of CdTe:Bi and CdTe:Bi:Yb were observed. Moreover, the surface appearance of these two sources was very much similar to those presented in section 4.2.1.2.1.

4.2.2.2.2 Optical Characterization: CL studies

Based in the work carried out by the Dr. Edgardo Saucedo et al. [15,18]. Two defect centres were identified for Bi- doped CdTe sources by photoluminescence and photoconductivity measurements. The first one, responsible for the high resistivity and the very good photoconductivity of the CdTe:Bi crystals, is associated with a deep level located at E_v+0.71 eV. The second, mainly present at high Bi concentrations, is considered to be responsible for the low resistivity and poor photoconductivity. It is an acceptor centre located at E_v+0.30 eV, and assigned to BiTe specie.

CL characterization. A CL image of a CdTe:Bi sample (**sample 1**) is shown in figure 4.10a. As for CdTe:Ge doped crystals, the sample exhibits a granular structure. Grain boundaries appear in this image as bright lines. The image shows high homogeneity. The interior of the grains is very homogeneous and neither precipitates nor other non-radiative recombination centres are observed [56]. Similar characteristics have been previously reported for other semiconductors and insulating materials and, are due to the deterioration of the boundaries by impurities and or point of defect. (As we previously mentioned in CL studies for CdTe:Ge:Yb).

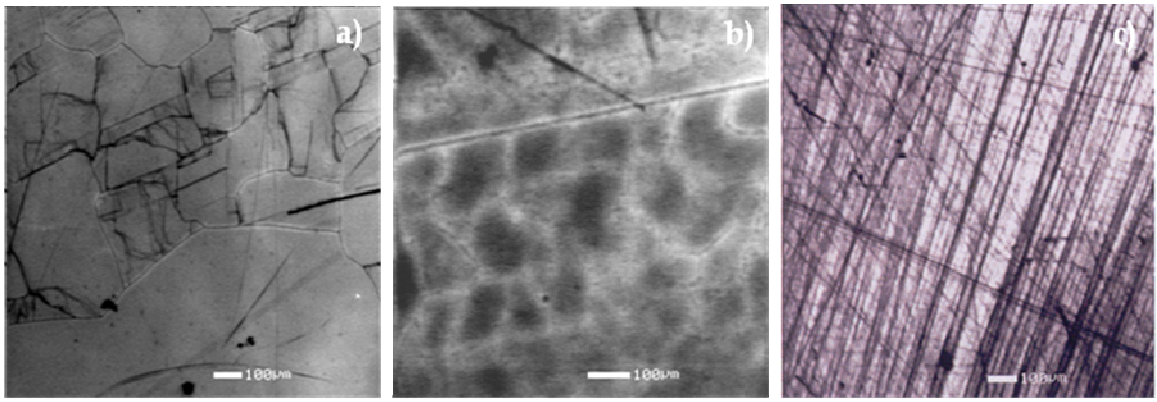

Figure 4.10. (a) CL image of the **(a)** sample 1 **(**Bi- doped with 1x10^{17} at./cm^3), **(b)** sample 2 (Bi- doped with 7x10^{17} at./cm^3) and, **(c)** sample 3 (Bi- doped with 1x10^{17} at./cm^3 and Yb-doped with 1x10^{18} at./cm^3).

As shown in figure 4.10b (**sample 2**) increasing the Bi concentration results in a loss of homogeneity of the samples surface. Moreover, it gives rise to higher number of grains surrounded by boundaries in which the bright bands extend up to about 50 μm.

In general, the sample 1 has a higher CL emission than sample 2. Moreover, its emission is rather homogeneous where a higher CL contrast is observed probably due to some inclusion of the same material with a higher Bi concentration (see fig 4.10a). The black lines, which are arbitrary distributed all over the area, probably due to the typical defects introducing during the polishing process. For sample 2, in figure 4.10b, it is also observed that the surface presents

the same dark line and inclusions due to the polishing process than those observed in sample 1. Also as seen in figure 4.10c, the main features observed in the CL images for **sample 3**, co-doped with Bi and Yb (Bi- doped with $1x10^{17}$ at./cm^3 and Yb- doped $1x\ 0^{18}$ at./cm^3), are parallel dark lines. Note that this result contrast in some sense with those obtained for the other two cases, where the lines were arbitrary distributed. Such distribution of lines has been previously reported for other semiconductors like GaSb:Te, [57,58] and it has been attributed to the variation in the dopant concentration. In order to determine which dopant gives rise to the striations, EDX maps for Bi and Yb were recorded. No spatial variations of any of these elements were detected. This suggests that the concentration of the element is below the detection limit of the EDX, although has a strong influence on the dopant sensitive CL measurements.

CL measurements show that in the sample with higher Bi content ($7x10^{17}$ at./cm^3) a dense network o highly decorated grain boundaries is formed whereas in the co- doped samples, dopant striations are observed which are probably due to the presence of Yb.

The CL spectrum for **sample 1** (figure 4.11) shows the near band gap emission band at 1.56 eV (this energy is connected with the excitonic transition involving the edge of the band) and two deep level bands centred at about 1.10 eV and 0.78 eV. Gaussian deconvolution of the most intense band, centred at 1.10 eV, shows that it has three components centred at 1.12 eV, 1.06 eV, and 0.96 eV. The first one can be associated to a level at about 1.10 eV below the conduction band of CdTe, which has been suggested to be related to V_{Te} [59, 60]. According to A. Castaldini et al., the other two bands, with an acceptor character are associated to the complex structure formed by tellurium vacancies and interstitial (V_{Te}- Te_i)) [51]. The low energy band at 0.78 eV is also complex and, it is the results of the deconvolution of two components centred at 0.78 eV and 0.77 eV, which are related to different states of an acceptor involving native V_{Cd} defects and impurities [61].

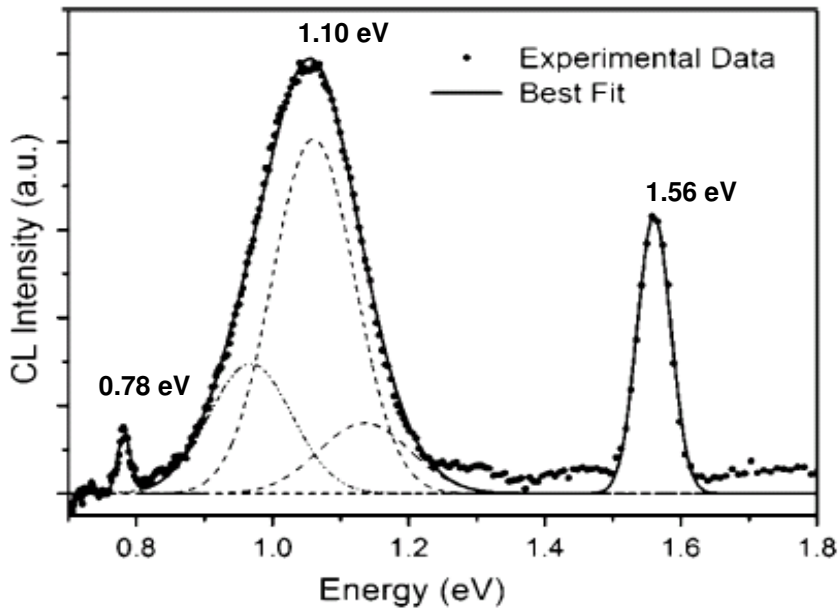

Figure 4.11. Measured (full circles), and fitted (solid line) CL spectrum for sample 1**(**Bi- doped with $1x10^{17}$ at./cm^3), with a Gaussian deconvolution (dashed lines) of the band centred at 1.10 eV.

By comparing with CL spectrum of CdTe:Ge:Yb sources (see figure 4.8), it can be deduced that the addition of Bi in the CdTe lattice gives rise to a dramatic reduction in the A-band related with V_{Cd}.

The CL spectrum for **sample 2** (figure 4.12) is noisier than for sample 1 due to a lower CL emission. It shows bands at about 1.45 eV and 1.35 eV emission bands [51], in addition to the near band gap emission at 1.56 eV and the deep level at 1.10 eV, which were also presented in sample 1.

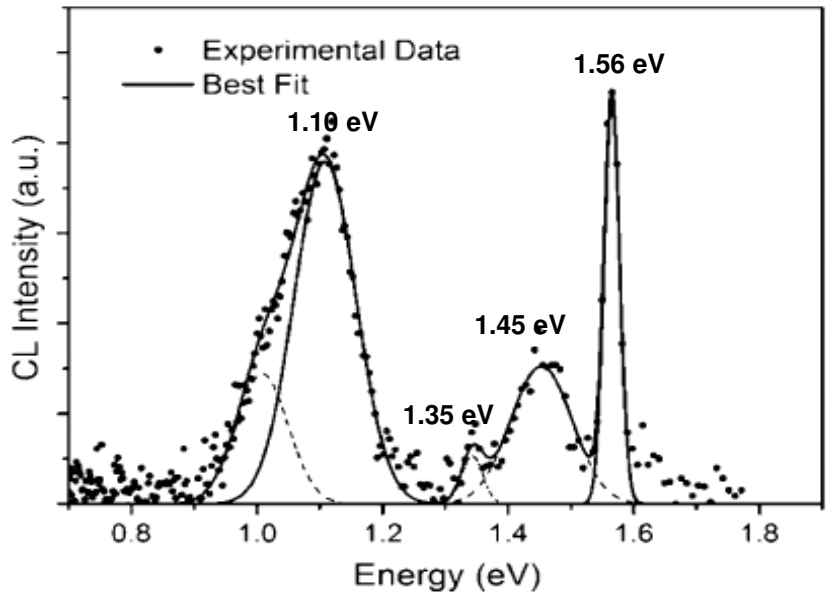

Figure 4.12. Measured (full circles) and best fit (solid line) CL spectrum for sample 2 (Bi- doped with $7x10^{17}$ at./cm^3), with a Gaussian deconvolution (dashed line).

As shown in figure 4.12, in comparison with sample 1 (see figure 4.11), two new peaks appear at 1.35 eV and 1.45 eV in the CL spectrum for the sample 2. These bands are related to the dopant. In agreement with previously reported luminescence results for Ge- doped and un-doped CdTe samples, these new peaks might correspond to A centres formed by V_{Cd} and Bi atoms [62,63]. In the CL spectrum for sample 1, the peak centred at 0.78 eV connected to native defects does not appear in this sample, suggesting that this sample presents a native defect concentration lower than sample 1.

As in the Bi- doped samples, the CL spectrum for **sample 3** (figure 4.13) shows the band gap emission centred at 1.56 eV, and the low energy band centred upon 1.10 eV. Nevertheless, the A-band centred at about 1.43 eV is less intense than for sample 2 and was not observed in sample 1 (which has the same Bi content as this sample). The existence of this additional band indicates that the presence of Yb also contributes to this emission, therefore suggesting the existence of a new radiative centre involving Yb atoms.

The influence of Yb is also observed in the band centred at 1.10 eV which is broader than in the other samples and shows a slight shift to higher energies with a maximum at 1.08 eV. Gaussian deconvolution of this band shows that it is formed by three emission peaks centred at 1.17 eV, 1.05 eV, and 0.95 eV.

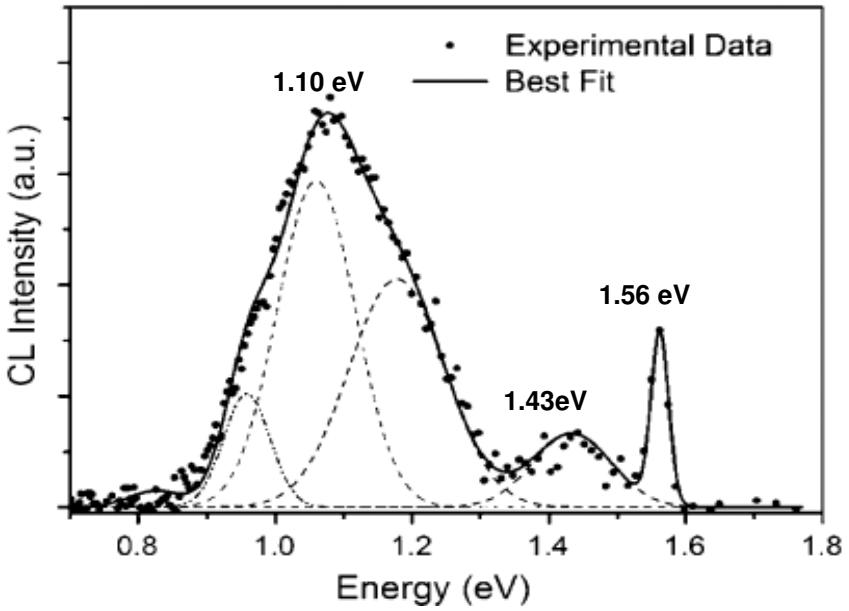

Figure 4.13. Measured data (full circles) and best fit (solid line) CL spectrum for sample 3, (CdTe:Bi:Yb), with Gaussian deconvolution (dashed line) of the band centred at 1.10 eV.

In comparison with CL spectra measured for sample 1 and sample 2, the spectrum for sample 3 shows a displacement at higher energies in one of the band present in the region from

0.90 eV to 1.25 eV. The origin of this displacement is not well understood. Probably it may be due to the presence of Yb which modifies somehow the recombination centre. Nevertheless, its study falls out of the scope of this thesis.

By comparing the CL intensity for the band centred at 1.10 eV to the other relative intensities for other bands for sample 3, one realized that it is higher than for the other two samples. Beside, the intensity of band gap at 1.56 eV in the case of sample 2 is high than those observed in sample 1 and sample 3.

Therefore, Bi- doping contributes to the appearance of the A luminescence band and, at higher Bi content a dense network of highly decorated grain boundaries is formed. In addition, Yb causes a blue shift of the deep level band centred at about 1.1 eV [56].

4.2.3 Study of the deterioration of $Cd_{1-x}Zn_xTe$ sources: reasons and consequences

In this section, the deterioration of $Cd_{1-x}Zn_xTe$ sources after several runs is going to be systematically studied in order to improve the quality of the $Cd_{1-x}Zn_xTe$ films growth from those sources and to obtain reproducible films.

4.2.3.1 Growth procedure

$Cd_{1-x}Zn_xTe$ sources were grown by the Bridgman method [16]. The electronic-grade 6N Cd, Te and Zn were used as raw materials. The materials (about 100 g in total) were charged and sealed in high-purity quartz ampoules. Prior to the growth process, the mixture was homogenized at 1200 ^oC in an oscillating furnace for 20 hours. During the Bridgman growth process, the $Cd_{1-x}Zn_xTe$ polycrystals were pulled down at 4–10 mm/h under a thermal gradient of 7 $^oC/cm$. The crystals were sliced perpendicularly to the growth direction into the 1.5–2 mm thick and 18 mm diameter wafers that were mechanically slandered with SiC powder and chemically polished in the 5% bromine-in-methanol solution and washed to remove the surface damage. Figure 4.14 shows an example of $Cd_{1-x}Zn_xTe$ ingot and slice sources.

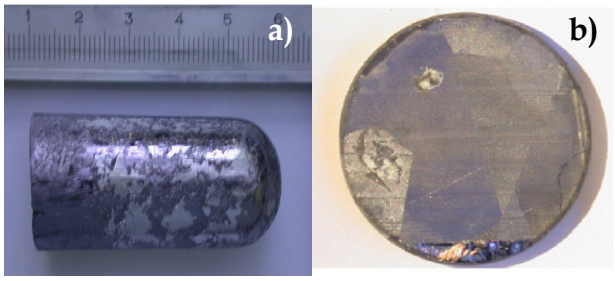

Figure 4.14. Photograph of a $Cd_{1-x}Zn_xTe$ polycrystal (a) ingot and (b) slice grown by Bridgman technique for the fabrication of VPE sources.

$Cd_{1-x}Zn_xTe$ films were grown on two different substrates, Si and Silicon oxide (SiO_x) 6-inches substrates. These substrates were mainly selected because of their low cost and the facility to obtain them in large areas. The substrate temperature range and the growth rate were selected to be between 600- 850 ºC and 1–10 nm/s, respectively.

4.2.3.2 Physical properties

The samples analyzed in this section, were cut from the central zone of the ingot, to diminish the effect of the different composition due to the segregation coefficient of the Zn in the CdTe, which usually is major than the unit [63,64].

As an alloy of CdTe, it is normal that this kind of material presents structural defects such as Te precipitates, twins, grain boundaries and clusters of dislocations. Because of this, effort has been put into the characterization of these sources to obtain more information about them [65].

Similar combined SEM, EDAX and, XRD characterization for $Cd_{1-x}Zn_xTe$ films is carried out to study the effect of source composition on the VPE large area films.

4.2.3.2.1 Structural and compositional characterization

As previously mentioned, one of the problems associated with this compound is to achieve an homogeneous Zn distribution along the ingot. This is due to the difficulties inherent to growth of ternary compounds, since its melting temperature significantly increases with Zn concentration [66,67], which makes the growth process a challenge. In this thesis, a Zn concentration of 4 at.% has been used.

Due to the fact that Zn atom is isovalent to Cd atom, when Zn is added to a CdTe lattice, the matrix sublattice is altered and the V_{Cd} is reduced. The addition of Zn to CdTe produces important changes in the base material characteristics, such as lattice constant, **α**, and energy band gap, $\mathbf{E_g}$, i.e. $\mathbf{E_g}$ increases in the range of 1.4 to 2.2 eV and, **α** in the range between 6.1 to 6.5 Å when adding Zn.

We have observed that the concentration and size of the precipitates in CdZnTe samples are slightly higher than in CdTe. This behaviour is a fact which in literature has been described by other authors [9,10]. The Zn distribution in the ingot measured by EDAX is shown in figure 4.15.

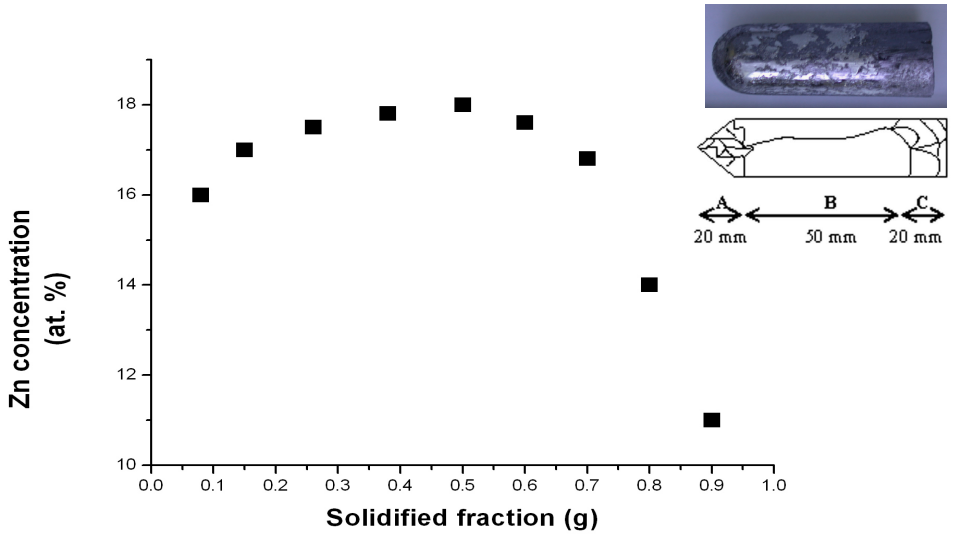

Figure 4.15. Typical distribution of [Zn] along the growth axis for $Cd_{1-x}Zn_xTe$ polycrystal derived from EDAX measurements.

In figure 4.15 is shown that in the A and C region (edges of the sources) the Zn concentration is non-uniform whereas that [Zn] is approximately constant in the B region (centre of the sources). This fact indicates that the solid-liquid interface is quite flat at this region. But the axial non-uniformity at the initial and end portion of the ingot, points out to a non planar solid-liquid interface at these places.

If we observe the figure and the inset with more detail, the polycristal can be studied in three different regions. In the segment A of the polycristal, the Zn concentration slightly increases when increasing the distance from the ingot, (namely since 0 to ~20 mm), being between 16-17 at.%. When the central segment B is reached, the solidification fraction is ~ 0.55 remains almost constant. However, in the segment C of the ingot, for high solidification fractions, a sudden decrease in the Zn concentration is detected. This behaviour is in agreement

with reported data [8] where it is shown that Zn content and the solidified fraction are related by the Pfann´s equation:

$$C_s = C_0 \cdot k \cdot (1-g)^{(k-1)} \tag{4.2}$$

where $\mathbf{C_s}$ is the Zn content measured at a point when the fraction solidified is **g**, **k** is the partition coefficient and, $\mathbf{C_0}$ is the initial content.

The anomalous segregation in the initial portion of the CZT crystal has been observed by many workers and, as it is associated with considerable supercooling of the tip region, under low gradient conditions. This kind of anomalous segregation behaviour is postulated to result from the burst of growth from the initially supercooled melt. In this initial portion, the growth is under conditions where melt mixing is not complete and the growth rate is varying, i.e. decreasing from the initial fast growth under non- equilibrium freezing conditions, to a slower steady-state equilibrium growth conditions.

Nevertheless, these measurements evidence that the Zn distribution along the growth-axes is quite homogeneous, however in order to obtain the optimum sources they have to be cut from the uniform part of $Cd_{1-x}Zn_xTe$ polycrystal.

4.2.3.3 Degradation of the sources after several deposition runs

A photograph of the same source taken prior to (a) and after (b) several deposition runs is shown in figure 4.16. This source is cut from the central area of the ingot. A simple visual inspection evidences that, the appearance of the source surface is significantly different prior to and after several deposition runs. The as- prepared source manifests the characteristic grey color for $Cd_{1-x}Zn_xTe$ compound (figure 4.16a). On the contrary, black and big size red spots are observed (figure 4.16b) at the source surface after several runs. These spots are areas of amorphous CdTe and ZnTe, respectively.

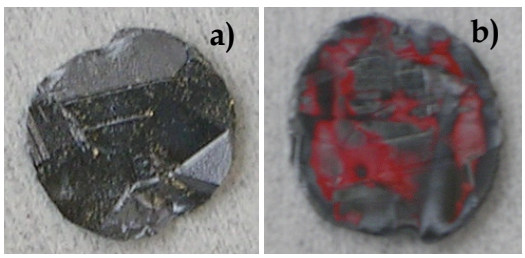

Figure 4.16. Photograph of a $Cd_{1-x}Zn_xTe$ polycrystal grown by Bridgman technique for the fabrication of VPE sources: (a) VPE sources as- prepared and, (b) after several VPE deposition runs.

More detailed information about the microstructural and compositional changes can be derived from SEM images (figure 4.17b) and EDAX data (figure 4.17c-d), respectively. For the sake of clarity, different regions have been separately analyzed as shown in figures 4.17 c-d.

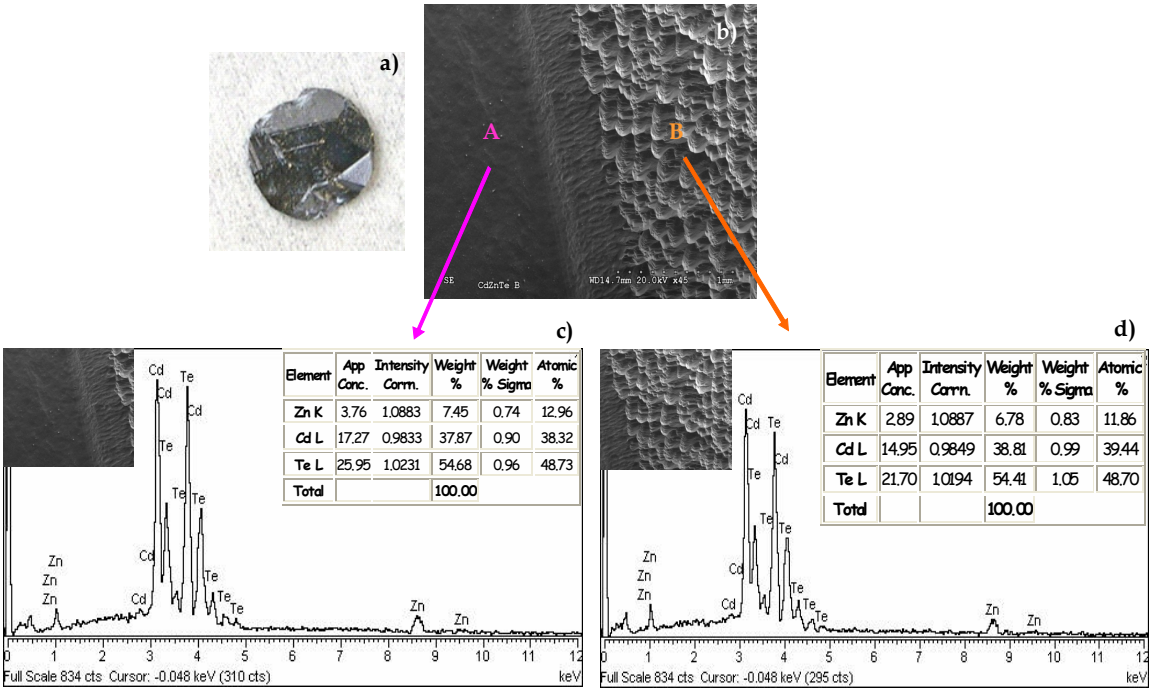

Figure 4.17. (a) Photography of the analysed source. (b) SEM images of different part of $Cd_{1-x}Zn_xTe$ source prior to VPE growth. (c) EDAX measurements of region A and (d) region B of $Cd_{1-x}Zn_xTe$ source.

In figure 4.17, we can observe that the as-prepared source manifests multi-grain structures without any specific features. However, presenting some region (zone B) where the size of the structures is slightly bigger than in zone A. For this source, we did not analyze the intermediate zone because we were mainly interested in studying the origin of the extreme contrast changes.

Apart from the morphological differences deduced from SEM images, EDAX data (listed in table 4.II) taken in the two different regions demonstrate that they present a very much similar chemical composition, indicating that the majority components Te, Cd and Zn are homogeneously distributed.

Element	Zone A. at %	Zone B. at %
Zn	7.45	6.78
Cd	37.87	38.81
Te	54.68	54.41
Total	100.00	100.00

Table 4.II. Brief overview of the chemical composition measured on the two region A and B for the as-prepared source.

The same characterization of the source was carried out after several depositions run. For this, efforts were made to analyse the same regions than in as- prepared sources (see figure 4.18a-d).

As shown in figure 4.18b SEM images evidence the existence of three regions (named A, B and C) which have significant differences in morphology. The region A presents dark colour and bigger structure than the other two regions. The region B is darker and less extensive than region A. And, the region C presents red color.

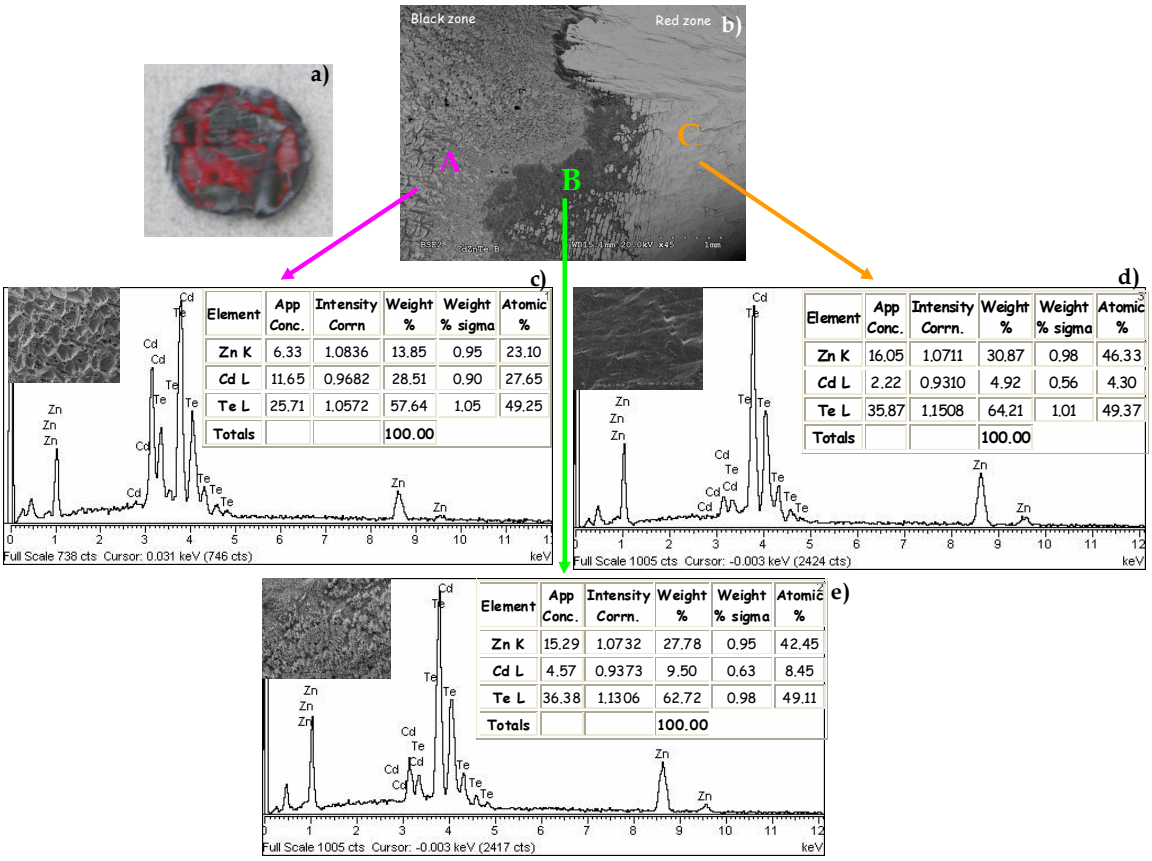

Figure 4.18. (a) Photography of a source after several deposition runs. (b) SEM images of different part of $Cd_{1-x}Zn_xTe$ source. (c) EDAX measurements of region A, (d) region B and (e) region C.

Region A corresponds to one of the **dark parts** of the source. EDAX measurements evidences that the Zn and Te concentration are higher than that for the as- grown source, (Zn concentration increases from 7.45 to 13.85 at.% and [Te] from 54.68 to 57.64 at.%), whereas the Cd concentration decreases from 37.87 to 28.51 at.%. Zone B **(also dark)** is located in between the intermediate part of zone A and zone C, where the increment of Zn and Te concentration (Zn concentration increases from 13.85 to 27.78 at.% and [Te] from 57.64 to 62.72 at.%), whereas the Cd decreases from 28.51 to 9.50 at.%) in comparison with zone A, can be appreciated. Region C corresponds to the red part of the source. The color is due to the excess of Zn with respect to other parts of the source. In the following table 4.III these compositional differences

are summarize. In contrast with the as- deposited source, the chemical composition of these three regions is no more homogeneous (see table 4.III).

Element	Zone A. at %	Zone B. at %	Zone C. at %
Zn	13.85	27.78	30.87
Cd	28.51	9.50	4.92
Te	57.64	62.72	64.21
Total	100.00	100.00	100.00

Table 4.III. Overview of the chemical composition measured on the three regions A, B and C of the source after several deposition runs.

To analyze the influence of the source state on the thin film structure and chemical composition, two samples were grown under the same conditions but using the two different sources: (a) a virgin source and, (b) a source that has been previously used during several deposition runs, (specifically three). The differences between them can be appreciated just by visual inspection as shown in figure 4.19.

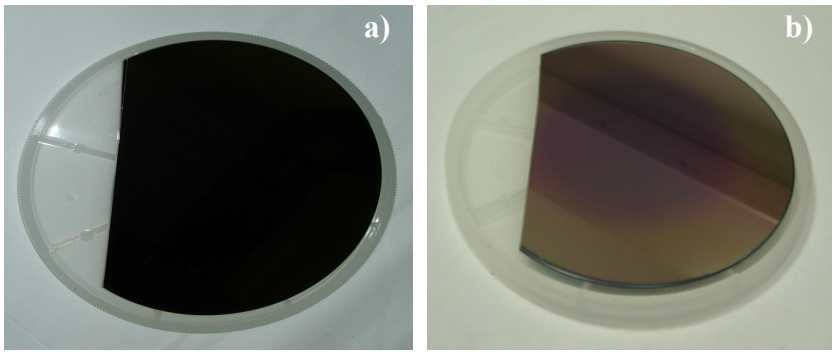

Figure 4.19. Photographs of $Cd_{1-x}Zn_xTe/SiO_2/Si$ films growth by VPE using (a) a virgin source and, (b) a source after several growths runs.

As expected, the samples grown by using the virgin source are completely uniform (in terms of chemical composition, microstructure, etc as shown hereafter) all over the area, whereas the other samples exhibit a well-defined red core region. Further, EDAX characterization, indeed, confirms that the dark brown core, which appears in figure 4.19b is due to an inhomogeneous enrichment of $Cd_{1-x}Zn_xTe$ layer with Zn.

The most critical factor determining the reproducibility of VPE process was found to be deterioration of source composition that results in an inhomogeneous enrichment of $Cd_{1-x}Zn_xTe$ layer with Zn. Therefore, as a summary of VPE experiments, figure 4.20 reports the evolution of Zn and Cd concentration on the surface of both $Cd_{1-x}Zn_xTe$ source and layer respectively, with the time of VPE growth.

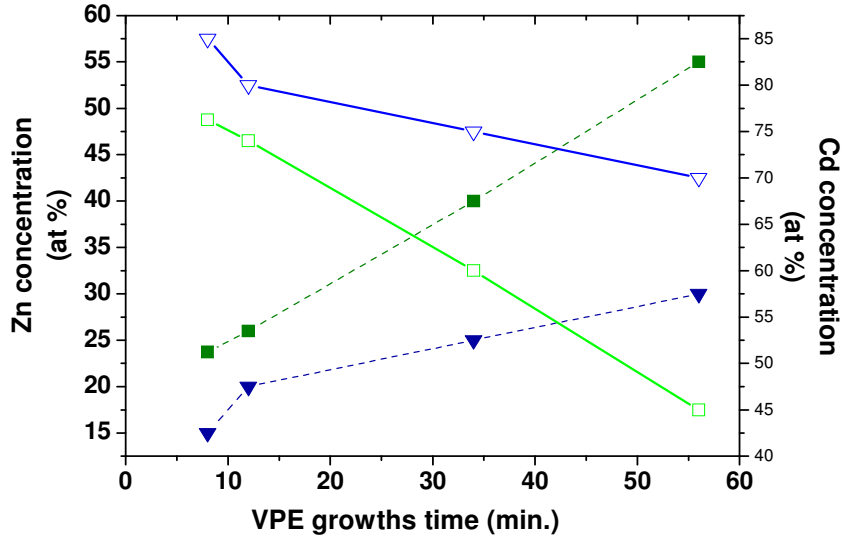

Figure 4.20. EDAX data on the evolution of the Zn and Cd concentration on the surface of $Cd_{1-x}Zn_xTe$ source (■-□) and $Cd_{1-x}Zn_xTe$ /Si layer (▼-▽) versus the time of VPE growth.

It is seen that an increase in deposition time, results in an increment of Zn content on $Cd_{1-x}Zn_xTe$ source surface. This fact is result of its decomposition in ZnTe and CdTe segregation. As a consequence, the Zn content in $Cd_{1-x}Zn_xTe$ layer increases, too. Therefore, taking into account all these results, figure 4.20 shows that within relatively short deposition time (less than 10–15 min), this effect is negligible. This allows us to grow in a well-control way with uniform and predictable composition in a thickness range of about 0.1-5 μm [68].

4.3 Conclusions

In this chapter we have demonstrated that the co- doping of CdTe sources with Ge as deep donor and, with Yb as rare-earth element is a promising way to obtain semi-insulating CdTe crystals with good transport properties. High resistivity ($5 \cdot 10^9$ Ω·cm) and lifetime (9 μs) were obtained confirming the beneficial effect of rare earth element. Moreover, we have shown that control of the Yb concentration is crucial for achieving electrical compensation. In addition, experimental findings testify that high resistivity sources of reasonably good structural quality can be grown with the Yb concentration below the value of $5x10^{18}$ at./cm^3.

CL measurements of Bi- doped samples with higher Bi content ($7x10^{17}$ at./cm^3) show the formation of a dense network of highly decorated grain boundaries. The co- doped samples show dopant striations which are probably due to the presence of Yb. Besides Bi doping contributes to the appearance of the A luminescence band. And, for CdTe:Bi:Yb, Yb causes a blue shift of the deep level band centred at about 1.10 eV.

We have also demonstrated that the prolonged VPE growth induces the continuous deterioration of source composition that gives rise to an inhomogeneous enrichment of $Cd_{1-x}Zn_xTe$ films with Zn. The fast VPE runs using the sources in the form of thin polycrystalline wafers provide the most uniform $Cd_{1-x}Zn_xTe$ films.

References

[1] "*Semiconductors for Room- Temperature Radiation Detector Applications*", Ed. Material Research Society, Pittsburgh (1993).

[2] "*Radiation detection and measurement*", G. Knoll, John Willey & Sons Inc., 3rd Ed., NY USA, 2000.

[3] M. Fiederle, C. Eiche, M. Salk, R. Schwarz, K.W. Benz, W. Stadler, D.M. Hofmann, B.K. Meyer, J. Appl. Phys. **84** ,(1998), 6689.

[4] O. Panchuk, A. Savitskiy, P. Fochuk, Ye. Nykonyuk, O. Parfenyuk, L. Shcherbak, M. Ilashchuk, L. Yatsunyk, P. Feychuk, J. Crystal Growth. **197,** (1999), 607.

[5] M. Zha, F. Bissoli, L. Zanotti, C. Paorici, J. Mater. Process. Technol. **143/144,** (2003), 425.

[6] M. Zha, T. Görög, A. Zappettini, F. Bissoli, L. Zanotti, C. Paorici, J. Crystal Growth. **234,** (2002), 184.

[7] A. Zappettini, T. Görög, M. Zha, L. Zanotti, G. Zuccalli, C. Paorici, J. Crystal Growth. **214/215** (2000), 14.

[8] "*Narrow gap cadmium-based compounds*", P. Capper, Emis datareviews series nº 10, Inspec Pub., 1st Ed., England 1994, Cap. B5.8 and B8.3.

[9] M. Fiederle, V. Babentsov, J. Franc, A. Fauler, K. W. Benz, R. B. James, and E. Cross, J. Cryst. Growth **243**, (2002), 77.

[10] G. Panin, J. Piqueras, N. V. Sochinskii, and E. Dieguez, Appl. Phys. Lett. **70**, (1997), 877.

[11] U. Pal, P. Fernández, J. Piqueras, N. V. Sochinskii, and E. Diéguez, J. Appl. Phys. **78**, (1995), 1992.

[12] N. V. Sochinskii, M. Lozano, G. Pellegrini, and M. Ullan, Nucl. Instrum. Methods Phys. Res. A **568**, (2006), 451.

[13] M. Fiederle, V. Babentsov, J. Franc, A. Fauler, and J. P. Konrath, Cryst. Res. Technol. **7/8**, (2003), 588.

[14] M. Fiederle, A. Fauler, J. Konrath, V. Babentsov, J. Franc, and R. B. James, IEEE Trans. Nucl. Sci. **51**, (2004), 1864.

[15] "*Crecimiento y caracterización de monocristales en volumen de CdTe dopados con Bi*", Edgardo Saucedo Silva. Tesis doctoral presentada en 2007 en la Universidad Autónoma de Madrid./ PhD Thesis, Unversidad Autónoma de Madrid (2007).

[16] E. Saucedo, O. Martínez, C.M Ruiz, O. Vigil-Galán, I. Benito, L. Fornaro, N.V. Sochinskii, E. Diéguez, J. Crystal Growth. **291,** (2006), 416.

[17] C.M. Ruiz, O. Vigil, E. Saucedo, G, Contreras- Puente and V. Bermudez, J. Phys.: Condens, Matter **18,** (2006), 7163- 7169.

[18] E. Saucedo, C. M. Ruiz, V. Bermúdez, E. Diéguez, E. Gombia, A. Zappettini, A. Baraldi, and N. V. Sochinskii, J. Appl. Phys**. 100**, (2006) 104901.

[19] A. Kadys, K. Jarasuinas, E. Saucedo, E. Diequez, J. C. Launay and D. Verstraeten, J Mater Sci: Mater Electron. **19**, (2008), S234-S238.

[20] E. Saucedo, J. Franc, H. Elhadidy, P. Horodysky, CM Ruiz, V. Bermudez and NV Sochinskii, Journal of Applied Physics **103**, (2008), 094901.

[21] P. Polynkin, V. Temayanko, J. Moloney, and N. Peyghambarian, Appl. Phys. Lett. **90**, (2007), 241106.

[22] J. F. Bisson, D. Koutznetsov, K. Ueda, S. T. Fredrich-Thornton, K. Peterman, and G. Huber, Appl. Phys. Lett. **90**, (2007), 201901.

[23] G. Chen, G. Somesfalean, Y. Liu, Z. Zhang, Q. Sun, and F. Wang, Phys. Rev. B **75**, (2007), 195204.

[24] Z. C. Xu, M. Yan, M. Li, Z. L. Zhang, and M. Huang, J. Appl. Phys. **101**, (2007), 053910.

[25] R. J. Xle, N. Hirosaki, N. Kimura, K. Sakuma, and M. Mitomo, Appl. Phys. Lett. **90**, (2007), 191101.

[26], H. Matsumoto, Y. Kawasaki, N. Ito, M. Enoki, and T. Ishihara, Electrochem. Solid-State Lett. **10**, (2007), B77.

[27] L. Zakharenkov. Microelectron. J. **26**, (1995), 55.

[28] A. Savchuk, S. Paranchych, V. Frasunyak, V. Fediv, Yu. Tanasyuk, Ye. Kandyba, and P. Nikitin, Mater. Sci. Eng., B **105**, (2003), 161.

[29] D. Wruck, R. Boyn, L. Parthier, and F. Henneberger, Semicond. Sci. Technol. **12**, (1997), 179.

[30] R. Watts and W. Holton, Phys. Rev. **173**, (1968), 417.

[31] N. Loiko, V. Konnov, Yu. Sadofyev, E. Makhov, A. Trushin, and A. Gippius, Phys. Status Solidi B **229**, (2002), 317.

[32] G. Panin, J. Piqueras, N.V. Sochinskii, and E. Diéguez, Appl. Phys. Lett. **70**, (1997), 877.

[33] Saucedo E, Fornaro L, Sochinskii NV, Cuña A, Corregidos V, Granados D, Diéguez E. IEEE Trans Nucl Sci **51**(6), (2004), 3105.

[34] S. Neretina, N.V. Sochinskii, P. Mascher, E. Saucedo, Mater. Res. Soc. Symp. Proc. **864,** (2005), E4.18.1.

[35] M. Schieber, et al., J. Crystal Growth **231**, (2001), 235.

[36] E. Saucedo, C.M. Herrero, L. Fornaro, N.V. Sochinskii, E. Diéguez, J. Crystal Growth **275,** (2005), 471.

[37] J. Franc, P. Horodyský R. Grill, J. Kubát, E. Saucedo, N.V. Sochinskii, J. Crystal Growth **286**, (2006), 384.

[38] P. Rudolph, Prog. Cryst. Growth and Charact. **29**, (1994,) 275-381.

[39] D. Wagner, P. Irsigler, and D. J. Dunstan, J. Phys. C **17**, (1984), 6793.

[40] N. V. Sochinskii, M. Abellán, J. Rodríguez-Fernández, E. Saucedo, C. M. Ruiz and V. Bermúdez, J. Appl. Phys. **91**, (2007), 202112.

[41] G. M. Martin, J. P. Farges, G. Jacob, J. P. Hallais, and G. Poiblaud, J. Appl. Phys. **51**, (1980), 2840.

[42] E. J. Johnson, J. A. Kafalas, and R. W. Davies, J. Appl. Phys. **54**, (1983), 204.

[43] M. Fiederle, C. Eiche, M. Salk, R. Schwarz, K. W. Benz, W. Stadler, D. M. Hofmann, and B. K. Meyer, J. Appl. Phys. **84**, (1998), 6689.

[44] G Panin, P Fernandez and J Piqueras**,** Semicond. Sci. Technol. **11,** (1996), 1354–1357.

[45] Raczynsnska, K. Fronc, J. M. Langer, A. Lemanska, and A. Stapor, Appl. Phys. Lett. **53**, (1988), 761.

[46] N. V. Sochinskii, E. Saucedo, , M. Abellán, J. Rodríguez-Fernández , P.Hidalgo, J. Piqueras, C. M. Ruiz and V. Bermúdez, E. Diéquez. J. Crystal Growth. **310**, (2008), 2076-2079.

[47] R. Kaplan, Solar Energy Materials & Solar Cells **85**, (2005), 545–557.

[48] R. Kaplan, Appl. Phys. A **64**, (1997), 171-175.

[49] A. Castaldini, A. Cavallini, B. Fraboni, P. Fernandez, and J. Piqueras, J. Appl. Phys. **83**, (1998), 2121.

[50] "*Cadmium telluride and related compounds."Chapter VI in the book "Physics and chemistry of II-VI luminescence semiconductors*", N. V. Sochinskii, V. N. Babentsov, and E. Diéguez. Ed. D. R. Vij and N. Singh (NOVA Sci. Publishers, Inc., New York, USA, 1996) pp.248-276.

[51] J. Aguilar-Hernández, M. Cárdenas-García, G. Contreras-Puente, J. Vidal-Larramendi, Mater. Sci. Eng. B **102**, (2003), 203.

[52] S.H. Song, J. Wang, Y. Ishikawa, S. Seto, M. Isshiki, J. Crystal Growth. **237–239**, (2002), 1726.

[53] U. Pal, P. Fernández, J. Piqueras, N.V. Sochinskii, E. Diéguez, J. Appl. Phys. **78,** (1995), 1992.

[54] G. Panin, J. Piqueras, N.V. Sochinskii, E. Diéguez, Appl. Phys. Lett. **70**, (1997), 877.

[55] Z. Sobiesierski, I.M. Dharmadasa, R.H. Williams, Appl. Phys. Lett. **53,** (1988), 2623.

[56] C.B. Davis, D.D. Allred, A. Reyes-Mena, J. González-Hernández, O. González, B.C. Hess, W.P. Allred, Phys. Rev. B **47,** (1993), 13363.

[57] P. Hidalgo, J. Piqueras, N. V. Sochinskii, M. Abellán, E. Saucedo, E. Diéquez.J. Mater. Sci 43, (2008), 5605-5608.

[58] Shaw DA, Thornton RP. J Mat Sci 3, (1968), 507.

[59] Ono H, Kamejima T, Watanabe H, Matsui J. Jpn J Appl Phys **25,** (1986), L130.

[60] Sobiesierski Z, Dharmadasa IM, Williams RH. Appl Phys Lett **53**, (1988), 2623.

[61] Davis CB, Allred DD, Reyes-Mena A, González-Hernández J, González O, Hess BC, Allred WP. Phys Rev B **47**, (1993), 13369.

[62] Stadler W, Hofmann DM, Alt HC, Muschik T, Meyer BK, Weigel E, Müller-Vogt G, Salk M, Rupp E, Benz WK. Phys Rev B **51,** (1995), 10619.

[63] Castaldini A, Cavallini A, Fraboni B, Polenta L, Fernández P,Piqueras J. Phys Rev B **54**, (1996), 7622.

[64] Liu Juncheng, Song Dejie, Zhang Hongying, and Zhai Senqiu, Cryst. Res. Technol, **42**, No8, (2007), 741-750.

[65] J.K. Radhakrishnan, B. S. Sunderseshu, Meenakshi Srivastava, G. L. Seth, R. Raman, R C Narula and R. K. Bagai, Bull. Mater. Sci., Vol **24**, No 6, (2001), 659-663.

[66] A. Hossain, A.E Bolotnikov, G.S. Camarda, Y. Cui, G. Yang, R.B James, Journal of Crystal Growth. **310**, (2008), 4493-4498.

[67] M. Fiederle, A. Fauler, and A. Zwerger, IEEE Transactions on Nuclear Science, Vol **54**, No 4, (2007), 769-772.

[68] N. V. Sochinskii, M. Abellán, J. Rodríguez- Fernández, J.L.Plaza, V.Carcelén, E. Diéguez, Journal of Crystal Growth **310** ,(2008), 1669-1673.

Chapter 5

Physical properties of CdTe- based thin films

Chapter 5

PHYSICAL PROPERTIES OF CdTe– BASED THIN FILMS

This chapter is devoted to the optimization of the growth method of CdTe- compound and CdZnTe thin films.

Although, there has been considerable progress in growth of epitaxial films by different techniques from vapor phases [1-5], its commercial use is still limited due to the problems arising from the complexity of the growth processes. In this thesis, we have developed a simple and efficient industrial-like process which allows the fast growth of large-area CdTe layers with uniform composition and thickness. The method could be of importance for further implementation in industrial facilities.

Moreover, the same way than in the previous chapter, the role of some dopants such as: Ge, Bi, Yb and Zn in the improvement of material properties is studied.

5. 1 Introduction

Considering that CdTe presents unique properties that make it appropriate for device applications, (as we just mentioned in chapter 4). Only few works in literature are devoted to the study of Bi- doped despite of its influence in the optoelectronics properties of CdTe- based solar cells and for X- ray detection applications. We have contributed to this research by showing that Bi is a suitable doping to obtain semi-insulating CdTe with high photosensitivity and excellent transport charge properties [6]. In this chapter, the quality of some CdTe:Bi films will be analyzed as a essential step for further development of CdTe:Bi- based devices [7].

As it has been previously shown (section 4.2.2) Bi- doping contributes to reduce the resistivity up to 5 orders of magnitude, and to increase photoconductivity [8]. Because of these reasons CdTe:Bi polycrystalline thin films have been suggested as a new alternative to be used as absorber layers in solar cells. CdTe has a band gap of 1.5 eV that matches well to the solar spectrum and, its absorption coefficient is very high for frequencies in the visible part of the electromagnetic spectrum. Thus, it only takes a few μm of material to absorb 90% of the incident light. As a result of these properties CdTe- based solar cells have received significant attention

and are considered a viable alternative to Si- based technologies. In fact, CdTe solar cells yield higher wattage per square foot, at a lower price per watt of capacity.

Besides, taking into account the studies carried out in the previous chapter, where, we have demonstrated that transport charge properties of CdTe:Ge doped could be improved by co- doping with rare earth, e.g Yb. We have studied CdTe:Ge:Yb layer, and experimental finding testify that homogeneous layer of reasonably good quality can be obtained.

Also special attention has been paid to Cd(Zn)Te- based heterostructures because of their potential use for X- and γ- ray radiation detectors operating at room temperature (see [9] and [10,11], respectively). The latest advances in this area suggest that Cd(Zn)Te- based epitaxial heterostructures (and particularly, nanostructures) could be of great concern for the development of high resolution multi-pixel imaging detectors [12,13]. These detectors could be considered as a natural evolution of the classic arrays made from Cd(Zn)Te bulk crystals.

Moreover, $Cd_{1-x}Zn_xTe$ layers grown on small size substrates have been proven to present interesting features required for nonlinear applications at optical wavelengths such as high nonlinear Kerr effect (similar to that in GaAs) and small losses due to the two-photon absorption effect. For this reason, $Cd_{1-x}Zn_xTe$ can be considered to be a good candidate for waveguide development on any kind of photonic devices which, as far as we know, have not been developed yet. Therefore, one of the objectives of the chapter is to demonstrate the capabilities of these films as waveguides at industry level. This requires the development of a simple and efficient industrial-like growth method to allow the fast growth of $Cd_{1-x}Zn_xTe$ large-area layers with an uniform composition and with a thickness comparable to wavelengths in the infrared range of the electromagnetic spectrum.(λ= 1550 nm).

5.2 Growth and characterization of CdTe:Bi films

In this section a detailed characterization of CdTe:Bi films is carried out, focussing on the study of its potential capabilities.

Previous studies have faced the enhancement of the efficiency of CdTe- based solar cells by improving the different parts of the device. However, as far as we know little or no effort has been devoted to improve the physical properties of the films. Therefore, in this chapter, taking into account that one of the main problems is related with the CdTe deposition is due to its polycrystalline nature. The grain boundaries associated with its morphology give rise to trapping centres that result in carrier recombination, diminishing the charge transport in the

cell. Therefore, we focus our studies on improving the quality of the films and the fabrication of a novel and reliable back contact based on Bi_2Te_3, which also allows diminishing the working function of the CdTe:Bi.

5.2.1 Growth procedure

Using the CdTe:Bi polycrystals studied in section 4.2.2 as evaporation sources, CdTe:Bi thin film with a thickness between 0.1-3 μm were simultaneously deposited on different substrates (Si, SiO_2, CdS/ITO, etc) by VPE technique [14]. CdS/ITO substrate was chosen for solar cells fabrication, whereas Si (1 0 0) was selected for RBS and XRD characterization.

The substrate temperature range and growth rate were selected to be between 500–750 ^oC and 1–10 nm/s, respectively. More details about the growth method can be found in section 3.1.2.

5.2.2 Physical properties

One of the major concerns was the study of physical and chemical properties of the thin films. So, the characterization was done using SEM, XRD and RBS techniques.

5.2.2.1 Morphological characterization

The morphological characterization of the films was done by SEM. SEM images for a CdTe:Bi film are shown in figure 5.1. Note that, the film grows conformal to substrate. The SiO_x substrates employed for this study present a patterning realized by means several technological processes needed for further experiments. However, we focus our attention in the morphology of the layer to study.

This film exhibits an uniform grain morphology with an average grain size under 100 nm. The surface consists in many islands compactly packed; (namely each crystal is in contact with adjacent). This is a typical feature of the VPE growth and polycrystalline layers (figure 5.1a).

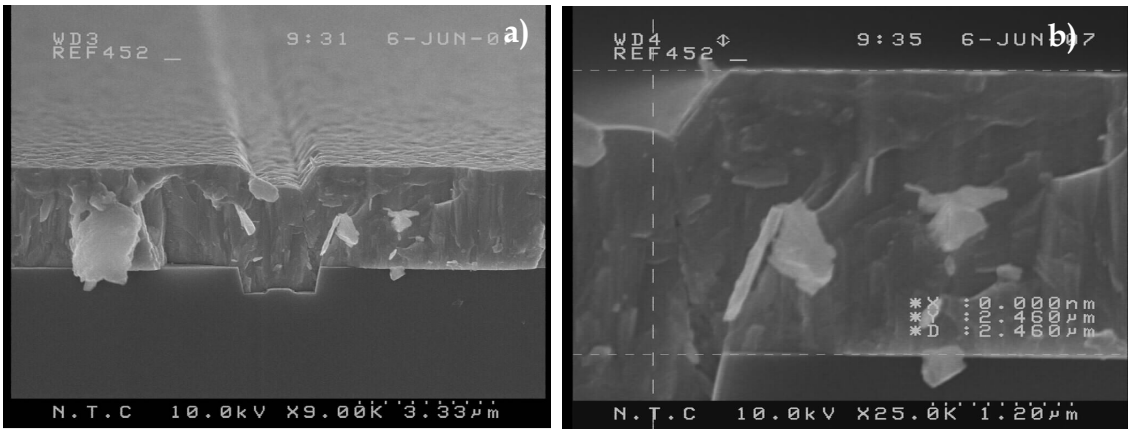

Figure 5.1. (a) Surface morphology and (b) cross-sectional SEM images for a CTe:Bi/Si film with a thickness of 2.46 µm.

In figure 5.1b, the cross-sectional image shows a film with a thickness of ~2.46 µm with good adhesion to the substrate. It can be observed that the film exhibits a compact columnar structure perpendicular to the substrate.

In order to study the thickness dependence of the surface appearance, SEM images were taken on films with different thickness. As shown in figure 5.2, no significant differences between the surface of CdTe:Bi films with 0.20 µm and 2.46 µm thickness, is appreciated. Moreover, in both cases the layers cover the substrate in a very uniform and compact way.

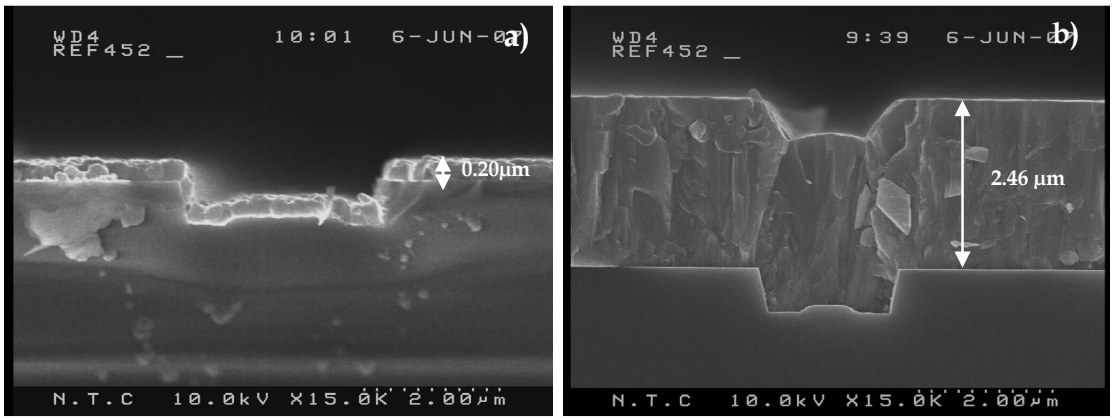

Figure 5.2. Cross-sectional SEM images of a CdTe:Bi/Si films with a thickness **of** (a) ~ 200 nm and (b) 2.46 µm.

5.2.2.2 Structural characterization

The crystal structure was studied by XRD in Bragg-Bretano geometry. Four Bragg peaks can be observed in the XRD pattern at 6.78º, 11.06º, 13.11º and 16.94º which are related to (111), (220), (311) and (331) CdTe reflections, respectively (see figure 5.3). Thus, the result evidences

that, the sample is polycrystalline and preferentially oriented along the (111) direction. By comparing the 2θ position of the (111) peak with that reported in literature [15], one can observe that for the as- grown sample the peak is a bit displaced to the left indicating that the films presents a tensile stress, typical of this kind of growth.

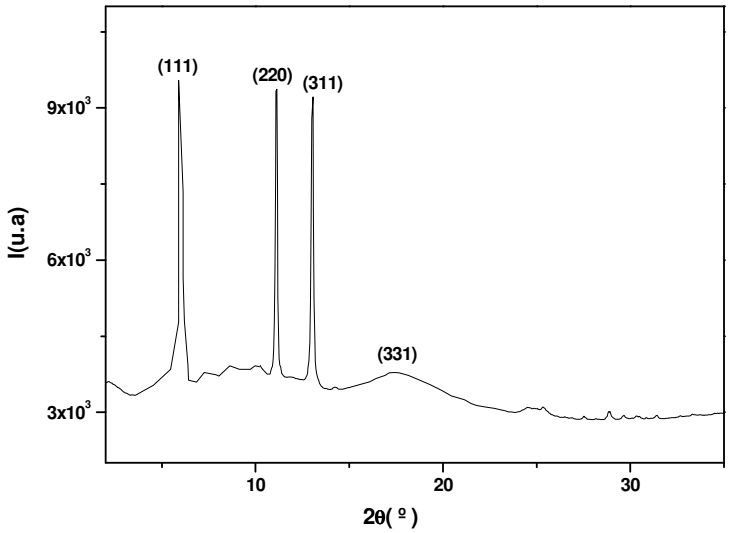

Figure 5.3. XRD pattern for a CdTe:Bi film.

To assess the crystalline quality, the full-width at half–maximum, FHWM, for the preferential orientation was calculated. For this sample, the FHWM obtained was 0.35º. This value is on the high side of the typical FHWM range for CdTe. Thus, this would be in agreement with the presence of some impurities which can deform slightly the lattice.

5.2.2.3 Compositional characterization

The elemental composition of the CdTe samples doped with Bi was characterised by means of Rutherford Backscattering Spectroscopy (RBS) under the conditions previously described in section (3.3.2.4). As shown in figure 5.4, the elemental composition was estimated by comparing experimental and simulated RBS data. For the simulation the SIMNRA computer code [M. Mayer, SIMNRA, Version 5.02, Max Plank Institut für Plasmaphysik] was used. These data evidence that the layer is composed by a 57 at.% of Cd, a 42 at.% of Cd and around 1 at.% of Bi. No impurity traces are detected in the CdTeBi layer within the resolution limit of the measurement.

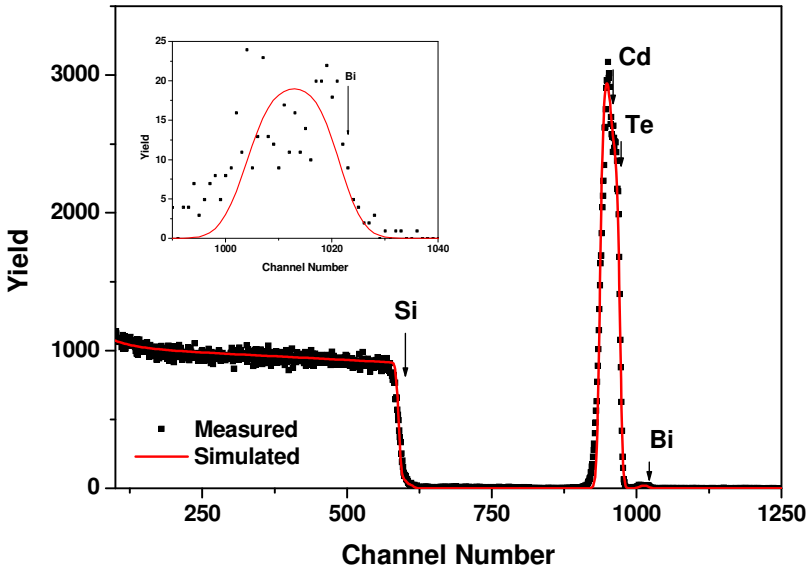

Figure 5.4. RBS spectrum for a CdTe:Bi thin film. Inset of Bi peak belonging at RBS spectrum of CdTe:Bi thin film.

It is important to highlight that, it the first time that the Bi presence is detected with this compositional technique. For this type of material, we have not found any reference in the literature.

5.2.2.4 Electrical characterization

The electrical properties of the films were characterised by Surface Photovoltage Spectroscopy (SPS) and by measuring the I-V characteristic curves.

CdTe:Bi deposited on Cadmium sulfide (CdS) and Indium tin oxide (ITO), (CdTe:Bi/CdS/ITO), samples were fabricated by VPE techniques for electrical characterization.

CdTe/CdS hetejunction is typically used as p-n junction. Therefore in order to study the junction properties, the SPS method was used [16-18]. It is well known that any change in the surface potential, causes a changes of equal magnitude in the surface work function, **W**. Thus, in absence of photochemical activity, the change in surface work function is equivalent to the Surface Photovoltage (SPV) measurement (in absolute value terms).

A typical SPV spectrum for a CdTe:Bi/CdS/ITO film is shown in figure 5.5.

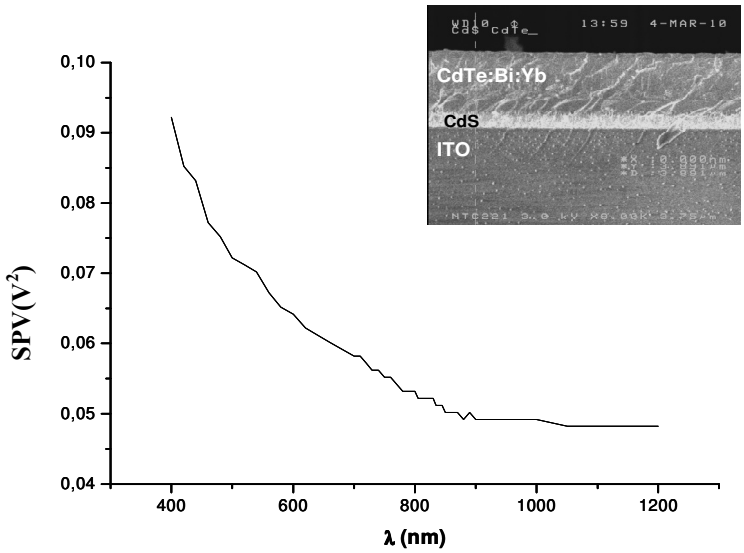

Figure 5.5. Typical SPS spectrum for a CdTe:Bi/CdS/ITO thin film.

It is seen that the incident light-induced surface charging is caused by the surface photovoltage. This fact is due to the generation of electron-hole pairs and to the charge separation in the CdTe:Bi layer. Indeed, at photon energies below the band gap, $\mathbf{E_g}$, the SPV is constant. This constant level corresponds to the work function **W**, at the given experimental conditions (air atmosphere).

The E_g value is calculated from SPS data by extrapolating $(SPV)^2$ to 0 as indicated in figure 5.6 [17].

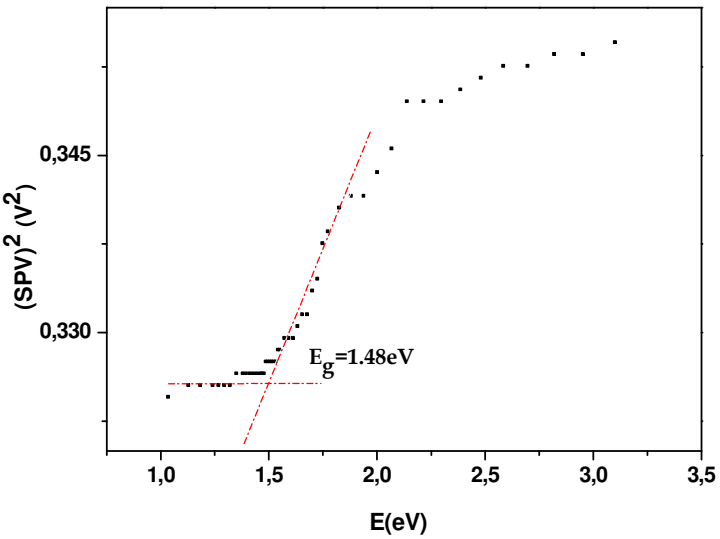

Figure 5.6. Estimation of optical band gap for a CdTe:Bi/CdS/ITO thin film.

Based on this method the E_g value is calculated to be 1.48 eV, which is in excellent agreement with the commonly accepted value of 1.45 eV for CdTe [14].

According to SPS data, CdTe:Bi film exhibits a p-type semiconductor behavior. This information may be achieved with the help of the sign of the knee associated with the SPV curve. The SPS signal is bent upward towards the surface which indicates that we are dealing with a p-type behavior, as expected. This information is very important because of the doping of CdTe is known to be non-trivial and subject to compensation mainly by anphoteric behavior of Bi-doping.

In order to obtain information about the the saturation current and the ideality factor, **dark I-V characteristics** were investigated. Our main contribution to this study is the innovation introduced in the back contact fabrication by means of a n-p-n heterojuntion formed by a Bi_2Te_3/CdTe:Bi/CdS hererostructure in Au/Bi_2Te_3/CdTe:Bi/CdS/ITO final solar cell, which presents a gradual variation of the band gap from 480 nm to 855 nm.

According to theory [19,20], the relation between the **current and the voltage** in a p-n junction is given by the equation (5.1):

$$J = J_{Osc}\left(e^{\frac{qV}{nkT}} - 1\right) \qquad (5.1)$$

where, **q** is the electron charge, **k** is Boltzman´s constant, **T** is the temperature in Kelvin degrees, $\mathbf{J_{Osc}}$ is the dark current and, **n** is the diode ideality factor with values between 1 and 3 for heterojuntions.

This equation is also valid if recombination in the contact space charge layer is negligible. This hypothesis will be assumed in this study [21]. A perfect match to theory is observed when n = 1 which indicates that the transport charge mechanism in the cell is diffusion.

The I-V characteristic curve measured under dark conditions is shown in figure 5.7. As shown, the I(V) curve can be well fitted by an exponential function which evidences that the junction voltage saturates at high bias and the electrons recombine at the back contact (in other words due to the presence of Schottky barrier under forward bias). This saturation occurs because of the back contact barrier and has nothing to do with the electron current. Therefore, we assume that the total current is equal to the hole current.

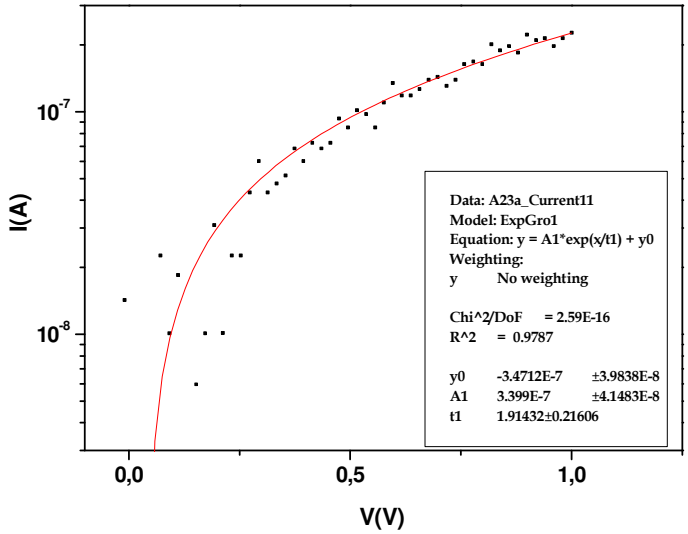

Figure 5.7. Dark I-V curve for back contact $Au/Bi_2Te_3/CdTe:Bi$ heterojuntion for a $Au/Bi_2Te_3/CdTe:Bi/CdS/ITO$ solar cell.

The obtained values for dark current and diode ideality factor were, $\mathbf{J_{osc}= 3.47\cdot10^{-7}A/cm^2}$ and **n= 1.91,** respectively. On the other hand, values of n close to 2 shows that the transport mechanisms are dominated by emission-recombination current [22-25]. The obtained value is similar than those previously reported for this kind of device which points out that a large variety of the recombination process are taking place at the spatial charge region.

From these parameters and assuming that the cell is operated at open circuit, I = 0, the voltage across the output terminals is defined as the open-circuit voltage, $\mathbf{V_{oc}}$ by equation (5.2):

$$V_{OC} = \frac{nkT}{q}\ln\left(\frac{J_L}{J_{Osc}}+1\right) \qquad (5.2)$$

where $\mathbf{V_{oc}}$ is the maximum voltage available for a solar cell, $\mathbf{J_{osc}}$ is the dark current, and $\mathbf{J_L}$ is the density of the light current generated by the light. The $\mathbf{V_{oc}}$ corresponds to the amount of forward bias on the solar cell due to the bias of the solar cell junction with the light-generated current.

Comparing the V_{oc} that we have measured to that reported for CdTe/ITO monocrystrals (890 mV) and to CdTe homounions deposited by close spaced sublimation, CSS, (820 mV), we observe that they are very much similar which indicates that our samples have a high quality. The efficiencies for these configurations are 13.4% and 9.7% respectively.

5.3 Growth and characterization of CdTe:Ge:Yb films

In this section, homogeneous films of reasonably good structural quality have been grown by VPE with Yb concentration below 5 x10^{18} at./cm^3.

5.3.1 Growth procedure

CdTe:Ge:Yb polycrystals were used (see section 4.2.1) as VPE sources, in order to grow CdTe:Ge:Yb films. The growth of CdTe:Ge:Yb (0.2–2) μm thick films was carried out on different (Si, SiO_2, Al_2O_2, $LiNO_3$, CdS/ITO, etc) substrates at temperatures in the range of 500–750 ^oC. The growth rates were selected to be in the range of 1–10 nm/s.

5.3.2 Physical properties

XRD, CL and XRF techniques were used to investigate the physical properties of these CdTe:Ge:Yb thin films.

5.3.2.1 Structural and compositional characterization

The structural characterisation of this film was carried out by XRD. XRD pattern measured for a CdTe:Ge:Yb film is shown in figure 5.8.

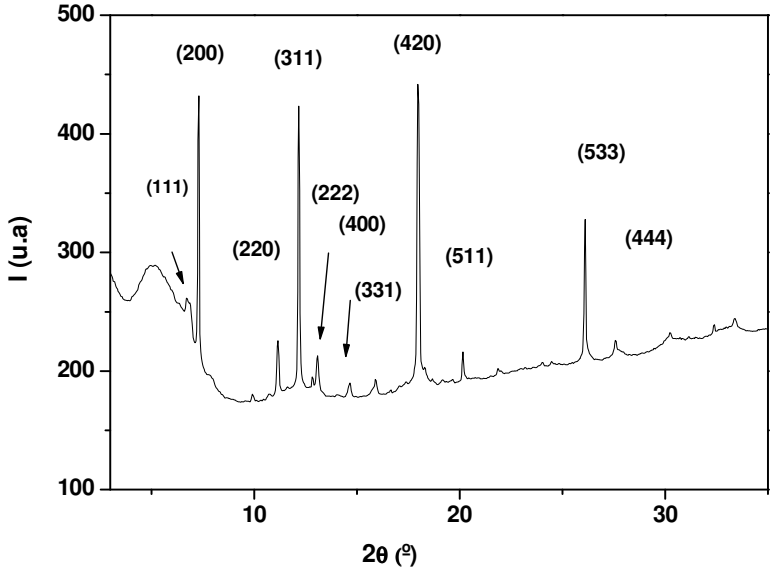

Figure 5.8. Typical XRD pattern for a CdTe:Ge:Yb/Al_2O_3 film.

The Bragg peaks located at 6.78º, 7.33º, 11.10º, 12.22º, 13.06º, 14.74º, 17.13º, 17.95º, 20.19º, 25.92º and 27.60º correspond to (111), (200), (220), (311), (222), (400), (331), (420), (511), (533), and (444) CdTe crystallographic directions, evidencing that the sample is polycrystalline and preferentially orientated along (420) direction. This result contrasts somehow with the typical (111) peak associated with preferential orientation obtained for other CdTe- based thin films. The difference in preferential orientation may be linked to the presence of Yb in this layer.

Comparing the value of the peak position of the preferential orientation (420) with the reported in JCPDS which has a theoretical value of 17.58º, it is observed that the peak is displaced to the right indicating that the film is to a compressive stress.

To check the crystalline quality of the layer, the FWHM was calculated for preferential orientation. The obtained value was 0.07º. This value is rather low for CdTe thin films, indicating a reasonably good quality of the film.

While information about the major elements can be obtained with EDX, the quantification of the trace and minor elements by means EDX analysis is difficult due to the detection limits of the technique. To overcome this problem, X- ray fluorescence (XRF) measurements were performed at the European Synchrotron Radiation Facility, ESRF, at the microprobe station ID18F.

XRF data were treated and analyzed by using the PyMCA code. This code allows us to identify the elemental composition and distribution of the major elements as well as, the presence of trace elements with good accuracy. The set up specification was detailed described in section 3.3.2.3.

The fundamental parameter method was used to determine the relative concentration. This method usually requires knowledge of all elements in standard samples [26]. Its application consists of two steps: calibration which is the prediction of the intensity of characteristic lines for a composition that is identical to the standard used, accounting for instrumental related factors, and then analysis. Using the calibration data, a first estimation of the composition of an unknown sample is possible, and later the theoretical intensities calculated and differenced with the measured one—by repeating those steps until the convergence is reached. The XRF spectra acquired for CdTe:Ge:Yb/ Si are shown in figure 5.9.

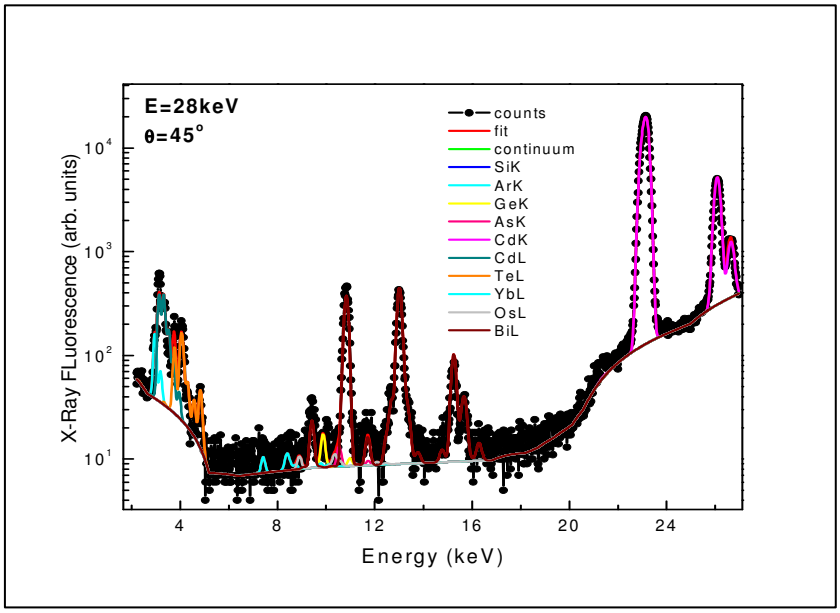

Figure 5.9. XRF spectra for CdTe:Ge:Yb/Si film recorder an excitation energy at 28 keV.

The elemental concentration calculated from these data is shown in Table 5.I.

Element	Group	Mass fraction
Ge	K	0.002543
As	K	0.9715
Cd	K	0.5
Cd	L	64.37
Te	L	29.48
Yb	L	0.003396
Os	L	0.004805
Bi	L	0.1024

Table 5.I. Overview of elemental composition for a CdTe:Ge:Yb/Si film.

These data agree quite well with that previously reported for this material. Note that the presence of Osmium (Os) could be due to the Os incorporation taking place during the deposition process (the boat where the sample was placed was made of Os) whereas, the presence of the Bi can be also attributed to the presence of impurities inherent to the source.

5.3.2.2 Optical characterization

The optical characterization of the films was carried out by CL. CL images are quite homogeneous and do not show any kind of contrast. For this reason they are not shown here. These results contrast somehow with those presented in section 4.2.1.2.3 for sources where a high contrast was observed.

A typical CL spectrum for a CdTe:Ge:Yb film is shown in figure 5.10. By comparing it with that shown in CdTe:Ge:Yb sources (see figure 4.8). It can be observed that the influence of Yb is also apparent in the 1.10 eV band that is narrower and more intense than in the sources and it is slightly shifted to higher energies. The Gaussian deconvolution of this band shows several components that have not been identified yet.

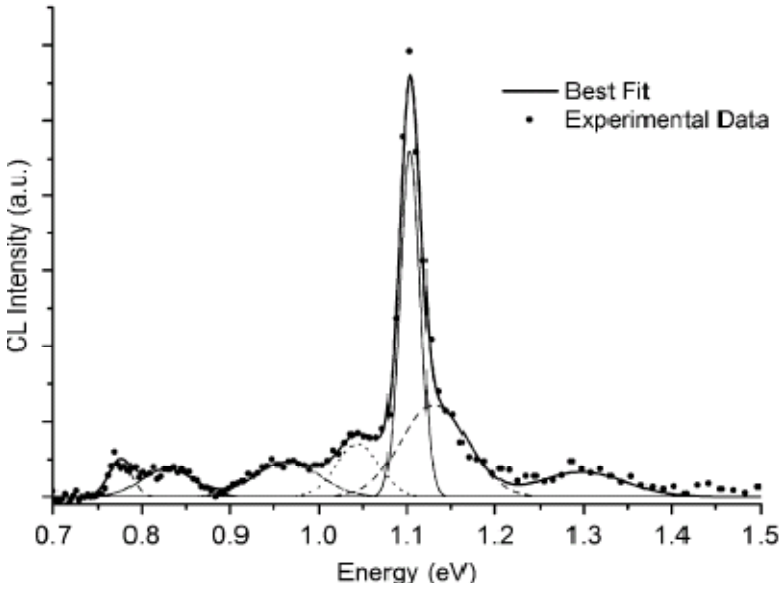

Figure 5.10. CL spectrum for a CdTe:Ge:Yb layer with the Gaussian deconvolution of the band centred at 1.10 eV.

Nevertheless, considering the high intensity of the peak centred at 1.10 eV and the thickness of the film between 1-2 μm, one may think that this peak is somehow connected to emission between Yb ions.

On the other hand, other remarkable difference in comparison with sources is that for films the highest energy band at 1.39 eV associated to radioactive recombination centres [27], does not appear.

5.4 Growth and characterization of $Cd_{1-x}Zn_xTe$ films

This section of the thesis is devoted to the study of the chemical and physical properties of CdTe- based films, which have been grown by using the $Cd_{1-x}Zn_xTe$ source characterised in section 4.2.3.2.

The main goal of the work is to develop a simple and efficient industrial-like growth method that allows fast growth of large-area CdTe films with uniform composition and thickness. The big milestone is to achieve films with homogeneous chemical composition.

5.4.1 Growth procedure

$Cd_{1-x}Zn_xTe$ films were grown on two different substrates, Si and Silicon oxide (SiO_x) 6-inches substrates. These substrates were mainly selected because of their low cost and the facility to obtain them in large areas. The substrate temperature range and the growth rate were selected to be between 600-850 ºC and 1–10 nm/s, respectively.

5.4.2 Physical properties

The morphological, structural and compositional properties of the$Cd_{1-x}Zn_xTe$ films have been investigated using by SEM, XRD and EDAX techniques.

5.4.2.1 Morphological characterization

The main feature observed in $Cd_{1-x}Zn_xTe$ films by a firstly visual inspection is that, they have a specular surface. Nevertheless, the most interesting features of the surface morphology have been investigated by employing SEM.

Typical SEM images of a $Cd_{1-x}Zn_xTe$ polycrystal film grown on SiO_2/Si are shown in figure 5.11.

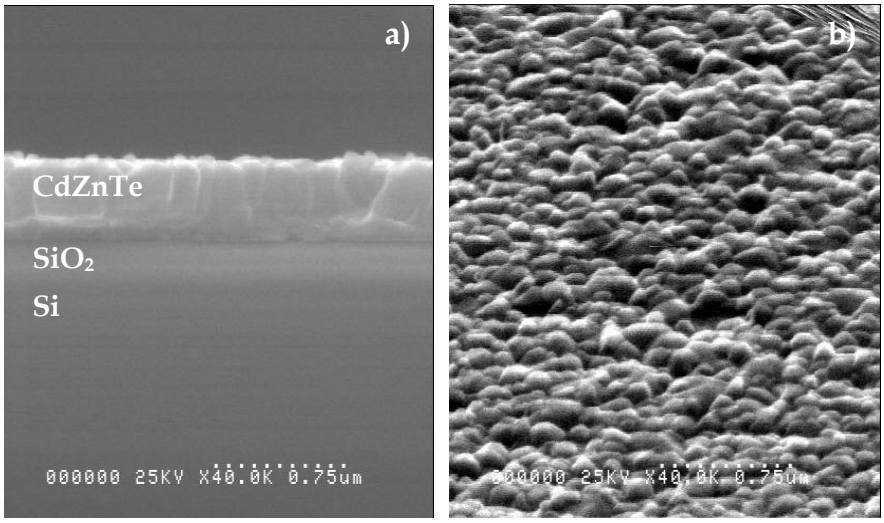

Figure 5.11. SEM (a) cross-section and, (b) morphological image of a CdZnTe/SiO_2/Si film.

The cross-section of the $CdZnTe/SiO_2/Si$ structure shows a well defined and very flat heterojuntion interface (figure 5.11a). This image reveals a good adhesion to the substrate with no evidence of crack through the polycrystal. It is observed that this film with a thickness of about ~500 nm presents a compact columnar structure perpendicular to the substrate very typical for films grown by VPE. The width of the columns is approximately of some dozens of nm.

More interesting information about the surface of the films can be derived from figure 5.11b. The image exhibits an uniform grain morphology. The surface consists of many quite compact islands (that seems to nucleate) randomly oriented, which uniformly cover large substrate areas. Besides, different grain size can be appreciated being the average grain size ~200 nm.

5.4.2.2 Structural characterization

In order to study the structural properties of these samples, XRD measurement were performed in Bragg- Bretano geometry.

Three Bragg peaks located at 23.68º, 39.11º and 46.11º are observed (with more intensity than the rest) on the XRD pattern for this sample (see figure 5.12).

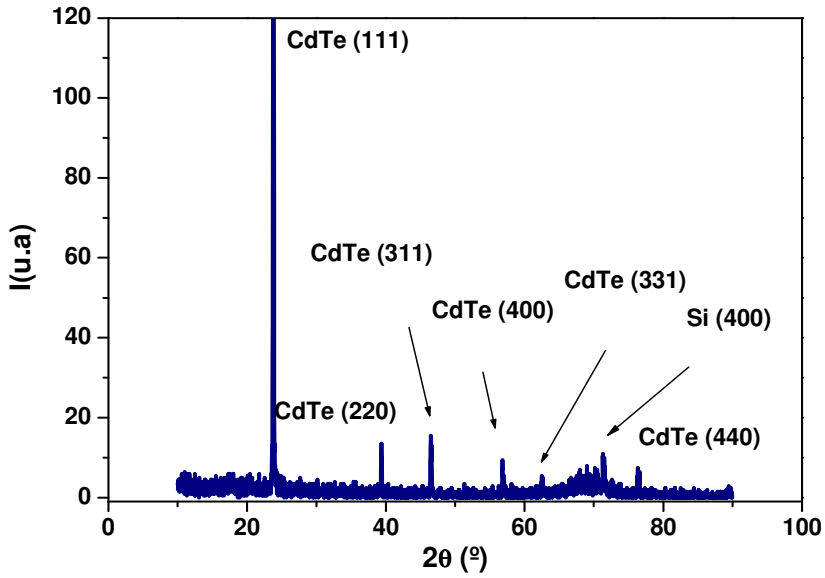

Figure 5.12. XRD spectra for a $Cd_{1-x}Zn_xTe/SiO_2/Si$ film.

These peaks corresponds to (111) (220) and (311) CdTe crystallographic directions. Thus, this result evidences that, the sample is polycrystalline and preferentially oriented along the (111) direction.

By comparing XRD spectrum for both films and that sources studied in section 4.2.3, one realizes that the two spectra are quite similar (see figure 5.13a). In the inset of figure 5.13b, it is shown a zoom of the (111) crystallographic direction for both film and source samples.

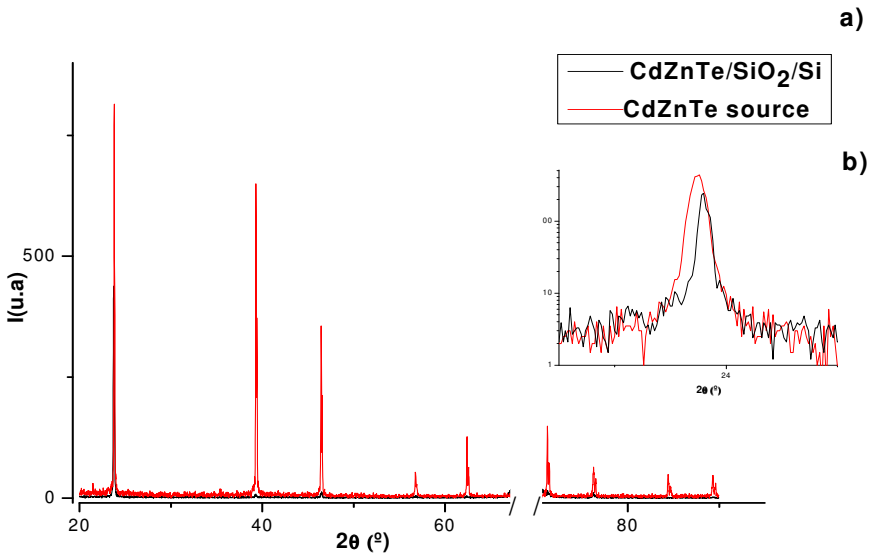

Figure 5.13. XRD patterns for a $Cd_{1-x}Zn_xTe$ source and a layer. The inset shows a zoom of the (111) peak for this two samples at logarithmic scale.

In order to assess the crystalline quality of this layer, linewidth measurements (full-width at half-maximum (FHWM)) was performed. Focusing on preferential orientation, the FWHM is 0.19º, a reasonably low value for crystals indicating good crystalline quality. This value is lower than for $Cd_{1-x}Zn_xTe$ source (0.24º), as it is expected.

5.4.2.3 Compositional characterization

The chemical composition of these samples has been studied by EDAX, as function of the source' deterioration, (after several runs), investigated in section 4.2.3 (see this section) [28].

5.5 Conclusions

From the sources studied in chapter 4, CdTe:Bi and CdTe:Ge:Yb films were grown with relative good crystallinity. In particular the first one has been demonstrated to be a promising alternative as absorber layer in solar cells. In this sense, our efforts were focused in the study of the back contact, where we obtain a strong ohmic contact or special device structures use to be quite difficult. One of the main conclusions of this chapter is the use of Bi_2Te_2 as a back contact for solar cell application. Our studies evidence that the use of this material notably decrease the work function of Au/Bi_2Te_2/CdTe:Bi heterojuntion which results very promising for further device development.

With respect to the CdTe:Ge:Yb, the experimental findings seem to point out that films with reasonable good structural properties can be grown by doping them with Yb at a concentration below the value $5x10^{18}$ at./cm^3 (which is estimated to be the Yb solubility limit for CdTe).

From the $Cd_{1-x}Zn_xTe$ sources studied in previous chapter, it is possible to obtain $Cd_{1-x}Zn_xTe$ films with quite quality. Therefore, we can consider that VPE technique is a well-control way to obtain films with uniform and predictable composition that could be considered for applications in photonics and radiation detectors.

References

[1] Castaldini A, Cavallini A, Fraboni B, Polenta L, Fernández P, Piqueras J. Phys Rev B **54**, (1996), 7622.

[2] Shaw DA, Thornton RP. J Mat Sci. **3**, (1968), 507.

[3] Ono H, Kamejima T, Watanabe H, Matsui J. Jpn J Appl Phys **25**, (1986), L130.

[4] Liu Juncheng, Song Dejie, Zhang Hongying, and Zhai Senqiu, Cryst. Res. Technol, **42**, No 8, (2007), 741-750.

[5] J.K. Radhakrishnan, B. S. Sunderseshu, Meenakshi Srivastava, G. L. Seth, R. Raman, R C Narula and R. K. Bagai, Bull. Mater. Sci., Vol **24**, No 6, (2001), 659-663.

[6] A. Kadys, K. Jarasuinas, E. Saucedo, E. Diéguez, J. C. Launay and D. Verstraeten, J Mater Sci: Mater Electron. **19**, (2008), S234-S238.

[7] E. Saucedo, J. Franc, H. Elhadidy, P. Horodysky, CM Ruiz, V. Bermúdez and NV Sochinskii, Journal of Applied Physics **103**, (2008), 094901 .

[8] E. Saucedo, C. M. Ruiz, V. Bermúdez, E. Diéguez, E. Gombia, A. Zappettini, A. Baraldi, and N. V. Sochinskii, J. Appl. Phys. **100**, (2006), 104901.

[9] G. Panin, J. Piqueras, N.V. Sochinskii, and E. Diéguez, Appl. Phys. Lett. **70**, (1997), 877.

[10] Saucedo E, Fornaro L, Sochinskii NV, Cuña A, Corregidos V, Granados D, Diéguez E. IEEE Trans Nucl Sci **51**(6), (2004), 3105.

[11] S. Neretina, N.V. Sochinskii, P. Mascher, E. Saucedo, Mater. Res. Soc. Symp. Proc. **864,** (2005), E4.18.1.

[12] T.O. Tümer, Sh. Yin, V. Cajipe, H. Flores, J. Mainprize, G. Mawdsley, J.A. Rowlands, M.J. Yaffi, E.E. Gordon, W.J. Hamilton, D. Rhiger, S.O. Kasap, P. Sellin, K.S. Shah, Nucl. Instr. and Meth. A **497**, (2003), 21.

[13] W. Li, Z. He, G.F. Knoll, D.K. Wehe, J.E. Berry, Nucl. Instr. And Meth. A **458**, (2001), 518.

[14] De Nobel, Philips Res. Rep. **14**, (1959), 361.

[15] Kessler F, Herman D and Powalla M. Thin Solid Films **480/481**, (2005), 491.

[16] Leeor Kronik, Joram Shapira, Surface Sciece Reports **37**, (1999), 1-126.

[17] J.M. Mwabora, K. Ellmer, A. Belaidi, J. Rappich, W. Bohne, J. Röhrich, Th Dittrich. Thin Solid Film. **516**, (2008), 3841-3846

[18] D. Gal, Y. Mastai, G. Hodes and L. Kronik, J. Appl. Phys., Vol. 86, No. **10,** (1999), 5573-5577.

[19] S. Sze, Physics of Semiconductor Devices, 2nd.ed (Wiley, New York, (1981), 245.

[20] E.H. Rhoderick, Metal- Semiconductor Contacts (Clarendon, Oxford, 1978), 77.

[21] A. Niemegeers and M. Burgelman, J. Appl. Phys. **81** (6), (1997), 2881-2886.

[22] "*Semiconductor Devices: Physics and Technology*", S. M. Sze, John Wiley and Sons, 2. Ed. USA (2001).

[23] Martin A. Green, solar Cells.

[24] "*Heterojunctions and Metal-Semiconductor Junctions*" A.G. Milnes and D.L.Feucht, Academic Press, USA (1972).

[25] "*Modificación de las propiedades optoelectrónicas por medio del dopado con Bi en células fotovoltaicas basadas en CdTe*", Carmen M. Ruiz Herrero. Tesis doctoral presentada en 2007 en la Universidad Autónoma de Madrid./ PhD Thesis, Universidad Autónoma de Madrid (2007).

[26] L. K. Herrera & A. Justo & A. Muñoz-Páez & J. A. Sans &G. Martínez-Criado Anal Bioanal Chem. **395**, (2009),1969–1975.

[27] N.V. Sochinskii, E. Saucedo, M. Abellán, J. Rodríguez-Fernández, P. Hidalgo, J. Piqueras, C.M. Ruiz, V. Bermúdez, E. Diéguez, Journal of Crystal Growth. **310**, (2008), 2076–2079.

[28] N. V. Sochinskii, M. Abellán, J. Rodríguez- Fernández, J.L.Plaza, V.Carceén, E. Diéguez, Journal of Crystal Growth **310**, (2008), 1669-1673.

Chapter 6

Thermal treatment of CdTe- based films growth by VPE

Chapter 6

THERMAL TREATMENT OF CdTe- BASED FILMS GROWN BY VPE

The latest advances in this area suggest that the **effect of stress and lateral defects** in CdTe- based epitaxial heterostructures on the recombination mechanisms could be almost completely eliminated by heating the substrate during the growth process and by post growth thermal annealing [1-2]. Namely, in the work of Neretina et al. [3], the strained structures of CdTe/Si have been thermally annealed at 400 ºC, 500 ºC, and 600 ºC for 10 s, concluding that the optimum annealing temperature, which gives rise to highest quality films, is 500 ºC. From these results, we continue studying the effect of thermal annealing at higher temperatures to investigate if further improvement on the quality of the CdTe layers can be achieved.

6.1 Thermal treatment of CdTe:PdI/Si films

CdTe:PdI polycrystalline layers were grown by VPE on Si(100) substrates at a substrate temperature of 300 ºC. The growth rate and time were in the range of 10-20 Å/s and 2-10 min, respectively [4]. The layers grown under these conditions are planar and homogeneous, having a thickness of ~ 400-800 nm as confirmed by perfilometry.

The thermal treatments were carried out using a Rapid Thermal Processing System, which by means tungsten halogen lamps and cold heating chamber walls allow fast wafer heating and cooling rates. The Rapid Thermal Annealing, RTA, setup located at CAI at the UCM was described in section 3.2. To protect CdTe:PdI/Si from any impurities, samples were enclosed in a graphite boat. The RTA temperature was selected to vary in the range between 450 – 1050 °C and the treatment elapsed 10 s.

6.1.1 Morphological characterization

The temperature evolution of the surface microrelief as characterized by SEM is shown in figure 6.1.

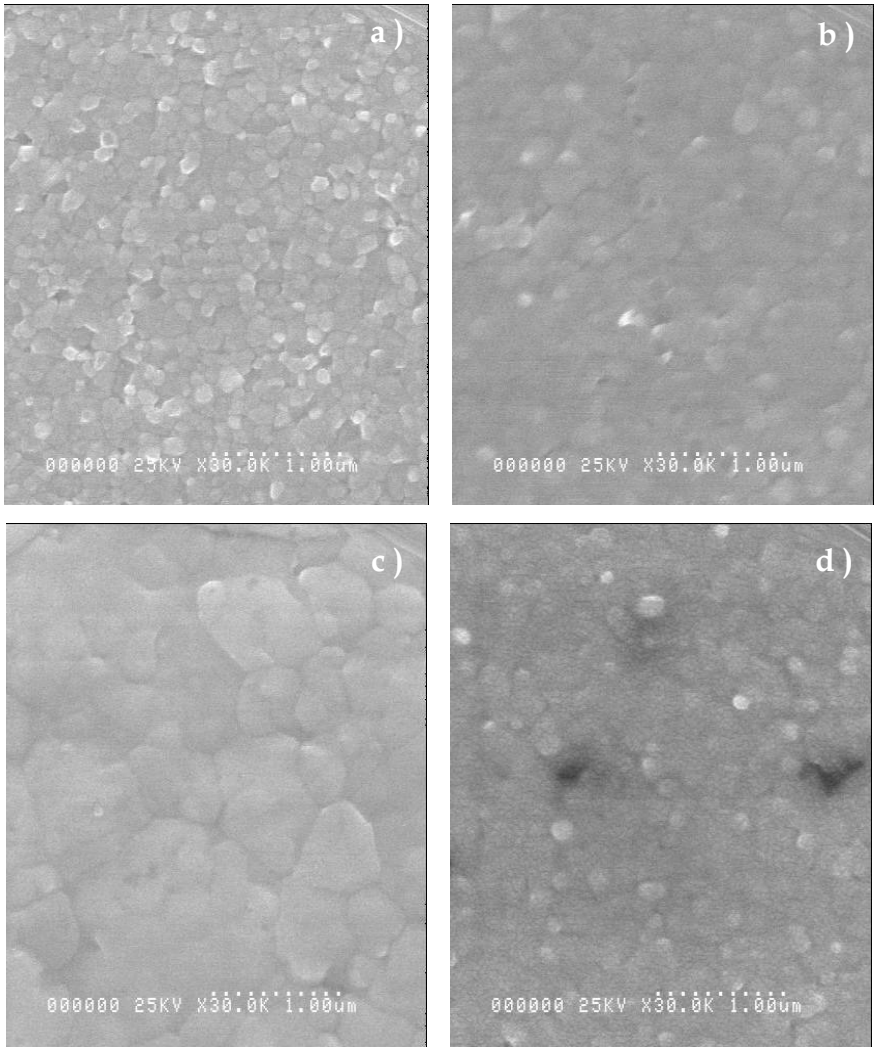

Figure 6.1. SEM images of CdTe:PdI/Si VPE layers: as- grown (a) and, after RTA treatment at 650 ^{o}C (b), 750 ^{o}C (c) and 900 ^{o}C (d).

As- grown CdTe:PdI/Si layer shows an uniform grain morphology, randomly oriented (see figure 6.1a). The grains present different average size covering all the substrate. Important changes can be observed in figure 6.1(b-d) by simple visual inspection for annealed films. Films heated up to 750 ^{o}C are formed by grains of different size compactly packed and uniformly distributed all over the substrate. In general, the RTA treatment results in a reduction of the surface roughness with a progressive increase of the grain size, by a factor of 3-5, and in the formation of cellular-like structures (fig. 6.1b-d). These cellular structures are originated by native point defects promoted by the climb processes [5].

As shown in figure 6.1d, films heated at ~ 900-1050 ^{o}C are damaged due to the high annealing temperatures. Indeed, a carefully inspection allows us to identify the presence of some holes which might be related to the generation of high stress during deposition at these elevated temperatures. Stress that might be associated to both the large difference in the thermal expansion coefficient between the Si substrate and the CdTe:PdI thin films ($\Delta\alpha/\alpha \approx 46.9$

% at 25 ºC) (2.6 ·10-6 K (at 250 K) for Si and 5 ·10-6 K(at 250 K) for CdTe:PdI), and the large lattice mismatch ($\Delta\alpha/\alpha \approx 19\%$) between them [6]. The presence of these holes is further corroborated by RBS. Figure 6.2 shows an RBS spectrum for the film annealed at 900 ºC. This spectrum can be only well fitted by assuming a certain amount of Si on the sample surface [7]. Since the deposited film does not contain any Si, this result corroborates the presence of holes in the films.

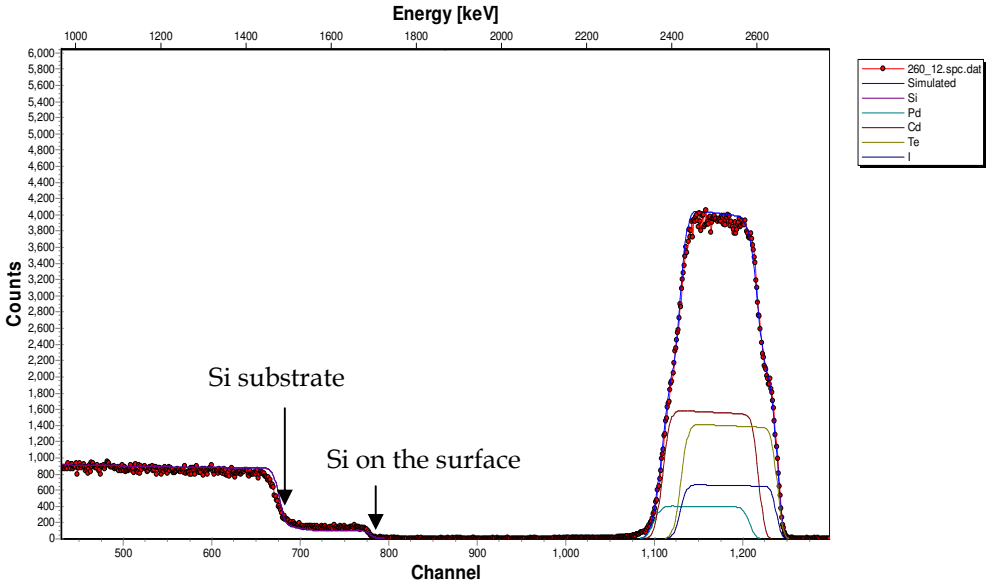

Figure 6.2. Measured (red dots) and simulated (colour lines) RBS spectrum for a CdTePdI layer annealed at 900 ºC.

Therefore, having in mind these preliminary results, we focus our interest on the study of the temperature range between 650-850 ºC. Since films annealed at higher temperatures 900<T<1050 ºC are severely damaged, they are not going to be further investigated.

More detailed information about the surface roughness was obtained by means AFM as shown in figure 6.3.

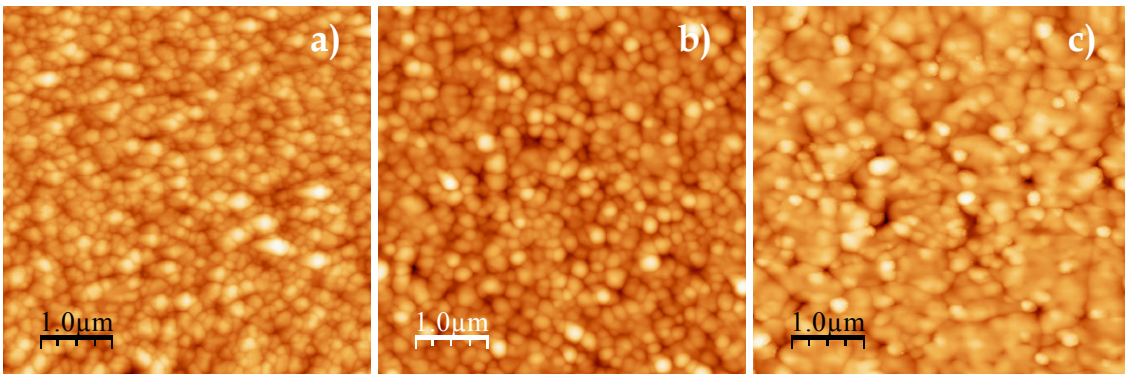

Figure 6.3. AFM images for CdTe:PdI/Si VPE layers: as grown (a) and, after RTA treatment at 500 ºC (b), and at 750 ºC (c).

Different grain size randomly distributed can be appreciated for all the studied samples. In agreement with SEM data AFM images show an enhancement in the grain size with rising temperature [8]. Moreover, the RMS (root mean square) of the roughness was calculated [9]. The measured values decrease with increasing temperature from 21.93 nm for as- grown to 15.91 nm for 750 ºC annealed samples.

The evolution of average grain size as a function of annealing temperature as estimated from SEM and AFM data is depicted in figure 6.4.

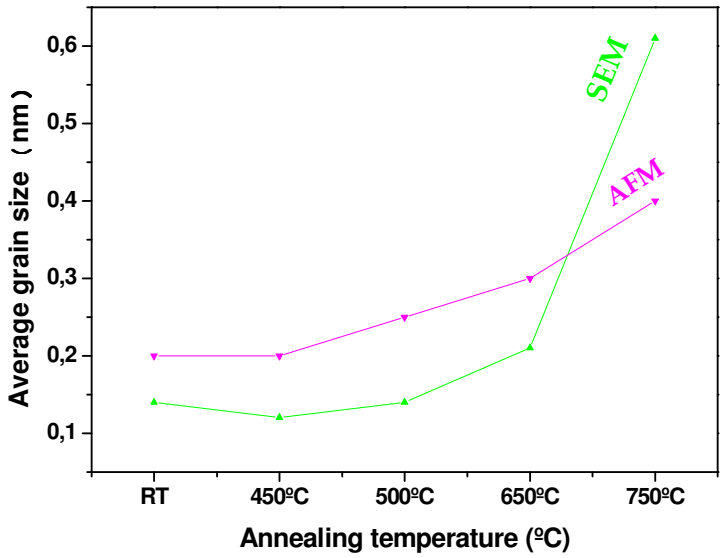

Figure 6.4. Evolution of the average grain size as a function of annealing temperature for CdTe:PdI films.

Both methods show the same trend. Nevertheless, the disagreement in the absolute values might be associated to the grain size dispersion and to the accuracy of the method.

Moreover, in order to study other aspects in the morphology of these samples, cross-sectional SEM measurements were carried out. As shown in figure 6.5 no significant differences between the cross-sectional images for as- grown and for annealed samples were observed. Both as-grown and annealed CdTe:PdI/SiO_2/Si structure show a well defined and very flat heterojuntion interface (figure 6.5a) revealing a good adhesion to the substrate with no evidence of crack through the polycrystal. It is observed that as- grown film of ~ 500 nm of thickness presents a compact columnar structure perpendicular to the substrate (very likely to that of similar samples grown by the same techniques, studied in previous sections).

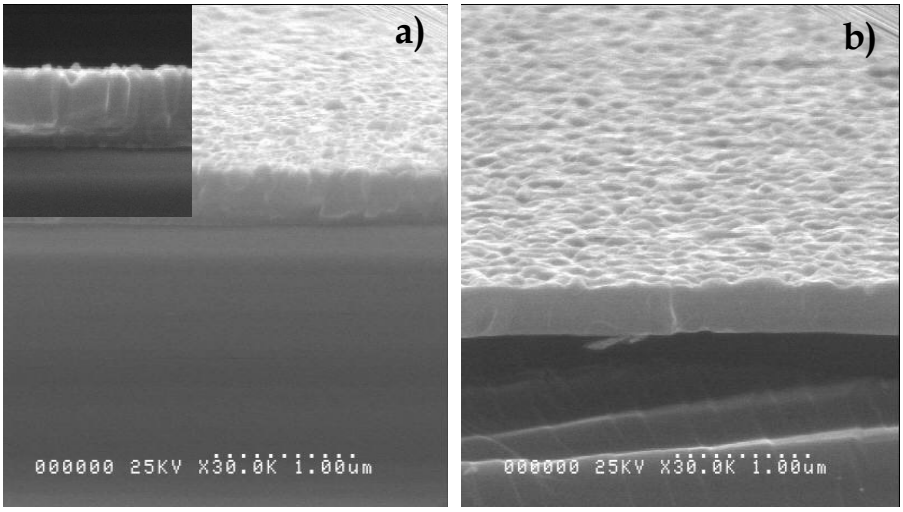

Figure 6.5. Cross-sectional SEM images for an as- grown (a) and a post- growth annealed at 650 ºC (b) CdTe:PdI/Si heterostructures, grown by VPE.

6.1.2 Structural characterization

The crystalline structure was studied by XRD. XRD patterns for CdTe:PdI as– grown and at annealed at different temperatures samples are shown in figure 6.6.

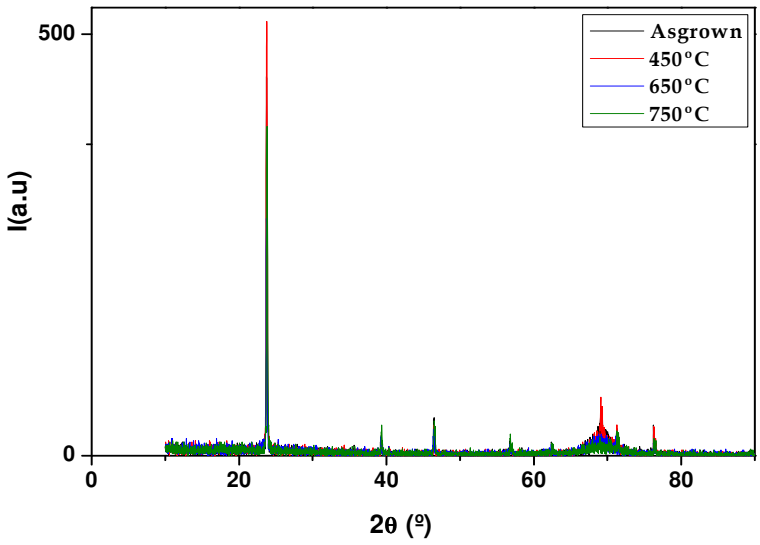

Figure 6.6. XRD spectra for CdTe:PdI/Si layers: as grown (black line) and annealed at 450 ºC (red line), 650 ºC (blue line) and, 750 ºC (green line).

Six Bragg peaks located at 23.75º, 39.31º, 46.43º, 56.82º, 62.33º and, 76.30º connected to the (111), (220), (311), (400), (331) and (511) crystaloghaphic directions are observed [10,11]. That indicates that all films are polycrystalline and preferentially oriented along the (111) direction. Nevertheless, as shown in table 6.I small variations in the 2θ positions and in the FWHM values are observed. In general, the 2θ positions are shifted to higher values (tensile stress) with

increasing annealing temperatures and the FWHM values decrease, which in agreement with SEM and AFM measurements indicates an enhancement of the grain size.

Sample	Centre	$FWHM_{(111)}$
As- grown	23.754	0.10556
Annealed at 450°C	23.757	0.10738
Annealed at 650°C	23.773	0.10207
Annealed at 750°C	23.811	0.10027

Table 6.I. Summarize of 2θ position for the (111) peak and FWHM value for as- deposited and annealed for CdTe:PdI/Si films.

By comparing the 2θ position of the preferential orientation with that reported in the literature, 23.759º, one can realize that for as- grown and for lower annealing (450 ºC), the peaks are slightly displaced to the left pointing towards a change in the stress state of the films, toward to tensile stress. However for annealing temperature higher than 450 ºC (650 ºC and 750 ºC) the peaks are displaced to the right indicating that the films are under compressive stress.

6.1.3 Elemental composition

The elemental composition of the samples was characterised prior to and after the RTA treatments by, Energy dispersive Spectroscopy (EDS) and Rutherford Backscattering Spectroscopy (RBS).

The elemental atomic percentage for as- grown and annealed films obtained by EDS technique is listed in Table 6.II.

Sample	Cd Atom.C.(atm.%) ± Error (%)	Te Atom. C.(atm.%) ± Error (%)	Pd Atom. C. (atm.%) ± Error (%)	I Atom. C. (atm.%) ± Error (%)
As- grown	48.18 ± 1.2	50.47 ± 1.7	0.02 ± 0	1.34 ± 0.2
Annealing at 450°C	47.89 ± 1.5	49.90 ± 1.9	0.57 ± 0.1	1.64 ± 0.4
Annealing at 500°C	47.97 ± 1.5	50.12 ± 1.9	0.53 ± 0.1	1.38 ± 0.4
Annealing at 650°C	45.98 ± 2.1	49.47 ± 3.2	0.94 ± 0.1	3.61 ± 0.4
Annealing at 750°C	49.36 ± 1.5	48.55 ± 2	0.79 ± 0.1	1.33 ±0.4

Table 6.II. Overview of compositional concentration for the CdTe:PdI films studied.

It is observed that as-grown samples are Te-rich. For samples heated at lower temperatures (up to 500 ºC), the Te and Cd concentration slightly decrease and the Pd and I concentration increases. However at 750 ºC the films become to be Cd-rich. According to these results, the sample with the best stoichiometry (the most balanced) has been found to be that annealed at 750 ºC. In figure 6.7 we show an example of EDS images for the sample annealed at 500 ºC.

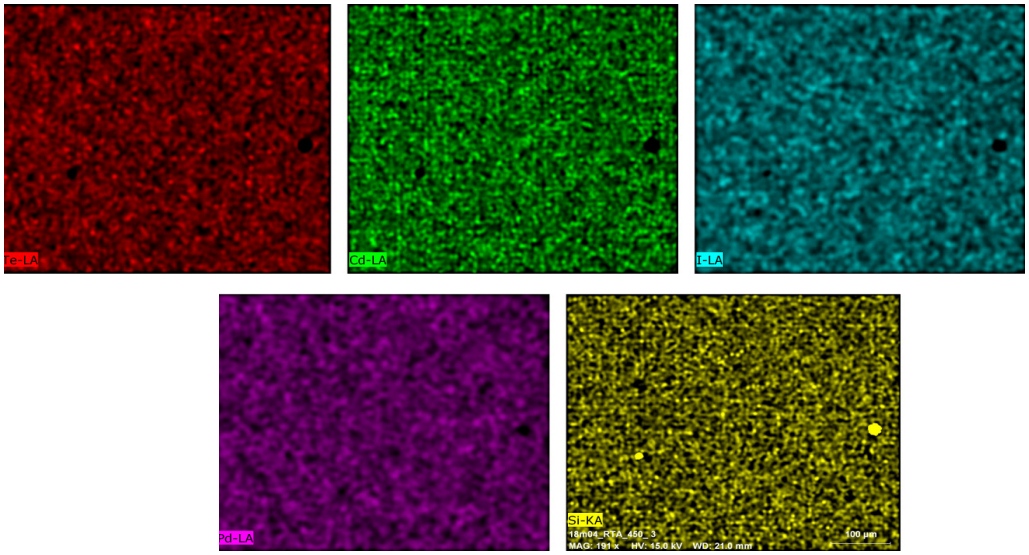

Figure 6.7. EDS images for a CdTe:PdI/Si annealed at 500 ºC**.** The color code for EDS measurement of each element is: red for Te, green for Cd, blue for I, violet for Pd and yellow for Si.

Typical measured (red dots) and simulated (colour line) RBS spectra for CdTe:PbI/Si annealed at 450 ºC and are shown in figure 6.8. These spectra illustrate that the films consists of Cd (44 at.%), Te (38 at.%), Pd (7 at. %) and I (9 at.%) deposited on a Si substrate. No other elements were detected within the resolution limit of the technique.

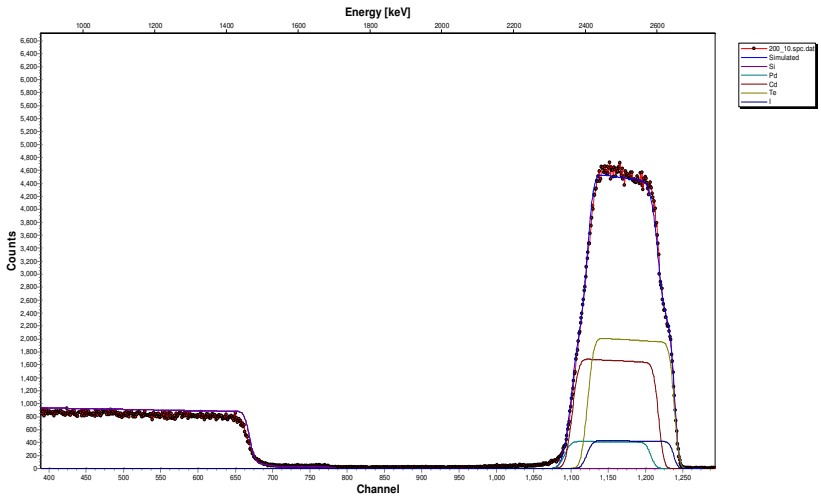

Figure 6.8. Measured (red dots) and simulated (colour line) RBS spectra for CdTe:PbI/Si annealed at 450 ºC.

6.1.4 Optical characterization

The optical properties of CdTe:PdI have been determined prior to and after annealing by means of the PL technique.

PL spectra measured at 20 K, (this temperature is sufficient to produce a satisfactory luminescence) for as- grown and annealed films are shown in figure 6.9.

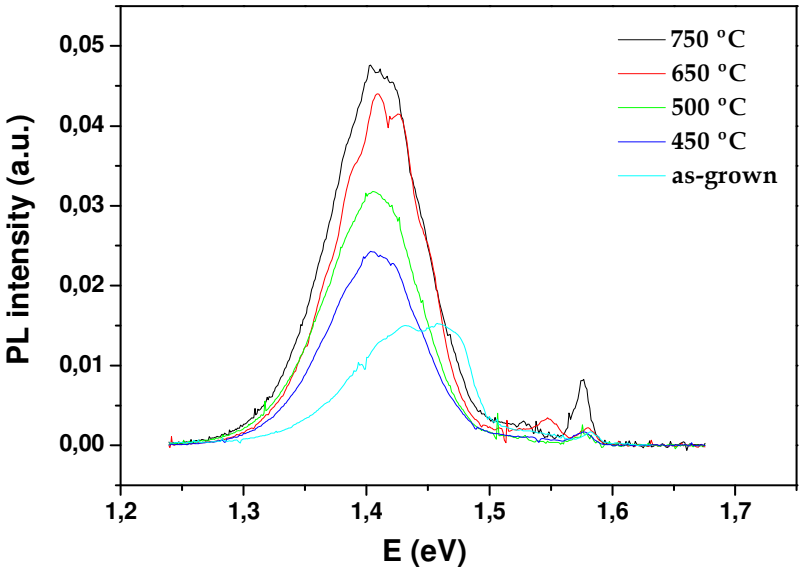

Figure 6.9. PL spectra for CdTe:PdI/Si layers (20 K): as grown (turquoise blue line) and annealed at - 450 °C (blue line), 500 °C (green line) , 650°C (red line), 750 °C (black line).

The measured spectrum for the as- grown film has two bands. The first band centred at 1.42 eV called A-band [12,13] is originated by the recombination of structural defects like dislocations or tensions in the lattice owed to defects in the shape of complexes. The acceptor part has a (V_{Cd} -D_{Te}) structure type [14] and, donor part has some superficial impurities [15]. The second band centred at 1.46 eV, generally called Y-band is originated by structural defects and it is related to the recombination process taken place in dislocation and grains boundaries [16]. On the other hand, the peak centred at 1.57 eV with very low intensity has a complex origin being formed by overlapping of transitions type donor- acceptor pair (DAP), leading to the conclusion that this is related to the $V_{Cd.}$ In particular, this peak is associated to the bound exciton A^0X [17].

The intensity of the A-band increases with rising annealing temperature. This fact is due to the increase in the V_{Cd} concentration and to disappearance of the Y-band. Moreover, the highest value of the emission associated to the recombination between donors and acceptors

pair at 1.57 eV, namely to A^oX transition is observed for the sample annealed at 750 ^oC as raises annealing temperature [18].

6.2 Study of the sub-bandgap photoluminescence from CdTe annealed films deposited on different substrates

In this section our efforts have been focused on studying the influence of the combination substrate type and thermal treatment on the physical properties of the CdTe films.

As previously mentioned the optical properties of CdTe films have been demonstrated to highly depend on their crystalline quality, in particular on the dislocation density at the film/substrate interface. Then, in this section, we study the influence of the lattice mismatch on the dislocation density, and therefore on the optical properties. For this purpose different substrates were selected. The substrate selection was oriented to industrial implementation and it has been mainly done according to the following criteria: a) decreasing the lattice mismatch, b) low cost and, c) availability in large wafer size.

In general, the lattice mismatch between CdTe and sapphire, GaAs, Si substrates is higher than 10% [19-23].

6.2.1 Thermal treatment of CdTe/Si

For this study CdTe films were deposited on commercial (100) Si substrates. The growth was carried out at evaporation temperatures ranging ~ 500-800 ^oC, and the growth rate was in the range of 0.05-0.2 μm/min (the variation of this value depends directly on evaporation temperatures).

6.2.1.1 Morphological characterization

The morphology of the films has been characterized by SEM and AFM. The layers grown under these conditions are planar and homogeneous, having a thickness of ~ 1-3 μm as confirmed by perfilometry. Both the surface and cross sectional SEM images for as-deposited CdTe/Si sample, annealed at 500 ^oC and 750 ^oC are shown in figure 6.10a-b.

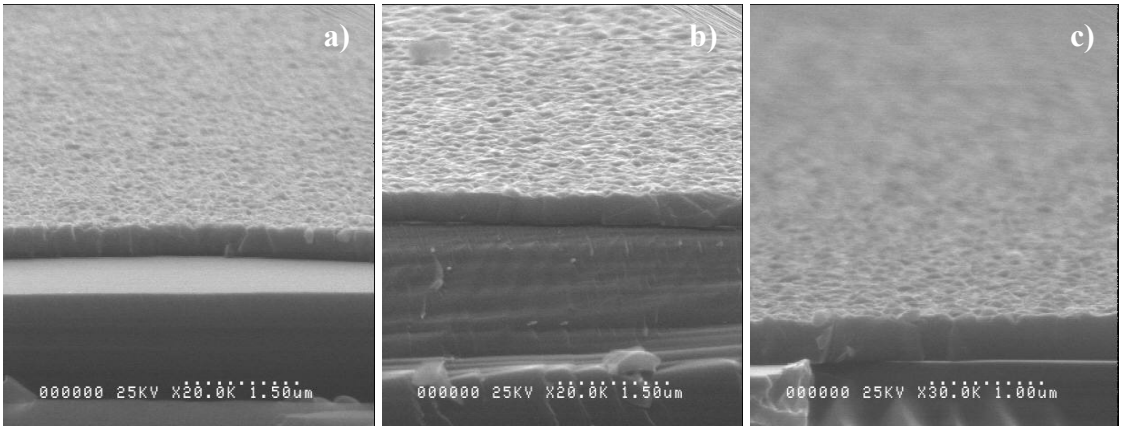

Figure 6.10. SEM images of a typical surface and, cross-section (a) for as- deposited CdTe/Si. And cross-section (b) for a sample annealed at 500 ºC and (c) for a sample annealed at 750 ºC.

No remarkable differences are observed between these samples. Moreover, both their surface morphology and the cross-section have the same characteristics than those presented in previous sections.

Comparing the cross sectional images for as- deposited and annealed samples, it is observed that all layers present a well defined and flat interface between the CdTe film and Si substrate, and exhibit good adhesion to the substrate. No evidences of cracks and large surface defects through the bulk are seen.

AFM images were taken to obtain additional and more precise information about surface roughness, shape and size of the grains. The images are shown in figure 6.11. In general, difference grains are observed.

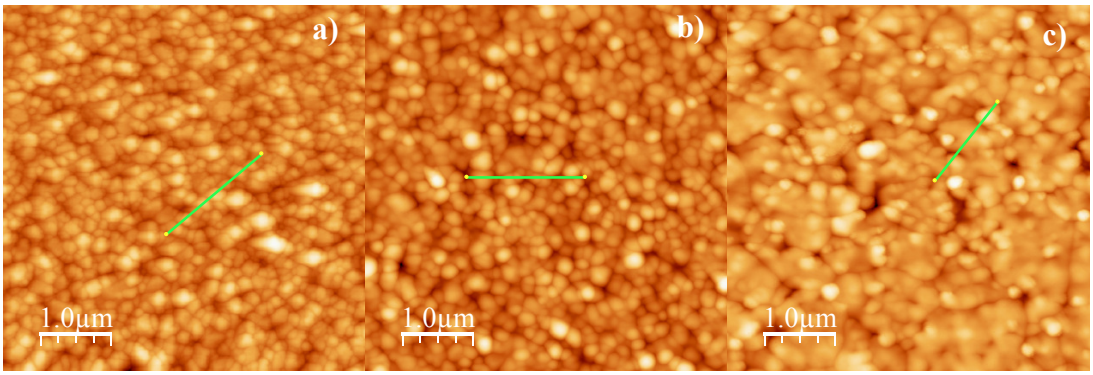

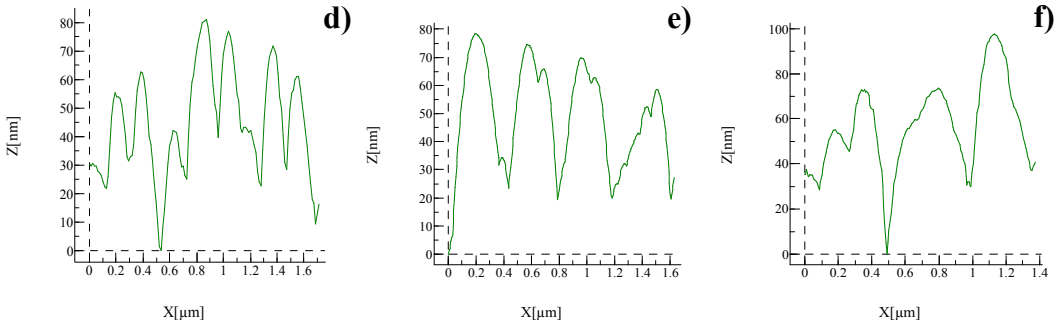

Figure 6.11. AFM images and profiles for a CdTe/Si film at RT (a,d), annealed at 500 ºC (b,e), and annealed at 750 ºC (c,f).

In agreement with SEM data, the as- grown sample exhibits uniform grains whose size vary from 100 to 200 nm. The RMS (RMS is calculated as the Root Mean Square between peaks and valleys of a surface measured microscopic), was calculated to be around 22.4 for these films. No significant changes on the sample surface were observed for those films annealed at temperatures lower than 750 ºC. However, for films annealed at 750 ºC an enhancement in the grain size for some grain is observed, namely there are grain of different sizes, and therefore the surface becomes to be less homogeneous.

The evolution of the roughness as a function of the temperature is depicted in figure 6.12 where, we can observe that the RMS value tends to decrease when increasing annealing temperature.

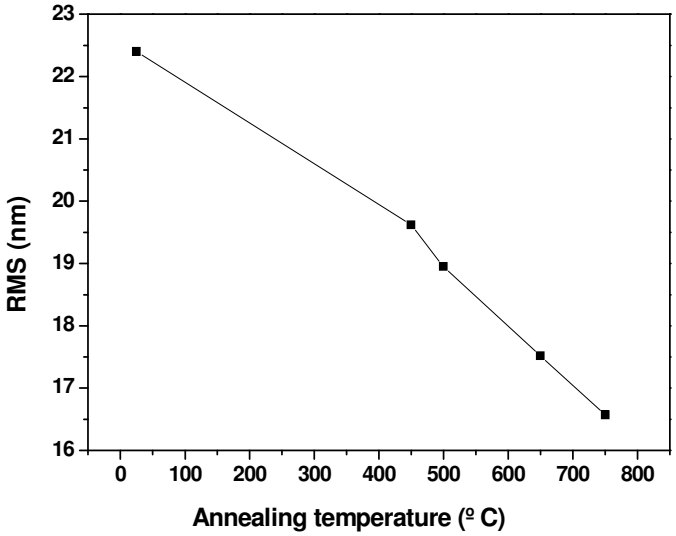

Figure 6.12. Evolution of the surface roughness for a CdTe/Si layers as a function of annealing temperature.

6.2.1.2 Optical characterization

Photoluminescence and transmittance measurements were carried out for as-grown and annealed layers, using Fourier-transform infrared spectrometer, FTIR. The excitation powers used for PL measurement were 0.3-0.5 W (Ti-sapphire laser at λ= 800 nm) and 10 mW (He-Ne laser at λ= 632.8 nm). This radiation allows studying the recombination levels in the bandgap of the CdTe layers with thicknesses less than 0.1 mm.

In figure 6.13, PL spectra for as- grown and annealed CdTe/Si films are compared [24]. The whole signal below 1.10 eV originates from the Si substrate. Therefore, the only emissions which are discussed are those observed at energies higher than 1.10 eV.

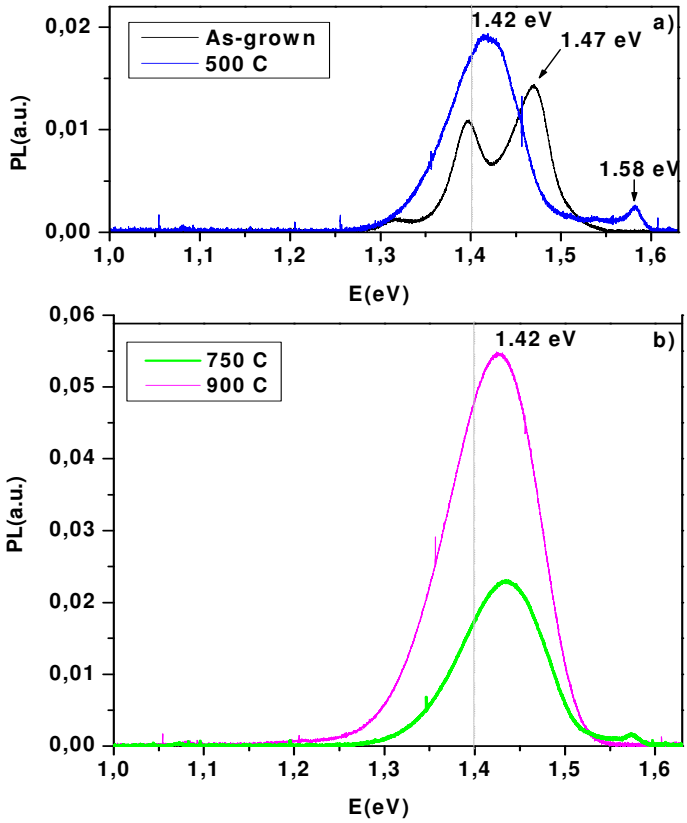

Figure 6.13. PL spectra (a) for as-grown (black line) and for annealed at 500 ºC (blue line), (b) at 750 ºC (green line) and at 900 ºC (dot black line) CdTe/Si samples.

Firstly, we discuss the PL spectrum obtained for the CdTe/Si as- grown sample, where the complex structure of the sub-bandgap in the range 1.20-1.53 eV. The spectrum mainly consists of two main PL bands. The first band centred at 1.40 eV is originated from recombination in A-center, composed from a V_{Cd} and a neighbouring atom impurity (Cl or Cu) [15]. The second band, peaking at 1.47 eV, is originated from the extended "dislocation" states. Similar bands were often observed in CdTe single crystals containing dislocations [25,26].

A clear increase of the A-center area is observed with rising annealing temperature, which is possible due to the increase of the V_{Cd} concentration. Moreover, for sample annealed at 500 ºC, a PL emission band develops at 1.58 eV. This band with low intensity can be ascribed to the mixture of the band to band, free, eX, and bound exciton, A^oX, emissions and it is due to the polycrystalline nature of CdTe [26], as well as, to the remained residual stress at the interface [26]. Another remarkable feature is the disappearance of the "dislocation" band located at 1.47 eV. All these facts suggest that dislocations and impurities around them can be diminished already at 500 ºC; this corresponds to a notable improvement in the crystalline quality of CdTe layer [26].

PL spectra for samples annealed at temperatures of 750 ºC are shown in figure 6.18b. In these spectra it is observed that the intensity of the peak located at 1.40 eV (corresponding to the A-band) increases and that it becomes broader. Thus, annealing led, at this temperature to a ~ 3-10% increase of the total PL intensity. This result evidences that, the presence of a strong 1.42 eV band is characteristic of either a compensated material or for poor quality crystals. This can be explained by an increase in the V_{Cd} density associated to both lost of crystallinity or decomposition of the films, corroborating the holes that appeared in the layer at thermal annealing above 750 ºC.

The FWHM of the A-centre emission together with the annealing temperature is depicted in table 6.III.

Temperature, T (ºC)	**FWHM (meV)**
500	80
750	100

Table 6.III. The FWHM evolution for A-centre emission band as a function of annealing temperature.

It is shown that as A-centre concentration increase with temperature, possibly, due to the increase in the V_{Cd} concentration.

The quality of the film influences possible losses which would be in the wall of CdTe waveguides.

6.2.2 Influence of CdTe growth onto sapphire substrate in the study of PL sub- bandgap

In order to check the influence of the substrate on the layer properties, CdTe layers have been grown under the same conditions onto commercial misoriented 3º off the (0001) sapphire substrate which was used to obtain CdTe films oriented along the direction onto (111) Si substrate.

6.2.2.1 Morphological characterization

SEM images of CdTe deposited on sapphire films are shown in figure 6.14. It is observed that these samples present a very much similar morphology to those deposited on Si.

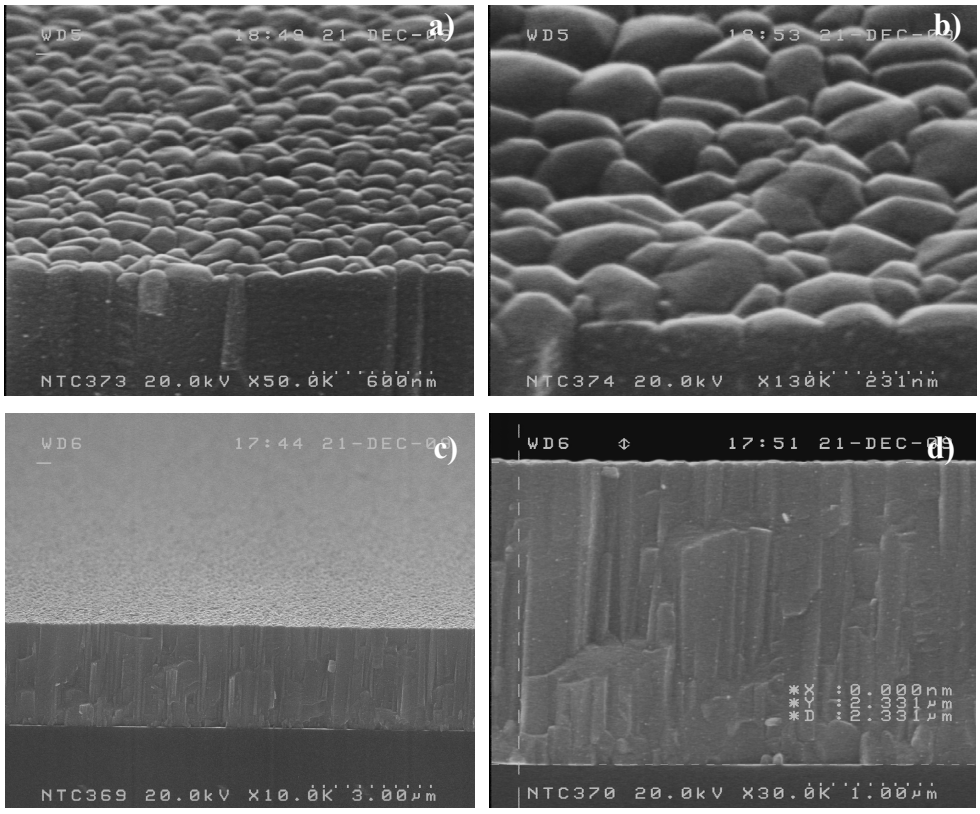

Figure 6.14. SEM images of a typical surface (a,b) and, cross-section (c,d) for a CdTe/Sapphire sample.

Under this condition, we obtained a 2.33 µm thick CdTe film uniformly formed over the entire substrate area. As in previous studies the film is formed by randomly distributed grains of different size between 120-220 nm. Moreover, the film present sharp flat interface with a good adhesion to the substrate (see figure 6.13 (c,d)). Cross-sectional images show that the

sample exhibits a columnar growth and is free from any macrodefects typical of this kind of material.

6.2.2.2 Optical characterization

The measured PL spectrum together with the best fit obtained for CdTe films grown on sapphire are shown in figure 6.15. One can see that it is similar to that for CdTe/Si and shown in figure 6.13.

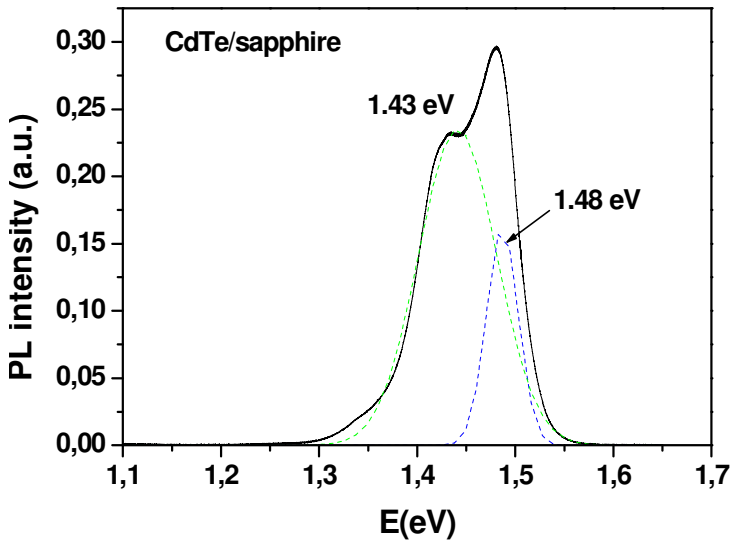

Figure 6.15. PL spectrum for as-grown CdTe/sapphire sample at 4.2 K (thickness of the CdTe layer is ~ 1.8 μm).

The sub-bandgap emissions dominate the spectrum. These two bands are identified to correspond to an A-center (1.43 eV) and "dislocation" band (1.48 eV). This feature can be observed for CdTe monocrystal, recombination at dislocations is responsible for a narrow emission band which is due to a weak electron-phonon interaction [27].

The transmission spectrum can be measured for samples deposited on sapphire but not for those deposited on Si since sapphire has been transparent in the 1.10-1.70 eV energy region.

The Transmission spectrum for CdTe/sapphire films is shown in figure 6.16. The principal characteristic of transmittance spectra for this thin film is the presence of maximum and minimum interferential. These values are related with the refraction index and absorption coefficient of the material.

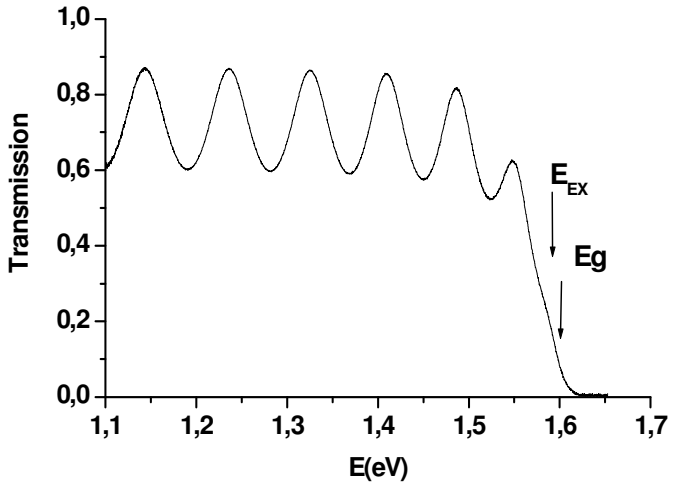

Figure 6.16. Transmittance for as-grown CdTe film on sapphire substrate at 4.2 K (thickness of the CdTe layer is ~ 1.8 μm).

Comparing the decomposed PL spectrum with the corresponding transmission spectrum, we can conclude, that the interference effect pronounced in the transmission spectrum can really deteriorate the shape of PL spectrum, namely, the PL spectrum of as- grown CdTe/Si sample shown in figure 6.13.

The determination of the semiconductor band gap, $\mathbf{E_g}$, within the parabolic approximation, where direct transitions between the BV and the BC are considered, can be calculated from the Swanepoel's equation to be:

$$\alpha(h\nu) = A(h\nu - E_g)^{1/2} \qquad (6.1)$$

where, **α** is the absorption coefficient, **A** is a constant, **hν** is the energy of phonons and $\mathbf{E_g}$ is the gap energy. According to this formula and considering the data depicted on the transmittance spectrum, the E_g value was estimated to be ~1.6 eV (extrapolation to α=0 in the α^2 versus *hν* plot (see figure 6.16)) [28,29].

In order to ensure that the origin of the 1.47-1.48 eV PL band differs from that of the 1.43 eV band, the dependence of the PL intensity on excitation power in the range from 0.05 mW to 0.6 W, is measured. The results are shown in figure 6.17. A similar dependence has been observed for those sample deposited on Si (not shown).

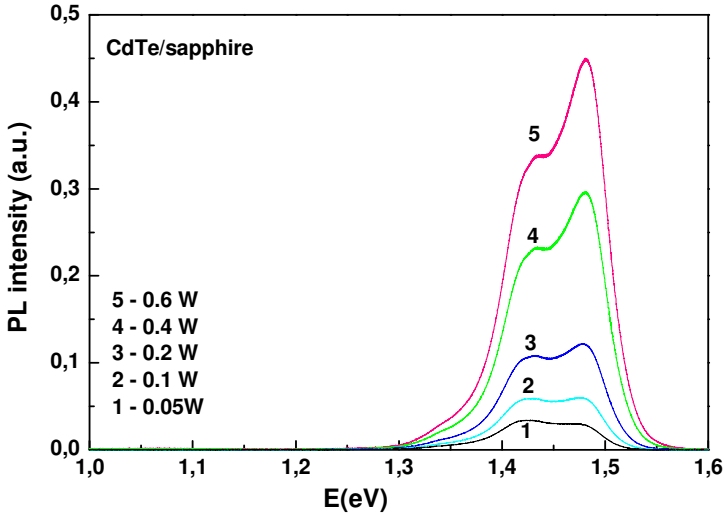

Figure 6.17. Dependence of PL spectrum vs the excitation power for the CdTe/sapphire sample (the excitation powers are indicated).

If we deconvolute these spectrums like those in figure 6.13, the same two sub-bandgap emissions that dominate the spectrum are observed. Nevertheless, in this particular case, one can see that the intensity of the "dislocation" PL band (1.48 eV) grows faster than that of the A-center band indicating the presence of some dislocation and/or grain boundaries.

After decomposition of these spectra, the dependence of the integrated intensities of PL band for the A-center and dislocation on excitation power is depicted in figure 6.18.

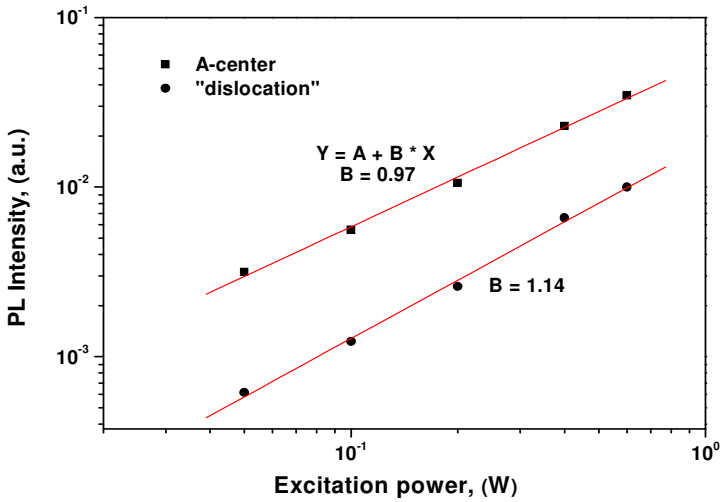

Figure 6.18. Dependencies of the integrated A-center and "dislocation" PL bands on excitation power at 4.2 K. Solid lines correspond with a linear fit.

It is observed that the PL intensity of the A-centre band increases sublinearly with excitation power, while the dependence for the "dislocation" band is linear. This fact unambiguously confirms that these two bands do not have the same nature.

6.3 Thermal treatment of SiO_2/ Cd(Zn)Te/SiO_2/ Si films

To complete the chapter, this section is devoted to the study of thermal treatment on encapsulated SiO_2/CdZnTe (40%)/SiO_2/Si films. This design gives a variation in the refractive index of the materials that will allow the light guiding. These multilayers are going to be used to fabricate CdTe- based waveguides. For that, CdZnTe polycrystalline films were grown on SiO_2/Si substrates at a substrate temperature of about 300 ^oC. With a growth rate and time ~ 15 Å/s and 4 min, respectively.

After that, the films were encapsulated with a layer of 500 nm of SiO_2 by Plasma Chemical Vapour Deposition (PCVD, Surface Technology 310 D/F) at 300 ^oC [30]. However for this case, the annealing temperature was selected to be varied in the range of 650-900 °C. The elapsed time was 10s.

6.3.1 Morphological characterization

The as- grown films deposited under these conditions present the same characteristics than those presented in previous cases. A typical SEM image of a CdZnTe/SiO_2 film is shown in figure 6.19a. It is observed that the studied film is quite planar and homogeneous; having a thickness of ~500 nm. It presents a compact columnar structure with approximately some dozens of nm. As shown in figure 6.19a, the cross sectional images of a CdZnTe/SiO_2/Si structure exhibits, as well as previous cases, a well defined and very flat heterojuntion interface pointing to a good adhesion between film and substrate.

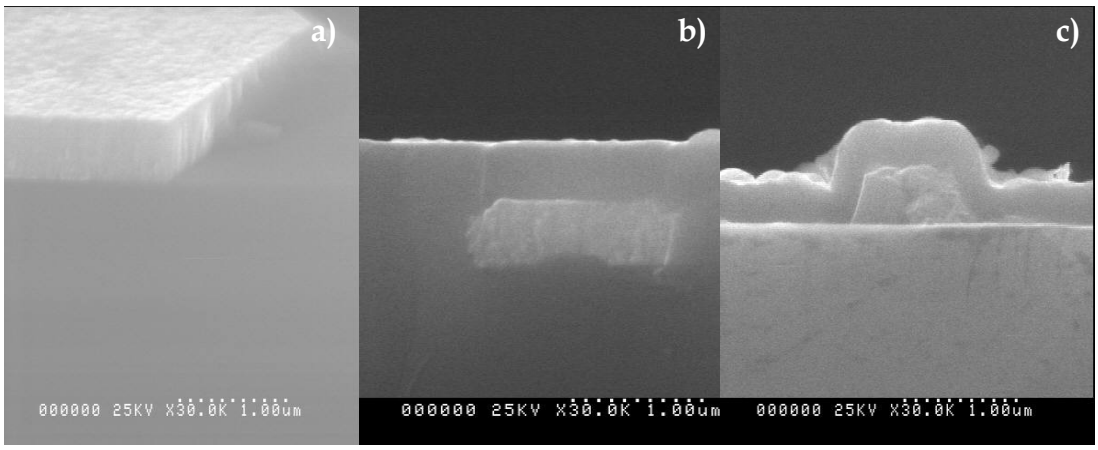

Figure 6.19. Typical SEM images of (a) a surface of CdZnTe/SiO_2 film), (b) cross-section of SiO_2/CdZnTe/SiO_2/Si encapsulated film and, (c) cross-section of SiO_2/CdZnTe/SiO_2/Si film annealed at 650 ^oC (c).

The results for a $SiO_2/CdZnTe/SiO_2/Si$ heterostructure annealed at 650 ºC can be observed in figure 6.19c. The film keeps a sharp flat interface with the substrate and a roughness surface with a microrelief height of ~ 50-60 nm. Although, these films were encapsulated, the same morphological characteristics than those films studied in previous sections can be observed.

6.3.2 Structural characterization

The structural characterization of the films was carried out by means XRD. θ -2θ scans for as- grown and annealed layers are shown in figure 6.20.

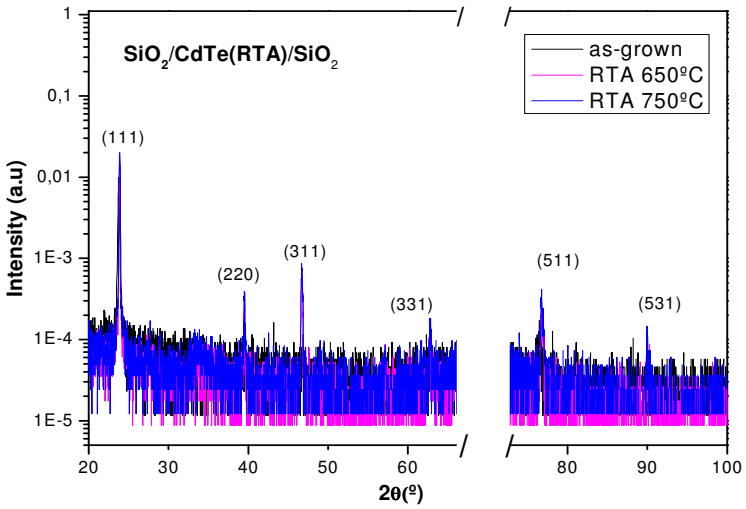

Figure 6.20. XRD spectra for $SiO_2/CdZnTe/SiO_2$ layer: as- grown (black line) and, annealed at 650 ºC (pink line), and at 750 ºC (blue line).

The patterns reveal that as in similar films (e.g. in CdTe:Bi samples) six Bragg peaks located approximately at 23.75º, 39.31º, 46.43º, 56.82º, 76.30º and 89.96º which are related to the (111), (220), (311), (331),(511) and (531) crystaloghaphic directions. Thus, these results evidence that, samples are policrystalline and preferential oriented along the (111) direction.

Considering the (111) peak and comparing its position such as for as- grown and annealed films with that for JCPDS database, one realize that for the as- deposited sample the peak is in the same position that the theoretical peak (see figure 6.21).

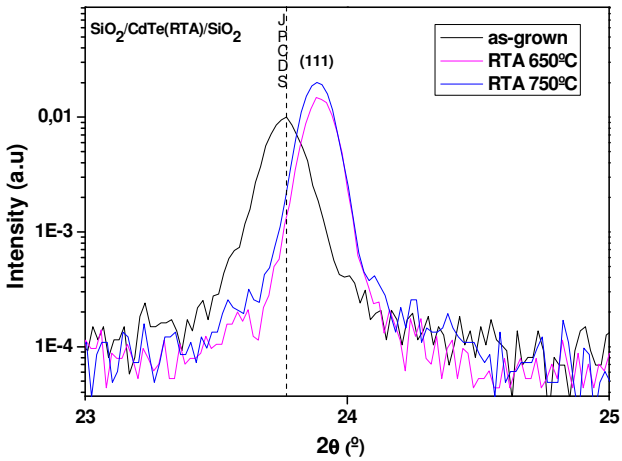

Figure 6.21. XRD spectra associated to (111) preferential direction for SiO_2/CdZnTe/SiO_2 as-grown (black line) and annealed at different temperatures, 650 ºC (pink line) and, 750 ºC (blue line).

Also, FHWM was calculated, in order to assess the crystalline quality of these layers. The 2θ positions together with the FHWM values for the preferential orientation are shown in table 6.IV. As increasing the annealing in the sample, the peaks are a little bit displaced to the right indicating a slightly compressive stress in the samples.

Sample	Centre	$FWHM_{(111)}$	Height
As- grown	23.759	0.13425	0.92822
Annealed at 650 ºC	23.896	0.10870	0.07245
Annealed at 750 ºC	23.886	0.10899	0.01992

Table 6.IV. Overview of variation of FWHM with diffraction angles for a SiO_2/CdZnTe/SiO_2 films.

The FHWM show changes in function of annealing temperatures. As increases the annealing temperature, there is a gradual decrease of these values, indicating good crystalline quality. These data evidence that annealing improves the crystalline quality of the layer. In this case the best result was obtained for the sample annealed at 650 ºC.

6.4 Conclusions

In this chapter, we have presented the experimental results on the remarkable improvement of the recombination quality of the CdTe films by post growth thermal annealing (RTA). We shown that heating the samples notably improves both its crystalline structure and its surface morphology and it allows to significantly reduce the typical concentration of native and foreign defects.

For the three studied cases, the substrate does not affect to the morphology of the films´ surface.

- For **CdTe:PdI/Si,** the increase in the PL peak intensity is in very good agreement with the data obtained from SEM measurement which shows an increase in the average grain size and a decrease in the grain boundaries, and by XRD measurement, where the FWHM decreases as the annealing temperature increase.

  This fact demonstrates that annealing promotes an improvement in the structural quality of the film. The optimum annealing temperature, which gives rise to highest quality films, is ~750 ^{o}C. Indeed, at very high temperature around 800 ^{o}C, the effect is the opposite: the stress is so high that the films appear damaged.

- For **CdTe/Si**, we found that annealing between 500- 750 ^{o}C is an important factor to improve recombination in CdTe layers. The intensity of the sub-bandgap band in as-grown samples of CdTe layers is ~3.5 times weaker as compared with the annealed samples, indicating the presence of a high defect concentration, which create non-recombination centres. Moreover, after annealing the band-to-band emission at 1.58 eV appeared in the spectrum. Therefore, we have found that annealing at 500 ^{o}C is an important factor to rembination in CdTe layer grown on both Si and sapphire substrates.

- Finally, for **encapsulated samples** the optimum annealing temperature is a bit lower than for samples without encapsulation, namely at approximately 650 ^{o}C.

Therefore, the achieved high crystalline quality stimulates good optical quality, and the heteroepitaxial layers encourage us to use these films, for example, as an optical waveguide in integrated silicon optics devices.

References

[1] M.S. Han, Y.S. Ryu, B.K. Song, R. W. Kang, T. W. Kim. Thin Solid Film **293**, (1997), 196-199.

[2] M. J. Hart, A. G. R. Evans. Semicond. Sci. Technol. **3**, (1988), 421-436.

[3] S.Neretina, N.V. Sochinskii, P. Mascher. Journal. Electron. Mater. Vol **34**, No.6, (2005),1333.

[4] N.V. Sochinskii, M. Abellán, J. Rodríguez-Fernández, J.L. Plaza, V. Carcelén, E. Diéguez, J. Cristal Growth **310**, (2008), 1669–1673

[5] R. Pascual, M. Sayer, A. Lo, S. Herbert, L. C. Rolim, and N. Townley. J. Appl. Phys. **79** (1), (1996), 493-499.

[6] J. Rams, N.V. Sochinskii, V. Munoz, and J.M. Cabrera, Appl. Phys. A **71**, (2000), 277.

[7] M. Mayer, SIMNRA, Version 5.02, Max Plank Institut für Plasmaphysik.

[8] H. Ebe and Y. Nishijima, Appl. Phys. Lett. **67**, (1995), 3138 .

[9] I. Horcas, R. Fernández, J. M. Rodríguez, J. Colchero, J. Gómez-Herrero, and M. Baro. Rev. Sci. Instrum., Vol. **78**, (2007), 013705.

[10] URL: http://database.iem.ac.ru/mincryst/index.php

[11] URL: http://www.icsd.iqfr.csic.es

[12] W. Stadler, D.M.Hofmann, H.C.Alt, T. Muschik, B.K.Meyer, E. Weigel, G. Müller-Vogt, M. Salk, E. Rupp, K.W.Benz, Phys. Rev.B **51**, (1995), 10619-10630.

[13] Cg, Barnett, Davis, D.D. Allred, A. Reyes-Mena, J. Gonzalez-Hernandez, O. Gonzalez, B.C. Hess, W.P. Allred, Phys. Rev B **47**, (1993), 13363-13369.

[14] Zimmermann, R. Boyn, C. Albers, K.W. Benz, D. Sinerius, C. Eiche, B.K. Meyer and D.M. Hoffmann, J. Crystal Growth **128**, 1-4, (1993), 593-598.

[15] V.N. Babentsov, Semiconductors **30**, (1996), 750-756.

[16] N. Armani, C. Ferrari, G. Salviati, F. Bissoli, M. Zha, A. Zappettini, L. Zanotti, J. Phys.: Condens. Matter **14**, (2002), 13203.

[17] D.P. Halliday, M.D.G. Potter, J.T. Mullins, A.W. Brinkman, J. Crystal Growth **220**, (2000), 30.

[18] M. Abellán, P. Hidalgo, J. Fernandez, N. Sochinskii, J. Piqueras. (In preparation).

[19] Y. Xin, N.D. Browning, S. Rujirawat, S. Sivananthan, Y.P. Chen, P.D. Nellist, S.J. Pennycook, J. Appl. Phys. **84**,(1998), 4292- 4299.

[20] M. Niraula, K. Yasuda, H. Ohnishi, K. Eguchi, H. Takahashi, K. Noda, Y. Agata, J. Cryst. Growth **284,** (2005), 15-19.

[21] J.M. Ballingall, W.J. Takei, Bernard J. Feldman, Appl. Phys. Lett. **47**, (1985), 599-601.

[22] S.O. Ferreira, I.R.B. Ribeiro, J. Suela, I.L. Menezes-Sobrinho, S.C. Ferreira Jr., S.G. Alves, Appl. Phys. Lett. **88** ,(2006), 244102.

[23] Y. Nishijima, K. Shinohara, H. Takigawa, Tilt growth of CdTe epilayers on sapphire substrates by MOCVD, H. Ebe, A. Sawada, K. Maruyama, J. Cryst. Growth **115**, (1991), 718-722.

[24] N.V. Sochinskii , M. Abellán, J. Rodríguez-Fernández , E. Diéguez , J. Franc , P. Hlidekc, P. Praus , V. Babentsov. SuperlatticeSuperlattices and Microstructures Vol. **45**, 4-5, (2009), 228-233.

[25] M.S. Han, Y.S. Ryu, B.K. Song, T.W. Kang, T.W. Kim, Thin Solid Films **293**, (1997), 196.

[26] Chul S. Kim, Ho B. Im, J. Amer. Ceram. Soc. **73**, (1990), 150.

[27] M.J. Angell, R.M. Emerson, J.L. Hoyt, J.F. Gibbons, L.A. Eyres, M.L. Bortz, M.M. Fejer, Appl. Phys. Lett. **64**, (1994), 3107.

[28] V.V. Ison, A. Ranga Rao, V. Dutta, P. K. Kulriya, D. K Avasthi and S.K. Tripathi. J. Phys. D: Appl. Phys. **41**, (2008), 105113- 105119.

[29] R. González-Arrabal, Y. González, L. González, M. García- Hernandez, F. Minnik and M.S. Martín- González. J.Appl. Phys. **105,** (2009), 073911.

[30] "*Contribución al establecimiento y caracterización de una tecnología de ataque de aleaciones III-V basadas en Indio mediantes haces de iones reactivos*". José Ramón Sendra Sendra. Tesis doctoral presentada en 1995 en la Universidad Politécnica de Madrid/ PhD Thesis, Universidad Politécnica de Madrid (1995).

Chapter 7

Technological process of CdTe- based films

Chapter 7

TECHONOLOGICAL PROCESS OF CdTe– BASED FILMS

This chapter is devoted to the study and development of technological processes that affect both the surface and the physical properties of the CdTe- based film.

For technological applications of CdTe films, as photonic bandgap structures onto semiconductors like waveguides and, other particular photonics and optoelectronics devices, or even for a typical production of pixel in a detector; it is necessary to develop several fabrication processes that affect their surfaces [1]. In the present thesis, we study the effect of the Reactive Ion Beam Etching (RIBE), process on the photoluminescence (PL) of CdTe epitaxial layers grown on sapphire by MOVPE.

Special attention has been paid to Cd(Zn)Te- based heterostructures because of its potential use for X- and γ- ray radiation detectors operating at room temperature (see [2] and [3,4], respectively). The latest advances in this area suggest that Cd(Zn)Te- based epitaxial heterostructures and, particularly, nanostructures formed by Cd(Zn)Te material into nanoporous alumina could be of great concern for the development of high resolution multi-pixel imaging detectors [5,6]. These detectors could be considered as a natural evolution of the classic arrays made from Cd(Zn)Te bulk crystals [7].

7.1 Effect of RIBE on CdTe films

Considering that RIBE process is a typical one to produce pixels and photonic bandgap structures onto semiconductors, we have studied the effect of RIBE process on PL properties for CdTe films. Moreover, the relation between changes in morphology and those in the PL spectrum has been achieved by means of Optical Microscopy (OM) and, Atomic Force Microscopy (AFM).

7.1.1 Effect of RIBE on the photoluminescence of CdTe films

This section is devoted to study the effect of the RIBE process on PL for CdTe layer grown on sapphire by Metalorganic Vapour Phase Epitaxy, (MOVPE).

In order to develop CdTe- based devices some lithographic processing is needed. Since CdTe processing cannot be carried out by chemical etch, RIBE has been demonstrated to be one of the most suitable techniques for CdTe processing.

7.1.1.1 Growth procedure

CdTe films were grown on a commercial sapphire substrate of misoriented 3° off the along the (111) direction, in a low pressure horizontal MOVPE reactor under optimal growth conditions [8,9]. Dimethyl cadmium and di-isopropil tellurium were used as precursors, the growth temperature was 340 °C, and the growth time was in the range of 2–4 hours. The thickness of the layers was in the range of 5–7 μm. The growth setup is placed at Laboratories of Consorzio Creo (L'Aquila, Italia) and the films were grown by Angelo Mercuri.

7.1.1.2 Physical properties

7.1.1.2.1 Relation between morphological and optical changes after RIBE processes

The as grown CdTe films were divided into several areas by optical lithography using a Karl–Süss MJB3 mask aligner (see figure 7.1). Some of these areas were protected with a 0.3 μm thick layer of aluminium evaporated over the photoresist. This method is commonly used in the fabrication process to estimate the etching rate of CdTe films.

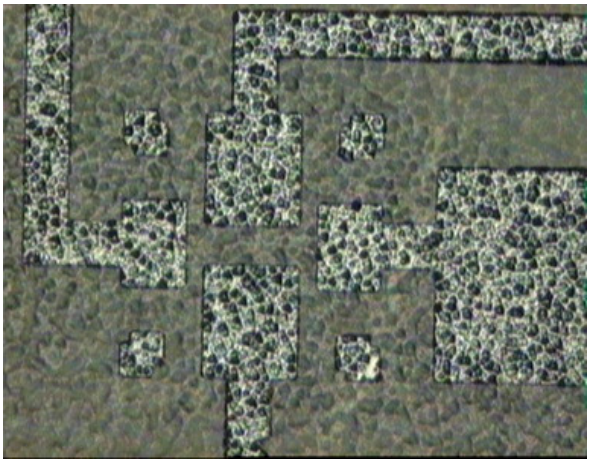

Figure 7.1. Typical optical microscope image of CdTe films after the photolithography process.

RIBE etch was performed on these samples using a RIBER reactor. The RIBE process was carried out under $(CH_4 + H_2)/N_2$ plasma atmosphere for 90 min. The ion energy was selected to

be 400 eV and the total reduction of films thickness was about 1.5 μm [10]. The surface of CdTe films after RIBE process is shown in figure 7.2.

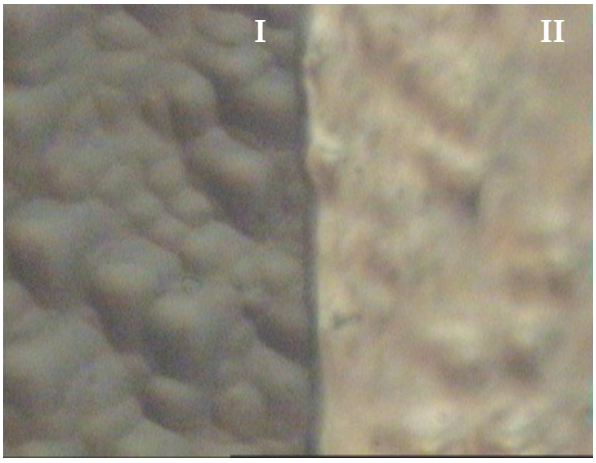

Figure 7.2. SEM image of an etched area of CdTe films (I), and CdTe films protected with Al (II) after RIBE process.

After that, the Al mask was removed by using orthophosphoric acid (H_3PO_4). Typical images of the CdTe films surface after the RIBE process and, removal of the photoresist protecting the original surface are picked in figure 7.2. It is observed that the etched (I) and as grown (II) areas have a similar microrelief with an average roughness of 400 nm. A weak increase in surface roughness by about 10%, was observed within CdTe zones that were exposed to the RIBE. This demonstrates that the RIBE process under optimum technological conditions does not introduce significant morphology modifications of the exposed surfaces with respect to that observed for the as-grown samples.

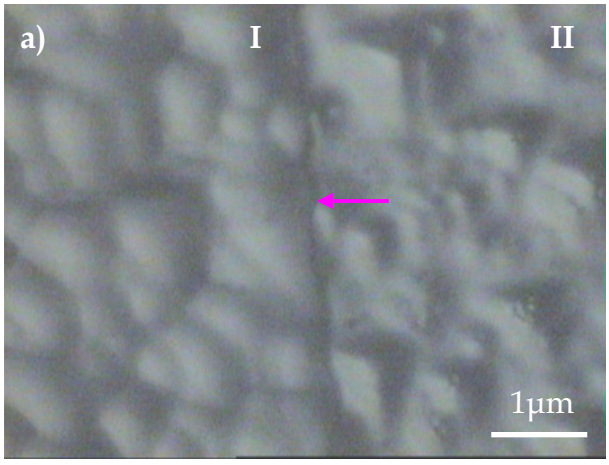

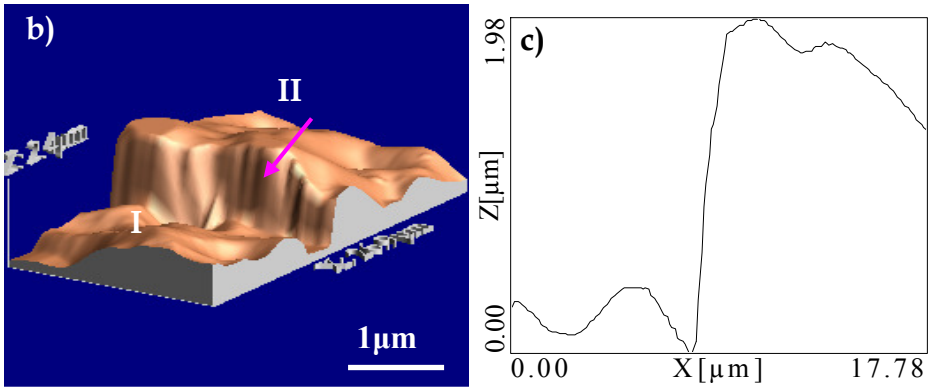

Figure 7.3. Surface microrelief for CdTe film recorded by optical (a) and atomic force microscope (b) after the RIBE process: (I) etched area, (II) protected area (as- grown morphology) and (c) AFM profile of the etch area. The arrows indicate the boundary between protected and unprotected areas.

After the RIBE process for both protected and unprotected areas [11], PL measurements were carried out at two different excitation conditions at 10 K:

(i) **Continuous wave (cw) configuration**, keeping the excitation constant to mainly obtain information on the structure of the electronic level participating in the radioactive recombination.

(ii) **Time resolved PL (TPRL),** to get information on carrier dynamics and recombination kinetics. (In this configuration, PL is excited using a pulsed excitation with light pulses of suitable duration).

The results under these conditions are shown in figure 7.4.

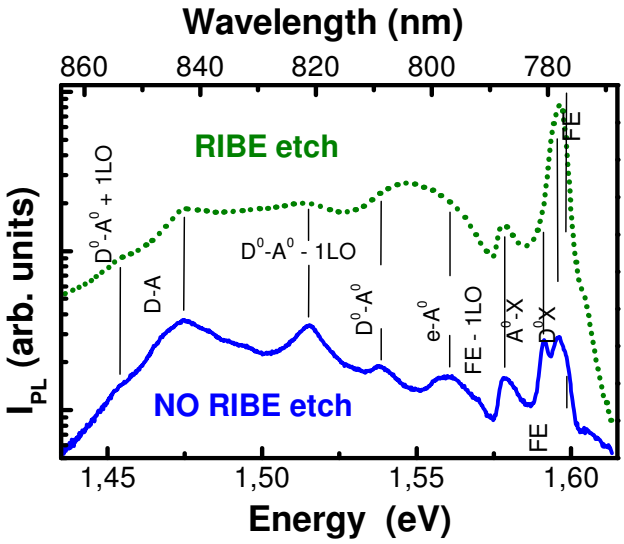

Figure 7.4. PL spectra at 10 K under near resonant conditions (710 nm) and low excitation power in zones of the CdTe surfaces with (dotted line) and without (continuous line) RIBE etch.

The assignation of the different recombination features in the zones without RIBE, where more lines can be resolved, is indicated in figure 7.4. This assignation has been done on the basis of previous studies carried out for similar CdTe samples [9,12,13]. The high energy part of the spectrum, (1.5-1.6) eV, is the sum of several excitonic contributions, particularly three lines narrower than 3 meV peaked at 1.591 eV, 1.595 eV, and 1.598 eV are observed, which are associated with acceptor bound-exciton (A°X), donor bound-exciton (D°X), and near free-exciton (FE) recombination, respectively [9, 12-15].

A high energy shoulder less intense than the exciton is observed at 1.606 eV. This shoulder is related to recombination lines, which is attributed to free carrier recombination and even above barrier donor related recombination due to phonon absorption [16]. The observation of this kind of recombination lines indicates the good optical quality of the as grown CdTe films. The broader line peaked at around 1.579 eV is associated to the 1-LO phonon replica of the free exciton (FE) recombination. The band at 1.560 eV is due to free electron-acceptor (eA°) recombination, whose corresponding phonon replica can be close to the energy of the neutral donor-acceptor (D°A°) transition, giving rise to the observed band peaked at around 1.537 eV [9]. The intense resonance at 1.515 eV is connected to the first phonon replica of the D°A° transition, and the weaker contribution at around 1.493 eV (deconvoluted at the low energy part of the PL spectrum) to a second phonon replica. The most intense PL band at 1.475 eV, together with a low energy PL shoulder, are associated with the carrier recombination through donor-acceptor pairs (DAPs) and its corresponding 1-LO phonon replica. These pairs can be due to the group I residual impurities and their complexes with V_{Cd}, which are common in bulk and epitaxial films of CdTe [9, 13, 17-20].

All the recombination features described above are mostly common for both etched and as- grown CdTe surface. The main differences are the emission intensity and the better definitions of the PL resonances in the zones without RIBE etch. The integrated intensity in the spectral regions of (1.435–1.540) eV (neutral and pair donor acceptor recombination) and (1.540–1.600) eV (FE and bound/free excitonic recombination) increases by factors of 8 and 14, respectively. At the same time, the emission is dominated by donor-acceptor pair recombination in the zones without RIBE, whereas is dominated by eA°-D°A° emission broad band at 1.547 eV in dotted line of figure 7.4 and acceptor bound exciton recombination in the zones with RIBE etch. It is worth noting that eA°-D°A° and also A°XD° X-FE recombination lines cannot be resolved in the experimental spectra for RIBE zones. In this case, two contributions can be deconvoluted by using Gaussian fits at 1.593 and 1.597 eV, the first one mostly due to A°X and the second to D°X-FE [11].

A straightforward question now is the origin of such changes between the PL spectra in both zones of the CdTe surface. The RIBE etch could introduce nitrogen impurities acting as acceptors if they substitute Te atoms [15]. In this case, an increase of the overall PL intensity can be expected if an increase of the acceptor concentration in the same proportion takes place. On the other hand, we cannot resolve eA° and D°A° contributions, as also occurs in the case of D°X and FE transitions. It could imply a simultaneous increase of acceptor and donor impurities. Nevertheless, from these results it cannot be concluded if the donors either were in the sample, but not participating in the recombination, or were introduced by the RIBE process. The time resolved PL (TRPL) experiments, results will support the last hypothesis, as explained below.

Figure 7.5 shows PL transients representative for the free/bound exciton recombination (a) and donor-acceptor pair recombination (b).

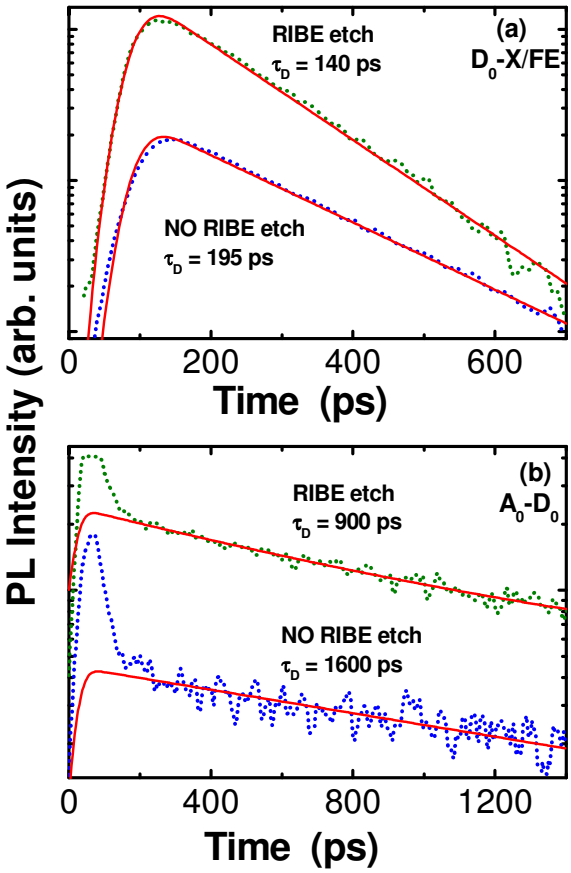

Figure 7.5. PL transients at 10 K under near resonant conditions and low excitation power in the zones with and without RIBE etch representative of the donor-bound-exciton/free-exciton (detection at about 1.596 eV) (a) and donor acceptor pair (b) recombination. Continuous lines are the best exponential fits to the experimental PL transients.

The PL decay time in the zones without RIBE etch is typically longer than that measured in the etched zones. Something similar occurs for lower detection energies (1.447–1.555) eV,

characterizing eA°, D°A°, and donor–acceptor pairs (DAP) recombination processes. Indeed, the PL transients over this broad energy range have a similar aspect to those shown in figure 7.5(b): a fast PL transient over the first 170 ps (rise plus decay), approximately, followed by a slow PL decay, longer for lower detection energies. On the one hand, we associate these slow decays to the impurity related recombination processes. On the other hand, the fast PL transients are very similar to the temporal response of the streak camera to the laser diffusion at the CdTe surface (system response), and it can be attributed to the fast transfer of carriers toward acceptor impurity levels prior to give rise to the different recombination paths observed in figure 7.4. The strong coupling with optical LO phonons in this material (Huang–Rhys factor around 1 or above [20, 21]) would be responsible of that fast carrier transfer and also of the appearance of replica of the main D°A° and DAP recombination channels. The D°A° and DAP recombinations are characterized with larger decay times when the emission energy is lower. Any discontinuity is observed at their corresponding phonon replica. As a matter of fact, the PL decay times are shorter in the zones with RIBE than in the zones without RIBE, diminishing the quantum efficiency. Therefore, we should measure longer decay times in the etched zones. This is due to the relation between radiative, assumed for the moment to be the same at zones with and without RIBE etch, nonradiative and effective decay time.

The effective decay time, τ_D, is described by the following equation:

$$\frac{1}{\tau_D} = \frac{1}{\tau_R} + \frac{1}{\tau_{NR}} \qquad (7.1)$$

where, τ_R is the radiative decay time and τ_{NR}, is the nonradiative decay time.

However, in our particular case and in contrast with this equation, we observe larger decay times in the virgin zones than in those etched. The simplest hypothesis to reconcile continuous wave and time resolved PL results is to assume an increase of the impurity concentration due to the RIBE process by a factor of around 10. Such an assumption would explain, the observed intensity increase in the eA°, D°A°, and DAP bands. In this way, it is possible a simultaneous increase of the PL intensity and a decrease of the non radiative times after the RIBE attack of CdTe. This is just the results shown in figure 7.6, where the dashed line represents the decay time values estimated by using equation (7.1), considering as radiative time the decay times measured in the zones without RIBE etch and using a nonradiative time around 2200 ps. This consideration was made by assuming that the radiative recombination times of the different processes in CdTe after RIBE etch do not significantly depend on the impurity concentration within the studied range.

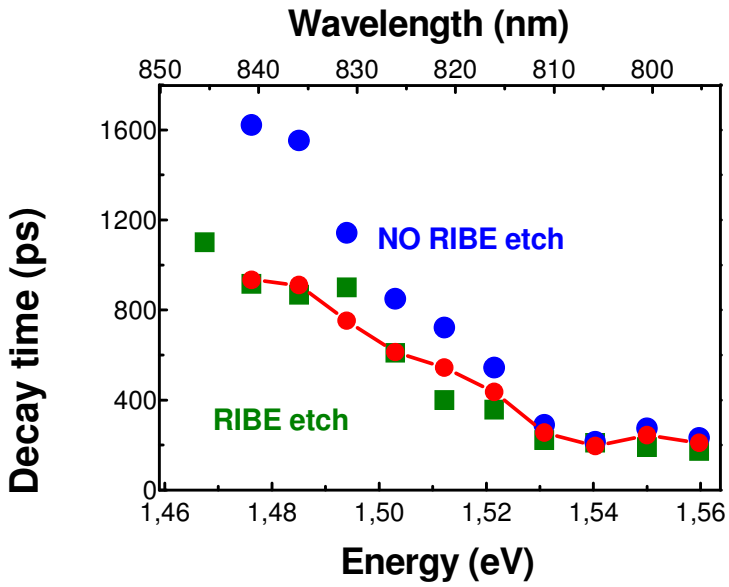

Figure 7.6. Emission energy dependence of the PL decay time in the zones without (circles) and with (squares) RIBE attack. The dotted line corresponds to the estimated decay time. For the estimation the Eq. (7.1) was used.

These results, demonstrate that at optimum conditions, the RIBE etch does not make significant morphological changes but it results in an increase of the concentration of acceptor impurities. This was revealed by an increase of the overall PL intensity and, simultaneously, a decrease of the PL decay time, more important on the low energy side of PL spectrum due to the recombination of carriers in acceptor pairs [11].

7.1.2 Nanostructures growth by etching process

During our etching studies, we could observe the formation of needle-shape like nanostructures when using specific dry etching conditions (for etching time longer than standard).

The following Optical Microscope image for an as– grown sample shows the presence of surface inhomogeneities that appear as a region with dark contrast (figure 7.7).

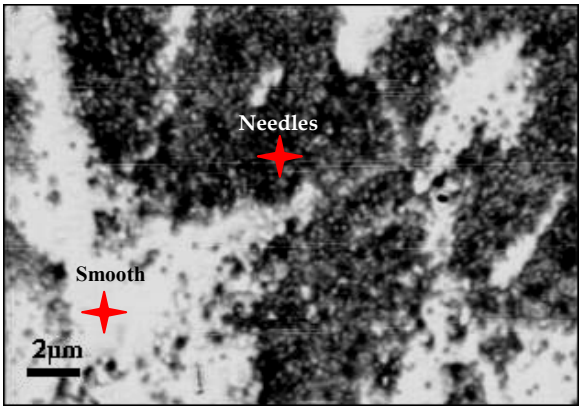

Figure 7.7. Typical optical image of CdTe surface obtained after an etching process.

More information about these microstructural changes in film surfaces can be derived analyzing in detail these dark regions by means SEM (figure 7.8). From this figure, one realizes that the etching layer is mainly constituted by nanocrystalline structures [22].

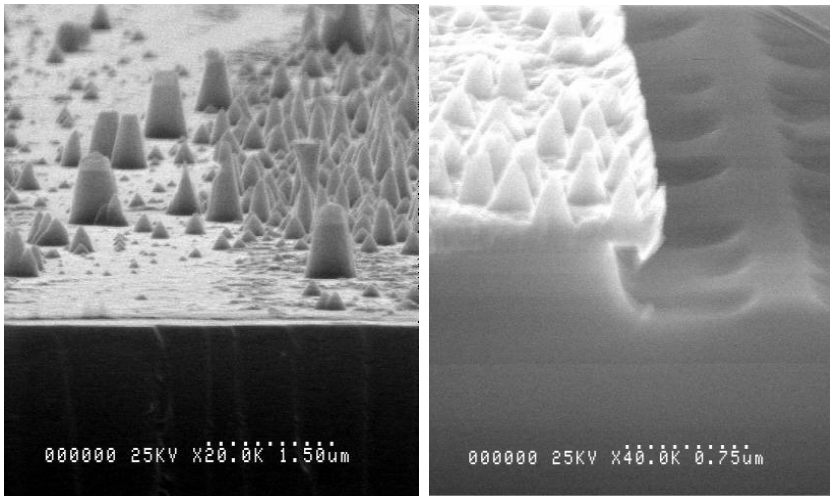

Figure 7.8. SEM images of needle shape like structures obtained after dry etching.

The formation of these needles was favoured with increasing the processing temperature and/or when the stoichiometry of the films differs from that of CdTe. The average needle size was inferred from SEM images to be in the range of ~ 37-74 nm.

It is noteworthy that these CdTe films were used to validate a method for fabricating CdTe buried waveguides for photonic applications. This technology will be detailed in Chapter 8 [23].

It must be taken into account that the (dry) etching was performed in O_2 atmosphere. O_2 usually is used to etch polymers that would otherwise tend to accumulate as a protective coating of carbon on the surface. Therefore, in order to check if the CdTe surfaces are carbon

free or not, Raman Spectroscopy measurements were carried out. A Raman spectrum is shown in figure 7.9.

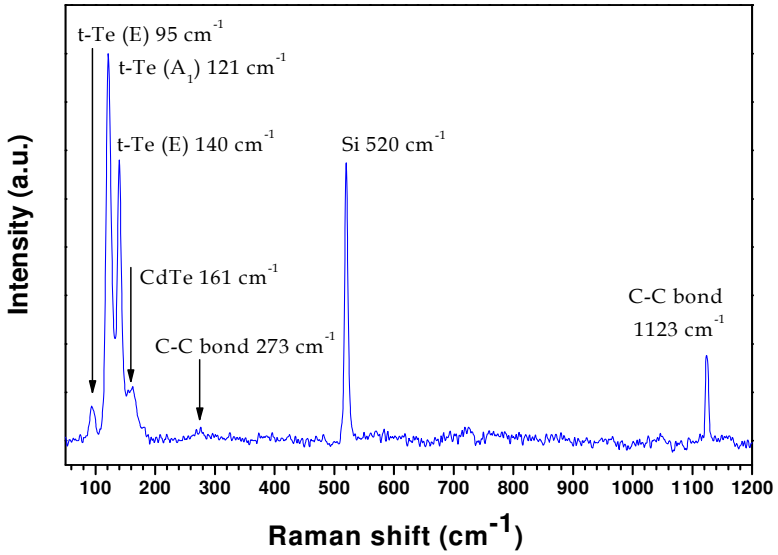

Figure 7.9. Raman spectrum of CdTe films after the etching process.

The most characteristic bands centred at 121 cm^{-1}, and 140 cm^{-1} corresponds to the A_1 and E phonons modes respectively. These Raman modes are attributed to the presence of compressive stress on Te precipitates in CdTe [24]. The weak mode observed around 95(E) cm^{-1} is characteristic of amorphous Te, (characteristic of Te trigonal) and indicates the presence of a trigonal lattice of Te [25]. Likewise, the peak at 141 cm^{-1} and 161 cm^{-1} are identified with transverse optic (TO) and the longitudinal optic (LO) phonons modes, respectively [26-28].

The mode 520 cm^{-1} is associated to Si. Because of its low intensity it can be concluded that [Si] is practically residual. The low frequency mode at 273 cm^{-1} and the high frequency mode 1123 cm^{-1} seem to be modes of C-C bonds which we could associate to the presence of some traces of the resist used during the etching process [25].

With a lower photon energy, a red or NIR laser do not promote the electronic transition (and hence the fluorescence), so the Raman scatter may be far easier to detect. Conversely, as the wavelength, is increased in the visible range, from the green to red, the scattering efficiency decreases, so longer integration times or higher power lasers might be required. For our purposes, a red laser was chosen, but no additional information was obtained.

Therefore, taking into account these considerations and having in mind that the major parts of polymers give rise to Raman spectra with a fluorescence background. Exciting these samples with a green laser (532 nm) may promote this fluorescence, and may swamp any underlay Raman spectra to such extent that it cannot be any longer detectable.

Afterwards, the sample was subjected to thermal treatment at 300 ^{o}C in H_2 atmosphere during 10 min with the purpose to decrease the surface roughness of the layer. Since the roughness would difficult the guidance of light through the sample.

As shown in figure 7.7, no relevant changes in either the morphological structure or in the average needle size are observed after the thermal treatment in both post- RIBE processed annealed and post- processed zones.

Raman spectra were measured by focussing the μ-beam in different regions of the sample. The results evidence that the **planar area** has a Raman spectrum (see figure 7.10a) dominated by Si mode, and has two modes (840 and 915 cm^{-1}) that can be associated to both LA modes of O-O and O-C-O bonds, respectively. This indicates that these bonds are generated in the photoresist layer by O_2 ion during the etching process. If the spectrum is observed without rectifying the base line (figure 7.10b), the base line sharply increases at low frequencies. This fact is indicative of the presence of a high reflectance material, most probably Au, since it was used for SEM inspection [22].

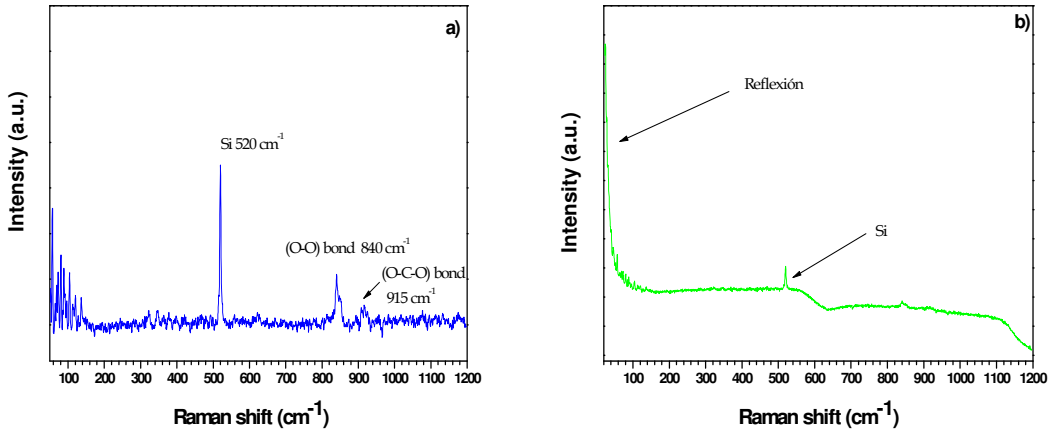

Figure 7.10. Typical Raman spectrum of the planar area of the sample after thermal treatment (a) with (b) without rectification of the base line.

The Dark area of the sample presents a Raman spectrum (figure 7.11) characterized by a dominant peak corresponding to the Te vibrational mode, which indicates a Te excess, due to the Cd evaporation in the surface, during the laser exposition.

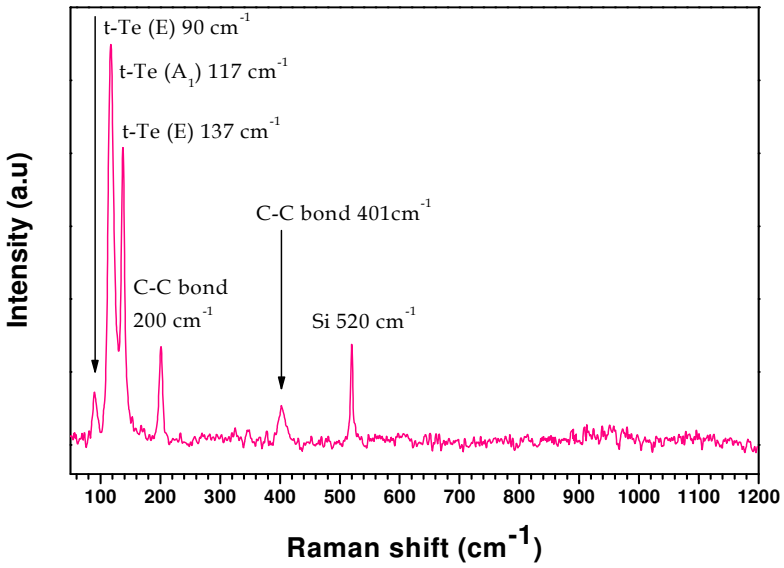

Figure 7.11. Raman spectrum of the dark area for a sample after thermal treatment.

The observation of Te optical modes on the surface has been reported by several authors [29-32]. However the origin of these modes is a subject of controversy. Shin et al. [30] have been attributed them to Te precipitates present as a part of growth process of CdTe. The authors conclude that the Te modes were due to small Te aggregates related with poor stoichiometry and gradually disappear with the increase of Cd contents. In a previous work of M. J. Soares et al. [33] showed by μ-Raman that visible radiation leads to the formation of Te aggregates on the irradiated surface, compromising any conclusion about Te inclusions on CdTe surface, and speculating that heating by laser light could break chemical bond and produce Cd evaporation, thus leaving an excess of Te in the surface. Namely, for excitation power densities to record a Raman spectrum, formation of Te aggregates on the CdTe sample surface only occurs if the excitation is above the gap. These higher temperatures give rise the optical damage, the photo-induced aggregation of Te involves hole [34] or vacancies [35] migration. This idea must be further explored and tested in the lab.

Besides we observe two additional peaks at 200 cm^{-1} and 401 cm^{-1} that according to the literature, are connected with aliphatic change associated with C-C bonds [25].

The differences between post-processed annealed and post-processed samples are shown in figure 7.12. It can be observed that after annealing the peaks are less intense indicating a deterioration of the films.

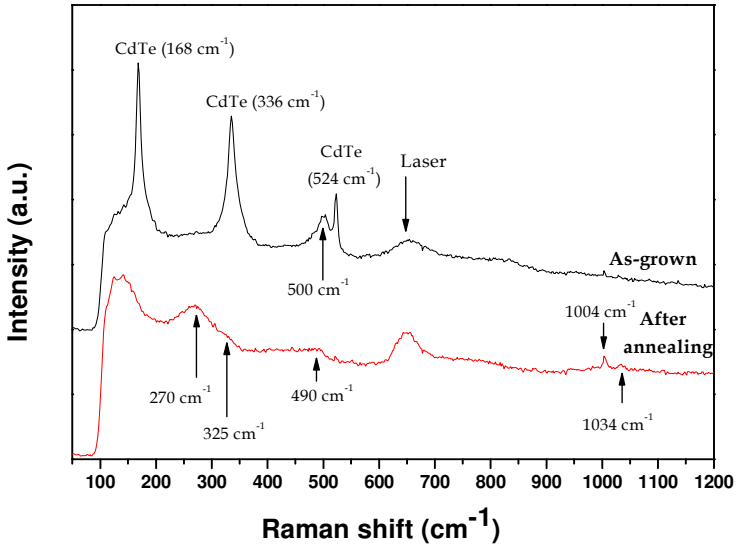

Figure 7.12. Raman spectra of the dark area for the as- grown sample (dark line) and after thermal treatment (red line).

However if now, we use a red laser, the effect observed is quite similar (see figure 7.13).

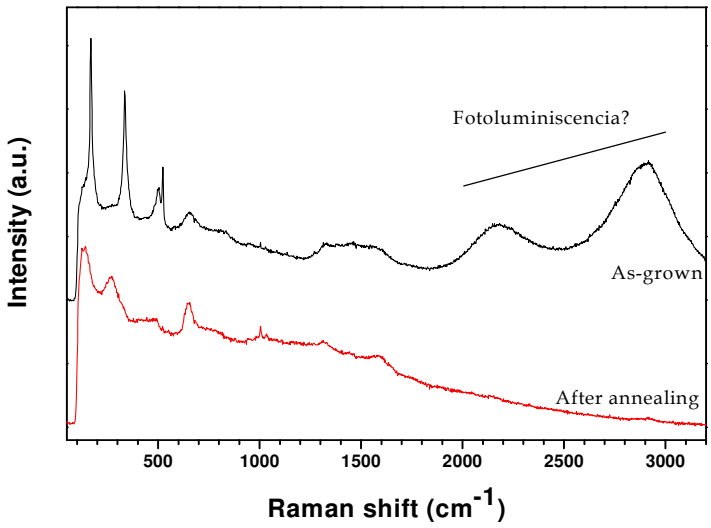

Figure 7.13 Raman spectra of dark area for the as- grown sample (dark line) and after thermal treatment (red line).

The annealed sample, presents again slight asymmetry and a broad peak centred at 161 cm^{-1} as well as, another less intensive and broader peak at 141 cm^{-1}. (These correspond such to LO and 2 LO phonons lines in CdTe, respectively). LO peaks show a red shift of 5 cm^{-1} compared to the CdTe bulk indicating that the film becames to deteriorate. In these two cases studied, it is clear that the peaks in the spectra of annealed samples are less intense than those

observed in samples without annealing. This effect seems caused by the diffusion of additional Te into CdTe films.

7.2 Vapor growth of CdZnTe columnar nanopixels into porous alumina

We have studied the growth of CdZnTe films into nanoporous alumina. The objective of this work is to investigate the formation of Cd(Zn)Te crystalline columnar nanostructures that may be very attractive for the fabrication of micropixels suitable for further development of X- and γ- ray high resolution imaging devices.

7.2.1 Growth procedure

Sochinskii et al. [36] demonstrate the formation of CdTe columnar nano and microstructures by vapour phase epitaxy (VPE) deposition of CdTe on (Ga)InSb layers grown by molecular beam epitaxy on semi- insulating GaAs (1 0 0) substrates. It was found that the In or Ga quantum dots, when they are present on the surface of (Ga)InSb layer, act as nucleation points for CdTe during the VPE process, leading to the formation of CdTe columnar structures.

Previous works also show the use of porous alumina as a template for CdTe columnar growth [37-39]. In our particular case, alumina templates with a porous diameter of 200 nm were purchased from Whatman. Alumina template with other pores sizes between 30 and 80 μm was fabricated at IMM in collaboration with Dra. Marisol Martin. The templates were produced from an aluminium foil (Alfa Aesar, 2.25 cm^2, 0.13 mm thick, 99.9995% purity) by mechanical and electrochemical polishing followed by an anodization process in oxalic acid a temperature of 6 °C.

Then, the Al foil/alumina conductor composite was soaked in a saturated $HgCl_2$ solution to remove the remaining Al from the bottom side and, later, the barrier layer of Al_2O_3 just above the Al was removed by inmersion in a saturated solution of KOH and ethylene glycol. More detailed information is described in [38].

The VPG of CdTe and $Cd_{1-x}Zn_xTe$ into porous alumina was carried out at evaporation temperatures in the range of 600–850 ^oC using binary and ternary sources. The growth sources were made from CZnTe polycrystals and elemental Cd and Zn (5% in weight of the total charge) to control the stoichiometry of the grown material. These conditions allow the CdZnTe nanostructures uniformly grown over the entire alumina area.

7.2.2 Physical properties

7.2.2.1 Structural characterization

A typical cross-sectional SEM image of CdZnTe growth in a porous alumina is depicted in figure 7.14. The image shows sharp and planar surfaces (arrows A and B) and an uniform bulk structure without voids or any other structural defects except those produced by cleaving.

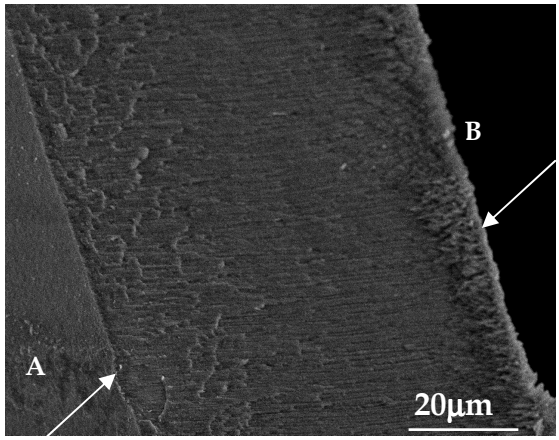

Figure 7.14. Typical SEM cross-section of CdTe grown into porous alumina structure.

The main specificity of the VPG process of CdZnTe using nanoporous alumina, which makes it different from the conventional VPE processes on planar substrates [9,16], is the accumulation of polycrystalline material on the alumina surface turned toward the growth source (arrow B). This is due to differences in the growth kinetics.

The enlarged SEM images of the cross section of CdZnTe in porous alumina structure are shown in figure 7.15 (a) and (b). Figure 7.15a evidences that, some of the porous are monolithically filled with the CdZnTe material (arrow A), while others are filled with CdZnTe dendrite like crystals. This peculiarity, which is better seen on a nano scale (figure 7.15b), suggests that some post growth processing such for example laser assisted recrystallization [8,12,17] or RTA treatment (as it is going to be demonstrate in chapter 8), could be required to improve the crystalline quality of these structures.

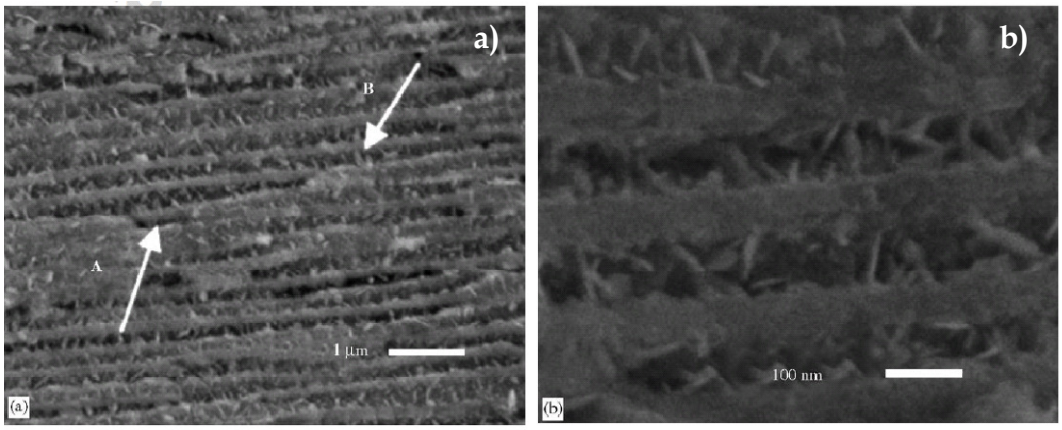

Figure 7.15. SEM images of a cross section of CdZnTe in porous alumina nanoestructure.

The surface morphology for CdZnTe in porous alumina structure is shown in figure 7.16. On a microscale (figure 7.16a), it is seen that CdZnTe columnar nanopixels are grown uniformly into porous alumina all over its area. Moreover, it is observed that by using a template with a regular distribution of porous, the CdZnTe columnar nanopixels could be grown in the form of arrays (arrow A), whereas a random distribution of porous resulted in a random distribution of nanopixels (arrow 2). The nanoscale image of figure 7.16b demonstrates that CdZnTe columnar nanopixels are grown only within the porous, and there are neither lateral growth on the alumina surface nor nanopixel overlap.

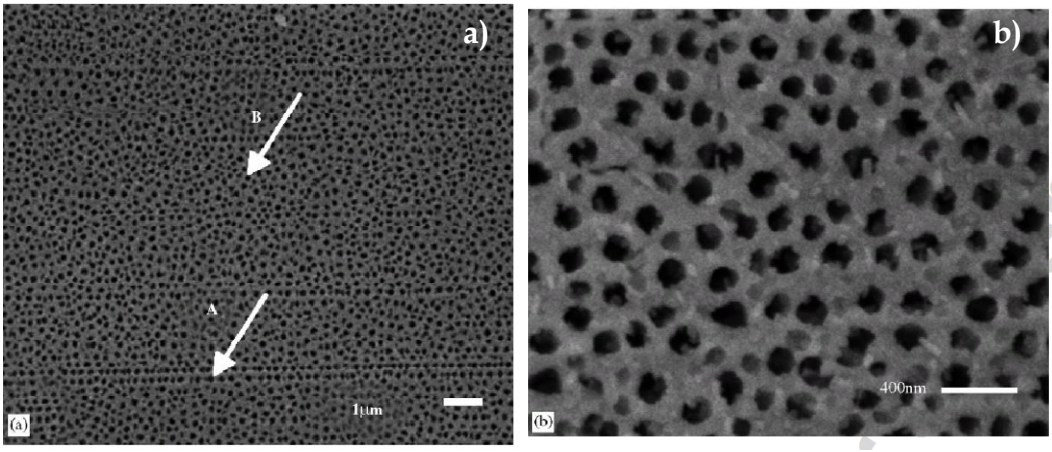

Figure 7.16. SEM images of the surface morphology of CdZnTe columnar nanopixels grown into porous alumina.

7.2.2.2 PL studies

Typical PL spectra of these structures were recorded at 10 K. In general, these spectra exhibit intense PL emission in the (1.2-1.8) eV spectral range, which is typical for CdZnTe crystals and epitaxial layers [2-4,9,40,41] (see figure 7.17). As expected, the spectra have similar

PL bands for CdTe and CdZnTe nanopixels, and there is a shift in the maximum of high- energy edge emission with an increase in Zn concentration. In the (1.2-1.5) eV range, the PL spectra have several well defined bands which indicate the presence of deep recombination levels in the bandgap of CdZnTe nanopixels. These levels have not been identified up to the right moment, but work is in progress. Moreover, a shift in the maximum of high-energy edge emission with increasing Zn concentration is observed.

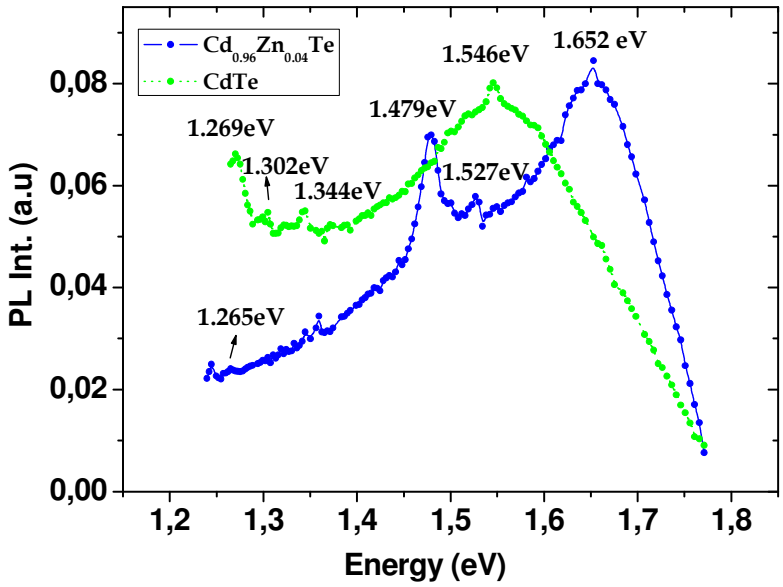

Figure 7.17. Low temperature PL spectra of two samples of CdTe and CdZnTe grown in porous alumina.

It is also worth noting that, as shown by the SEM images (figure 7.14 and 7.15), each sample is highly inhomogeneous and partly made of nanowhiskers with diameters of up to a few tens nm. These nanowhiskers could show a large exciton blue shift with respect to bulk CdTe and CdZnTe, due to quantum confinement effects. It is likely that a different distribution of nanowhisker sizes could account for the different intensity distribution in the PL spectra of CdZnTe in porous alumina structures [42].

7.3 Conclusions

We demonstrate the effect of RIBE process on the PL properties of CdTe/sapphire MOVPE layers. We have found out that at optimum conditions, the RIBE etch does not cause significant morphological changes but it results in an increase of the concentration of acceptor impurities. This was revealed by an increase of the overall PL intensity and, simultaneously, a decrease of the PL decay time, more important on the low energy side of PL spectrum due to

the recombination of carriers in acceptor pairs. Indeed, in order to obtain CdTe- based devices some lithographic process were needed.

By specific dry etching conditions, namely longer that standard, we have observed the formation of needle-shape like nanostructures. The formation of these needles was favoured with increasing the processing temperature and/or when the stoichiometry of the films differs from that of CdTe.

The possibility to form the Cd(Zn)Te in porous alumina nanostructures is demonstrated by VPE. The growth of Cd(Zn)Te columnar nanostructures with PL properties compatible with those of the bulk material and planar epitaxial layers have been demonstrated. The formation of these material structures make very attractive and promising for the development of a new generation of sensor and could serve as a basis for micropixels suitable for further development of X- and γ- ray high resolution imaging devices.

References

[1] A. R. Alija, L. J. Martínez, A. García-Martín, M. L. Dotor, D. Golmayo, P. A. Postigo. Appl. Phys. Lett., **86**, (2005), 141101.

[2] "*Cadmium telluride and related compounds."Chapter VI in the book "Physics and chemistry of II-VI luminescence semiconductors*", N. V. Sochinskii, V. N. Babentsov, and E. Diéguez. Ed. D. R. Vij and N. Singh (NOVA Sci. Publishers, Inc., New York, USA, 1996) pp.248-276.

[3] M. Fiederle, V. Babentsov, J. Franc, A. Fauler, K.W. Benz, R.B.James, E. Cross, J. Cryst. Growth **243,** (2002), 77.

[4] E. Saucedo, C.M. Herrero, L. Fornaro, N.V. Sochinskii, E. Diéguez, J. Cryst. Growth. **275,** (2005), 471.

[5] T.O. Tümer, Sh. Yin, V. Cajipe, H. Flores, J. Mainprize, G.Mawdsley, J.A. Rowlands, M.J. Yaffi, E.E. Gordon, W.J. Hamilton, D. Rhiger, S.O. Kasap, P. Sellin, K.S. Shah, Nucl. Instr. and Meth. A **497,** (2003), 21.

[6] N.N. Kolesnikov, V.V. Kveder, R.B. James, D.N. Borisenko, M.P. Kulakov, Nucl. Instr. and Meth. A **527,** (2004), 73.

[7] W. Li, Z. He, G.F. Knoll, D.K. Wehe, J.E. Berry, Nucl. Instr. andMeth. A **458,** (2001), 518.

[8] N.V. Sochinskii, E. Diéguez, E. Alves, M.F. da Silva, J.C. Soares, S. Bernardi, J. Garrido, F. Agulló -Rueda, Semicond. Sci. Technol. **11**, (1996) ,248.

[9] N. V. Sochinskii, V. Muñoz, V. Bellani, L. Viña, E. Diéguez, E. Alves, M. F. da Silva, J. C. Soares, and S. Bernardi, Appl. Phys. Lett. **70**, (1997), 1314.

[10] J. V. Anguita Estefania. (Private Comunication).

[11] J. Martinez-Pastor, D. Fuster, M. Abellán, J. Anguita, and N. V. Sochinskii. Journal of Applied Physics **103,** (2008), 056108.

[12] P. Fernandez, J.Optoelectron.Adv.Mater.**5**, (2003), 369.

[13] P. Fernández, J. Piqueras, N. V. Sochinskii, V. Muñoz, and S. Bernardi, Appl. Phys. Lett. **71**, (1997), 3096.

[14] J. M. Francou, K. Saminadayar, and J. L. Pautrat, Phys. Rev. B **41**, (1990), 12035.

[15] E. Molva, J. L. Pautrat, K. Saminadayar, G. Milchberg, and N. Magnes,Phys. Rev. B **30**, (1984), 3344.

[16] J. Lee, N. C. Giles, and C. J. Summers, Phys. Rev. B **49**, (1994), 11459.

[17] J. Rams, N. V. Sochinskii, V. Muñoz, and J. M. Cabrera, Appl. Phys. A: Mater. Sci. Process. **71**, (2000), 277.

[18] E. Alves, M. F. da Silva, J. C. Soares, N. V. Sochinskii, and S. Bernardi, Nucl. Instrum. Methods Phys. Res. B **136–138**, (1998), 220.

[19] N. V. Sochinskii, C. Reig, V. Muñoz, and J. Alamo, J. Cryst. Growth. **192**, (1998), 342.

[20] N. D. Vakhnyak, S. G. Krylyuk, Yu. V. Kryuchenko, and I. M. Kupchak, Semicond. Phys., Quantum Electron. Optoelectron. **5**, (2002), 25.

[21] M. Soltani, M. Certier, R. Evrard, and E. Kartheuser, J. Appl. Phys. **78**, (1995), 5626.

[22] M. Abellán, V. Izquierdo-Roca and J. Anguita (In preparation).

[23] M. Abellán and J. Anguita. J.Physic D: (Submitted).

[24] A. S. Pine and G. Dresselhays, Phys. Rev, B, Solid State **4**, No 2, (1971), 356- 371.

[25] Horiba database.

[26] P.M. Amirtharaj and F. H. Pollak, Appl. Phys. Lett. **45**, (1984), 789.

[27] Campos C. E. M, Ersching K , de Lima, J. C , Grandi T. A , Hohn H , Pizani P. S. Journal of alloys and compounds **466** (2008), 80-86.

[28] S. Perkowitz and R.H. Thorland, Phys. Rev. B **9**, (1974), 545.

[29] M. J. Soares and M. C Carmo, in: David L. Andrews (ed.). Raman spectroscopy and Light Scattering Technologies in Material Science, Proc. SPIE **4469**, (2001), 57.

[30] S. H. Shin, J. Bajaj, L.A. Moudy, and D. T. Cheung, Appl. Phys. Lett, **43**, (1983), 68.

[31] P. M. Amirtharaj and F.H. Pollak, App. Phys.Lett **45**, (1984), 789.

[32] A. Picos- Bega, M. Becerril, O. Zelaya, Angel.R. Ramirez Bon, F.J. Espinoza Beltrán, J. Gonzalez Hernandez, S. Jiménez Sandoval, and B. Chao, J. App. Phys **83**, (1998), 760.

[33] M.J. Soares, J.C. Lopes, M.C. Carmo, and A. Neves. Phys. Stat. sol. (c)**1**, No.2, (2004), 278-280 (2004). Micro- Raman study of laser damage in CdTe.

[34] R. J. Nemanich, D.L. biedgelsen, R. A. Street, and L. E. Fennell, Phys. Rev. B **29**, (1984), 6005.

[35] S. Sugai, Jpn. J. Appl. Phys. **30**, (1991), L1083.

[36] N.V. Sochinskii, J.P. Silveira, F. Briones, E. Saucedo, C.M. Herrero, Fornaro, V. Bermúdez, E. Diéguez, J. Cryst. Growth. **275,** (2005) ,131.

[37] M.S. Martín-González, A.L. Prieto, R. Gronsky, T. Sands, A.M. Stacy, Adv. Mater. **15**, (2003), 2003.

[38] M.S. Martín-González, G.J. Snyder, A.L. Prieto, R. Gronsky, T. and, A.M. Stacy, Nano Letters **3**, (2003), 973.

[39] A.L. Prieto, M.S. Sander, M.S. Martín-González, R.Gronsky, T. Sands, A.M. Stacy, J. Am. Chem. Soc. **123,** (2001), 7160.

[40] E. Saucedo, V. Corregidor, L. Fornaro, N.V. Sochinskii, J. Silveira, E. Die´guez, Eur. J. Phys.: Appl. Phys. **27**, (2004), 207.

[41] E. Saucedo, L. Fornaro, N.V. Sochinskii, A. Cunña, V. Corregidor, D. Granados, E. Diéguez, IEEE Trans. Nucl. Sci. NS-**51,** (2004) ,3105.

[42] N.V. Sochinskii, M. Abellán, M. Martín Gonzalez, E. Saucedo, E. Diéguez, F. Briones. Nuclear Instruments and Methods in Physics Research A **568,** (2006), 455–458

Chapter 8

CdTe- and Cd(Zn)Te- based waveguides: Development of fabrication methods

Chapter 8

CdTe-AND Cd(Zn)Te- BASED WAVEGUIDES: DEVELOPMENT OF FABRICATION METHODS

In this chapter we report on theoretical and experimental results on the use of CdTe and Cd(Zn)Te as core materials for the development of all- optical photonic devices. We include the design of optical waveguides for strong field confinement, the technological processes of fabrication and optical characterization of optical waveguides based on CdTe and Cd(Zn)Te.

The idea of using (CdTe compounds) Cd(Zn)Te as optical material for implementation of highly dense all- optical photonic integrated circuits is intended to overcome the limitations in terms of nonlinear interaction that occurs in Si (mainly, the high values of two-photon absorption (TPA) and the induced free-carried absorption) whilst preserving the main advantages of the Silicon-on-insulator, SOI- based photonic technology: high index contrast (small size of the photonic components) and manufacturability with CMOS tools and process (which ensures large scale fabrication and low cost of manufacturing).

8.1 Introduction

Cd(Zn)Te exhibits an interesting optical behaviour at wavelengths around 1.55 μm (third optical communications window): a high index of refraction (n = 2.74), which allows a strong confinement inside the material; a high Kerr coefficient (n_2 = 5.23x10^{-13} cm^2/W [1]), and low TPA, that is theoretically negligible if the material is properly doped with Zn. Thus, it seems feasible to use thin CdTe films grown on a low-index substrate (in the same way that it is done with SOI, photonics [2]) to create highly compact all- optical devices with a nonlinear performance better than that provided by Si. In fact, the optical properties of CdTe are similar to those of GaAs compounds, with the advantage that it could be expected that CdTe film could be processed in an intermediate step of a CMOS manufacturing line, as it is the case of SOI- based photonics.

In this chapter, some results on the use of Cd(Zn)Te as core material for the development of all- optical photonic devices are reported, including the design of waveguides for strong field confinement, technological processes to grow Cd(Zn)Te on large wafers (suitable for high-

volume manufacturing) and the fabrication and optical characterization of optical waveguides with a CdTe core.

8. 2 Optical properties of Cd(Zn)Te

8.2.1 Linear optical properties

As mentioned in previous chapters, the optical properties of CdTe make it transparent in the infrared: from close to its bandgap energy 1.56 eV (795 nm) up to wavelengths larger than 20 μm. At optical communication wavelengths, λ = 1550 nm, the refractive index is n=2.74 [3]. The refractive index as well as, the absorption, **k**, of CdTe as a function of the photon energy [4,5] is shown in figure 8.1. Absorption can be considered negligible at the chosen wavelength of 1550 nm.

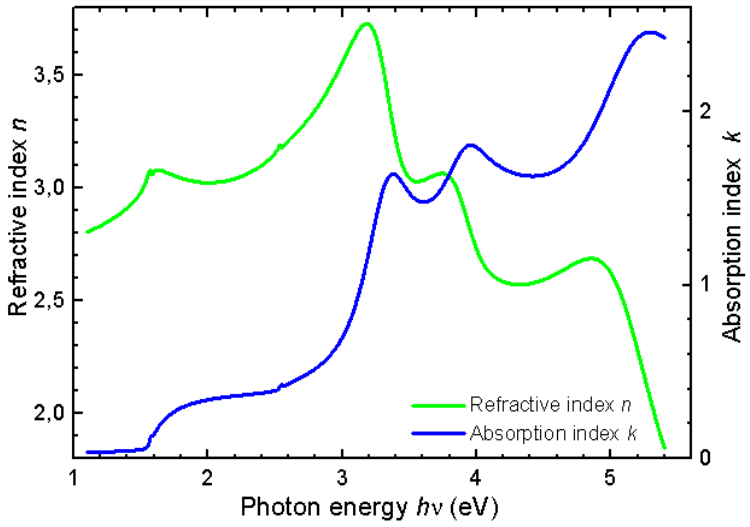

Figure 8.1. Refractive index (green line), **(n)** and, absorption (blue line) **(k)** as a function of the photon energy in eV, (extracted from [5]).

In order to implement all- optical photonic circuits at optical communication wavelengths, it is important to avoid undesired TPA as much as possible. One possible way to do this is doping CdTe with Zn, whose bandgap energy is E_g=2.30 eV in the same way that GaAs is doped with Aluminum (Al) to reach the same objective. The aim is to introduce a certain percentage of Zn so that the gap energy of the compound is shifted upwards beyond 1.6 eV. This issue is addressed in the next section. However, it is noteworthy that the insertion of Zn does not appreciably modify the linear response of the $Cd_{1-x}Zn_xTe$, since the linear refractive index of ZnTe is also 2.73 at 1550 nm [6].

8.2.2 Nonlinear optical properties

For the realization of high speed all- optical devices, nonlinear materials with high values of the nonlinear Kerr effect, in addition to negligible linear and nonlinear absorption, are required. The optical Kerr effect, or AC Kerr effect, is an instantaneous nonlinear effect that produces a variation in the refractive index of the materials proportional to the optical intensity (or square of the electric field). This effect permits the control of light with light, which makes possible the implementation of all- optical devices. In comparison, another effect that permits the control of light with light, free carrier refraction induced by TPA [7], is slower than the Kerr effect, with response times of the order of nanoseconds (ns). Therefore it is not suitable for ultrafast applications.

The variation of the material refractive index, **Δn,** is proportional to the optical intensity ,**I,** by a factor known as Kerr coefficient or nonlinear refractive index, $\mathbf{n_2}$, so that $\mathbf{\Delta n = n_2 I}$. For direct bandgap semiconductors, the nonlinear refractive index can be expressed as:

$$n_2(esu) = K' \frac{\sqrt{E_p}}{n_0 E_g^4} G_2(\hbar\omega / E_g) \qquad (8.1)$$

where, $\mathbf{K'}$=3.4x10^{-8}, $\mathbf{E_p}$=21 eV is practically constant for a wide variety of direct gap semiconductors. Energies are in eV and n_2 in cm^2/W, and $\mathbf{G_2}$ is a universal function [8]. In the same approximation the (degenerate) TPA coefficient **β** is given by:

$$\beta = \frac{K\sqrt{E_p} F(2\hbar\omega / E_g)}{n_0^2 E_g^3} \qquad (8.2)$$

where K= 3.1x10^3 (empirical), **F** is another universal function [9], (of the ratio of the photon energy ħω and E_g).

These expressions model quite well the behaviour of the nonlinear refractive index and absorption coefficient. Theoretically, the TPA absorption becomes zero at frequencies below $E_g/2$. This would also make negligible the slow modulation of the refractive index owing to the creation of free carriers. Therefore, since we are looking for all- optical applications at 1550 nm the objective is to introduce a percentage x of Zn in the $Cd_{1-x}Zn_xTe$ such that the resulting E_g > 1.6 eV. If a linear variation of E_g with x is assumed this condition would be fulfilled at x_{min} = 0.06. Hence, this is the minimum percentage of Zn that has to be include to avoid TPA.

However, this will also produce a variation in the value of the nonlinear refractive index. For instance, figure 8.2 depicts the nonlinear index obtained from equation (8.1) for CdTe, $Cd_{0.8}Zn_{0.2}Te$ and ZnTe as a function of the wavelength.

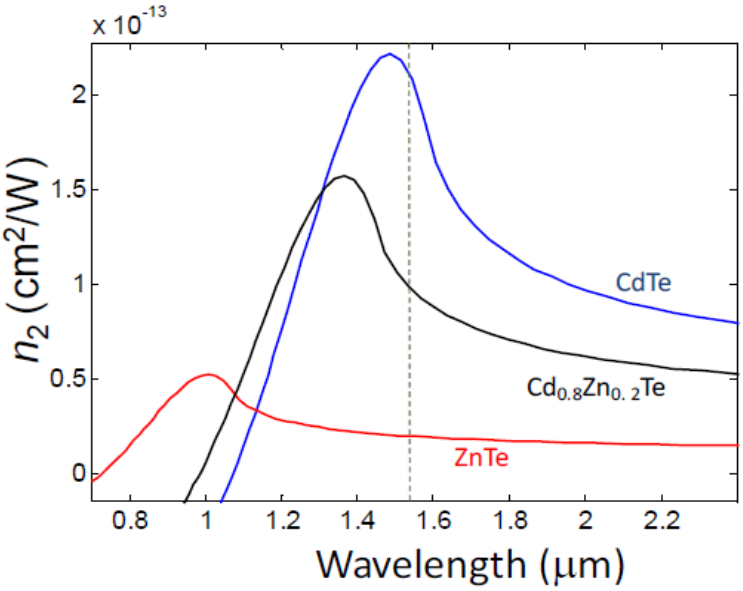

Figure 8.2. Theoretical nonlinear refractive index (**n_2**), as a function of the photon energy in eV from equation (8.1).

Since the working region is 1550 nm, as shown by the vertical dashed line in figure 8.2, it can be appreciated that avoiding TPA has the negative effect of a reduction of the value of n_2. For CdTe at 1550 nm, we obtain $n_2 = 2.8 \times 10^{-13}$ cm²/W, which is about half of the experimental value $n_2 = 5.23 \times 10^{-13}$ cm²/W recently reported in [1]. In addition β=1.5 cm/GW, is very close to the value of 1.8 cm/GW measured in [1].

Despite of the fact that equations (8.1) and (8.2) are quite simplistic models and that the measured values in [1] could have some inaccuracies owing to the use of experimental setup, it can be seen that there is a close agreement between theoretical and experimental results. The value of the nonlinear index is reduced to $n_2 = 1 \times 10^{-13}$ cm²/W when x=0.2. However, no TPA should be present in this case. If we consider the figure of merit $F = n_2/\beta\lambda$, commonly used when studying nonlinear optical properties of semiconductors, it is easy to see that ideally a zero TPA would result in an infinite figure of merit. Anyway, all these theoretical results should be verified by measuring the nonlinear properties in real samples. However, it can be stated that Cd(Zn)Te displays a nonlinear optical behaviour similar to that of AlGaAs, with the additional benefit that the CdTe technology could become, at least in some processes, compatible with CMOS technology.

8.2.3 Cd(Zn)Te optical waveguides

It has been shown that Cd(Zn)Te displays a large refractive index (n = 2.74). Moreover, the compound can be tailored to avoid TPA at such wavelengths whilst having a quite large value of the Kerr coefficient. However, the value of n_2 is still very small and very long distances would be required to achieve appreciable effects. For instance, a nonlinear phase shift of $\boldsymbol{\pi}$ radians that could be used to implement all-optical switch using a Mach- Zehnder interferometer. A very interesting choice to strengthen the nonlinear interaction between the optical field and the nonlinear material is the use of waveguides designed to have a strong confinement of the optical field in the nonlinear core [7], which can be achieved in our particular case owing to the high index of refraction. In our approach, Cd(Zn)Te is growth on large area SOI silica substrates in order to be compatible with CMOS processes (as it is done in Si photonics). Thus, a first choice to create waveguides with strong field confinement is the use of strip (or channel) waveguides consisting of a rectangular Cd(Zn)Te core surrounded by low index claddings. In our analysis we consider that the cladding is SiO_x, which could be achieved by depositing SiO_x on the top of the fabricated waveguides after being etched, as it is done with Si strip (or channel) waveguides. We analyzed this waveguide by means of the Beam Propagation Method (BPM). Two polarizations were considered: TE- like (Transversal Electric, E field mainly in the horizontal direction) and TM- like (Transversal Magnetic, E field mainly in the vertical direction). The rectangular core has a width, **w,** and a height (thickness) **h**. The values of **w** and **h** have to be properly selected to ensure single mode propagation as well as, a strong confinement of the field in the nonlinear Cd(Zn)Te core. The single mode region for both the Cd(Zn)Te strip waveguide was obtained and is depicted in figure 8.3. It should be emphasized that waveguides should work in the single mode region to ensure a proper performance in all- optical devices. As rule, it can be stated that w + h < 900 nm to ensure single mode performance.

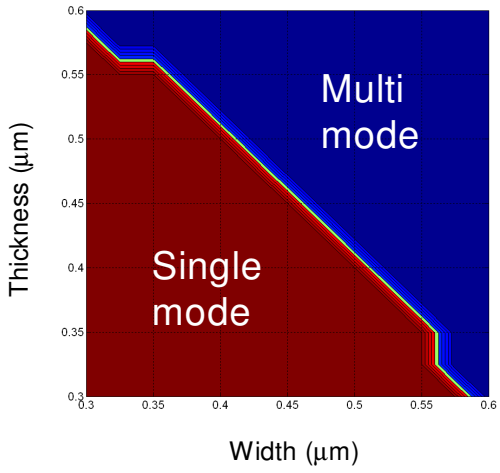

Figure 8.3. Single- and multimode region for the symmetric Cd(Zn)Te strip waveguide.

The electric field profiles for the TE- like polarisation and two different sizes of the waveguide core: (a) thickness of 500 nm, width of 300 nm; (b) thickness of 300 nm, width of 500 nm are shown in figure 8.4. These dimensions are chosen to observe field distributions for the cases **w > t** and **w < t**. Red and blue color stands for high and, amplitude of the field, respectively in all the field profiles obtained with BPM. If the figures were rotated 90º, then they would depict the profiles for the TM- like polarisation. It can be observed that the field is well confined in the core, mainly for the case of the waveguide in figure 8.4b. Since the electric field is mainly oriented in the horizontal direction, there are discontinuities at the lateral sidewalls (for the case of TM- like polarisation these discontinuities would occur at the upper and lower boundaries of the core).

For nonlinear applications, propagation losses owing to etching-induced roughness (main source of losses in high index contrast waveguides) at the lateral sidewalls should be minimised. Since the amount of roughness losses is proportional to the rough area, thinner cores with t < w are preferred. In addition, a high confinement of the electric field in the nonlinear core is required. Thus, the optimum choice in terms of use in all-optical applications would be the case depicted in figure 8.4b: TE-polarized optical field in a core with **t < w**.

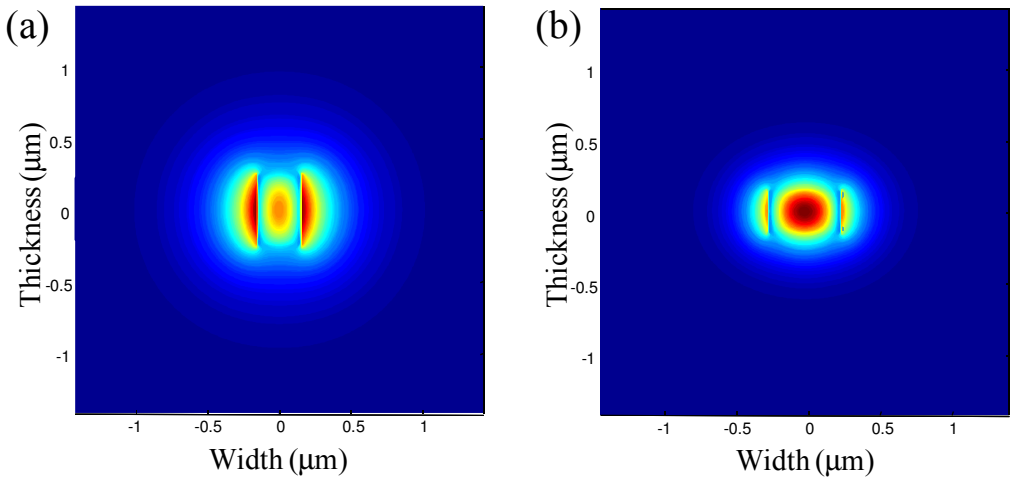

Figure 8.4. Transverse field profile of a symmetric CdZnTe strip waveguide for TE-like polarization: (a) thickness of 500 nm, width of 300 nm; (b) thickness of 300 nm, width of 500 nm. The profiles for TM-like polarization can be obtained by rotating 90º the plots.

A typical parameter used to model nonlinear interaction in optical waveguides is the effective area, $\mathbf{A_{eff}}$, which relates the optical intensity with the optical power, **P,** is:

$$I = \frac{P}{A_{eff}} \qquad (8.3)$$

In a waveguiding structure that includes a nonlinear core [10], the effective area can be calculated as follows:

$$A_{eff} = \frac{\left(\int_{-\infty}^{+\infty} \int |F(x,y)|^2 \, dxdy \right)^2}{\int_{-NLR}^{+NLR} \int |F(x,y)|^4 \, dxdy} \qquad (8.4)$$

where **F(x,y)** is the field profile of the waveguide mode and NLR corresponds to the nonlinear region.

The effective area must be minimized for a maximum efficiency of the nonlinear effect for a given input power. Therefore, the optimum waveguide parameters for nonlinear applications are those that yield a minimum effective area. In the optimization process we assume that the non linearity induced on the CdZnTe material does not depend on the field polarization. Additionally, we must ensure that the dimensions that minimize the effective area accomplish the single mode condition in figure 8.2. Under these assumptions we obtained that a minimum value about A_{eff} = 0.35 μm² is obtained for **h** between 300 – 380 nm and t between 500 - 550 nm. Our values are close to that obtained using the results reported in [11], where it is stated that the maximum effective nonlinearity for a specific core shape occurs always for nearly the same area in all cases. For a given wavelength, the maximum effective nonlinearity occurs for a height to width ratio of 1.4:1 and the field polarized along the long axis. For the case of our Cd(Zn)Te strip waveguide, the optimum area of the core is w x h = 0.2 μm². A relationship of 1.4:1 provides the optimum dimensions of the rectangular core for a wavelength of 1550 nm where longer side is 531 nm and, shorter side is 379 nm.

The technological processes needed to fabricated the Cd(Zn)Te strip waveguide include: a) growth of Cd(Zn)Te material (with the proper percentage of Zn) and a certain thickness (t) on a SiO_x substrate with a sufficient thickness to avoid leakage into the bottom Si layer; (b) etching of the Cd(Zn)Te material to form waveguides of width , **w**; (c) deposition of an upper SiO_x cladding. Step (b) has a clear technological difficulty, since the etching of such a small Cd(Zn)Te waveguides has not been reported so far (see our attempts in following sections). In addition, the etching process must be quite accurate in order to ensure low propagation losses. Using the results in [12], it can be derived that a mean roughness below 10 nm is mandatory in order to keep propagation losses below 20 dB/cm for the optimum waveguides dimensions and TE-like polarization. Such a small roughness is a quite challenging value taking into account the current state of the art in Cd(Zn)Te etching and optical waveguides using this material as core,

CdTe-based waveguides have not been reported so far. Thus, it makes sense to consider an alternative Cd(Zn)Te waveguide as that depicted in figure 8.5. It consists of a Cd(Zn)Te layer loaded by a strip of SiO_x. Thus, it is called strip-loaded Cd(Zn)Te waveguide. The top strip can also be fabricated by depositing silicon nitride, Si_3N_4, (n = 2) instead of SiO_x on the top of the Cd(Zn)Te layer.

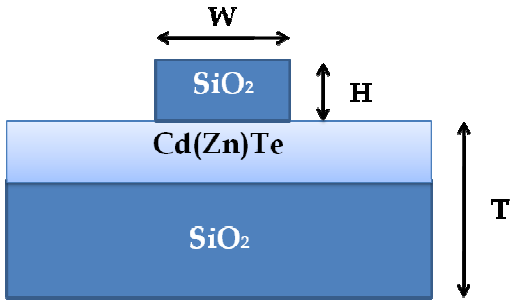

Figure 8.5. Cross-sectional view of the proposed alternative strip loaded CdZnTe waveguides.

From a fabrication point of view, this structure is much easier to build, since there is no requirement to etch the CdTe layer, the roughness of the dielectric is less critical and it is known that SiO_x and Si_3N_4 can be smoothly etched by dry or wet etching. Thus the expected sidewall roughness is expected to be very low and propagation losses below 10 dB/cm can be achieved. Additionally the horizontal contrast of the material properties of the waveguide is not so high as in the dielectric, so the fundamental mode is expected to be less sensitive to the roughness at the expense of having a smaller confinement. This implies smaller sensitivity to nonlinear effects and the requirement of higher overall dimensions (for example, large curvature radius to avoid high bend losses) of the devices implemented using this waveguide. The electric field profile of the fundamental mode is depicted in figure 8.6 for both polarisations. As in the case of the strip waveguide, it can be seen that higher confinement is obtained for TE- polarization (horizontal electric field).

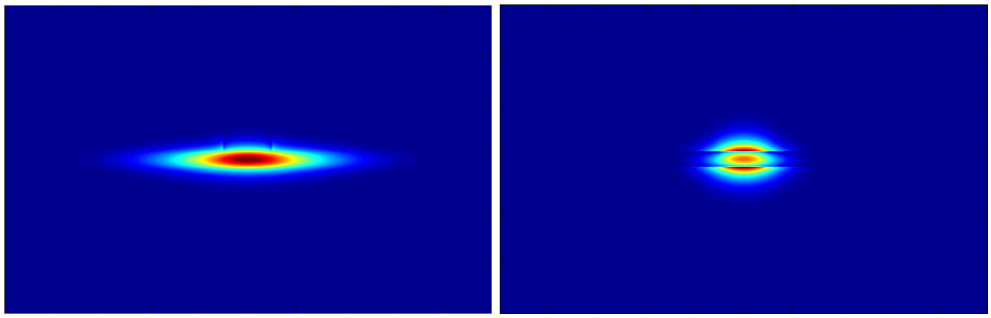

Figure 8.6. Transverse profiles of the alternative waveguide for the TE-like (left side) and TM-like (right side) fundamental modes respectively.

The waveguide dimensions can be optimised in order to reduce the effective area of the fundamental mode. In principle, since the confinement is not strong in the horizontal dimension

and the etching of the SiO_x is expected to be of small roughness, minimum propagation loss will not be considered as a useful criterion to optimise the waveguide dimensions. The tighter the confinement of power in the Cd(Zn)Te slab is, the more sensitivity to the nonlinear effects will be achieved. This optimisation has been carried out by using BPM. It has been observed that the effective area scarcely depends on the dimensions of the top strip load. Since a minimum effective area maximises nonlinear effects, the optimum dimensions for each polarisation will be: T = 300 nm for TE and T = 450 nm for TM. The minimisation of the effective area for the TM polarisation occurs in a region where the waveguide is multimode. Since in the single-mode region TE polarisation provides smaller effective areas, we think this is more suitable than the TM polarisation for the implementation of the final device. BPM simulations, was made at NTC laboratories in collaboration with Dr. Francisco Cuesta, and shows that the effective area for a H = 0.2 μm thick and W = 1 μm wide Si_3N_4 strip-loaded Cd(Zn)Te waveguide (T = 0.3 μm) TE polarisation the effective area is 0.82 μm^2. Then, for the waveguide with a 300 nm layer of CdZnTe and a Si_3N_4 strip of 1 μm x 0.2 μm and for the TE polarization we obtain a very small effective area and low propagation losses. Moreover, a straightforward coupling to an external optical fibre is achieved, in comparison with the previously designed strip waveguide.

8.3 Development of CdTe- based waveguides

As the three logical phases: materials, waveguides and validation device which are undertaken in this chapter. In this section efforts have been put on waveguides fabrication process.

For the development of the CdTe waveguides, the first step was the growth of $CdTe/SiO_2$ and $CdZnTe/SiO_2$ high quality films by VPE technique. We have demonstrated the viability to obtain CdTe compounds with relatively good quality crystalline in large areas [13].

Then, we report different methods to fabricate waveguides. The fabrication of waveguides based on CdTe requires the use of (efficient) high-resolution lithography techniques such as electron beam lithography (EBL) and dry etching techniques, which provides a controllable fabrication process [2,14].

By using these methods, waveguides between 300- 500 nm can be reproducibly fabricated and the control of all fabrication parameters is relatively easy to achieve. However, this was accomplished using special conditions such a very small size e- beam and a very precise alignment system.

For this study, CdTe (500 nm)/SiO_2 (3.9 μm)/Si samples were used and, for all waveguide fabrication processes we begin cleaning the substrate with an O_2 plasma. Finally, the polymethylmethacrylate (PMMA, C_7H_8O, C_6H_5-O-CH_3) is used as a high-resolution positive resist for EBL application [14,15].

A very uniform PMMA (a solution of 9% 950 K PMMA in anisole) layer with a thickness of 13000 Å, was spin-coated at 4500 rpm on the sample surface and subsequently annealed at 170 ºC for 75 min in a convection oven [16]. (Note that the value and the stability of the temperature are very important to obtain reproducible results). Afterwards, the waveguide were fabricated by an EBL system at IMM, which has a resolution of approximately 10 nm. The lithography process depends principally on parameters like the intensity of the electron beam current, the intrinsic parameters of the design, the exposition time, and the focus on the sample. All these parameters are calibrated to obtain the values that yield a reproducible lithography process.

In our case, and due to the size of the motives, small variations in the focus can cause alterations in the waveguide size. We worked with stripe arrays of 500 nm in 2 μm of period in working areas of (100x 100) μm^2 and (300x 300) μm^2. To achieve these patterns with our E-beam equipment, we determined that the optimal dose should be 250 $\mu As/cm^2$, the exposures were carried out at 25 KeV electron beam energy and the beam current was 80 μA.

During the exposition, the chemical properties of the resist are locally modified, however this allows to selectively removing either the exposed or the non- exposed parts submerging the sample into a chemical agent known as developer. In our case, the developer is made of Methyl isobutyl ketone (MIBK) diluted with IPA. In order to obtain the largest resolution, the proportion was chosen to be MIBK: IPA, 1:3. Thus, the sample is submerged for 2 min in developer and, afterwards, rinsed with IPA for 40s and dried with Nitrogen. Figure 8.7 shows a PMMA strip of 500 nm fabricated by EBL [17-22].

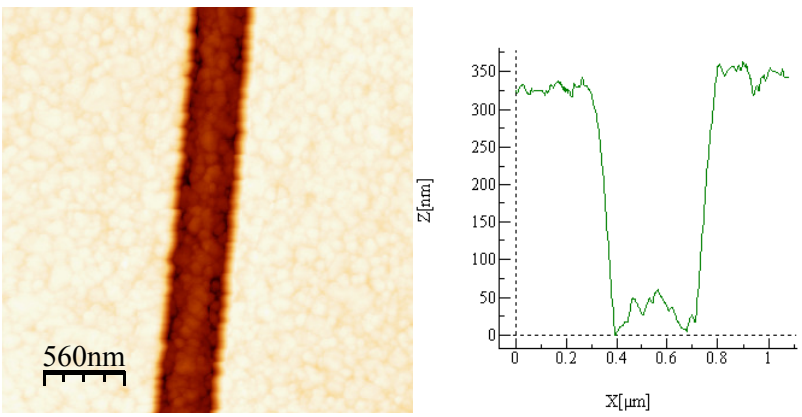

Figure 8.7. AFM images of CdTe waveguides after EBL process.

Both RIBE and RIE, used for patterned etching, require a mask to protect the portions that are not to be etched. The etching quality in most patterned etching application is limited by the mask, rather than the etching process itself.

Ideally, a masking material should have significantly lower etch rate in comparison to the target material. However, the resist etch rate normally is comparable to many target materials. Based on this fact, we use PMMA as mask for the CdTe film.

Following this process, the pattern was transferred by RIBE etching and CH_4/H_2 + N_2 gases mixture [23] were used. The etching time depends on the reactive ion current which was produced by the plasma. This current was measured with a Faraday cup situated in front of the sample. The CdTe etch factor connects the ion current density measure to the etch thickness in a period of time. Then, to obtain the etch factor for CdTe we have to measure the etch thickness and divide by the theoretical thickness. Finally, the etch thickness can be obtained multiplying the average of reactive ions current by the total etch time. If we take into account these values, the etch rate was calculated by the equation: $v_a = k \cdot \overline{J_{cup}}$ where, *k* is the etch factor and $\overline{J_{cup}}$ is the average of ions current density.

In our case the etching was performed using an electron cyclotron resonance reactive ion etching system, Tepla RIB-ETCH 160 ECR system reactor, in a CH_4/H_2 (15% of CH_4 in the mixture) + N_2 (nitrogen is added to get stable ECR plasma discharges) plasma atmosphere. The etch characteristics are strongly affected by the ion energy (beam voltage and microwave energy). The ECR source is excited by a 2.45 GHz microwave power supply and the magnetic field is steered by an electromagnet.

The standard etch condition used in our studies were at room temperature, 400 eV of beam energy, 975 G ECR magnet, 300 microwave power, ~ 10^{-4} mbar of pressure, -450 acceleration voltage, and CH_4/H_2 flow: 14 sccm; N_2 flow: 6 sccm for 48 min [24]. Due to the high thickness in comparison with the etch speed that we obtain with this mixture of gases, we have to carry out the process in two steps. For this, a Current density of the beam ($\mathbf{J_{cup}}$) about 251 μA/cm², was used. This leads to an etch rate of 14 nm/min for PMMA resist, and 3.3 nm/min for CdTe film, and the total reduction of the layer thickness was about 160 nm. Argon can also be used instead of N_2 to get stable ECR plasma but its use can increase roughness due to the possible different Cd and Te sputtering yields [25,26]. Some of these parameters were varied but these standard conditions represent the optimal process. Etch depth was determined by perfylometer measurements. Perfylometer has been used to study the etched profile and the roughness respectively.

PMMA's remainings in the surface of the sample were found. Therefore, we have to rinse the sample in warm acetone for 10 min, followed by subsequent rinses in acetone, methanol and IPA and dry with nitrogen. Nevertheless, organics remains still in surface of the sample. Hence, a O_2 plasma is used to eliminate them completely.

On one hand, the clean process is very important due to the presence of resist' remaining that maintains the samples dirty. This might lead to imperfections on the transferred structures. On the other hand, ion bombardment usually results in some degree of damage to resist, making it harder to remove by standard procedures. Alternatively, the amount of damage, and therefore the difficulty of removal after etching, can be reduced by diminishing the ion energy.

Finally, the surface morphology was studied by SEM and AFM. For instance, figure 8.8 shows an example of PMMA A9 stripes perfectly cleaned after the fabrication process.

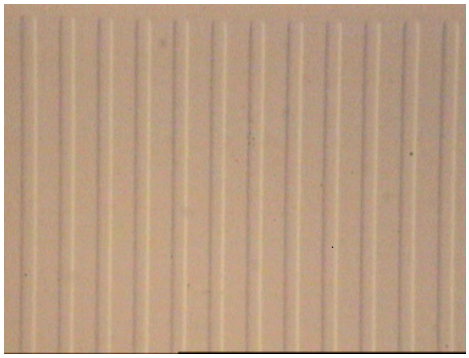

Figure 8.8. Typical optical images of waveguides fabricated by PMMA A9.

However, AFM images of the figure 8.9 shows some problems which appeared during the cleaning process. These problems give rise mainly as consequence of the inhomogeneous etching performed in roughness structures.

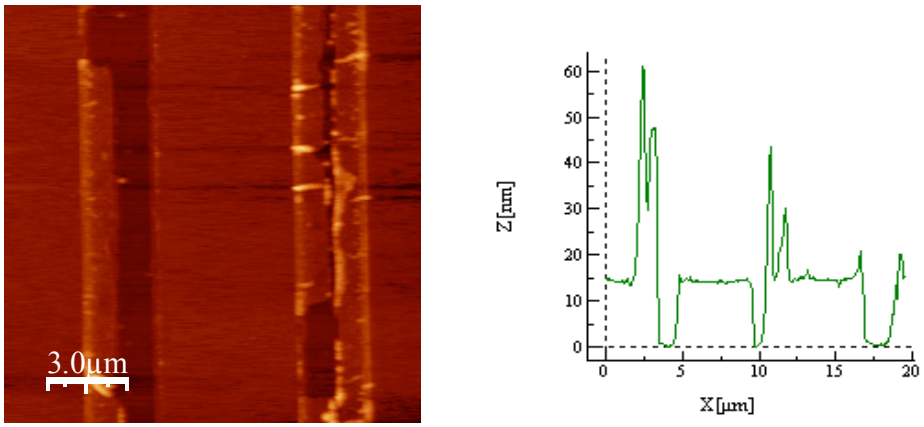

Figure 8.9. AFM images of CdTe waveguides after RIBE attack and lift-off process.

The **main drawback** of CdTe submicron structures made by the combination of EBL and RIBE process is the **large roughness at the edges of the CdTe structure, due to the use of a**

single PMMA layer. In the following AFM images (figures 8.10 a, b, c and d) we can observe the difference in CdTe surface roughness before and after the etching process:

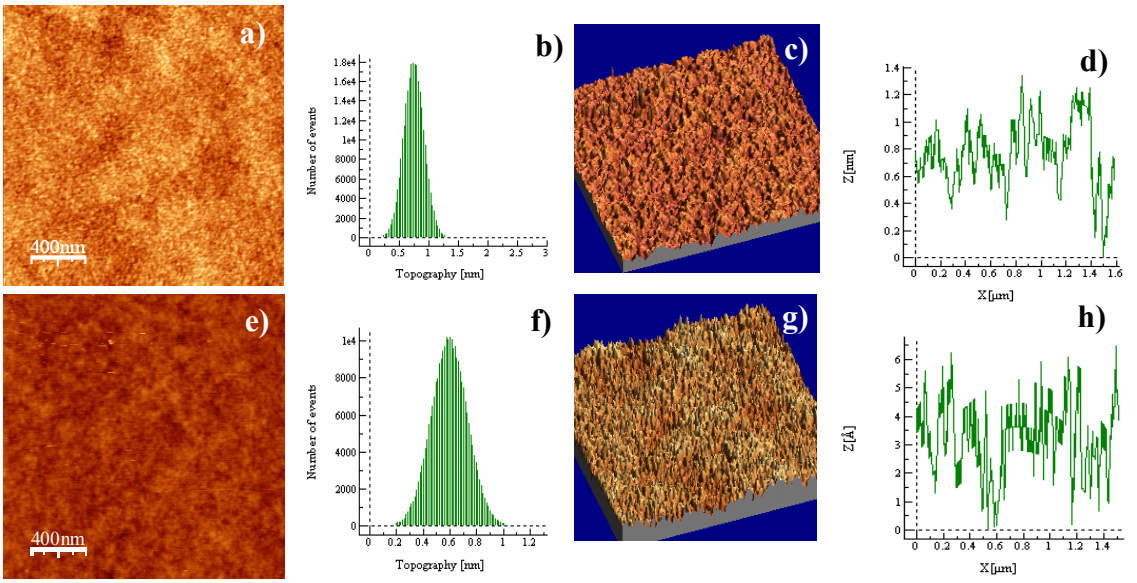

Figure 8.10. AFM images of (a,c) surface roughness and profile (b,d) for CdTe film before the etching and surface roughness (e,g) and profile (f,h) for CdTe film after the etching.

From SEM images shown in figure 8.11, we can conclude that because of the low specimens reactivity, the RIBE process result in a **low etch rate of CdTe.** This imply very slopped lateral walls on the waveguide (no vertical sidewalls) and **high etch rate of PMMA** due to high roughness (bad topography) of the waveguide lateral walls (sidewalls width no uniformity).

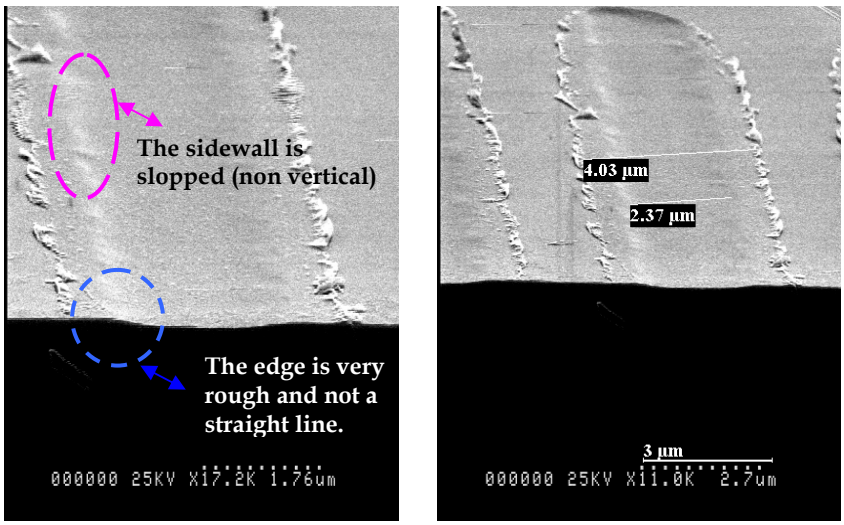

Figure 8.11. SEM images that show that the sidewall is slopped (non vertical). And the edge is very rough and not a straight line.

These results about the sloped sidewalls could be expected since Methyl free radicals are created in the plasma. But they cannot easily reach the CdTe surface by diffusion because the

distance between the plasma region and the sample is more than half a meter. On the other side, the N_2 reduces the concentration of methyl radicals in the plasma by the formation of the more stable CN radicals. It seems that these CN radicals cannot easily etch CdTe (although they can etch InP for instance) [27].

During this part of the thesis, it was required to develop several technological processes to fabricate CdTe- based waveguides, due to the inherent complexities in the CdTe material, namely:

1) Use of Al as a mask during etching (in the same way as previously study). This process includes: EBL with PMMA, Al evaporation, lift-off, etching, Al etch in ortho-phosphoric acid (H_3PO_4)). It is expected a low CdTe etch rate. Better results than those for Negative EBL resist are plausible.

2) EBL Bi-layer resist scheme for CdTe/Si submicron structures for lift-off processing.

3) Use of RIE instead of RIBE .Since in RIE systems the concentrations of methyl free radicals is much higher than in RIBE systems. In this case, the sample is INSIDE the plasma region where the concentration of methyl radicals is high and N_2 is not necessary.

4) Use of Negative Electron Beam Resist. (Lower degradation than PMMA so less sidewalls roughness). Low CdTe etch rate is expected.

8.3.1 Use of Aluminium as a mask in etching process

Masks based on other materials have also been fabricated. Similar etching studies of metal-based masks using Al, Cr and Ti have been reported [25,26].

Keeping the same etching conditions that in section 8.3. The technological process presented in this section includes: EBL with PMMA, Al evaporation, lift-off, dry etching, and Al etch in H_3PO_4.

For this particular study, samples of CdTe (500 nm)/SiO_2 (3.9 μm)/Si were used. A mask pattern was defined by conventional EBL and lift-off process. For that, a PMMA A9 resist layer was spin coated at 4500 rpm on the samples afterwards annealed at 170 ^oC during 75 min. The EBL conditions were the same that in section 8.3. In this case, arrays of stripes with width of 2

μm and period of 5 μm, in working areas of (100x100) μm were fabricated. After the development, 600 Å Al layer was deposited over the substrate, for lift-off process.

Lift-off is a simple method for film patterning. During the lifting-off, the resist under the film is removed with acetone, taking the film with it, and leaving only the film which was deposited directly on the substrate. The Al deposition was performed at the IMM by means of electron beam evaporation. The quality of the Al layer is not very critical. On the other hand, it is noteworthy that resist will outgas very slightly in vacuum systems, which may adversely affect the quality of the deposited film.

The duration of lift-off will depend on the film quality (generally, the higher film quality, the more impermeable it is, and the longer it will take for lift-off). As a rule of thumb, keep the substrate submerged in acetone until the whole film has been lifted-off and there are no traces of film particles (once particles dry on the substrate, they are notoriously difficult to remove).

Subsequently to lift-off, the RIBE process was carried out under $CH_4/H_2 + N_2 + Ar$ plasma atmosphere for 7 min. A flow of 14 sccm of CH_4/H_2 (15 % of CH_4 in the mixture), 6 sccm of N_2 and 8.5 sccm of Ar was used, resulting in ~10^{-4} Torr, ion energy of 400 eV and microwave power of 300 W, [28]. Under these conditions the obtained etch rate were 57.1 Å/min for Al and 485.71 Å/min for CdTe. Finally, we remove the Al mask with template H_3PO_4. This acid is highly soluble in water and it breaks down in touch with metals, producing toxic smokes. This substance is moderately acid, so etching the Al produces a flammable gas. The sample is etched until a change in its colour is noticeable. The H_3PO_4 reacts with Al following the reaction:

$$\mathbf{H_3\,PO_4 + Al \rightarrow Al\,(PO_4) + H_2}$$

The reaction was stopped with desionizated water. In subsequent AFM (figure 8.12) and SEM (figure 8.13) images, we can see the results of the previously described process.

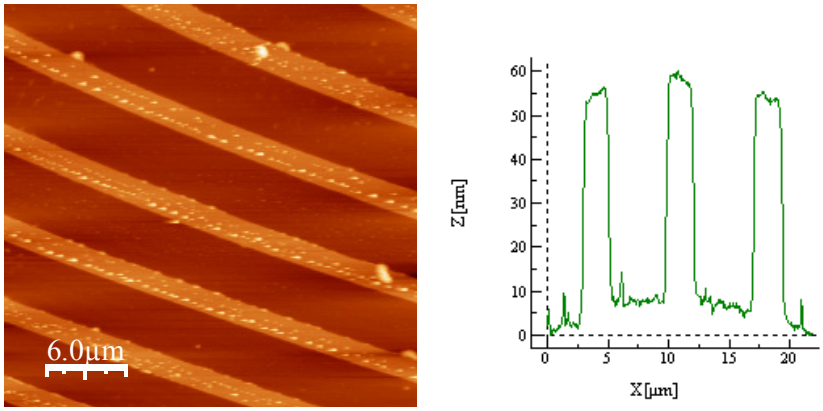

Figure 8.12. AFM images of a CdTe waveguides using Al mask during the etching.

Note that, during Al deposition, the substrate does not reach temperatures high enough to burn the resist. But, we found some problems, as shown in figures 8.13 and 8.14, with this technique due to the appearance of nucleation centres. The Al grows forming bubbles, being this deformation permanent. (The small bubble goes out for the big one). When we perform the lift-off process, we realize that Al settles with a certain energy that is liberated during the lift-off. This reduces the quality of the samples. With the Ion-Milling (with Ar), we see that remaining of the initial roughness, hence being a good replica of the previous surface.

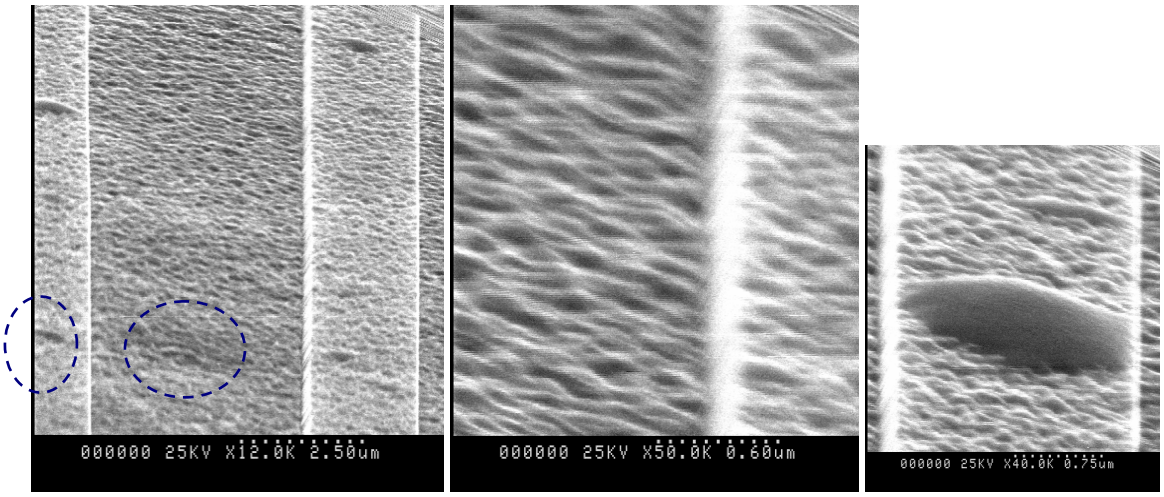

Figure 8.13. SEM images of CdTe waveguides using Al mask.

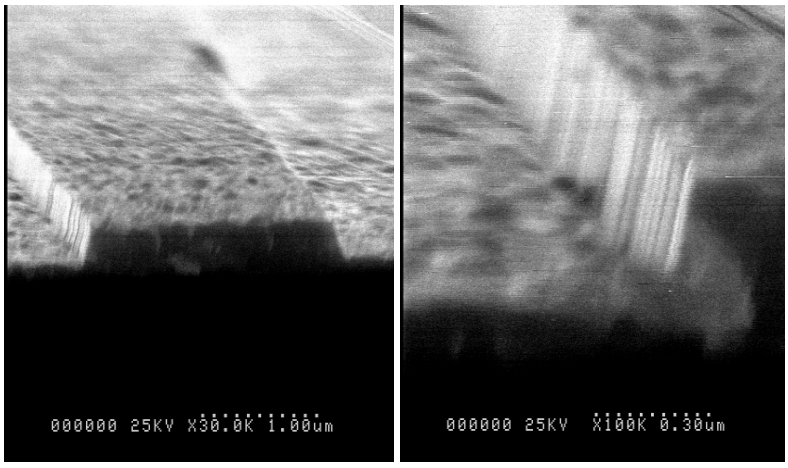

Figure 8.14. SEM images of the surface roughness and the edges for CdTe.

As shown in figure 8.15, the trenching effect is a typical problem associated to Ion Milling.

Figure 8.15. Typical trenching effect caused by Ion Milling.

The trenching is due to the increased etch depth near to sidewalls, where the reflected ions and energetic forward-sputtered material from the sidewalls causes additional sputtering. Taking this result into account, the trenching effect can be explained in terms of the electron shading effect, since electrons can impinge on the sidewall of the resist patterns while ions cannot negatively charge the upper part of the resist sidewalls. This charge suppresses the electron density in the trench, inducing an excess ion bombardment near the sidewall of the trench [29]. A common technique for controlling this effect is varying the angle of incidence while rotating the target [30].

8.3.2 EBL Bi-layer resist scheme for CdTe/Si submicron structures for lift-off processing

As we studied in the previous section, the main drawback of CdTe submicron structures made by combination of EBL and conventional lift-off processes is the large roughness at the edge of CdTe structure, as shown in figure 8.16. This is due to the use of single PMMA resist layer [31].

Figure 8.16. Schematic of CdTe submicron structures made by using a single layer polymer resist.

To solve this roughness problem with PMMA resist, a bi-layer resist of two polymers with different lithography characteristics was used (see figure 8.17) [31].

Figure 8.17. Schematic of CdTe submicron structures made by using a bi-layer polymer resist.

The bottom layer consists in a copolymer (PMMA-MA33%) which was deposited on Si(100) substrate and baked at 210 °C. After that, the coated substrate was covered by a PMMA (950 K PMMA A4) resist layer and baked at 170 °C. The bottom layer has both lower molecular weight and higher sensitivity than the upper resist layer [32], and the total thickness of resist bi-layer onto substrate surfaces was in the range of 0.8–0.9 μm.

Then, in order to characterize the undercutting of the bottom copolymer layer, nanopatterning was performed by EBL at 25 kV and different exposure doses were examined in the range from 150 to 600 μC/cm². Finally, the development was carried out in MIBK (4 methyl-2 pentanone): IPA (2 propanol) (1:1). After that, the length and shape of the bi-layer in the optimum range between 250-500 μC/cm² were characterized and are shown in the figure 8.18 [31].

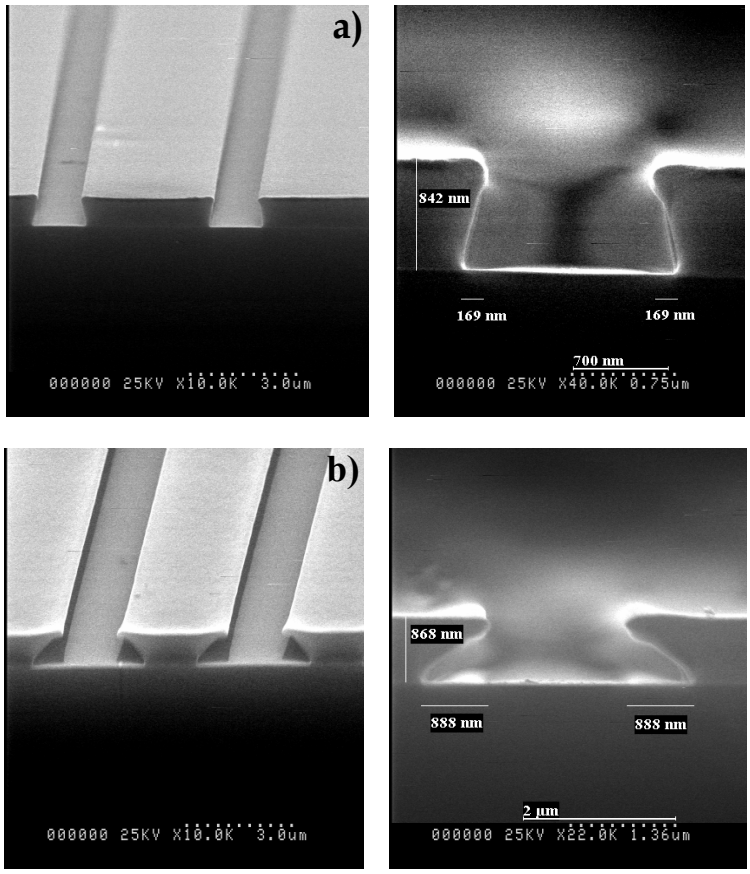

Figure 8.18. SEM images of undercutting length and shape of the resist layers, for: (a) 250 μC/cm² (b) 500 μC/cm² exposure doses.

We can observe that an increase of exposure dose, results in a more pronounced undercutting shape and a decrease of its profile angle. Moreover, it was found that the lift-off process shows optimum performance when the profile angle is about 45º. And it becomes non efficient when the profile angle is smaller than 15º. Subsequently CdTe films were grown on the surface of nanoprofiled Si substrates by VPE [13]. As examples, figure 8.19 demonstrates several AFM images of CdTe waveguides made by a combination of VPE and a flat lift-off processing using a bi-layer resist.

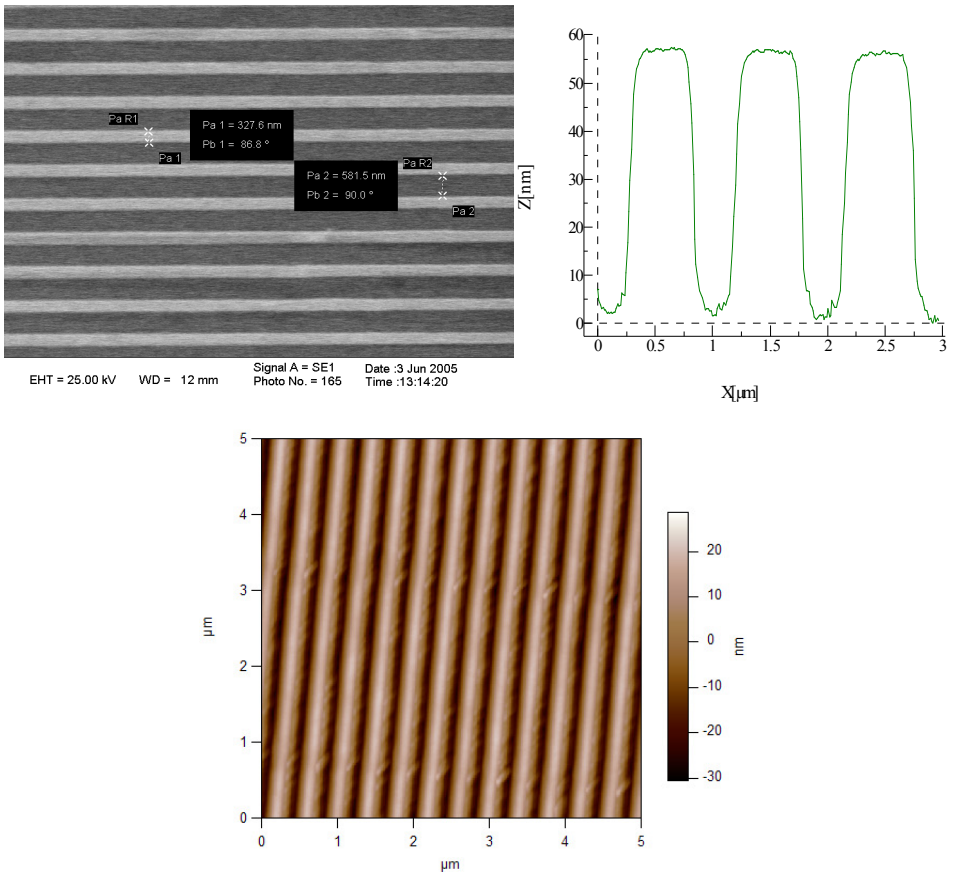

Figure 8.19. AFM images of CdTe waveguides made by thermal evaporation and lift-off processing using a bi-layer resist.

It can be seen that CdTe waveguides of submicron size obtained in this way, are uniform all over the substrate surface. In addition, they present a well-defined shape and the stripes are well separated. Thus, it is possible to obtain very flat CdTe submicron structures with a well defined shape by incorporating a bi-layer resist into the lift-off processing. This should be an important step for further development of waveguides for photonic structures [31].

8.3.3 Planarization of CdTe waveguide imbued in SiO_2 by etch-back technology

In this section, we are going to validate an alternative method to fabricate CdTe buried waveguides. Taking into account that PECVD SiO_x layers are the commonly used insulators during the processing of multilevel integrated circuits, a CdTe waveguide has to be buried in it and has to be planarized to get a fully compatible planar structure. Then, we describe how the etch-back method can be used to planarize CdTe layers grown by VPE [33,34].

The fabrication of CdTe waveguides embedded in SiO_x, consists on the following steps (figure 8.20) [35].

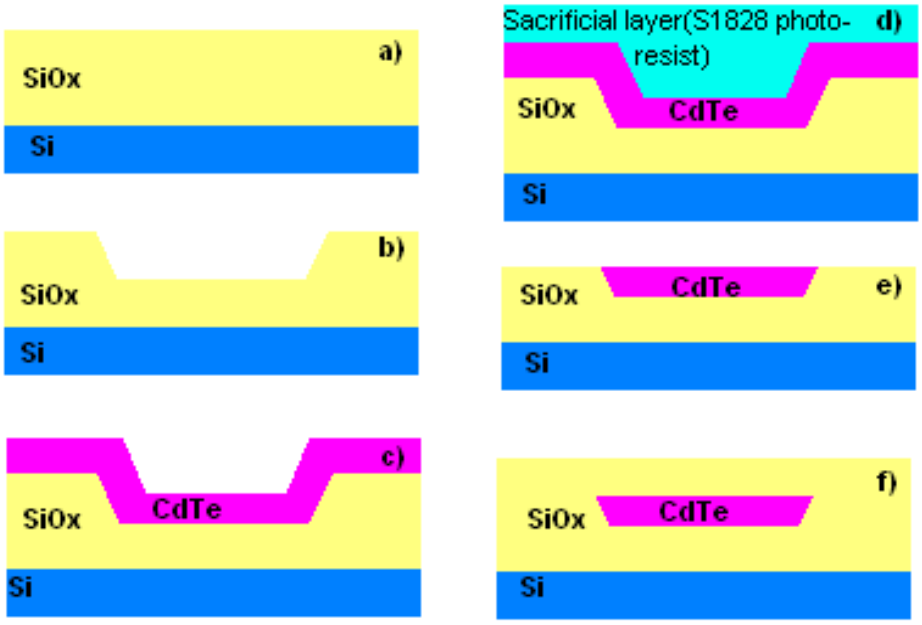

Figure 8.20. Fabrication of 0.65 µm thick CdTe buried waveguides: a) 3 µm of SiO_x deposited onto Si substrate by PECVD technique, b) 0.65 µm U-shaped fabrication by standard lithography and dry etching, c) CdTe deposition by VPE, d) Sacrificial layer deposition, e) Etch-Back processing step, f) Deposition of SiO_x thin film by PECVD to complete the embedded waveguide fabrication.

A SiO_x layer was firstly deposited (figure 8.20a) onto Si wafer. U-shaped grooves in the SiO_x layer were patterned by standard DUV lithography and Reactive RIE, in CEA-LETI laboratories (figure 8.20b). The depth of the grooves should be equal to the thickness of the CdTe waveguide. Once the substrate was patterned, 0.65 µm CdTe layer was deposited onto the patterned SiO_x/Si wafer by VPE technique, (figure 8.20c). This deposition technique leads to a conformal coating as shown in figure 8.21 a) and b).

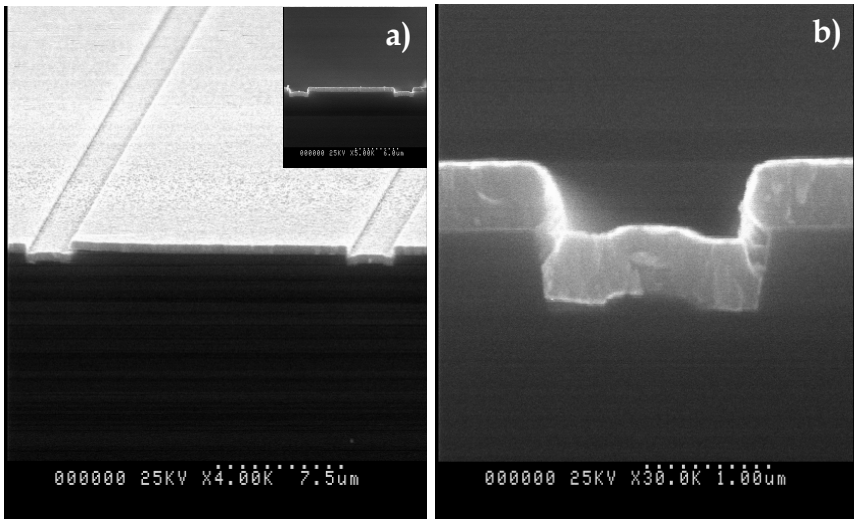

Figure 8.21. SEM (a) surface of samples and, (b) cross-section of trenches etched in SiO_x and covered with CdTe.

After that a sacrificial layer of S1828 photoresist was spin coated onto the CdTe surface at speed of 4000 rpm for 60 seconds; and baked at 115 ^oC for 30 min (figure 8.20d). The thickness of the photoresist was 3.2 µm. A cuasi- planar surface is reached allowing for the next etch- back processing step, as shown in figure 8.22.

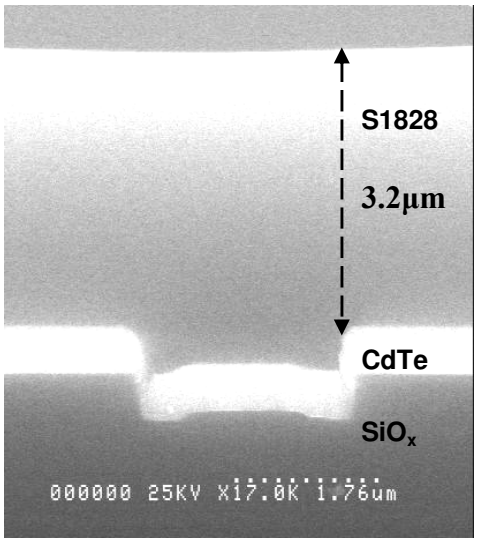

Figure 8.22. SEM images of sacrificial layer of S1828 photoresit onto $CdTe/SiO_x/Si$ substrate.

For this experiment the etching condition has been developed using RIE. The etch- back step consists of two sequential etching processes. The first one is the ICP etching of the sacrificial layer in such a way that the initial surface flatness is kept. The second part is the subsequent etching of the structure under conditions such that the etch rate of both the sacrificial layer and the CdTe layer to be planarized are similar. After that, the CdTe which was

deposited outside the U-shaped grooves was eliminated as shown in figure 8.20e). Finally, the wafer was cleaned and an upper cladding layer of 500 nm of SiO_x was deposited by PECVD at 300 ^oC (figure 8.20f)) [35].

It is noteworthy that the first key step is the deposition of the sacrificial layer. A planar surface must be obtained to overcome the total lack of planarization of 463 nm showed in figure 8.22. This is achieved with a 3.2 µm thick photoresist layer. A thicker layer would minimize the lack of planarization of 85 nm as shown in figure 8.23, but in compensation etch- back processes do not so long.

The second key step is the etch- back of a sacrificial layer keeping the original flatness. The principal issue that we have to take into consideration is to obtain the faster etch rate without warming and polymerizing the sacrificial layer, that would gives rise to a nonlinear etch rate with time. The etch was done using environmental O_2 (50 sccm), ICP power of 200 W, RF plasma power of 75 W (self bias of 152 V), chamber pressure of 40 mTorr, temperature at 0 ^oC, for 11.5 minutes leading to an etch rate of 270 nm/min for S1828 photoresist. Note that, O_2 plasma has been used for polymers that would otherwise tend to accumulate a protective coating of carbon on the surface. In the case of etching polymers with O_2 plasma, the etch rate was higher than that with Ar plasma [35].

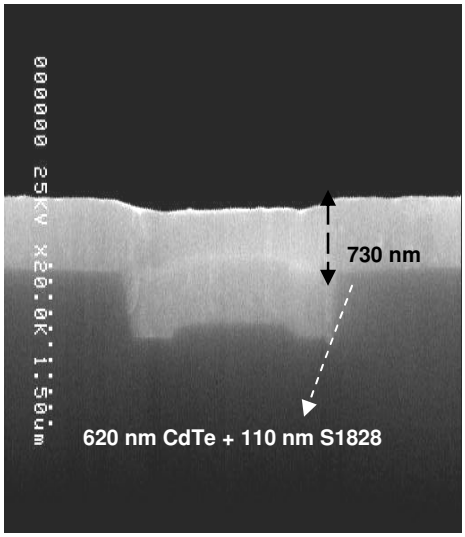

Figure 8.23. SEM image after the first etching step of etch- back process.

Other important consideration is the control of the end point of the etching process. Naturally, the end point of the etching is when the sacrificial layer over the CdTe outside the grooves is completely removed. Our RIE system does not have any end point detector. Then, we have consider this end point as the one leaving 110 nm of the sacrificial layer as shows in

figure 8.23, where we can observe that the lack of planarization is about 95 nm. This is similar to the lack of initial planarization (85 nm) shown in figure 8.23. This fact no was considerate as a big problem to reach our final objective (light guiding).

The third and last critical step is the CdTe etching outside the U-grooves. The essential requirement is that the CdTe etch rate is equal to the remainder sacrificial layer etch rate inside the grooves. A number of methods have been employed in order to get a good CdTe etching, including RIBE and RIE.

Originally chlorine based plasma was used for etching II-VI compounds, but this chemistry had turned to the use of CH_4 /H_2 mixtures being less corrosive and toxic [26]. In our preliminary results, we used CH_4/ H_2 (15% of CH_4 in the mixture) + N_2 in a RIBE-ECR system. N_2 was added to get stable ECR plasma discharges. Ar can be used instead of N_2 to get stable ECR plasma but its use caused roughness due to the different Cd and Te sputtering yields [25].

The same problems related with the free radicals created in the plasma commented in section 8.3 were found. To solve these problems we used RIE system instead of RIBE [36,37]. In RIE- ICP systems methyl free radicals concentration is much higher than in RIBE systems. In this case, the wafer is inside the plasma region where the concentration of methyl radicals is high and N_2 is not necessary to initiate the discharges. This fact made us consider the RIE etching as more effective in the planarization process.

We have studied the RIE conditions of S1828 photoresist and CdTe in CH_4+Ar mixtures. Here, Ar is added to improve the uniformity and to increase the etch rate through the removal of the some etch products of low volatility. Etch conditions like gas flow ratio, pressure and power were varied to obtain similar etch rate for both materials. The best conditions were achieved when CH_4 flow = 1sccm, Ar flow = 12 sccm, ICP power = 200 W, RF power = 20 W, pressure = 5 mTorr. In that case the CdTe etch rate = 33 nm/ min and the S1828 etch rate = 31 nm/min. This flow ratio is similar to the date given for M. Neswal [26] to obtain the maximum etch rate.

The etch back process ends after 19 minutes when all the CdTe layer deposited on the field of the wafer is removed. The result of the processes is shown in figure 8.24. It can be observed the good flatness of the top surface except at the border of the groove. Note that at these sites the deposited CdTe layer was under mechanical stress making the etch rate of that a little higher than at the central parts of the groove and outside it. This mechanical stress of the CdTe layer as deposited can be clearly seen in the inset of figure 8.24, which is a magnification

section of figure 8.21. However, this problem is not critical as shown in figure 8.25, because the further SiO_x PECVD conformal deposition process fills and completely imbued the CdTe waveguide.

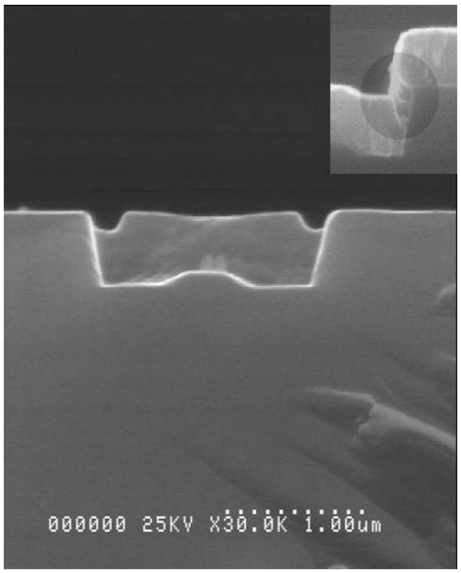

Figure 8.24. SEM image of a CdTe processed sample after having suffering an etch- back

Finally, the embedding process finishes with a thin film deposition of SiO_x by PECVD [30]. The SiO_x was deposited by Enhancement Chemical Vapour Deposition technique (PECVD, Surface Technology 310 D/F) in IMM. The process temperature was limited by the type of CdTe used. Then, we deposited at 300 ^oC. The plasma was generated by a radiofrecuency of 13.56 MHz and the precursors gases were NO_2 and 2% SiH_4 dilute in N_2. The gases flow was 1400 sccm and 400 sccm. Hence, the deposition rate obtained was 22nm/min at 650 mTorr of pressure.

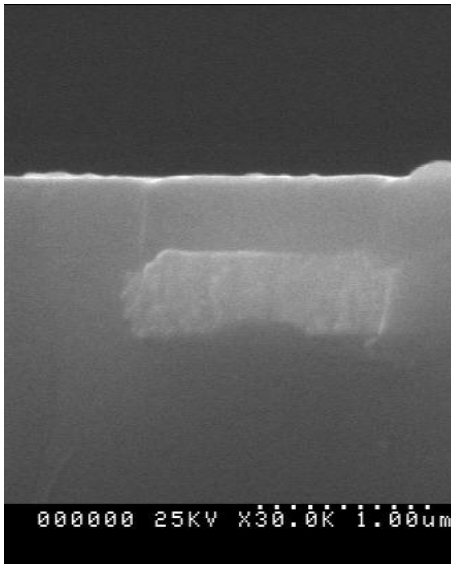

Figure 8.25. SEM image for a CdTe waveguide imbued in a SiO_x layer.

8.3.4 Use of Negative Electron Beam Resist

Finally we performed a process to fabricate CdTe- based waveguides. The goal was to obtain 0.5 µm waveguides using **MA-N 2405 as negative** resist, and patterning by EBL technique. This resist has lower degradation than PMMA and, therefore, less sidewalls roughness. Thus, taking into account this fact, higher CdTe etch rate are not expected.

In this particular case, two layers of MA-N 2405 resist were spin coated onto the CdTe surface at speed of 2000 rpm for 60s and bake at 90 ºC for 30 min. The thickness of the photoresist (which is also valid for EBL technique) was 1.72 µm. The fabrication process of the waveguides by EBL was similar to those previously reported. Thus that the waveguide has a width of 500 nm and a length of 6 mm. Afterwards, the development was carried out by LDD-26W during 40s. And the same RIE conditions were used for etching the CdTe that in the case 8.3.3, but in this case, the etch rate were 370 Å/min for the resist and 326 Å/min for CdTe polycrystal. A typical image of a waveguide fabricated with this method is shown in figure 8.26.

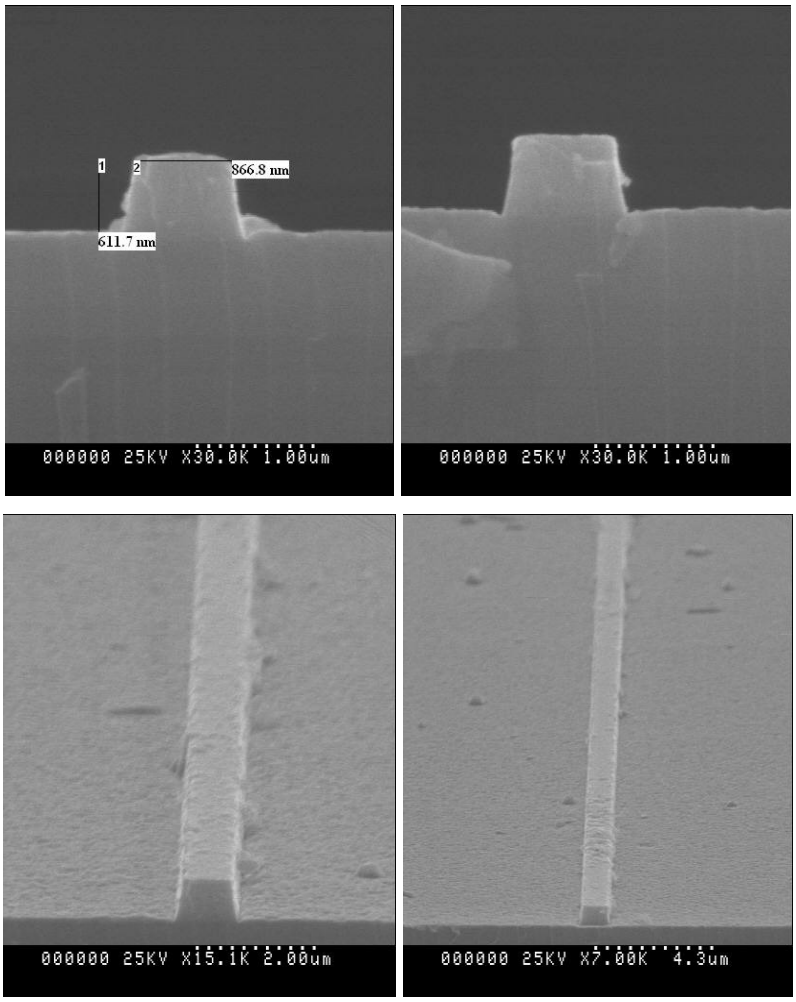

Figure 8.26. SEM images of CdTe waveguides after RIE etching.

Subsequent to the fabrication processes, CdTe waveguides were embedded with a 400 nm of SiO_x, which was deposited by PCVD at T= 300 ºC, during 15 min, for single mode high- index contrast waveguide. The deposition rate was 22 nm/min. In the following figure 8.27, SEM images show a cleaved edge of a CdTe waveguide embedded in SiO_2.

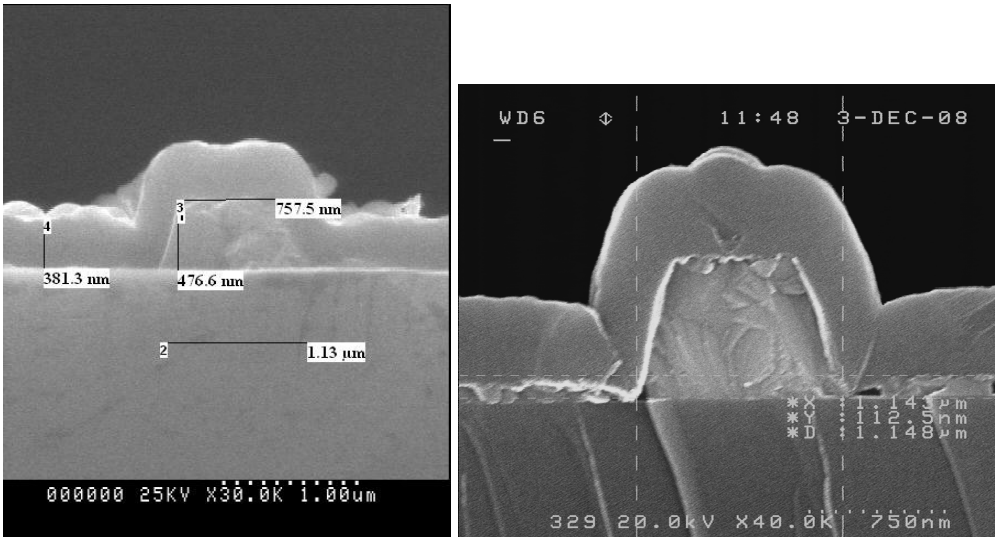

Figure 8.27. SEM images of CdTe waveguide embedded in SiO_x PCVD.

During the SiO_x deposition some problems appeared and in subsequent section are explained more detailed. This fact could be connected with the quality of the layer. Besides, CdTe/SiO_x heterostructures have a large lattice mismatch and thermal expansion coefficient difference and, as consequence, the interface region contains dense dislocations that deteriorate the quality of the film. Therefore, to improve the surface of CdTe film a RTA treatment in different atmospheres was used. The post-growth treatments studied in previous sections have been shown to produce an important quality improvement of films, revealed by a dramatic reduction of the density of structural defects.

8.3.4.1 Study of the post growth treatment

After the thermal treatment, some irregularities in the layer were observed. Amongst the problems originated during the thermal annealing, we can consider that the SiO_x deposited by PECVD equipment, is not stoichiometric and with H_2 interstitial high level doped (rich in H_2). Therefore, since deposition was made at 300 ºC, and the RTA at higher temperature 600-800 ºC, some boils in SiO_x layers appeared. The boils are due to the high mobility of H_2 interstitial which shows a trend to run away.

For this particular case we had problems with P_R. It is possible that there was more concentration of H_2 inside SiO_x. (H_2 run away in the same way than in an explosion). In figure 8.28, we can see some of this boils.

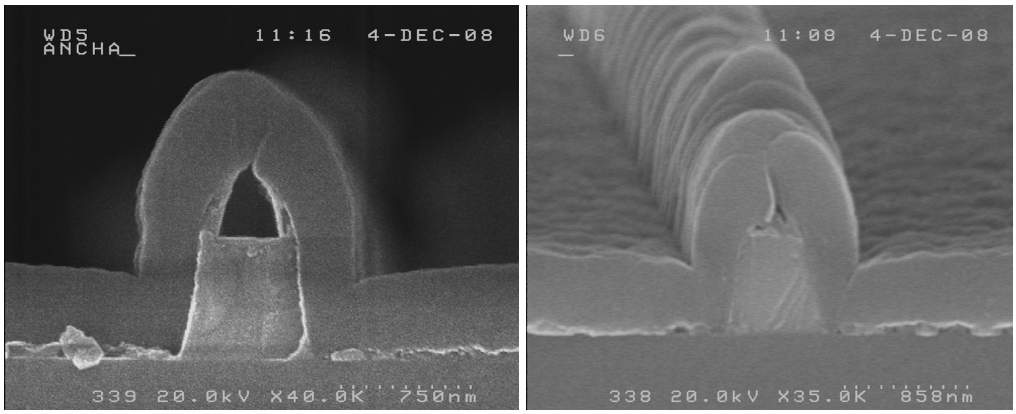

Figure 8.28. SEM images of boils in SiO_x layer.

To solve these problems, we should make the annealing with forming gas. Forming gas is a mixture of N_2 + H_2 (9:1). With this 10%, a partial pressure rich in H_2 could be created and H_2 does not run away out of SiO_x because, $P_{H2\ outside} > P_{H2\ inside.}$ The solution should be maintained at one atmosphere of H_2 the balance between H_2 of SiO_x and H_2 atmosphere of RTA annealing.

Something to take into account is that there exist 55 nm CdTe thin layers over the SiO_x surface. This fact is not very important; because the extremes of waveguides are free of CdTe. Posterior studies are going to be realized with Ar + H_2 (9:1), because N_2 is always a reactive gas, and with H_2 some problems appeared.

8.4 Measurements of propagation losses in strip-loaded CdTe waveguides

Previous to waveguide fabrication, we have presented in chapter 6 multiple Cd(Zn)Te samples grown by VPE that were characterized. In this section we emphasize that two important properties to be taken into account are:

- **Roughness**, the surface roughness must be lower than 10 nm;
- The real and imaginary part of the refractive index, **n**, to reach **k** values below 10^{-5}.

For this specific sample whose characterization is shown in figure 8.29, the measured roughness on the top surface was 8.03 nm. Other samples with thickness about 350 nm also displayed top surface roughness about ~ 10 nm, achieving the proposed objective.

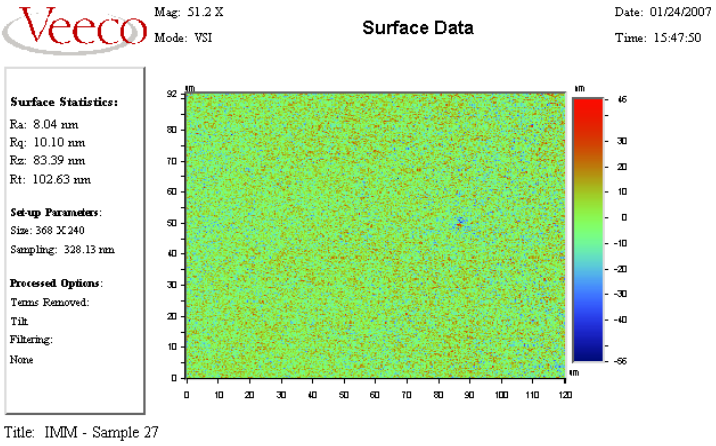

Figure 8.29. Characterization of the surface roughness (measurement = 8.04nm) of a Cd(Zn)Te layer with thickness 1350 nm fabricated by VPE.

However, measurements of **k** using ellipsometry showed that our aim 10^{-5} could not be achieved, as in the case shown in figure 8.30. All measurements display **k** values of the order of 10^{-3}, very far from our objective. Thermal annealing cycles were carried out to improve crystal quality, but a significant reduction of the **k** value was not observed. The high values of losses could be attributed to the polycrystalline behaviour of the deposited material. Better crystallinity had been observed using other substrates as sapphire but, in contrast, not so suitable for mass-manufacturing. As a result, it seems that the VPE deposition of Cd(Zn)Te films on SiO_2 does not produce semiconductors films with a sufficient quality to be implemented as optical devices. However, it deserves to be mentioned that the process could be further optimized to diminish losses, although it is not clear if the aimed **k** value could be reached [38].

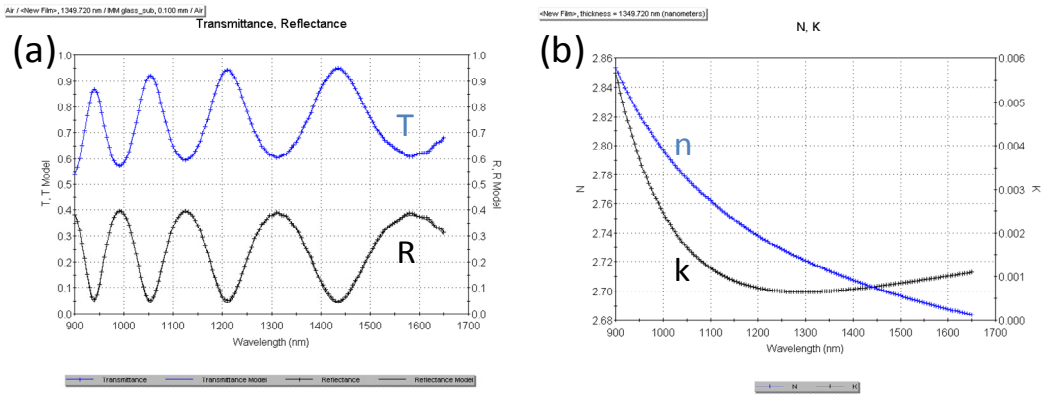

Figure 8.30. Measurements of a Cd(Zn)Te film by ellipsometry: (a) Transmittance and reflectance; (b) real *n* and imaginary *k* parts of the measured index of refraction. At 1550 nm, $k=10^{-3}$.

Having in mind that, the optical properties of both the substrate and CdTe films at the telecom frequency of 1550 nm are of the outmost importance to this work. SiO_2, with an index of refraction of n=1.5, was chosen as an appropriate substrate due to the substantial index mismatch that it has with CdTe. The polycrystallinity and the average of the grain size of the CdTe film leaves the imaginary part of the refraction index suspects and makes the patterning of waveguide structures difficult. CdTe films deposited on sapphire offer an intriguing alternative where such issues could be avoided. In this scenario, the index of refraction mismatch would be somewhat smaller as sapphire has an index of n=1.75. Ellipsometry measurements for CdTe films deposited on this substrate also yielded a value of n=2.7.

Therefore, taking into account these drawbacks, some samples as strip-loaded CdTe waveguides were fabricated. Although the k values measured by CIP were a bit high (between 10^{-3} -10^{-4}), the aim was to prove that light can be guided in such a kind of waveguide. These samples were measured in NTC laboratories. Figure 8.31 shows a preview of a sample.

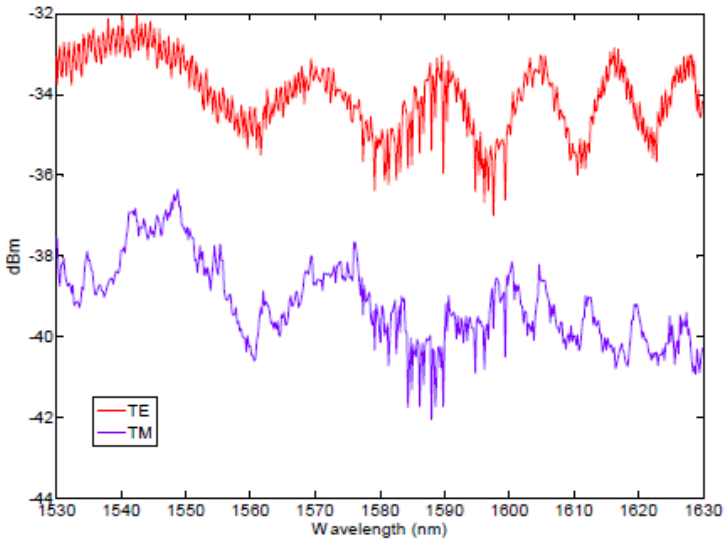

Figure 8.31 Recorded transmission spectra of the strip-loaded CdTe waveguides for both Te and TM polarisations.

The setup used is not prepared for so thin samples (waveguides too short) so the conditions for the input and output of light were not optimal. However, some important results were obtained. The measured spectra are shown in figure 8.32 for both polarisations. Coupling was better for TE polarization, which is also the most appropriate to obtain a high field confinement inside the nonlinear region. Figure 8.32 shows the recorded spots at the output of the waveguides. Although there is a significant scattering, mainly due to the scattering losses in the CdTe material and to some irregularities on the top of the samples, it can be seen that light is well confined in the waveguides [38].

This would be considered as the first experimental demonstration of light guiding along a CdTe waveguide.

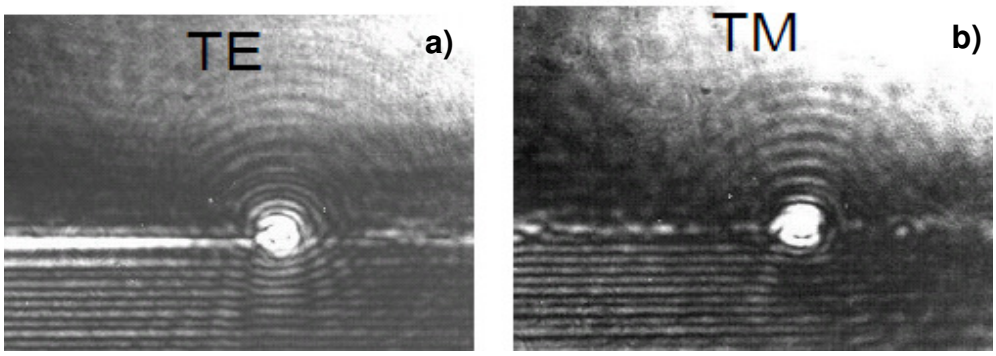

Figure 8.32. Light spots observed at the waveguide output for both polarisation and confirming that light is confined in the CdTe waveguide despite of the high losses.

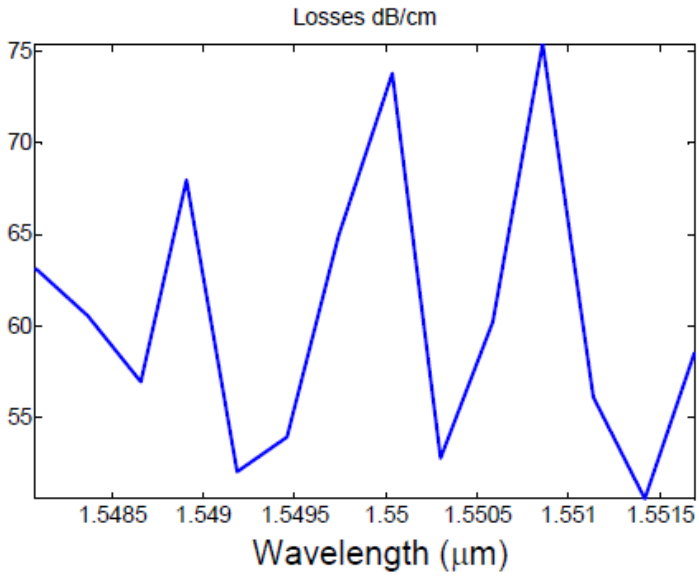

Figure 8.33. Propagation losses for TE polarisation estimated by means of the Fabry-Perot method.

Propagation losses were estimated by means of the Fabry-Perot method. Specifically, figure 8.33 depicts the measured spectra for both TE and TM polarizations. A better performance was observed for TE polarization, although losses were quite high (of the order of 40 dB/cm) mainly owing to the high k value (about 10^{-3}) of the underlying CdTe core. This is confirmed by the taken light spots, as shown in figure 8.30a-b, where a great scattering is appreciated. As before, by improving the growth process or by alleviating the lattice mismatch between the cladding and the CdZnTe material, losses could be significantly reduced. This is an interesting way to follow in order to develop all optical devices, since the linear and nonlinear optical characteristics of the CdZnTe material are comparable to AlGaAs in terms of performance and there exits also the possibility to manufacture the device in CMOS lines, as in the case of Silicon photonics.

On the other hand, the high confinement of light in very small areas and the use of the slow waveguiding structures may give rise to a heating in the nonlinear material which in turn induces a change in its optical properties. This will imply the enlargement of the nonlinear interaction length in the MZI making thus the thermal effects less restrictive.

However, these losses can be highly reduced if the CdTe material presents lower losses and the process of creation of the waveguides is optimised. This is quite encouraging, mainly if it is considered that CdTe grown on sapphire could present much lower absorption losses.

Our future work is going to focus on annealing these samples to improve the quality of CdTe films and, then the propagation losses would be lower.

8.5 Conclusions

Experimentally, several techniques for fabrication CdTe waveguides have been studied. Better results have been observed in fabrication of waveguides with negative electron beam resist. However, it is necessary to refine the fabrication processes to get higher quality waveguides, principally for the roughness characteristic of this material. Therefore, we think that this is a starting point of a technology that could be an interesting alternative to III-V semiconductor based devices with the possibility of low cost fabrication if made compatible with CMOS processes.

All of these theoretical and simulation results are quite encouraging. First, Cd(Zn)Te shows a quite high refractive index as well as negligible linear absorption at 1550 nm wavelengths, which is an important starting point for the implementation of high density integrated photonic circuits. Second, it shows very interesting nonlinear properties: a relatively high Kerr coefficient (which is the responsible for nonlinear all-optical switching in sub nanosecond speeds) and TPA (which also gives raise to free-carrier absorption) can become negligible by introducing a certain amount of Zn.

Based in these considerations, it is feasible to design single mode waveguides (strip and strip loaded) with high confinement of the field in the nonlinear region (effective area below 1 μm^2), which enormously nonlinear interaction. Therefore, this material seems a suitable choice for the fabrication of compact all optical devices such as switches or logical gates. If the fabrication processes could be made compatible with CMOS manufacturing lines, these devices could be fabricated at low cost and in high volumes.

The main observed limitation is the high losses of the growth Cd(Zn)Te layers, which is thought to be mainly due to both surface roughness and the lattice mismatch between the semiconductor and the SiO_2 lower cladding. So for futures studies must be guiding in this sense.

Future work should establish if the superior film quality obtained for the sapphire substrate is able overcome the deficiencies presented by amorphous SiO_2. It is mandatory to improve the quality of the grown Cd(Zn)Te layers in order to develop all-optical devices that can compete with other current technologies such as those based on III-V semiconductors.

References

[1] Tatsuura, S., Matsubara, T., Mitsu, H., Sato, Y., Iwasa, I., Tia, M., and Furuki, M. Appl. Phys. Lett. **87**, (2005), 251110.

[2] Lipson, M. J. Lightwave Technol. **23**, (2005), 4222-4238.

[3] Schubert, D.W., Kraus, M.M., Kenklies, R., Becker, C. R. and Bicknell-Tassius, R. N. Appl. Phys. Lett. **60**, (1992), 2192-2194,.

[4] Toshifumi, T., Adachi, S., Nakanishi, H. and Ohtsuka, K. Jpn. Appl. Phys. **32**, (1993), 3496-3501.

[5] URL: http://www.ioffe.ru/SVA/NSM/nk/A2B6/zncdte10.html.

[6] Marple, D. T. F. J. Appl. Phys. **35**(3), (1964), 539-542.

[7] Almeida, V. R., Barrios, C. A., Panepucci, R. R. and Lipson, M, Nature **431**, (2004), 1081-1084.

[8] Sheik-Bahae, M. D., Hagan, J. and Van Stryland, E.W, Phys. Rev. Lett. **65**, (1990), 96-99.

[9] "*Non linear Optics*". Robert W. Boyd. (2008) Ed. Elseiver.

[10] Sanchis, P., Blasco, J., Martinez, A. and Marti, J. J. Lightwave Technol. **25**(5), (2007), 1298 - 1305.

[11] Foster, M.A., Moll, K.D. and Gaeta, A.L. Opt. Express **12**(13), (2004), 2880-2887.

[12] Barwicz, T. and Haus, H. A. J. Lightwave Technol. **23**(9), (2005), 2719-2732.

[13] N.V. Sochinskii, M. Abellán, J. Rodríguez-Fernández, J.L. Plaza, V. Carcelén, E. Diéguez, Journal of Crystal Growth **310**, 5 (2008), 1669-1673.

[14] T.Nishimura, H. Aritome, S. Namba. Journal of Quantum Electronics. Vol. **QE-16**, No.12 (1980), 1337.

[15] W. Chen and H. Ohmed, J. Vac. Sci. Technol B. **11,** (1993), 2515.

[16] URL:www.microchem.com/products/pds/PMMA_Data_Sheet.pdf.

[17] P. B. Fischer, and S.Y. Chou. Appl. Phys. Lett. **62**, (1993), 2989.

[18] E.D. Fabrizio, L. Grella, M. Gentili, M. Baciocchi, L. Mastrogiacomo and P. Morales. Jpn. J. Appl. Phys, Part 2. **36**, (1997), L70.

[19] M. A. Guillorn, D. W. Carr, and R. C. Tiberio, J.Vac.Sci. Technol. B**18,** (2000), 1177.

[20] J. I. Goldstain, D.E. Newbury, P. Echlun, D.C. Jou, A.D Roming Jr. C.E. Fiori, and E. Lifshin. Plenium Press (2nd Editions), New York and London (1992).

[21] "*Fundamentals of Microfabrication*", Marc, J. Madou (2002).

[22] J. Michael Köler, Antje Wiegend (Wiley-VCH).

[23] J. R. Sendra, J. Anguita, J. J. Pérez-Camacho, and F. Briones. Appl. Phys. Lett. 67, (1995), 3289.

[24] J.V Anguita (Comunication private).

[25] S. J. Pearton and F. Ren. J. Vac. Sci. Technol,B **11** (1), (1993), 15-19.

[26] M. Neswal, K.H. Gresslehber, K. Lischka, K.Lubke. J. Vac. Sci Technol.B **11**(3) (1993).

[27] J.R. Sendra and J. Anguita. Jpn. J. Appl. Phys. Vol **33**, (1994), L 390- L 393.

[28] R.E.Lee. J.Vac. Sci. Technol **16**, (1979), 164- 170.

[29] H.C Lee, S. Beckx and S. Vanhaelemeersch. 2nd International Symposium on Plasma Process Induced Damage. May 13-14, Monterey, CA. Copyright 1997 American Vacuum Society.

[30] "*Contribución al establecimiento y caracterización de una tecnología de ataque de aleaciones III-V basadas en Indio mediante haces de iones reactivos,*" J. R. Sendra, Tesis Doctoral, Universidad Politécnica de Madrid, E.T.S.I. Telecomunicación, Instituto de Microelectrónica de Madrid, Madrid (1996).

[31] M. Abellán, J. Anguita. Microelectronics Engineering; Vol.: **84**; (2007),1117 –1119

[32] R.E. Howard, E.L. Hu, L.D. Jackel, IEEE Trans. Electron Dev. ED- **28** (11) (1981) 1378–1381.

[33] A. D. Williams, T D. Moustakas. Mater. Res. Soc. Symp. Proc. Vol. **892,** (2006), FF14-11.1-11.6.

[34] B. Degroote, N. Collaert, R. Rooyackers, M. R. Baklanov, W. Boullart, E Kunnen, M. Jurczak, S. Vanhaelemeersch. Microelectronic Engineering **83**, (2006), 570–576.

[35] M. Abellán and J. Anguita. Journal of Physic D, (Submitted).

[36] W. R. Chen, S. J. Chang, Y.K. Su, W.H. Lan, A.C. H. Lin and H. Chang. Jpn.J. Appl. Phys. Vol **39**, (2000), 3308-3313.

[37] Akira Higa, Atsushi Nishihira, Hiroyuki Toyama, Masaaki Yamazato, Takehiro MAaehama, Ryoichi Ohno and Minoru Toguchi. Japanese Journal of Applied Physics Vol. **44**, No. 9A, (2005), 6714–6718.

[38] Martinez, F. Cuesta-Soto, J. Garcia, J. Marti, N.V. Sochinskii, M. Abellán, J. Rodriguez-Fernandez, S. Mengali, A. Mercuri, C. Corsi, I. Reid, M. Robertson, S. Neretina, R.A. Hughes, J. Wojcik, J.S. Preston, P. Mascher, Proc. of SPIE 6996, 699608/1-699608/12 (2008).

Chapter 9

Summary and Conclusions

Chapter 9

SUMMARY AND CONCLUSIONS

The work presented in this thesis describes growth methods and characterization of CdTe– based sources and thin films. The wide variety of results obtained clearly illustrates the power of using such techniques for high- volume manufacturing.

The optimization of the growth method of CdTe and CdZnTe sources and thin films and, the role of some dopants such as: Ge, Bi, Yb and Zn in the improvement of material properties have been studied. Some results include:

- The co- doping of CdTe sources with Ge as deep donor and, with Yb as rare-earth element has been proved to be a promising way to obtain semi-insulating CdTe sources with good transport properties. High resistivity ($5 \cdot 10^9$ Ω·cm) and lifetime (9 μs) were obtained for these films confirming the beneficial effect of rare earth dopant. Moreover, we have shown that the control of the Yb concentration is crucial for achieving electrical compensation. Experimental results evidence that high resistivity sources of reasonably good structural quality can be grown when the Yb concentration is lower than ~$5x10^{18}$ at./cm^3.

- Bi- doping has been proved to be a second possibility to obtain CdTe semi-insulating sources. CL studies show that samples with a Bi content higher than $7x10^{17}$ at./cm^3 present a dense network of highly decorated grain boundaries. Besides Bi- doping contributes to the appearance of the A luminescence band. The Yb and Bi co-doped samples present striations which are probably due to the presence of Yb. Moreover, Yb has been found to originate a blue shift of the deep level band centred at about 1.10 eV.

- We have shown that several VPE deposition runs induced the continuous deterioration of source composition that results in an inhomogeneous enrichment of $Cd_{1-x}Zn_xTe$ with Zn. This point is very important because it has been found out that long VPE growth runs give us to inhomogeneous samples, which is very undesirable.

- A simple and efficient industrial- like growth method which allows the fast growth of large- area CdTe films with uniform composition and thickness was developed.

- From the sources studied in chapter 4, CdTe:Bi and CdTe:Ge:Yb films were grown with relative good crystallinity. In particular the first one has demonstrated be a promising alternative as absorber layer in solar cells. In this sense, our efforts were focused in the study of the back contact, where we propose a new material ($Au/Bi_2Te_2/CdTe:Bi$ heterojuntion) to be use as back contact. This material has resulted to be a perfect alternative to commonly used back presenting much better properties.

- With respect to the CdTe:Ge:Yb, the experimental findings seem to point out that films with reasonable good structural properties can be grown by doping them with Yb at a concentration below the value $5x10^{18}$ at./cm^3 (which is estimated to be the Yb solubility limit for CdTe).

We have presented the experimental results on the remarkable improvement of the recombination quality of the CdTe films by post growth thermal annealing. We shown that heating the samples notably improves both its crystalline structure and its surface morphology and it allows to significantly reducing the typical concentration of native and foreign defects. Among the results obtained it is important to mention:

- Heating the samples at temperatures below 900 ^oC notably improves both its crystalline structure and its surface morphology and it allows significantly reducing the typical concentration of native and foreign defects increasing PL intensity.

- Heating the samples at temperatures higher than 900 ^oC generates stress and induced film deterioration originating holes which goes all along the film thickness.

For the three cases studied, the substrate type does not affect the morphology of the films´ but originates changes in their optical and macroscopic properties.

- For **CdTe:PdI/Si,** the increase in the PL peak intensity is in very good agreement with the data obtained from SEM measurement which shows an increase in the average grain size and a decrease in the grain boundaries, and by XRD measurement, where the FWHM decreases as the annealing temperature increase.

  This fact demonstrates that annealing promotes an improvement in the structural quality of the film. The optimum annealing temperature, which gives rise to highest quality films, is ~750 ^oC. Indeed, at very high temperature around 800 ^oC, the effect is the opposite: the stress is so high that the films appear damaged.

- For **CdTe/Si**, we found that annealing between 500-750 ºC is an important factor to improve recombination in CdTe layers. The intensity of the sub bandgap band in as-grown samples of CdTe layers is ~3.5 times weaker as compared with the annealed samples, indicating the presence of a high defect concentration, which create non-recombination centres. Moreover, after annealing the band-to-band emission at 1.58 eV appeared in the spectrum. Therefore, we have found that annealing at 500 ºC is an important factor to recombination in CdTe layer grown on both Si and sapphire substrates.

- Finally, for **encapsulated samples** the optimum annealing temperature is a bit lower than for samples without encapsulation, namely at approximately 650 ºC.

Therefore, the achieved high crystalline quality stimulates good optical quality, and the heteroepitaxial layers encourage us to use these films, for example, as an optical waveguide in integrated silicon optics devices.

We demonstrate that RIBE etch does not cause significant morphological changes in of but it results in an increase of the concentration of acceptor impurities. This was revealed by an increase of the overall PL intensity and, simultaneously, a decrease of the PL decay time, which is more important on the low energy side of PL spectrum due to the recombination of carriers in acceptor pairs.

We show the possibility to grow Cd(Zn)Te in porous alumina nanostructures with PL properties comparable with those of the bulk material and planar epitaxial layers. These structures are very attractive and promising for the development of a new generation of sensor and could serve as a basis for micropixels suitable for further development of X- and γ- ray high resolution imaging devices.

Finally, theoretical and experimental results on the use of CdTe and Cd(Zn)Te as core material for the development of all- optical photonic devices were obtained. The results have shown that:

- Negative electron beam resist has been observed to be the best technique to fabricate CdTe waveguides. Although, it might be necessary to refine a bit more the fabrication processes to get higher quality waveguides. We think that this is a starting point of a technology that could be an interesting alternative to III-V semiconductor based devices with the possibility of low cost fabrication if made compatible with CMOS processes.

- The high losses in the growth Cd(Zn)Te layers has been shown to be the main observed limitation for further improvement. Thus, furhter studies must be performed.

FINAL REMARKS

The last chapter of the thesis is intended to demonstrate that past work should lead to future studies into the growth modes of CdTe. Although, all of these studies have left unanswered questions, however, they have pointed out the way to carry out further research. So we propose as future works:

For instance and despite of the promising properties, it is noteworthy that **CdTe:Bi** has been poorly investigated in comparison with other dopants, and has interesting properties in **solar cells applications.**

- The fabrication of devices with CdTe:Bi films at a concentration close to 10^{18} atm/cm^{-3} and a less thickness to reduce the effect of series resistance and, maximize the photoconductive properties in the region of absorption.

- It is known that the most difficult to be addressed and most vulnerable component of CdTe solar cells is the fabrication of stable low resistance **back contact**. There are many procedures for producing a back contact to CdTe, but most researchers admit that fabrication of the low resistance contact is more art than science. Most procedures to form a back contact include: 1) an etch or surface preparation step; 2) application of a film containing Cu, Hg, Pb, or Au ; and 3) a subsequent heat treatment above 150 °C. Therefore, it would be interesting to **manufacture a device with CdTe bilayer**. The closer CdTe- based with a low concentration of Bi with a thickness optimum to maximize absorption properties and, a second conductive layer doped heavily to reduce the total series resistance of the device and back contact. In this sense, based in our Bi_2Te_3 preliminary studies, we propose Bi_2Te_3 as promising candidate. We think that it would be a robust contact for this kind of modules.

While the results presented in this thesis demonstrate a good way to fabricate **waveguide**, little is still know about these structures. In the future films with higher quality should be established. It is mandatory to improve the quality of the grown Cd(Zn)Te layers in order to develop all-optical devices that can compete with other current technologies such as those based on III-V semiconductors.

- The waveguides proposed have high index contrast and they can have large propagation losses due to the sidewall roughness originated from fabrication imperfections. Therefore, effort will be adress to optimise the fabrication processes developing specific to minimise sidewall roughness and, thus, propagation losses. Propagation losses between 10 and 20 dB/cm are target.

- In addition, we consider that it could be interesting to study the fabrication- induced damage in the optical properties of the films.

Appendices:

Appendix A

SUMMARY OF THE PRINCIPAL PROPERTIES OF CdTe

In subsequent table we summarize the most important structural and chemical-physics properties of the CdTe, at room temperature.

Property		Reference
Structure	Zinc Blende	[1]
Spatial group	F43m	[1]
Molar mass	240.0	[1]
Lattice constant	6.481	[1]
Band gap	1.47 eV	[2]
Electron mobility	1100 $cm^2 \cdot V^{-1} \cdot s^{-1}$	[3]
Holes mobility	100 $cm^2 \cdot V^{-1} \cdot s^{-1}$	[3]
Electron effective mass	$0.11m_0^*$	[1]
Holes effective mass	$0.6m_0^*$	[1]
Melting point	1092°C	[1]
Density	5.85 g/cm^3	[2]
Thermal conductivity$_{(s)}$	1.5 $Wm^{-1} \cdot K^{-1}$	[5]
Thermal conductivity$_{(l)}$	1.5 $Wm^{-1} \cdot K^{-1}$	[5]
Specific heat capacity	210 $J/Kg \cdot K$	[2]
Thermal expansion coefficient	$5.9 \times 10^{-6}/K$	[6]
Refractive index	2.67 (@10 μm)	[1]

$m_0^* = 9.11 \cdot 10^{-28}$ g

References

[1] "*Semiconductors and Semimetals: Cadmium Telluride*", K. Zanio, Ed. Academic Press, London (1978).

[2] "*Semiconductors: Data Handbook*", Otfried Madelung, Springer Ed., 3rd Edition, Berlin 2004, Secc. 2.39, 232.

[3]. R. Romestain, C. Weisbuch, Phys. Rev. Lett. 45 (1980) 2067.

[4] "*Narrow gap cadmium-based compounds*", P. Capper, Emis data reviews series nº 10, Inspec Pub., 1st Ed., England, 1994, Cap. B5.8 y B8.3.

[5] W. Shyy, H. Ouyang. J. Cryst. Growth 173, (1997) 352-366.

[6] "*Properties of II-VI Compound Semiconductors*". Palmer, D W (March 2008).

Appendix B

SUMMARY OF THE PRINCIPAL PL EMISSION FOR CdTe

In subsequent table we summarize the most important PL emission related with CdTe.

Energy (eV)	Assignation	Observation	Ref.
1.5965	X	Free exciton	**[1,2]**
1.59314	D-X,D =F	Donor bound exciton (F as donor)	**[1]**
1.59309	D-X,D =Ga	Donor bound exciton (Ga as donor)	**[1]**
1.59305	D-X,D =Al	Donor bound exciton (Al as donor)	**[1]**
1.59302	D-X,D =In	Donor bound exciton (In as donor)	**[1]**
1.59296	D-X,D =Cl	Donor bound exciton (Cl as donor)	**[1]**
1.5892	A-X, A= Na, As, Cu	Acceptor bound exciton (Cu, Na, or As as acceptor)	**[3]**
1.5900	(A^0-X), A^0= V_{Cd}	Acceptor bound exciton (V_{Cd} as acceptor)	**[5]**
1.585	A-X, A^0= Au	Acceptor bound exciton (V_{Cd} as acceptror)	**[6]**
1.575	A-X, A^0= Unknown X-LO		**[2]**
1.547-1.549	(e,A^0), A^0= Na, Li A= (V_{Cd}-2D)$^-$	Acceptor bound exciton (Na or Li as acceptor)	**[2]** **[7]**
1.541	DAP, related with (eA^0)		**[8]**
1.490	(D^0A^0) or (eA^0)A =Ag		**[9]**
1.491	DAP,A=Ag	Donor- Aceptor pair transition between hydrogen like donor level and acceptor level correlated with the structure (V_{Cd}-D_{Cd}) or (V_{Cd}-D_{Cd})	**[3]**
~1.475	Y	Band realated to defects	**[10]**
1.467	ZPL_{Cl}	Zero Phonon Line of the A- band as Cl as donor	**[11]**
1.410		Relationated with V_{Cd}	**[12]**
1.48		Relationated with V_{Te}	**[12]**
1.17	V_{Te}-Te_i	1.10 eV band. Te_i in a tetrahedral site Tellurium Vacancies and intersticial	**[13]**
1.08	V_{Te}-Te_i	1.10 eV band. Te_i in an octahedral site	**[13]**
0.82-0.90	$Ge^{+2/+3}$, $Sn^{+2/+3}$	Related with deep centres	**[14]**

Nomenclature used:

X – Free exciton.
D – Donor impurity.
A – Acceptor impurity.
ZPL – Zero Phonon Line.
D-X – Luminescence Donor bound exciton (D).
A-X – Luminescence Acceptor bound exciton (A).
eA - electron- acceptor recombination.
DAP – Donor-acceptor recombination.
D^0X – Neutral donor bound exciton

References

[1] J.M. Francou, K. Saminadayar, J.L. Pautraut, Phys. Rev. B **41,** (1990), 12035.

[2]W. Joerger, M. Laasch, T. Kunz, M. Fiederle, J. Meinhardt, K.W. Benz, K. Scholz, W. Wendl, G. Müller-Vogt, Cryst. Res. Technol. **32**, (1997), 1103.

[3] E. Molva, K. Saminadayar, J.L. Pautraut, E. Ligeon, Sol. State Comm. **48,** (1983), 955.

[4] J.P. Chamonal, E. Molva, J.L. Pautrat, Solid State Commun. **43**, (1982), 635.

[5] S.H. Song, J.F. Wang, M. Isshiki, J. Crystal Growth **257**, (2003), 231.

[6] "*Narrow gap cadmium-based compounds*", P. Capper, Emis datareviews series nº 10, Inspec Pub., 1st Ed., England, 1994, Cap. B3.4.

[7] Hwa-Yuh Shin y Chermg-Yuan Sun, J. Cryst. Growth **186**, (1998), 354-361.

[8] D.P. Halliday, M.D.G Potter, J. T. Mullins, A.W. Brinkman, J. Cryst Growth **220**, (2000),30-38.

[9] M. Fieredrle,T. Feltgen, M. Rogolla, J. Meinhardt, J. Ludwing, K. ruge, K.W Benz, Nuc. Instrum. Meth., A **434**, (1999), 152-157.

[10] N. Armani, C. Ferrari, G. Salviati, F. Bissoli, M. Zha, A. Zappettini, L. Zanotti, J. Phys.: Condens. Matter **14**, (2002) ,13203.

[11] W. Stadler, D.M. Hofmann, H.C. Alt, T. Muschik, B.K. Meyer, E. Weigel, G. Müller-Vogt, M. Salk, E. Rupp, K.W. Benz, Phys. Rev. B **51**, (1995), 10619.

[12] Ch. Barnett Davis, D.D. allred, A. Reyes-Mena, J. Gonzalez-hernandez, O. Gonzales, B.C. Hess, W.P. Allred, Phys. Rev. B **47**, (1993), 13363- 13369.

[13] J. Krustok, V. Valdna, K. Hjelt, H. Collana, J. Appl. Phys. **80,** (1996), 1757.

[14] M. Fiederle, V. Babentsov, J. Franc, A. Fauler, J.P. Konrath, Cryst. Res. Technol. **38**, (2003), 588.

List of publications

1.- N.V. Sochinskii, **M. Abellán,** M. Martín Gonzalez, E. Saucedo, E. Diéguez, F. Briones. "Vapour growth of Cd(Zn)Te columnar nanopixels into porous alumina" Nuclear Instrum. and Meth. A 568(1), pp. 455-458 (2006). -A

2.- **M. Abellán**, J. Anguita, N.V. Sochinskii "EBL Bi-layer resist scheme for CdTe submicron structures for lift-off processing" Microelectronic Engineering Vol. 84, Issue 5-8, pp. 1117-1119 (2007). – A

3.- N. V. Sochinskii, **M. Abellán**, and J. Rodríguez-Fernández, E. Saucedo, C. M. Ruiz and V. Bermúdez, "Effect of Yb concentration on the resistivity and lifetime of CdTe:Ge:Yb codoped crystals". Applied Physics Letters 91, 202112 (2007).

4.- D. Fuster, **M. Abellán**, J. Anguita and N.V. Sochinskii"Effect of reactive ion beam etching on the photoluminescence of CdTe epitaxial layers". Applied Physics Letters 103, 056108 (2007).

5.- P. Hidalgo, J. Piqueras,N.V. Sochinskii**, M. Abellán**, E. Saucedo, E. Diéguez "Cathodoluminescence study of CdTe crystals doped with Bi and Bi:Yb". J.Master Sci (2008) 43:5605-5608.

6.- N.V. Sochinskii E. Saucedo, **M. Abellan**, J. Rodríguez-Fernández, P. Hidalgo, J. Piqueras, C.M. Ruiz, V. Bermúdez, E. Diéguez. "Growth and characterization of CdTe:Ge:Yb" J. Crystal Growth 310 (2007) 2076-2079.

7.- N. V. Sochinskii**, M. Abellán**, and J. Rodríguez-Fernández, J.L.Plaza, V. Carcelen, E. Dieguez, "Effect of source composition on the vapor phase epitaxy of Cd_{1-x} Zn_xTe large-area layers". J. Crystal Growth 310 (2007) 1669-1673.

8.- A. Martínez, F. Cuesta-Soto, J. García, J. Martí, N.V. Sochinskii, **M. Abellan**, J. Rodríguez-Fernández, S. Mengali, I. Reid, M. Robertson, S. Neretina, R. A. Hughes, J. Wojcik, J.S. Preston and P. Mascher "Cadmium telluride: a silicon-compatible optical material as an alternative technology for building all-optical photonic devices" Proc. SPIE, Vol. 6996, 699608 (2008).

9.- Sochinskii, N.V , **Abellán, M**. , Rodríguez-Fernández, J. , Diéguez, E. , Franc, J. , Hlidek, P., Praus, P. , Babentsov, V. "Sub-bandgap photoluminescence from as-grown and annealed layers of CdTe ".Superlattices and Microstructures. Volume 45,Issue 4-5, April (2009) 228-233.

10.- **M. Abellán** and J. Anguita." Fabrication of CdTe waveguides imbued in SiOx by VPE growth and etch- back technology". (Submitted: Journal of Physics D).

11.- **M. Abellán**. V. Izquierdo- Roca.and J. Anguita. " Nanostructures growth by etching process" (In preparation).

12-. M. Abellán, P. Hidalgo, J. Rodriguez- Fernandez, J. Piqueras and N.V. Sochinskii "Effect of Thermal treatment of CdTe:PdI/Si films" (In preparation).

Contribution to conferences

***M Abellán**, J. Anguita, N.V. Sochinskii
2nd NanoSpain Workshop, Barcelona (Spain), Marzo 2005
"Nanoprofiled Si substrates for heteroepitaxy of strongly lattice-mismatched semiconductor compounds"
Poster presentation.

*N.V. Sochinskii, **M. Abellán**, M. Martín Gonzalez, J.P. Silveira, F. Briones
10th European Symposium on Semiconductor Detector, Wildbad Kreuth, Germany, Junio 2005
"Growth of CdTe columnar nanopixels".
Poster presentation.

***M. Abellán**, J. Anguita, N.V. Sochinskii
TNT2005 "Trends in Nanotechnology", Oviedo (Spain), Agosto 2005
"Substrate nanoprofiling for heteroepitaxy of high-Z semiconductor compounds" .
Poster presentation

***M.A. Abellán**, J. Anguita, N.V. Sochinskii
MNE 2006 International Conference on Micro- and Nano-Engineering, Barcelona (Spain), September 2006.
"EBL Bi-layer resist scheme for CdTe submicron structures for lift-off processing".
Poster Presentation

*N.V. Sochinskii, **M. Abellán**, J. Rodríguez, E. Saucedo, C.M. Ruiz, V. Bermúdez, E. Diéguez
Room-Temperature Semiconductor Detectors – RTSD, San Diego, California, USA, October 2006
"Semi insulating CdTe crystals and large area layers co-doped with rare earth elements"
Oral conference

*A. Martínez, F. Cuesta-Soto, J. García, J. Martí, N.V. Sochinskii, **M. Abellán**, J. Rodríguez-Fernández, S. Mengali, I. Reid, M. Robertson, S. Neretina, R. A. Hughes, J. Wojcik, J.S. Preston and P. Mascher. SPIE, 2008. *"Cadmium Telluride: a Silicon-compatible optical material as an alternative technology for building all-optical photonic devices"*.
Oral conference